Università degli Studi di Torino
Doctoral School of the University of Torino
PhD Programme in Chemical and Materials Sciences 36th Cycle

The structure-properties relationship in Co-based Heusler alloys for spintronic applications

Alessandro Difalco

Supervisor:
Prof. Alberto Castellero

Università degli Studi di Torino

Doctoral School of the University of Torino

PhD Programme in Chemical and Materials Sciences 36th cycle

The structure-properties relationship in Co-based Heusler alloys for spintronic applications

Candidate: **Alessandro Difalco**

Supervisor: Prof. **Alberto Castellero**

Jury Members: Prof. **Mauro Palumbo**
Università degli Studi di Torino
Dipartimento di Chimica

Prof. **Eric Alleno**
Université Paris Est Creteil, CNRS – Centre National de la Recherche Scientifique
Institut de Chimie et des Matériaux Paris-Est

Prof. **Stefano Boldrini**
CNR – Consiglio Nazionale delle Ricerche
Institute of Condensed Matter Chemistry and Technologies for Energies

Head of the Doctoral School: Prof. Eleonora Bonifacio
PhD Programme Coordinator: Prof. Bartolome Civalleri

Torino, 2024

Index

Abstract

As the interest for materials suitable for spintronic applications and spin-injection processes have consistently increased in last years, Co-based Heusler compounds received great attention, owing to their ability to potentially achieve 100% spin-polarization at room temperature, as a consequence of their half-metallic density of states. Despite being considerate promising for such purposes, the properties of Co_2HfSn and Co_2ZrSn Heusler alloys have not been yet fully understood, since defects were found to play a huge role on their transport, magnetic, and half-metallic behavior. In this work, we extensively investigated the correlation between the crystallographic structure and metallurgical microstructure of such compounds with their electronic, magnetic, transport, and thermal properties. The experimental results were compared with those obtained by DFT calculations both in pristine and defective systems.

Samples were obtained by different processing methods i.e. arc melting, melt spinning, spark plasma sintering. In Co_2ZrSn, Rietveld refinement of X-rays diffraction patterns allowed to evaluate the occupancy of Co-sites, which depends on the processing route. The lattice parameter linearly scales with the occupancy fraction in the Co-site for the different samples. Since all samples were nominally stoichiometric, those with a larger vacancy concentration on the Co-site in the Heusler phase showed a larger amount of Co-rich secondary phases, in agreement with the matter balance.

For both alloys, the transport and magnetic (i.e. magnetic moment, Curie temperature) properties were measured for bulk samples obtained by arc-melting, followed by annealing, and by rapid solidification (melt-spinning), followed by spark-plasma sintering. The different behavior of Seebeck coefficient, electrical and thermal conductivities, and magnetization were explained in terms of different degrees of vacancy concentration on the Co-site. Electrical resistivity (R) measurements at low T showed a change of regime from a R/T^2 to a R/T^x ($1<x<5/3$) dependency, which was explained in terms of a change of electron scattering mechanisms. Such explanation is not incompatible with a crossover from a half-metallic to an itinerant ferromagnetic state.

The band structure and the electronic density of state (DOS) were computed by density functional theory, both for the pristine structure and for a defective supercell containing vacancy on the Co site. For low concentrations of vacancies, the band gap in the minority spin DOS is maintained, indicating a half-metallic behavior also in the defective compound. The formation enthalpy of Co vacancy was estimated to be 0.001 eV and 0.004 eV for Co_2ZrSn and Co_2HfSn, respectively, indicating that such defect is already stable at extremely low temperatures.

1. Introduction to spintronics

It is recognized by a large number of epistemological experts, science philosophers and historians that scientific and technological knowledge have increased faster in the last 150 years than during the remaining history of mankind [1–5]. The progress in aeronautics is often taken as an example to put the previous claim into perspective. In fact, since the construction of the first aeroplane in 1903, it took only 58 years to achieve the first human spaceflight, and only 66 years to successfully land on the surface of the moon. Another often cited example of such concept is atomic energy. Although the first reliably quantitative atomic model was proposed by Rutherford and Bohr in 1913, the first nuclear reactor was built barely 29 years later in 1942. Fourth generation nuclear reactors are expected to be available for commercial use as soon as 2030. Nevertheless, perhaps the most remarkable example of exponential technology growth in the last century is the advancement in electronics and computer science. Despite its limitations, Moore's law, according to which the number of transistor inside integrated circuits doubles about every two years, is often used as an immediate tool to demonstrate the giant progresses in microelectronics occurred starting from 1970s.

Improvements in computational power resulting from such exponential increase have been the driving force of the outstanding global economic growth of the last century, as well as that of deep changes in society and ethical values. The industry has undergone a radical transformation thanks to this exponential growth in computing capacity. Automation and production efficiency have significantly increased, allowing companies to produce goods at a previously unimaginable pace. This increase in industrial output has had a direct impact on the global economy, pushing towards greater productivity and value creation. The ability to design increasingly complex and powerful machines has revolutionized sectors such as automotive, aerospace, and consumer electronics, making consumer good products more accessible and reliable. Automation driven by increased computing capacity has revolutionized processes in various sectors. Moreover, the ability to perform complex tasks with precision and efficiency through computer-controlled machines has significantly improved productivity and reduced production costs. This had a significant impact not only on the global economy but also on the nature of human work, shifting the workforce from repetitive tasks to roles that require more creativity and problem-solving. The microelectronics-driven revolution of society becomes outstandingly evident when personal technologic devices, such as personal computers and smartphones, are considered. From expensive and cumbersome machinery accessible to only a few, computers have become personal items that most people in many parts of the world find indispensable in daily life. Smartphones, evolved from early cell phones, are now powerful pocket computers that offer unprecedented access to information, entertainment, and services. The Internet, which has developed in parallel with this hardware growth, has revolutionized the way we communicate, work, and play, making the world more connected than ever.

The exponential increase in computing capacity has also had profound social implications. Access to information has become almost unlimited, reshaping education, politics, and media consumption. Knowledge and learning have become more accessible, with online educational resources offering opportunities for education to anyone with an Internet connection. However, this has also raised issues related to privacy and security, as the amount of personal data generated and collected through online devices and services has increased exponentially.

Silicon-based logic devices have, as a matter of fact, become an industry of strategic importance also in a geopolitical perspective, making the improvements transistor-based integrated circuits crucial for world's economic and political stability. Despite such growth, a lot of concern recently aroused, as physical limitations such as tunnel-effect phenomena, current leakage and overheating are increasingly hindering a further scale-down of transistor's dimensions. In particular, the problem of controlling the current flow in proximity of the gate electrode is becoming increasingly difficult as the size of transistors shrinks at nanoscale. Although multi-gate MOSFETs, such as FinFETs and GAAFETs, helped to mitigate such problems, significant source-to-drain current leakage, and limited options for gate metals and channel materials still affect transistors when dimensions are furtherly scaled down. In fact, it was reported by microprocessor architects that semiconductor advancement limits have slowed the industry down since around 2010, dropping the pace of the predicted growth down to a cadence of two and a half years instead of two. In 2016, it was stated by Intel Corporation,

one of the world's largest semiconductor-chip manufacturer by revenue, that improvements in MOSFET devices have slowed starting from the "22-nm" process nodes [6]. It is important to note that since 1997, process nodes have been named purely on marketing bases, as neither gate length, gate pitch, metal pitch, or any other physical dimension of the integrated circuit is actually twenty-two nanometers. As a matter of fact, the IRDS (International Roadmap for Devices and Systems) road map shows indeed an actual contacted gate pitch of 51 nm for the 5-nm generation chips, commercialized starting from 2020. Gate pitches of 48 nm are typical of 3-nm chips (first marketed in 2022), while a gate pitch of 45 nm is predicted for the 2.1-nm integrated circuit which production is forecasted between the year 2024 and 2025 [7].

At the current rate of progress, an endpoint is predicted at about a decade from now, as far as the metric scale-down of integrated circuits is concerned, when the metal pitch of transistors will be by that time nearing the resolution limits of extreme-ultraviolet lithography (EUVL). In 2020, Dr. Paolo Gargini, chairman of IRDS, and head of the first submicron process development team at Intel Corp. in 1985, stated that by 2029 the limit of lithography will be reached, suggesting that the only way forward from that point to increase transistor density would be node-stacking [8].

In order to overcome these shortcomings, research on new materials plays a prominent role. Alternative semiconductors as InGaAs are seen as promising in replacing doped silicon for high-speed, low-power logic devices. Quantum well and tunnel field-effect transistors based on III-IV compound semiconductors are receiving great attention as alternatives to traditional MOSFETs. Graphene in various forms, especially as nanoribbons, was also studied; however, its application remains potential. More ambitious are other approaches that don't rely on physical scaling, or in a change of material. Most prominently, spin-based logic and memory options have been extensively studied on a laboratory scale, becoming recently also an industrial reality.

1.2 Fundamentals of random access memories

The first electronic random access memory (RAM) was first introduced in 1947 with the developing of the Williams-Kilburn tube [9]. The working principle of this device is quite simple: a grid of luminous dots is displayed on a cathode-ray tube, causing the accumulation of an electric charge is consequently accumulated in correspondence of each spot. This can be read by a thin metal sheet placed in front of the display, allowing the computer to determine if a "0" or "1" is written in each location. A periodic refreshing of the grid was needed as the intensity of the spots on the display faded over time. The refreshing operations is performed with the same basic method of the writing process using external circuitry. This was a turning point for computer technology, as the speed of electronic memories finally matched those of the electronic components inside calculators, greatly outperforming previous mechanical or acoustic-based devices. The Williams-Kilburn tube remained a crucial of components of calculators until mid-1960s, when it was replaced by more advanced magnetic-core memories.

Despite being an obsolete design, Williams-Kilburn tube's operative processes are extremely similar to those of modern semiconductor-based DRAMs, and can be used as a didactic tool to explain the fundamental principles of RAMs. As an example, let's imagine a magnetic tape in which a certain quantity of data is stored, *i.e.* a playlist of songs. In order to listen to the last song on the playlist, the magnetic tape must be unrolled by a specific length, requiring a certain amount of time. Similarly, to enjoy the second or third song, the tape has to be unrolled by a shorter length, requiring less time. The first song on the playlist is immediately accessible, as it is not necessary to unroll the tape by any length. This is method of storing information is called direct-access memory, and it is typical of devices like hard-disks, CD-RWs, DVD-RWs, and, of course, magnetic tapes. In such memories, the time required to read and write data strongly depends on their physical location inside the storing medium as a consequence of mechanical limitations, such has unrolling speed, rotation speed, arms movement, etc.

On the contrary, the random access memory is a form of electronic computer memory which can be read or changed in any order. In fact, in such devices, data can be read or written basically at the same speed independently on their physical location inside the memory. Taking the Williams-Kilburn tube as an example,

each spot on the fluorescent screen can be read and written at the same time, since the electrons emitted by the cathode-tube collide with the screen simultaneously. Despite being both direct memories and RAMs used basically for data storage, their specific role inside computers is profoundly different. On the one hand, the first device is used for long term storage of information both inside and outside calculators. On the other hand, random access memories are primarily used as temporary storage and working space for operating systems and applications inside computers. Here, the programs which are to be executed by the CPU are loaded inside the RAM. At the end of their use, these are deleted from the memory; thus, data, if not opportunely saved inside and hard-drive, are lost at the end of the operation. Modern RAMs contains circuitries able to connect data lines to the addressed storage location, usually accessing more than one bit of storage by the same address. For this reason, RAMs usually possess multiple data lines, from which the nomenclature "8-bit", "16-bit" etc. derives.

RAM units are based on memory cells, which are the fundamental building block of a computer memories. This is an electronic circuit which store one bit of binary information: a logic 1 can be stored setting the cell at high voltage, while a logic 0 is set when the voltage level is low. Modern dynamic RAMs (DRAMs) are based on memory cells composed of one transistor and one capacitor, in which the charge is stored. Since the charge slowly leaks away from the capacitor, the circuit must be "refreshed" periodically by flowing electric current. Different types of RAMs are based on different architectures of memory cells with consequent advantages and disadvantages; however, DRAMs are by far the most widespread, as the great storage density with low cost per unit overcame until now the detriment of a rather high power consumption. Memory cells are usually arranged inside RAM units in arrays, typically organized in sets of address lines. Multiplexing and demultiplexing circuits are used to set and read values (defined as sequence of bits) inside memory cells.

In order to actuate their purpose, memory cells must be able to be correctly perform basic tasks:

- *Writing*: the operation of setting and modifying the value (1 or 0) of the cell. In Williams-Kilburn tubes this was performed by modifying the direction of electronic beams inside the cathode-tube; whereas, in modern DRAM cells, the writing process is executed operating the transistor integrated in the cell.
- *Reading*: the operation of assessing the value of the cell (without modifying such value). In DRAMs, the reading process is destructive, as it removes the charge in the memory cells of an entire array's row. In order to overcome this issue, specialized latches, one for each memory cell column, called sense-amplifiers are built on the chip to temporarily store the data. During the operation, sense amplifiers rewrite the data inside memory cells after the reading process.
- *Refreshing*: the process of periodically reading the data and immediately rewrite the read information in the same location without modification. The purpose of this procedure is to preserve the information stored in memory cells, since, as time passes, the charge stored in the memory cell's capacitor leaks away. Without being refreshed, stored data would eventually be lost.

While the reading and writing process are fundamental for any computer memory device, the refreshing operation is typical of the so-called dynamic (or volatile) memories, such as the abovementioned dynamic DRAMs. Dynamic memories require a constant supply of power in order to store data. In such systems, information is typically lost as power is switched off. RAM units whose architecture does not require information to be periodically refreshed, and can therefore store data for long periods of time, are called static (or non-volatile) random access memories (SRAMs). Although static memory devices are nowadays usually associated with direct-access memories, such has hard-disks, flash drives, magnetic tapes etc., SRAMs were the most widespread type between mid '60s and mid '80s. Even if they require less power as no refreshing is needed, the memory cell architecture of semiconductor-based SRAMs, which consists in a 6 transistors circuit, was found to be more complicated and less down-scalable compared to that of a DRAM. Besides, significant current leakage was found to occur when the cell's temperature increase, paving the way for DRAMs to become the industrial standard for computer industries starting from the mid '80s.

1.3 Spintronic devices

As already mentioned in previous sections, despite the growth of DRAMs and semiconductor-based memory devices, physical limitations linked to transistor's down-scaling, charge leakage, and power consumption already started to increasingly hinder further developments of such technology. Non-volatile memories would resolve power consumption issues; however, semiconductor-based SRAMs are affected by poor down-scalability and high current leakage. Starting from mid '80s, a rather high effort was put in order to solve these limitations, resulting in a plethora of innovative and out-of-the-box approaches.

Magnetic-core memories were the predominant form of random access memories between about 1955 and 1975. Toroidal rings (cores) of a hard magnetic material were used as memory cells (each core could store one bit), and arranged in X-Y arrays contacted by electrical wirings. The writing process would require to electrify one X and one Y wire to half of the required power, thus only the single core at the intersection would receive sufficient energy to be written. The direction of the current would determine the direction (clockwise or counter-clockwise) of magnetization, determining the storage of a 1 or 0. With the advent of purely semiconductor-based SRAMs, this technology rapidly became obsolete as affected by poor memory density. Developments of magnetic RAMs remained marginal until mid '80s, when the discovery of the giant-magnetoresistance (GMR) effect, and the increasingly evident limitations of transistor-only SRAMs units stimulated once again the research on magnetic random access memories (MRAMs).

MRAMs work on the principle of spintronics. Instead of relying only to charge properties of electrons like conventional semiconductor electronics, spintronics devices make use of electron's spin properties. The integration of spintronic devices inside semiconductor-based memories is seen as an effective way to achieve further down-scaling of integrated circuits, reduce current leakage, and strongly decrease power consumption. The storage of information based on magnetic materials was also proved to provide non-volatility and unmatched endurance with respect to resistive memories [10]. In 1990s, the invention of magnetic tunnel junctions (MTJs) opened the possibility to achieve significant magnetoresistance effect at room temperature, allowing better cell reading. In early 2000s however, the research in MRAMs declined as the at that time existing writing techniques (performed by switching the MTJ magnetization) were not scalable, effectively hindering the achievement of high memory-densities. In mid 2000s however, the application of spin-torque transfer (STT) effect as a physical principal to perform the writing process fuelled once again the interest for such technology. With such technology, STT-based MRAMs (STT-RAMs) were found to be easily down-scalable, reliable, and relatively cheap to manufacture [10].

As 2024, the production of STT-MRAMs and their direct improvements (such as spin-orbit transfer MRAMs and domain-wall MRAMs) is an increasingly strategic industrial reality. Companies like Honeywell, Everspin, Samsung, Avalanche Technologies, Intel Corporation, and Netsol are currently among the largest producers of such devices by revenue, while other chip manufacturers like IBM, Toshiba, TSMC, and UMC have already started the development of proprietary STT-RAMs production lines, or have partnered with the before-mentioned sector-leaders to market their own version. The market growth of such sector becomes evident considering that in 2020 the global revenue for MRAMs market was estimated around 892 million USD, while the prediction for 2025 is around 5 billion. The compound annual growth rate (CAGR) was reported being around 35.8% from 2018 to 2025 [11]. Other market size analysis and forecast services quantify the MRAM market worth 1.49 billion USD in 2024, while a net worth of 7.03 billion is predicted for 2029, implying a CAGR of 36.43% [12].

1.3.1 Working principles of MRAMs

The typical configuration of a MRAM memory cell consists in a transistor and a magnetoresistive element, quite similar to a DRAM cell which contains a transistor and a capacitor. A transistor is needed in the MRAM cell to provide the current needed for the writing operation, and to amplify the voltage difference between the 1 and 0 state. If in a classic DRAM cell the information is stored as electric charge inside the capacitor, in a MRAM it is the resulting resistance of the magnetoresistive element which determines the value of the cell [13].

The first example of magnetoresistive element, which is the component that fundamentally stores binary digits, typically consisted in a spin-valve [10]. This is a layered structure which relies on the physical phenomenon of giant magnetoresistance to store the information, as shown in Figure 1.

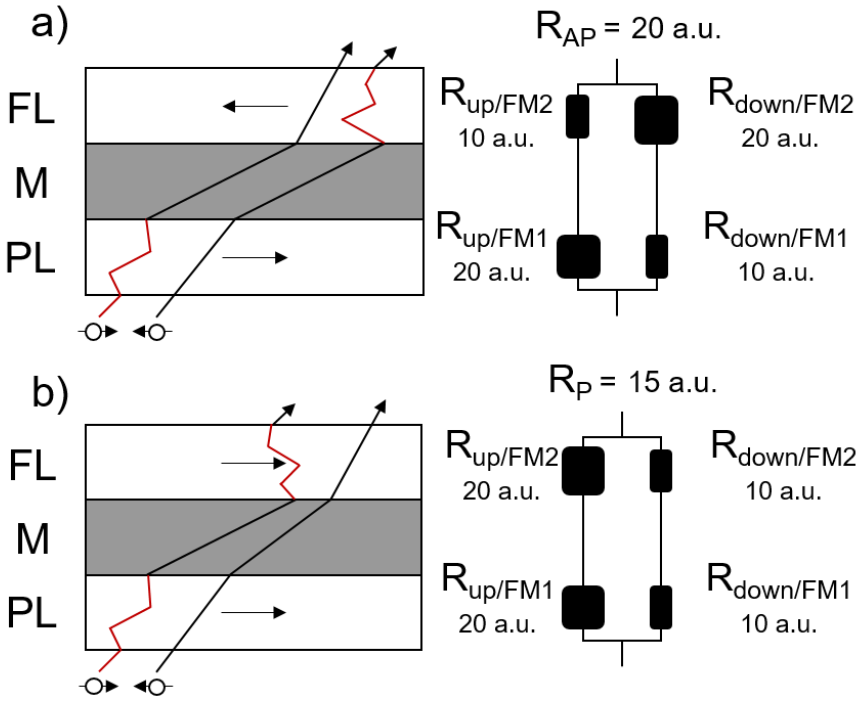

Figure 1: Schematic representation of a spin-valve in the a) antiparallel, b) parallel configuration. FL is the free layer, PL the pinned layer, and NM is the non-magnetic layer. R_{AP} and R_P are the electric resistances in the antiparallel and parallel configuration, respectively.

Giant magnetoresistance (GMR) occurs in systems composed of two ferromagnetic layers separated by a non-magnetic metal. When an electrical current flows across such structure, the total resistance depends on the mutual magnetization's orientation of the two of ferromagnetic elements: this will be lower if the two magnetic moments are parallel, or higher if they are antiparallel. This happens because the two different spin states of electrons (up, and down) are scattered differently when they flow inside ferromagnets, as the density of states of such materials is non-identical for their majority and minority-spin sub-bands. The resistance's difference at the end of the junction makes the reading process possible in spin-valves, as a binary 1 (low resistance, hence high voltage) is associated to the parallel, and a binary 0 (high resistance, hence low voltage) to the anti-parallel configurations, respectively. A similar effect, namely tunnel magnetoresistance (TMR), occurs when an insulator is used as a separation film instead of a conductive metal. Early models of magnetic memory cells based the GMR effect were rapidly abandoned in favour of TMR-based devices, or magnetic-tunnel junctions (MTJs), as they were affected by poor reading signal. Representative orders of magnitude of MTJs are of few nanometres, as a thicker insulator layer would make the tunnelling of electrons between the two ferromagnets impossible. Contrary to spin-valves, resistance differences typical of MTJs are sufficient to produce the voltage swing required for applications in integrated circuits, thus their widespread use to the detriment of GMR-based cells [10].

As already discussed previously, a memory device should be able to perform three main operations: reading, writing, and storing binary digits. In MRAMs, these tasks are fulfilled as follows:

- The reading operation is performed by sensing the resistance of the MTJ. This is done by flowing an electric current through the layered system and evaluating the final voltage at the end of the circuit to distinguish between 0 and 1 states.

- The writing operation is carried out by changing the orientation of one layer of the junction (called free layer). This has been historically performed in various ways; however, current state of the art MRAMs writing operations are based on the spin-torque transfer effect.
- The storage of information relies on the magnetic anisotropy of the free layer which retains the "written" magnetization over time. In MTJs, the magnetization of the pinned layer (PL) is fixed, while that of the free layer (FL) can vary to store binary 0 and 1 digits. In order to switch the orientation of magnetization, and energy barrier must be overcome. Since the magnetization of the PL must never be changed, materials with intrinsically high magnetization-switch activation energy are used; whereas, for the FL, materials with non-negligible magnetic anisotropy are selected. Magnetic anisotropy should be sufficiently high to store the value of the memory cell typically for 10 years. The energy barrier (E_B) for the switching of the free layer is proportional to $K_u V$ (with K_u the magnetic anisotropy constant, and V the volume of FL). Thus, K_u must be tuned to be sufficiently higher than the thermal energy $k_B T$ (60 times is considered the standard to achieve an information retention of approximately of 10 years), and sufficiently small to allow the writing process to occur without errors. From an engineering point of view, MTJs are classified based on the storage mechanism: junctions in which the magnetization of the ferromagnetic layers is parallel to the film plane are called in-plane MTJs, while perpendicular MTJs have the magnetization perpendicular to the film's surface [10].

1.3.2 Reading mechanisms: GMR and TMR

From an engineering perspective, a minimum voltage difference of 0.2 V between the low and high resistance states is required to read the value of a memory cell correctly and reliably. As already mentioned, in MRAMs magnetoresistance (MR) is responsible for such difference, thus being the physical principle of their reading mechanism.

The MR effect was first discovered in 1856 by Thomson [14], when the electrical resistance of various metal was measured to be different depending on the orientation of magnetic field. This was later found to be caused by spin-orbit effects; in fact, the scattering of electrons travelling along the lattice is different as the medium's electronic density is slightly deformed by the change of magnetization's orientation. Being this effect intrinsically anisotropic (as they are most of the crystalline structure-dependant properties), it was called anisotropic magnetoresistance (AMR). Compounds showing high AMR effect, like NiFe Permalloy, were used in earlier generations hard-disks [15].

In late 1980s, surprisingly high values of magnetoresistance were independently measured by Fert and Grünberg in layered systems. The discovery of such giant-magnetoresistance effect worth them the Nobel prize in physics in 2007, as the application of GMR in digital memory devices revolutionized hard-disks and data-storage technologies [16]. GMR effect is ultimately the result of spin-dependent electron's scattering phenomena inside ferromagnetic materials, as schematically depicted in Figure *2*.

In ferromagnetic materials, the total magnetic moment is antiparallel to the direction of total spin at the Fermi level (E_F), and the magnitude of electron scattering depends on the filling of the band responsible for magnetic moment. In non-magnetic materials (NM in Figure *2*), both the minority and majority spin sub-bands of the density of states are shaped and filled equally, meaning that +1/2 and -1/2 electrons will be evenly scattered. Contrariwise, in FM mediums, the DOS is different for the two spin states. Since the majority spin are conducted in the majority sub-band and minority spin in the minority sub-bands, they will undergo a different amount of scattering. In particular, majority spin electrons will come across a larger magnitude, as the majority sub-band is more filled than the minority. Considering the structure of a spin-valve in Figure *1*, when the magnetization of the two films is parallel one spin state will be the minority for both the layers, experiencing low scattering in both. When magnetization is anti-parallel, each spin-state will be the majority for one of the two layers, implying large scattering along the route [17]. Representing the scattering's magnitude like electrical resistors as in Figure *1*, it is straightforward to note that the parallel configuration determines the least total resistance, while the anti-parallel is the one that hinders electron's conduction the most. GMR-based

layered devices, called spin-valves, were able to generate magnetoresistances up to 10-20%, which were insufficient to generate the voltage drop required for a reliable reading process.

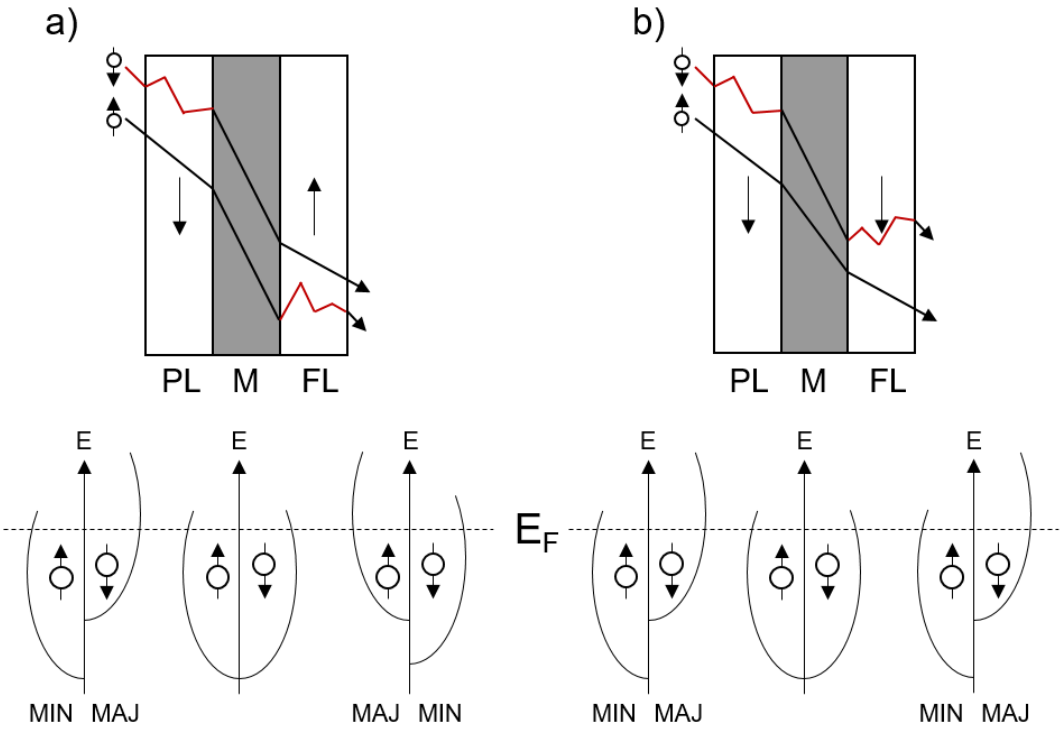

Figure 2: Density of states of each layer of a spin-valve and their effect on the conduction of +1/2 and -1/2 spin electrons in the a) antiparallel, and b) parallel configuration. MIN and MAJ indicate the majority and minority spin sub-bands, respectively, of the ferromagnetic materials.

In 1995, tunnel magnetoresistance (TMR) was first reported at room temperature [18], dramatically changing the research on MRAMs. From early magnetoresistances values of 15-16%, TMR of more than 600% were demonstrated at laboratory scale, while the current industrial standard is around 100-200%, providing sufficient voltage difference for reliable reading of memory cells [10]. Unlike GMR, where the resistance difference was driven by spin-dependent scattering in ferromagnets, in TMR this is based on spin-dependent tunnelling. In fact, when two FM layers are separated by a thin-enough insulator film, the number of electrons tunnelling from one FM to the other is higher when their mutual magnetization are parallel, and lower when anti-parallel [17].

A schematic representation of a MTJ is depicted in Figure 3. Considering the parallel state, both majority and minority-spin electrons are "free" to tunnel from FM1 to FM2 through the insulator (INS) thanks to the strong matching of the density of states sub-bands. On the contrary, in the anti-parallel state, the larger mismatch between ferromagnets' DOS (which sub-bands now strongly differs in shape and filling) hinders the tunnelling of majority-spin electrons, effectively reducing electric conduction. Since the parallel configuration implies lower resistance than the anti-parallel, exactly like in spin-valves, the storage of binary digits is possible [17]. The magnitude of such effect is given by the TMR ratio figure of merit [10]:

$$TMR = \frac{R_{AP} - R_P}{R_P} \tag{1}$$

A model proposed by Julliere [19] is also frequently used to express the TMR ratio in terms of the spin-polarization of the two ferromagnetic materials. Spin-polarization (P) is expressed as a function of the spin-dependent densities of states at the Fermi level (D):

$$P = \frac{D_{+1/2} - D_{-1/2}}{D_{+1/2} + D_{-1/2}} \tag{2}$$

where +1/2 electrons are considered those with spin parallel to the magnetic field, and -1/2 those anti-parallel. With *P* defined as such, TMR ratio can be rewritten as:

$$TMR = \frac{2P_1P_2}{1 - P_1P_2} \tag{3}$$

with P_1 and P_2 the spin-polarization of the two ferromagnets. When no voltage is applied to the MTJ, electrons can tunnel in both directions at equal rate; however, if a potential is present, electron will now tunnel preferentially towards the positive electrode. Assuming that spin is conserved during tunnelling, the current is therefore described as split in two independent components, one for each spin state.

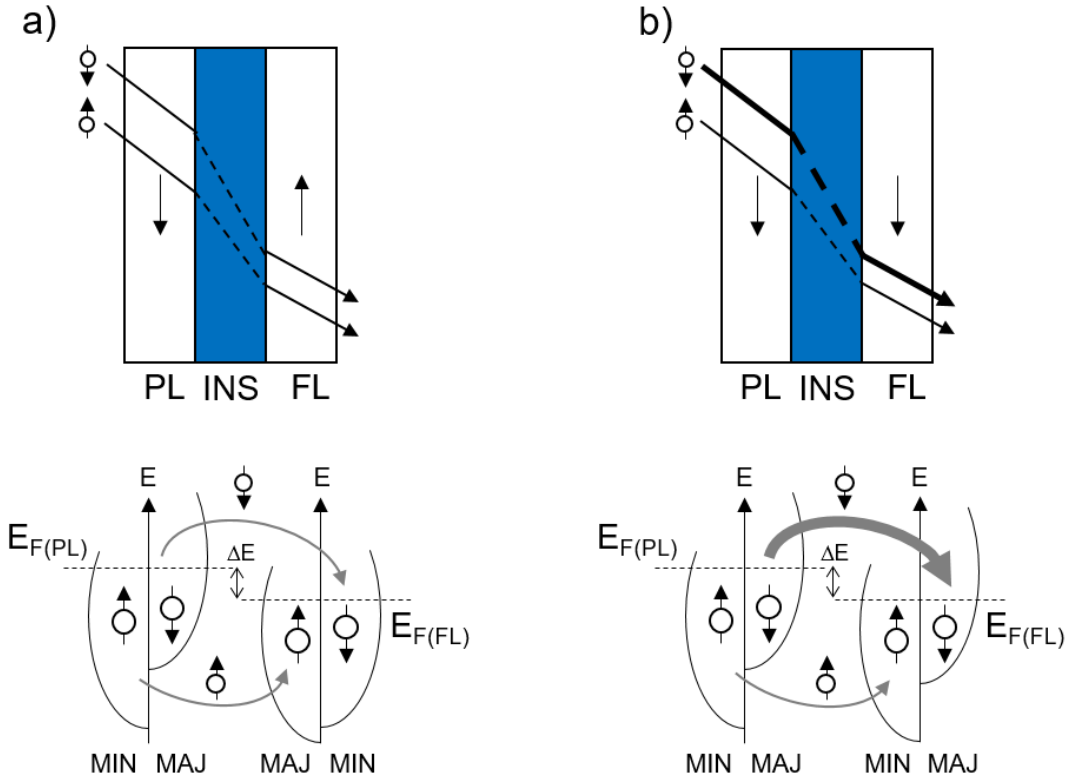

Figure 3: Schematic representation of a magnetic tunnel-junction (MTJ) and of the density of states of each ferromagnetic layer in a) antiparallel, and b) parallel configuration. $E_{F(PL)}$ and $E_{F(FL)}$ are the Fermi levels of the pinned layer and free layer, respectively. ΔE is the difference between the Fermi energies of the two ferromagnets, which is an indicator of bands' mismatch. The density of state of the insulator (INS) is not considered in the figure, as electrons are assumed to tunnel through the layer conserving their properties. The thickness of the arrows represents the amount of tunnelling electrons.

TMR ratio, and thus reading speed and efficiency, can be enhanced acting on numerous factors, such FM/INS band matching, layers' crystalline compatibility, film thickness, stack architecture etc., however, increasing ferromagnets' spin-polarization is perhaps the most straightforward. If both P_1 and P_2 are 1, meaning that both FM layers have 100% spin-polarization, TMR becomes infinite. In this condition, the MTJ becomes a switch, able to shift between a state low resistance and one of infinite resistance. Such 100% spin-polarization is peculiar of half-metallic ferromagnets, in which conduction of electron is fully spin-polarized [10]. Examples of such materials are CrO_2 and various Co-based Heusler alloys, which properties are of high interest in spintronics [20]. Experimental proof of half-metallicity and close-to-100% conducted electrons spin-

polarization was found, for example, at the $La_{0.7}Sr_{0.3}MnO_3$ /$SrTiO_3$ interface by Bowen et al. [21], in which spin-polarizations up to 99.6% were reported. Later, a *P* value of 93% was reported for the Co_2MnSi Heusler alloy by Jourdan et al. [22] at the interface with MgO. For Co_2MnSi, TMR ratios of 1995% and 354% were measured at 4.2 and 300 K, respectively [23], allowing their practical implementation in MTJs. Values between 50% and 90% were also observed for the CoFeCrAl Heusler-ordered alloy [24]. Furthermore, half-metallicity was predicted and indirectly observed for numerous other compounds [25]. The research on materials able to show such properties is a hot topic in spintronics and MRAM technology.

As far as the insulator is concerned, layers of amorphous materials like AlO_x led to maximum TMR ratios of 70% [26]. On the other hand, crystalline materials like MgO proved to be extremely effective, as figures of merit up to 1000% were reached in laboratory scale for the CoFeB/ MgO/ CoFeB junction [27]. From a metallurgical point of view, an orientation along the (001) direction is considered essential for MgO, as both the surfaces of the film must be textured along that crystallographic direction in order to maximize band matching with ferromagnetic materials. At the current state of MRAM technology, the CoFeB/ MgO/ CoFeB magnetic tunnel-junction is considered the benchmark for industrial application [10,27].

1.3.3 Writing mechanisms: field-assisted and spin-transfer torque

The writing process is the operation of changing the value of a memory cell from 0 to 1, and vice versa. In spin-valves and MTJs this is achieved by switching the magnetization of the free layer. Historically, this has been achieved in various ways, the oldest of which was to apply an external magnetic field in proximity of FL.

External field writing-driven MRAMs were the first to be developed. They consisted of a rather complicated architecture, since a sufficiently high magnetic field had to be applied only in correspondence of the selected cells to be written. In such systems, the magnetic field is brought directly to the specific memory cell powering two separate lines to half of the required intensity, similarly to what already done for earlier magnetic-core memories [28]. As the field that must be applied to obtain a successful switch is inversely proportional to the area of the storing element, down-scalability of was found to be problematic. From a practical point of view, field-assisted MRAMs with dimensions smaller than 90 nm were found to be infeasible due to the large current requirements (up to 10 mA for cell sizes of approximately 100 nm) [10,29].

The idea of using spin-transfer torque as the principle for writing magnetic memory cells nevertheless revived the research and commercial interest for MRAM technology [30]. The magnetization switching is here obtained by flowing a spin-polarized current (SPC) through the free layer. When a SPC is injected into a thin-enough ferromagnetic film, the angular momentum carried by electrons can be transferred into the layer, flipping the orientation of its magnetization as a result of ferromagnetic resonance. This effect is highly observable at a nanometric scale; whereas, at higher scales, phenomena like spin-scattering and spin-mixing hinder the transport and the injection of SPCs. The intensity of the switching current linearly scales with the size of the film, meaning that as the dimensions of the cell shrink, the required current diminish as well. As this method finally ensured convenient scalability towards smaller dimensions and simpler cell's architecture, STT-MRAMs rapidly become the state of the art for commercially marketed MRAMs [10,17,30]. Currents down to approximately 1 μA were found to be sufficient to write a junction of around 10 nm in size [27].

As illustrated in Figure 4, in STT-MRAMs, the writing process is different depending on the final state to be obtained. If the cell must be switched from the antiparallel to the parallel configuration (Figure 4a), a current is sent from PL to FL. When the electrons flow through the pinned layer, the ones having minority-spin are scattered, while the majority electrons tunnel towards the free layer. PL acts in this case as a spin-filter, allowing only majority-electrons to be directed into FL. This selection process is called polarization (or spin-filtering), and efficiently occurs only when the filtering layer is thick enough. As spin-polarized electrons reach FL, their spin angular momentum exerts a torque on FL's magnetization. If the intensity of the spin-polarized current is high enough, the exerted torque would be sufficient to ultimately flip the magnetization, allowing the system to reach the parallel state. Vice-versa, if the cell has to be written from the parallel to the antiparallel configuration (Figure 4b), the current is directed from FL to PL. As the free layer is not-thick enough to act as a polarizer, the current reaches the pinned layer in an unpolarised state. Here, only the majority-spin electrons

are allowed to tunnel and flow into the PL, while those having minority-spin are scattered back. Being the reflected current spin-polarized, a spin-toque is applied on FL, causing its magnetization to switch [10].

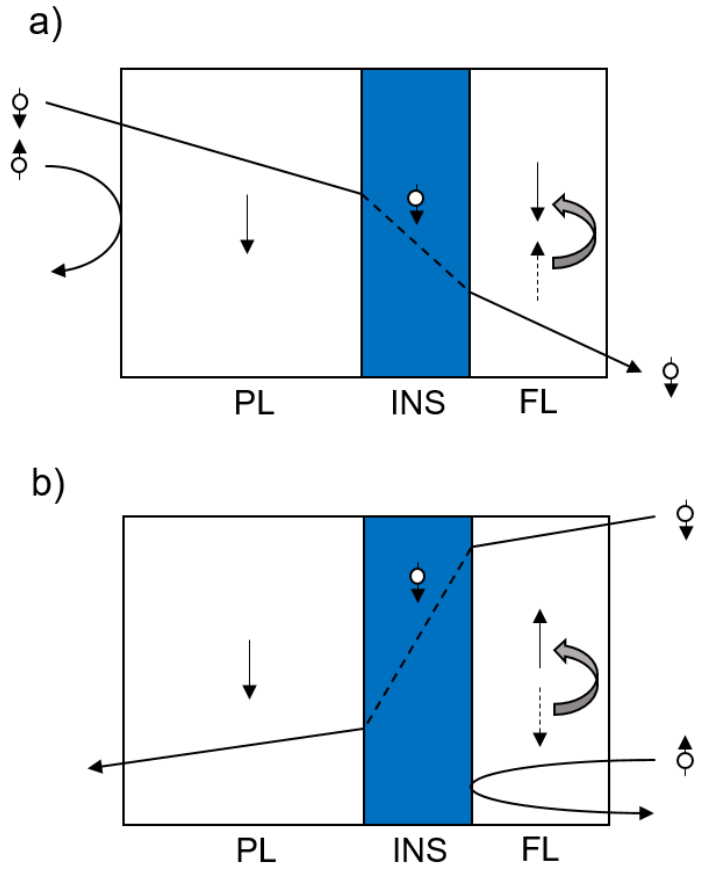

Figure 4: Schematic representation of the writing mechanism in STT-MRAMs. a) From and antiparallel to parallel, b) from parallel to antiparallel configurations. PL is thicker than FL.

The optimization of the current required for the writing process is a key factor in MRAM engineering. In fact, this has to be strong enough to ensure irreversible magnetization switch, but low enough to avoid excessive power consumption. The critical current J_W is given by [31]:

$$J_W = \left(\frac{\alpha}{\eta}\right)\left(\frac{2e}{\hbar}\right) M_s t H_K + 2\pi M_s \tag{4}$$

with *Ms* the saturation magnetization, H_K the anisotropy field, *t* the film's thickness and α the Gilbert damping constant, which measures the magnetization relaxing rate. η is the STT efficiency parameter, which is proportional to the spin-polarization of the injected current.

1.3.4 Storage methods: in-plane and perpendicular MRAMs

MRAMs can be classified in two main categories based on the architecture of the MTJ component, namely in-plane and perpendicular MRAMs. In the first class, magnetizations of PL and FL are parallel to the film's plane; whereas, in the second class the magnetization is perpendicular.

In-plane MRAMs were the first to be developed as they are the easiest to manufacture. Additionally, being the switching filed in early field-assisted MRAMs in-plane with respect to the MTJ's layers, in-plane magnetic fields were easier to be switched by such writing method. Nevertheless, the main drawback of such architecture is poor down-scalability due to the increase of magnetostatic fields with the shrinking of cell's size. In fact, significant magnetization curling at the edge of the films was found to occur when dimensions are scaled down,

leading to the formation of undesirable magnetic vortexes [32]. One way to minimize the presence of such vortexes is fixing the aspect ratio (length/width) of the layers to be equal or more than 2, implying the use of elliptically shaped junctions instead of cylindrical. However, MTJs with elliptic shape are not optimal as they require larger space than cylindrical, decreasing information density [33]. Besides, magnetization curling is also known for causing anomalous switching related to thermal stability issues. For these reasons, dimensions of in-plane MRAMs cannot be scaled down enough to guarantee sufficient cells density [32].

As already mentioned, the thermal stability factor Δ must be larger than 60 to assure a data retention goal of at least 10 years. In case of a uniform rotation of magnetization, as in MTJs, Δ can be expressed as follows [18]:

$$\Delta = \frac{H_K M_s V}{2 k_B T} \tag{5}$$

with V the the volume, and T the temperature. Considering the properties of the state of the art CoFeB/ MgO-based MTJs, values of $\Delta > 60$ result for cell dimensions not inferior to 60 nm, limiting the miniaturization of in-plane cells to such ultimate size.

The fabrication of films with perpendicular magnetic anisotropy (PMA) allows to significantly reduce magnetostatic fields in MTJs, as magnetization is enabled to be stabilized perpendicularly to the film-plane [10]. The first alloys used in this applications were well-established PMA materials such as GdFe/CoFe and other transition metal alloys such as TbFeCo and GdFeCo. Nevertheless, all of these were affected by nearly unavoidable oxidation issues [34]. Unexpectedly, the solution for such material problem came again from CoFeB, which was already predominantly used in in-plane MRAMs. In fact, CoFeB was found to show significant perpendicular magnetic anisotropy when for film's thicknesses smaller than 1.5 nm [35]. CoFeB/MgO based perpendicular magnetic tunnel-junctions (pMTJs) were observed to show TMR ratios higher than 100% as well as good thermal stability and low J_W [36].

1.3.5 Issues and improvements

Although the introduction of STT-MRAMs solved a large quantity of issues related to reliability and cost-effectiveness, important challenges are still present as a result of a relatively young technology compared to that of silicon-based industry. Failure issues can be divided into correctable (fixable) and non-correctable (non-fixable).

Fixable errors are caused by the properties of FL, and can be solved by sending a new signal to the cell (namely, by attempting to re-read or re-write). These issues are frequently caused by thermal fluctuations, which can cause reversals of magnetization orientations. Possible solutions would be to increase the intensity of the writing current, or increasing the time of the current pulse during the reading process; however, breakdowns of the insulator layer were found to occur when the current flux is too high [35,37]. Non-fixable errors are usually caused by the issues with the insulator layer. The breakdown of the oxide film leads to irreversible degradation of the MTJ. During the reading process, a significant resistance difference has to occur between the 0 and 1 states; therefore, thin oxide barriers must be used in order to avoid disturbs during the reading operation [37]. Furthermore, since the reading and writing operation in STT-MRAMs share the same access path through the junction (see Figure *3* and Figure *4*), the value of the memory cell can mistakenly be switched during the reading process if the current flux is too high.

To solve such problems, two main paths can be followed. On the one hand, the research on current state-of-the-art (mainly CoFeB and MgO), and in new innovative materials is crucial. On the other hand, developing new solutions on the architecture and engineering of memory cells plays a key role as well. As the perspectives of new materials in spintronics will be discussed in detail in the next section, this part will be focused on the latter topic.

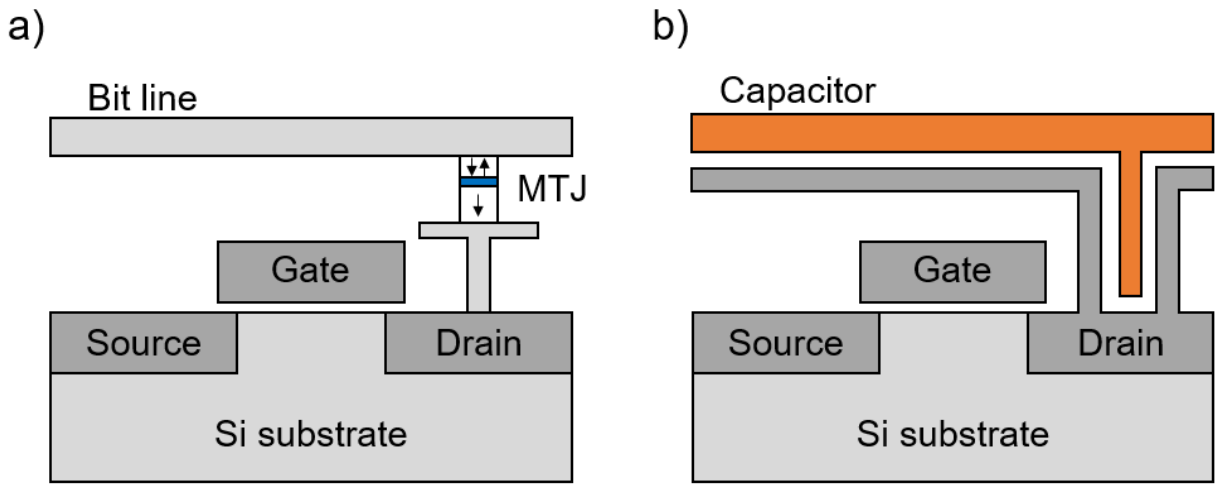

Figure 5: Representation of a a) STT-MRAM memory cell, b) stacked-capacitor DRAM memory cell.

The basic architecture of a STT-MRAM memory cell is shown in Figure 5. As already mentioned, a STT-MRAM cell differs from a common DRAM cell fundamentally because of the resistive element: a MTJ for the first (Figure 5a), and a capacitor, which can be built in various forms, for the latter (Figure 5b). A transistor is present on both, as it provides the necessary current to perform the reading and writing operations. In comparison to resistive RAMs, STT-MRAMs achieve faster switching speed up to 100 times [10]. Switching speed was found to be directly proportional to the applied writing current and inversely proportional to the resistance-area product of the MTJ [10]. Increasing the current and reducing the thickness of the insulator barrier are the most straightforward methods to achieve faster writing; however, a careful optimization has to be carried out to avoid breakdowns of the insulator barrier [15]. Other methods involve the tilting of FL with respect to PL in pMTJs. It was reported that a 5° tilt angle led to an improvement of 30% of the switching speed, while simultaneously reducing the current by 36% [38]. In orthogonal spin-transfer MRAMs, a spin-polarization layer is magnetized perpendicularly to FL, leading to large STT effect and fast writing speed. With such system, reliable writing has been achieved with current pulses of approximately 550 ps, leading to a speed in the range of 2 GHz [39]. Increasing the spin-transfer torque efficiency (η) is also beneficial for writing efficiency, as J_W is inversely proportional to η (see Equation 4). The use of dual MTJs, which are composed of two PLs and one FL, was found to double the STT efficiency compared to a MTJ having the same resistance-area product [40].

Improvements that involve more drastic changes in memory cells architecture are also under investigation. Alternative spin-based memories such as Spin-Hall effect (SHE) based MRAMs are receiving attention due to potential lower thermal stability induced retention failure rate, and lower writing delay. In such devices, spin-polarized currents are produced inside FL using the Spin-Hall conduction properties of certain metals, such as Pt and β-Ta, which are deposited as thin-films adjacently to the MTJ ferromagnetic layer. In fact, SHE is a phenomenon in which spin-orbit coupling cause the deflection of electrons of different spin in different directions, ultimately generating spin-polarized currents. Such SPCs are produced transversally to the applied charge current [41]. Spin-orbit interaction was also found to generate a torque on magnetization similarly to what already observed for the spin-transfer torque effect. In spin-orbit torque MRAMs (SOT-MRAM) a current flow through an electrode, the write line, adjacent to FL. The direction of magnetization of the free layer is decided by the verse of the current. Although in such architecture the reading and writing path are separated implying a higher degree of reliability, SOT-MRAMs memory cells are more complex as they consist in a 2-transistor circuit with an additional line for writing. Although spin-orbit effect is quite efficient for magnetization switching, the physical principle causing such phenomenon has not yet been fully understood, requiring more fundamental research before a large scale commercial use [42]. Other practical improvements on the STT-MRAM cell include the application of a voltage to the FL/insulator interface to reduce the magnetic anisotropy of the free layer, enabling the writing process to be performed at lower currents [43]. The voltage

control of magnetic anisotropy (VCMA) is based on the fact that electric fields were observed to change the occupancy of atomic orbitals at the interface. This effect, coupled with spin-orbit interactions, leads to a change of anisotropy. Also in this case, not a clear physical explanation has yet been provided, as only a qualitative description based on the Rashba effect has been proposed [44]. Other devices like domain wall memories and skyrmion racetrack memories are currently under intensive study; however, due to the complicated nature of the physical principles on which they are based on, more extensive research is still required [10].

2. Innovative materials in spintronics

As already mentioned, the current state-of-the art for MTJs built inside commercially available STT-MRAMs is the CoFeB/ MgO/ CoFeB junction. Faster and more reliable MRAMs are those which boost the efficiency of the reading and writing processes, and can also store data for a sufficient amount of time. Besides the already discussed engineering improvements, in order to enhance the reading efficiency, it is necessary to increase the TMR ratio, while to boost the writability one has to lower the critical writing current J_w. Ultimately, this leads to the need of maximize Equation 1-3, and minimize Equation 4. Also, to keep the data safely stored for a time of more than 10 years, the result of Equation 5 should be at least higher than 60.

Considering Equation 3 and 4, it can be noted how the spin-polarization, *P*, is present in both. In Equation 4, *P* is an explicit term and leads to a TMR ratio that tends to infinite when its value is 1. In Equation 4, *P* is not explicit; however, the STT efficiency parameter η directly depends on spin-polarization, meaning that high values of *P* minimize J_w. It is easy to understand that the research on materials exhibiting high spin-polarization (possibly even above room temperature) is of major importance in spintronics, as such parameter is simultaneously beneficial both for the reading and writing of MRAMs [10].

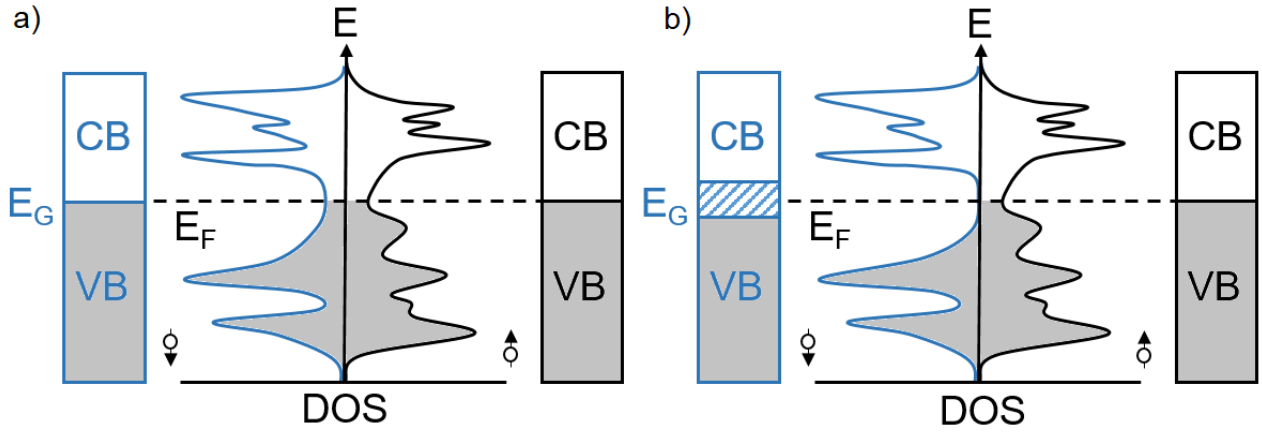

Figure 6: Representation of the density of states of a a) ferromagnetic compound, and b) half-metallic ferromagnet. VB is the valence band; CB is the conduction band.

Half-metallic ferromagnets (HMFs) are materials which recently attracted extensive interest due to their ability to potentially achieve 100% spin-polarization. Such property arises from the peculiar DOS of these compounds, schematically shown in Figure 6. In ferromagnetic materials, the imbalance of electrons having spin 1/2 and -1/2 can be described with two separate sub-bands of the DOS diagram. Here, despite the presence of a majority-spin channel (black) and a minority-spin channel (cyan), the density of states at the Fermi level is not zero for both. In a half-metallic ferromagnet, a band-gap is present in correspondence of E_F in the minority-spin sub-band, leading to a conductor-like majority band and a semiconductor-like minority channel. This peculiar electronic structure is responsible for several interesting properties which are of high interest in spintronic applications, the most important being probably their ability to achieve theoretical 100% *P*. In fact, when a current is directed through a HMF, electrons having majority spin are free to flow across the material as they travel following the conductive channel. Nevertheless, electrons having minority spin are not able to be conducted, as the access to CB in the minority-spin sub-band is hindered by the presence of the band gap [25,45].

Co-based Heusler alloys, which are ternary compounds of X_2YZ stoichiometry (where, X, Y are transition metals, and Y is a p-group element) and $L2_1$ crystal structure, have been reported to show half-metallic properties. Direct proof of half-metallicity was found for example for Co_2MnSi [22], Co_2FeAl [46] and $Co_2FeAl_{0.5}Si_{05}$ [47]. Spin-polarizations up to 93%, leading to TMR ratios of 354% at room temperature were measured for Co_2MnSi [22]. Evidence of half-metallicity was found for a large number of other Co-based

Heusler compounds, such as Co_2FeSi [48], $Co_2V(Al,Ga)$ [49], $Co_2Ti(Si,Ge,Sn)$ [50], Co_2ZrSn [51], Co_2HfSn [52,53], as well as others [54].

Concerning the transport properties of HMF materials, in 2014 Boona et al [55]. described the spin-dependent Seebeck effect as the result of the spin-dependence of the electronic density of states in ferromagnetic materials, where each spin component (up and down) give rise to a separate thermopower contribution (S_{up}, and S_{down}). According to the Stoner model, being the two spin-populations mutually independent, each population will have independent internal conductance and will form separate conduction channels (G_{up} and G_{down}). If a thermal gradient ΔT is imposed, the total thermopower of the material, $S\Delta T$ (S is the Seebeck coefficient), is obtained by considering the two spin channels as two voltage generators connected in parallel. Therefore, the total current density j created by the thermal voltage inside the material will be equal to $j = (G_{up} + G_{down})S\Delta T$. This is ultimately the sum of two different terms, j_{up} and j_{down}, which are describable as:

$$j_{up} = G_{up}S\Delta T \; ; j_{down} = G_{down}S\Delta T \tag{6}$$

At this point, if zero-current density conditions are imposed ($j = 0$), the resulting spin accumulation which will occur at the edges of the material (and that will decay over the spin-scattering diffusion length) is the spin-dependent Seebeck effect. This is the result of the imbalance between the number of spin-up and down electrons displaced from their equilibrium state when a temperature gradient is imposed, and represents the spin accumulation density caused by such gradient. The spin-injection process occurs when a non-magnetic (NM) layer is positioned in contact with the HMF spin-voltage generator. In this configuration, the NM material will act as a spin-sink, and the accumulated spin-voltage will result in a polarized spin-current (inside the limits of the spin diffusion length of the material). Although the presence of a HMF/NM interface is not a necessary condition for the occurrence of spin-dependent Seebeck effect, it is within this layered configuration that thermal spin-injection found the majority of interest in spintronics, as spin-Seebeck effect was found to be an effective way to generate and transport SPCs even over relatively long distances. A more extensive discussion on the properties of Co-based Heusler alloys will be performed in the next section; nevertheless, it is already possible to state that, since Heusler compounds are known to be among the most promising thermoelectric materials, the study of their spin-Seebeck effect is well embedded in a solid and established research and competence framework. Moreover, their potentiality as spin-injectors makes them suitable for other spintronic applications besides those in MTJs, such as in spin-lasers, sensors and actuators [20].

Ferromagnetic oxides thin films have been also extensively studied due to their various and highly tunable electronic properties. Fe_2O_3, which show spinel ferrite structure, is one of the most studied. Showing a magnetic moment of 4.1 mB and a high Curie point at 850 K, it has been predicted to be half-metallic. Subsequent spin-resolved photoemission measurements reported spin-polarizations up to approximately 80% [20]. The substitution of one Fe ion with divalent metal ions such as Mn, Co and Ni was found to possibly increase the half-metallic properties. Despite the promising perspectives, their half-metallic behavior was found to be extremely sensible to film's imperfections as antiphase boundaries, atomic-site disorder and dislocations. High quality of films are indeed crucial for achieving satisfactory half-metallicity and spin-filtering [20]. CrO2, which has rutile structure, has been proved to be half metallic at low temperature. Point contact Adreev reflection (PCAR) measurements indicated spin-polarization of 90% at low temperature, however half-metallicity at room temperature has not yet been demonstrated [56]. A phase transformation is known to occur above 391 K which is major the cause of the reduction of half-metallic properties [57]. Double perovskites such as Sr2FeMoO6 (SFMO) also achieved high *P* at low-T (approximately 80%) and a T_C of 420 K. Their high reactivity with water and the loss of half-metallicity as a result of site disordering are the main obstacles to overcome [58].

Magnetically doped semiconductors such as (Cd,Mn)Te, (In,Mn)As and (Ga,Mn)As are versatile materials as the carrier density of the semiconductor is tailored via doping with ferromagnetic elements. In fact, their magnetic properties can be tuned by increasing the carrier density by applying an electric field, photoexcitation or heating [59]. The main issue with such materials is the low Curie point, as the perspective for a reliable

ferromagnetic semiconductor at room T remains elusive. Dilute magnetic semiconductors (DMS) like (In,Mn)As and (Ga,Mn)As are considered promising; however, the upper achieved T_C is around 330 K [60,61]. Recently discovered (Ba,K)$(Zn,Mn)_2As_2$ DMS compounds are considered more promising even if their T_C remains still around 230 K [62].

2.1 Heusler alloys

Heusler alloys are a family of highly ordered ternary intermetallic compounds, usually divided in two sub-categories: half-Heusler alloys with XYZ stoichiometry (X, Y are transition or alcaline metals, Z is a p-block element) and $C1_b$ structure, and full-Heusler (referred here simply as Heusler, or FH) with X_2YZ stoichiometry and $L2_1$ structure. Both categories attracted a lot of attention in spintronics, as they currently are in fact the most studied materials for such application.

Concerning half-Heuslers (Figure 7a), the most well-known compound is NiMnSb [63], as in 1983 de Groot at al. [64] predicted by ab-initio calculations its half-metallicity with a 100% spin-polarization at the Fermi level. Its half-metallic behavior was later experimentally verified in single crystals by multiple techniques, such as infrared absorption [65] and spin-polarized positron annihilation [66,67]. Interestingly, in thin films half-metallicity was found to be hindered by Sb and Mn segregations at the surface, leading to a maximum 58% spin-polarization [68]. Despite the well-known half-metallicity of NiMnSb [69], a large number of half-Heusler compounds are semiconductors, like TiNiSn, or conductors, which exhibit high Seebeck coefficient (S) and thermoelectric figure of merit (zT) [70].

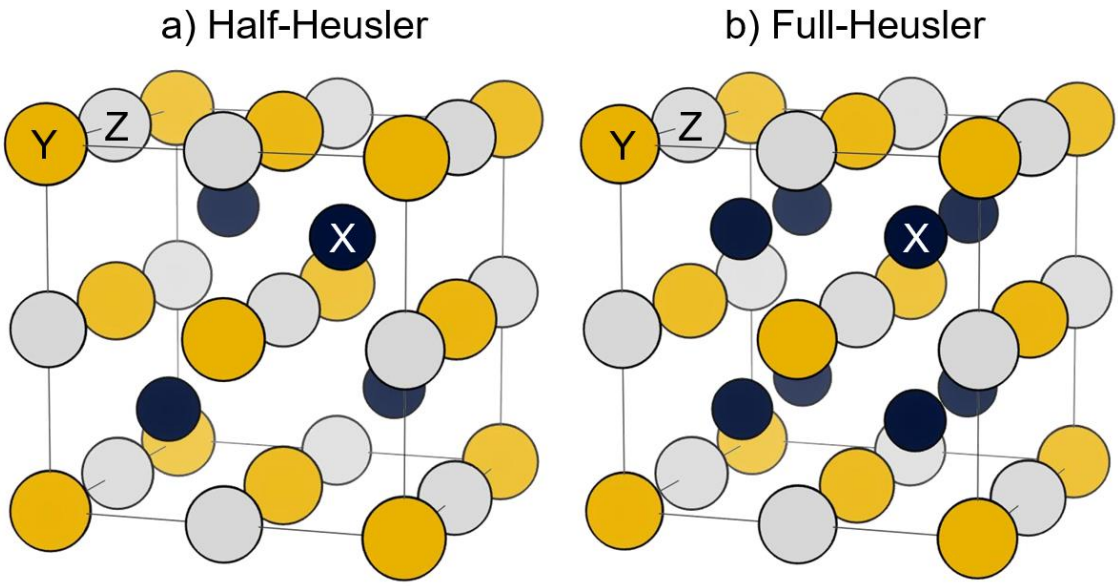

Figure 7: Schematic representation of the (a) half-Heusler, and (b) full-Heusler structure.

Considering full-Heusler compounds (Figure 7b), they were the first to be discovered in 1903 by Franz Heusler after the synthesis of the Cu_2MnAl. Such alloy was found to be ferromagnetic even if none of its constituent element is magnetic by itself [71]. This evidence immediately highlighted the non-trivial nature of the electronic structure of such compounds, actively stimulating further researches. The mechanisms behind the stabilization of the ferro- or antiferromagnetism of Heusler alloys was studied in a seminal work by Kübler et al. in 1983 [72]. The prediction of half-metallicity of several full-Heuslers was performed with ab-initio calculations by several Japanese research groups, such as Ishida et al. for Co_2MnZ (Z= Si, Ge) [73], and Fuji et al. for Fe_2MnZ (Z= Si, Ge) [74]. Subsequently, the half-metallicity of Co_2MnAl and Co_2MnSn was experimentally investigated by Brown et al. [75], leading to further studies as thin films grown on MgO substrates [76]. Finally, in 2004, MTJs based on Co_2MnSi [77] and $Co_2Cr_{0.6}Fe_{0.4}Al$ [78] were first assembled, paving the way for all the subsequent Heusler alloys' applications in spintronics. Currently, Co-based Heusler compounds are the most promising candidates to achieve half-metallicity at RT, as they are characterized by

Curie point well above room temperature, good lattice matching with major substrates, large magnetic moment, and high compositional versatility [20]. As already mentioned, the main obstacle to such objective is represented by atomic disorder, symmetry break in proximity of film's surface, misfit dislocations, and other symmetry breaking structural perturbations. More in general, the properties of many Hesuler alloys can be predicted by a simple account of their valence electrons [79]. For instance, closed-shell compounds, like Fe_2VAl, are semiconductors which found applications in energy harvesting technologies. On the contrary, non-magnetic Heusler with approximately 27 valence electrons display superconductive behavior [79]. Magnetic Heusler materials have found applications in a widespread range of fields thanks to their multifunctional properties, such as magneto-optical [80], magnetocaloric [81], magneto-electric (half-metallic ferromagnetism), and magneto-structural features [82]. Other peculiar properties include shape-memory effect, topological insulators, Kondo systems, and compounds displaying heavy-Fermion behavior.

As the experimental part of this work will concern the study of Co-based full-Heusler compounds, in the present section most of the attention will be focused to such category. A more detailed explanation on the properties of half-Heusler alloys is provided in Ref. [83], which is left to the reader's discretion.

2.1.1 Crystal structure

The X_2YZ Heusler compounds crystallize with the L21 Cu_2MnAl prototype structure in a cubic space Fm3m (225) group. Here, the X atom occupies the 8c (1/4, 1/4, 1/4) Wyckoff position, while Y and Z are located at 4a (0, 0, 0) and 4b (1/2, 1/2, 1/2), respectively. This structure fundamentally consists of four interpenetrating fcc sublattices, two of which are equally occupied by X. Y and Z, which are respectively the least and most electropositive elements, form a NaCl-type lattice, being both octahedrally coordinated. All tetrahedral holes are filled by X.

Another effective way to describe the Heusler structure is by considering it a CsCl-like superstructure. In fact, assuming the disorder of Y and Z sites and a shifting of the unit cell by (1/4, 1/4, 1/4) with respect to the Fm3m cell, the combination of both X-site fcc sublattices leads to a simple cubic lattice. At this point, Y and Z atoms occupies the center of the simple cubic lattice, resulting in the CsCl-like superstructure. The derivation of the $L2_1$ as an ordered CsCl-type (B2) structure is crucial for understanding several thermodynamic and electronic properties of Heusler compounds. It is indeed known that in multiple FH alloys an order-disorder transition at a certain temperature occurs, while others solidify with a fully ordered $L2_1$ cell directly from the melt. For example, in Fe_2VAl, the B2-$L2_1$ transition was observed to occur at approximately 1100°C. Heating this system up to 1250°C, another order-disorder transition can be observed, this time from the partially ordered B2 to a fully disordered bcc A2 (W-type) structure. The A2 cell is obtained by disordering also the X sites as well as Y and Z, leading to a disordered bcc solid solution. Such rather complicated solidification path is luckily not always present, as other FH like Co_2ZrSn congruently crystallize with the $L2_1$ structure directly from the liquid. The order-disorder relationship between the $L2_1$ and B2 structures led to the rule-of-thumb which states that mixing two binary intermetallics with CsCl structure will result in a FH comnpound. The disorder of the Y and Z site is often observed in half-metallic Heusler compounds; however, this was observed to usually not significantly affect their half-metallicity. On the contrary, the disorder on the X-site was found to deeply influence half-metallic properties, leading in some cases to a complete loss [79,83,84].

As it will be discussed next, the local symmetry of constituent atoms is crucial for the hybridization of atomic orbitals, which ultimately determines the compound's electronic structure with all electronic-related properties. Hence, understanding which are the effect on symmetry of lattice distortions or atomic intermixing is fundamental. Possible symmetry breakings of $L2_1$, leading to the following structures are the most common:

- D03-type structure: mixing X and Y, or X and Z atoms in their crystallographic position conserves the Fm3m space group; however, the $D0_3$ BiF_3-type structure is obtained.
- B2-type structure: as mentioned before, this is the result of random intermixing of Y and Z atoms in their positions. In such system, Y and Z sites become equivalent. As a consequence, a CsCl-type cell is formed, with the X atom occupying the center (1b Wyckoff position), and randomly surrounded by Y and Z atoms (1a Wyckoff position). The symmetry is lowered to a Pm3m space group.

- A2-type structure: this is obtained by a random intermixing of all X, Y, and Z atoms, representing a further loss of symmetry from the B2 structure. All the Wyckoff positions are equivalent, being 2a for all atoms. This W-type structure has Im3m space group.
- X-type structure: also known as inverse Heusler, it has F43m space group and $CuHg_2Ti$-type structure. This is formed when the atomic number of the Y atom is higher than that of X. Half of X and Z atoms form a NaCl lattice, while the remaining X and Y occupy the tetrahedral sites, forming a second rock-salt sub-lattice. Examples of inverse Heusler alloys are Mn_2CoGa and Cr_2CoGa.
- Y-type structure: also known as quaternary Heusler, it is a LiMgPdSn-type structure with F43m space group. This is formed when all four interpenetrating fcc sub-lattices of the L21 structure are occupied by a different atom. Examples of quaternary Heusler are CoFeMnZ (Z= Al, Ga, Si, Ge) [85].
- Tetragonal distortions: this is typical of Mn_2YZ compounds in which the two Mn atoms are prone to two different local symmetries, cubic and tetragonal [79]. The elongation along the *c* axis result in a I4/mmm space group and a Mn_2NiSn-type structure. The tetragonal unit cell can be visualized by rotating the cell axis by 45°, leading to the X atoms in a 4d Wyckoff position (0, 1/2, 1/4), Y in 2b (0, 0, 1/2), and Z in 2a (0, 0, 0). The inverse Heusler are also subjected to tetragonal distortion, in which only one Mn occupies the 2b position, while the second share the 4d with Y.

The loss of symmetry of the Heusler structure can be studied with several experimental techniques, the most widespread of which is XRD or neutron diffraction. A case study on the effect on XRD peak intensities of several symmetry-breaking point defects in Co_2ZrSn and Fe_2VAl compounds will be presented in Section 7; nevertheless, it is possible to state that, in general, disorder on the octahedral and tetrahedral sites manifest in the intensity of the (111) and (200) superstructure reflexes, respectively. The presence and the intensity of such reflections are strongly related to the scattering coefficients (hence, to the atomic number) of the alloy's constituent elements.

2.1.2 Electronic structure

In the L21 structure, all X atoms are chemically equivalent, as the both their sub-lattices are surrounded by the same environment. Although they are located on second neighbor positions, the mutual interaction of X atoms is crucial to explain the electronic and magnetic properties. It has to be also remarked that in Heusler compounds, even in the presence of atoms with large atomic number, orbital magnetism and spin-orbit interactions can usually be neglected as they were found to play a minor role [86].

Being Co2MnAl one of the most studied half-metallic Heusler alloy in spintronics, in this section this compound will be taken as a case-study for the description of the electronic structure of half-metallic FH compounds. Here, the Co moment is large, positive, and is originated by two unoccupied bands in the minority-spin conduction band, as better explained in Figure 8. If all their majority states are occupied, Co atoms have together a total moment of approximately 2 μ_B. The Z atom have instead small and negative magnetic moment which is about an order of magnitude lower than that of Co. Co_2MnAl and Co_2MnGa have 28 valence electrons, presenting both an experimental and calculated total magnetic moment of 4 μ_B. Considering the similar Co_2MnSi and Co_2MnGa, they have 29 valence electrons, showing magnetic moments of 5 μ_B [87,88].

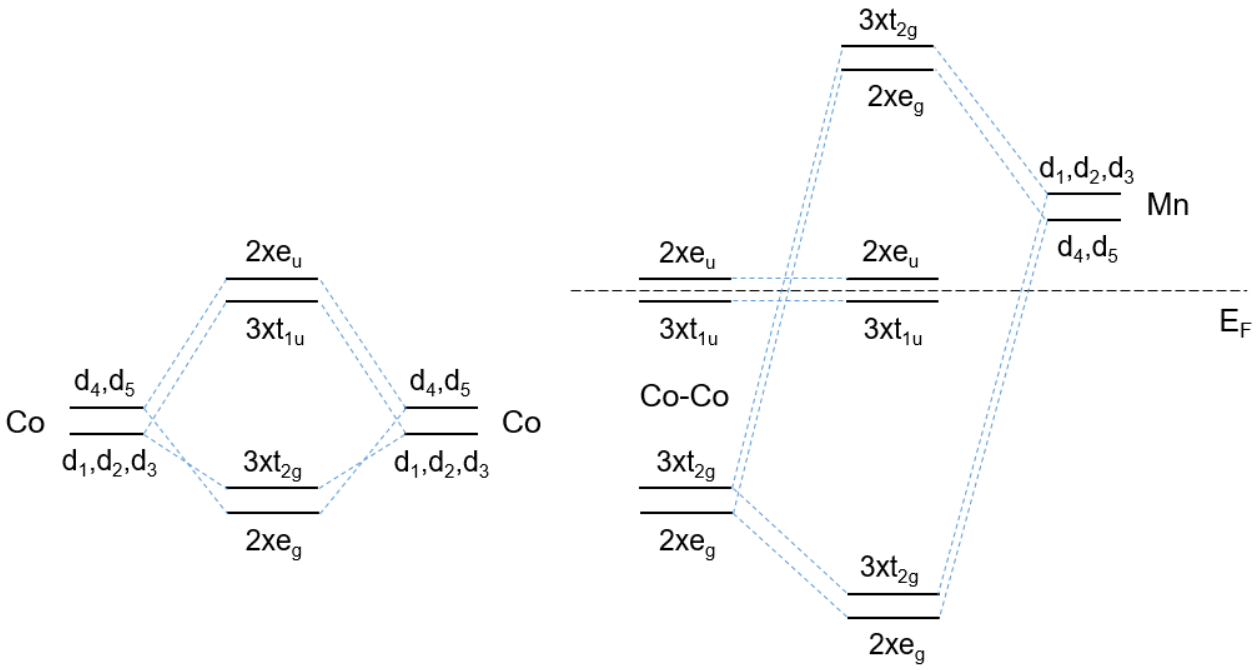

Figure 8: Atomic hybridization of Co and Mn atoms un Co2MnAl explaining the origin of the band gap in the minority spin sub-band. d_1, d_2, d_3, d_4, d_5 are the d_{xy}, d_{yx}, d_{zx}, $d_{r\hat{}2}$, $d_{x\hat{}2-y\hat{}2}$ orbitals, respectively. The coefficient of each orbital indicates its degeneracy.

Co atoms hybridization is crucial in determining Co_2MnAl magnetic and electronic properties. Since the four sp-bands of the Z element, as well as the sp-bands of Co and Mn, are located far below the Fermi level, only the hybridization of the 15 d states of Co and Mn are important in determining the electronic structure near E_F. As represented in Figure 8, the 5 d-orbitals of Co are divided into twofold degenerate d_4,d_5 ($d_{r\hat{}2}$, $d_{x\hat{}2-y\hat{}2}$, respectively) and threefold degenerate d_1, d_2, d_3 (d_{xy}, d_{yx}, d_{zx}, respectively) orbitals. Since the e_g can only couple with e_g orbitals, and since the same is valid for t_{2g}, the hybridization of two Co atoms form two sets of bonding (e_g and t_{2g}), and two set of antibonding (e_u, and t_{1u}) orbitals, which correspondent degeneracy is indicated by the respective coefficient. Considering the hybridization of the Co-Co and Mn d-orbitals, the double degenerated e_g hybridize with d_4, d_5, forming a bonding e_g state which is very low in energy, and an unoccupied antibonding well above the Fermi level. Similarly, the t_{2g} states couple with d_1, d_2, d_3, creating 6 new orbitals, 3 of which are bonding and occupied, while and other 3 are anti-bonding and above E_F. The e_u and t_{1u} orbitals of Co cannot couple with any of the d-orbitals of Mn, since none of these are compatible with the *u* symmetry representation, being orthogonal to the e_{1u} and t_{1u} states. This is the reason behind the fact that, as predicted by ab-initio calculations, in half-metallic Co-based Heusler alloys, the DOS at the Fermi level is usually almost exclusively determined by the bands of Co atoms. The t_{1u} states, which lies below E_F are therefore occupied, while the e_{1u} are located just above E_F. In total, accounting for the degeneracy of each orbital, 8 minority d-bands are filled, and 7 are empty. This means that all 5 Co-Mn bonding bands are occupied, and all 5 Co-Mn antibonding bands are empty, while the Fermi energy lies between the 5 non-bonding Co bands. Since the minority band contains 12 electrons per unit cell (4 occupying the low lying s and p bands of the Z element, and 8 the Co-like minority d bands, namely $2xe_g$, $3xt_{2g}$, and $3xt_{1u}$), and since 7 minority bands are unoccupied ($2xe_u$, $2xe_g$, $3xt_{2g}$), the largest possible magnetic moment for a FH compound is 7 μ_B and occurs when all majority d-states are occupied. Considering the total number of electrons in the system, both majority and minority, it is possible to conclude that the magnetic moment of a Heusler compound can be predicted by a simple account of valence electrons (Z_t), according to the following equation, which took the name of Slater-Pauling (SP) rule:

$$\mu = Z_t - 24 \tag{7}$$

In Figure 9, several Heusler compounds were arranged displaying their total magnetic moment (μ) per unit cell as a function of their total number of valence electrons. Because of the strong hybridization, no evidence is present of FH compounds having a moment of 7 μ_B. Systems with 30 valence electrons should have μ of 6 μ_B; however, none of them reach this exact value, as Co_2MnAl being the closest with 5.8 μ_B [83]. This happens because while the two Co atoms have no problem to contribute with a total of 2 μ_B to the total moment because of the empty e_u states, the Mn-related moment is limited by its hybridization with an upper limit of approximately 3 μ_B. Having 24 valence electrons, Fe_2VAl is nonmagnetic, while Co_2VAl, which have two electrons more, has accordingly a moment of 2 μ_B. Compounds with less than 24 Z_t like Mn2Val and Mn_2VGe are predicted to follow the SP rule showing negative moment. A negative total spin moment would mean that the minority band (which exhibit the half-metallic gap) is more occupied than the majority sub-band.

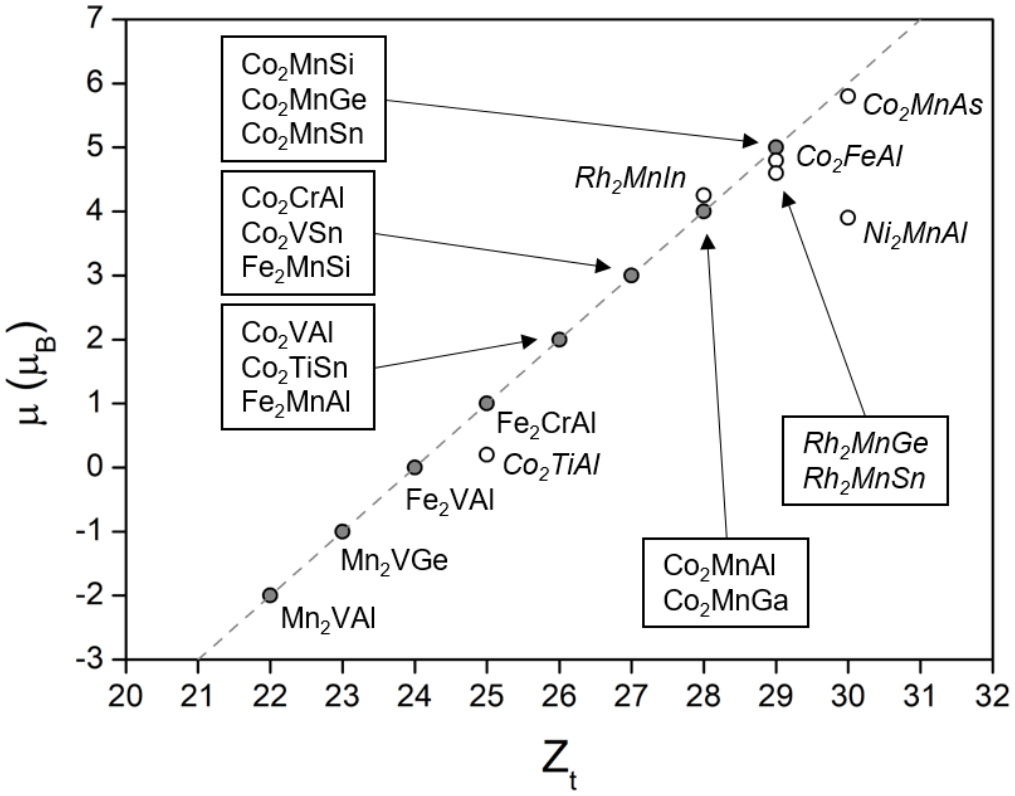

Figure 9: Magnetic moment as a function of number of valence electrons of a collection of Heusler compounds. The dashed line represents the values predicted by the Slater-Pauling rule. Grey and white circles are the alloys found to follow and not follow the SP rule, respectively. Data are from Ref. [50,83,89].

The SP rule described in Figure 9 is to be referred to pristine, defectless compounds. The occurrence of defects or distortions in the Heusler lattice can dramatically lower the magnetic moment, introducing states in the half-metallic gap. The occurrence of Co anti-sites in Co_2MnAl and Co_2MnSi was found to destroy the half-metallicity, while the disorder of the Y and Z atoms left the half-metallic properties unaltered. Interestingly, in Co_2MnSi, a small stoichiometric surplus of Mn replacing Si was observed to not have effect on the minority spin band gap, while in Co_2MnAl, the same situation involving Mn and Al led to a complete loss of half-metallicity [90]. Vacancies are also extremely common defects occurring during film's growth or bulk samples' solidification. In Co_2CrZ and Co_2MnZ alloys, vacancies occurring at the Co-site completely disrupt the half-metallic properties; whereas, vacancies involving the Y and Z element leave the gap unaltered.

Thermal and excitations' effects were also found to introduce levels or progressively smear out the minority spin gap. Spin-orbit interactions can theoretically cause a coupling of the two spin sub-bands, leading to the introduction of states; nevertheless, this effect is weak in FH alloys, leaving spin polarization in most cases as high as approximately 99% [91]. Excitations effects which can potentially lead to the introduction of levels in

the gap can be described in the adiabatic approximation of static spin-waves, which are accounted as superpositions of spin-up and spin-down states. At higher temperatures, magnons (or spin-waves) progressively smear out the gap, driving the system to the paramagnetic state above T_C [92]. At low temperatures, the magnons-electrons interactions cause non-quasiparticles excitations in the minority gap above E_F [93]. This was also described as the only form on spin-scattering mechanism possible to occur at low-T in half-metallic ferromagnets [94]. It is to be added that in the first case, spin-wave excitations introduce new states both above and below the Fermi level; whereas, in the latter case, the non-quasiparticle excitations introduce additional bands only at and above E_F [83].

2.1.3 Electron scattering and transport properties

For transition metals, phonon-related electrical resistivity is modeled by the Bloch-Grüneisen equation (Equation 5), which takes into account the scattering of electrons with acoustic phonons.

$$R(T) = A\left(\frac{T}{\Theta_R}\right)^{\beta} \int_0^{\Theta_R/T} \frac{t^{\beta}}{(e^t - 1)(1 - e^{-t})}\, dt \tag{8}$$

With R the resistivity, T the temperature, and Θ_R the Bloch-Grüneisen temperature, which usually match with the Debye temperature. Under Θ_R, electrons are assumed to deviate only by a small angle after the interaction with phonons, while, above such limit, electrons will be scattered by a large angle because of the higher energy of phonons as T increases. The resistivity over temperature predicted by the Bloch-Grüneisen law can be separated in different regimes, as shown in Figure 10a. At sufficiently high temperatures, resistivity linearly depends on T (β equals to 1 in Equation 5). In such range, electron-phonon scattering quantitatively dominates on grain boundary-related and impurity-induced scattering, as phonons have sufficient frequency to intensively perturb the electron density. Approaching a certain crossover temperature, the resistivity starts to fall less drastically, as a $R \propto T^{\beta}$, with $3 < \beta < 5$, regime is reached. This occurs in proximity of the Bloch-Grüneisen temperature, which is usually equivalent to the Debye temperature. Here, the lower frequency of phonons reduces the angle with which electrons are scattered, thus causing the slower decrease of R. The exact value of β depends on the nature of conduction electrons and on the shape of the Fermi surface. For T approaching absolute zero, R scales with T^0, meaning that phonon-induced resistivity becomes negligible. This happens as in such conditions phonon frequency is such small to have no effect on electron density.

In ferromagnetic and nearly ferromagnetic materials, the contribution of magnons (or spin-waves) has also to be taken into account. Magnons are defined as quasi-particles, or collective excitations of the electronic spin structure in a crystal lattice. Considering electrons in their wave form, an equivalent quantum-mechanical picture is to describe such excitations as quantized spin waves. At low T, only long wavelengths are excited, implying only weak relative deviations of first-neighbor's spin. In this case, electrons keep locally their spin orientation, including those responsible for current conduction. As prescribed by the Goldstone rule [94], in absence of anisotropy, magnetization can rotate without energy barrier. The spin of current carriers will follow accordingly the rotation, preserving the polarization at the Fermi level. Quantitatively, the contribution of spin waves on electrical resistivity has been modelled by several authors; nevertheless, a nearly complete description was provided in 1975 by Ueda et al. [95]. Here, the resistivity is descripted as in Equation 9.

$$R = \frac{m}{ne^2}\frac{3}{4}\frac{\varepsilon_F}{\hbar}\left(\frac{G}{2V}\right)^2 \rho_s \rho_d \left(\frac{k_F^*}{k_F}\right)^4 \left(\frac{\varepsilon_F^*}{\varepsilon_F}\right) \bar{R}(T) \tag{9}$$

$$\bar{R}(T) = T^{-1} \int_0^{2k_F/k_F^*} q^3\, dq \int_{-\infty}^{\infty} \omega n(\omega)[n(\omega) + 1] F(q, \omega) d\omega \tag{10}$$

$$F(q, \omega) = \frac{1}{3\rho_d} Im[2\chi_{ZZ}(q, \omega) + \chi_{\mp}(q, \omega) + \chi_{\pm}(q, \omega) \tag{11}$$

Here, m and n are the effective mass and the number of density of s-electrons, respectively, ε_F the Fermi energy of the s and d bands measured from the bottom of the band, G the coupling constant, ρ_s and ρ_d the density of states of the s and d bands respectively at the Fermi level, k_F and k_F^* the Fermi wave vectors of the s and d bands respectively, n(ω) the Bose function, and χ_{zz}, χ_{-+}, χ_{+-} the dynamical susceptibilities of the d-band electrons at their equilibrium. $\bar{R}(T)$ is a dimensionless quantity which express the temperature dependence of R, as described in Equation 10. Here, the reduced units $q/k_F^* \rightarrow q$, $\hbar\omega/\varepsilon_F^* \rightarrow \omega$, and $k_BT/\varepsilon_F^* \rightarrow T$ are used. F(q,ω) is the form factor, as written in Equation 11.

By considering only the spin wave (or magnon) contribution, this is given by:

$$\frac{3}{2}[\bar{R}(T)]_{sw} = \frac{\pi f_\zeta(0,0)}{\alpha}\frac{1}{T}\int_0^{q_c} q^3 \frac{\omega_q n(\omega_q)[n(\omega_q)+1]}{\left|\partial f\zeta'(q,\omega_q)/\partial\omega_q\right|}dq \qquad (12)$$

where ω_q is the spin wave (magnon) frequency, q_c the cut off wave vector of the spin wave, and $f_\zeta(q,\omega)$ the reduced transversal dynamical susceptibility of the non-interacting electron system under a given magnetization. Considering this last parameter as in an electron gas, Equation 12 can be solved analytically, giving two results in the following limits (with Z(n) defined as in Equation 15):

$$\frac{3}{2}[\bar{R}(T)]_{sw} = \frac{\pi f_\zeta(0,0)}{\alpha}\frac{3\Delta^2}{8\zeta D^2}Z(2)T^2 \qquad (T \to 0) \qquad (13)$$

$$\frac{3}{2}[\bar{R}(T)]_{sw} = \frac{\pi f_\zeta(0,0)}{\alpha}\frac{3\Delta^3 q_c^2}{8\zeta D}T \qquad (T \to T_C) \qquad (14)$$

$$Z(n) = \Gamma(n+1)\zeta(n) \qquad (15)$$

with Γ(n) the gamma function and ζ(n) the Riemann's zeta function. From Equations 13 and 14, the most important aspect to note is that for temperatures approaching absolute zero, magnon-related resistivity follows a T^2 law, while approaching T_C it is linearly dependent with the temperature.

In the specific case of ferromagnetic materials, electrical resistivity can be described as the sum of a spin wave (magnon) contribution and temperature-induced spin fluctuations (spin-flip). Depending on the temperature of the system, the following equations were obtained:

$$3[\bar{R}(T)]_z = \frac{\pi(1+\delta_\zeta)C}{2\alpha A^{3/2}}Z(2)\frac{T^2}{\delta_\zeta^{1/2}} \qquad (T \ll T_C) \qquad (16)$$

$$3[\bar{R}(T)]_z = \frac{2\pi(1+\delta_\zeta)C^{2/3}}{3\alpha A^{5/3}}Z(5/3)T^{5/3} \qquad (T \lesssim T_C) \qquad (17)$$

$$[\bar{R}(T)] = \frac{2\pi(1+\delta)C^{2/3}}{3\alpha A^{5/3}}Z(5/3)T^{5/3} \qquad (T \gtrsim T_C) \qquad (18)$$

$$[\bar{R}(T)] = \frac{\pi(1+\delta)}{\alpha}\left[\frac{2r^2}{A} - \frac{\delta}{2A^2}\ln\frac{\delta+4Ar^2}{\delta}\right]T \qquad (T \gg T_C) \qquad (19)$$

For temperatures sufficiently lower than T_C, the resistivity is mainly induced by spin waves, and is indeed proportional to T^2 (Equation 16). Approaching T_C, a $T^{5/3}$ trend is followed, with Equations 17 and 18 being identical at the Curie point. After T_C, spin fluctuations contribute linearly in determining the total electrical resistivity of a ferromagnetic material. For nearly-ferromagnetic materials, equations determined by Ueda et al. [95] are qualitatively the same as those above.

As already mentioned, the behavior of ferromagnetic materials, as well as that of HMFs, is described in the assumption of two separate sub-bands for majority and minority spin. Accordingly, electronic scattering can be seen as a sum of $R_{\uparrow}$, $R_{\downarrow}$, and $R_{\uparrow\downarrow}$ contributions (up electrons are assumed as majority). In half-metallic ferromagnets, $R_{\downarrow}$ corresponds to the resistivity induced by the existence of a semiconductive-like band gap in the minority sub-band. On the other hand, $R_{\uparrow}$ is the resistivity strictly related to majority electrons, such as low-T spin waves, which, according to the Goldstone rule, do not imply spin mixing. Finally, $R_{\uparrow\downarrow}$ is caused by temperature-induced inelastic transitions across the gap. These should only appear when kT is comparable with the band-gap energy, E_G.

In half-metallic ferromagnets, as NiMnSb, the measurement of electrical resistivity was found to give peculiar results, which were interpreted as evidence of the presence of an actual band gap on the minority spin sub-band [69,94]. The resistivity trend as a function of T of NiMnSb is shown in Figure 10b.

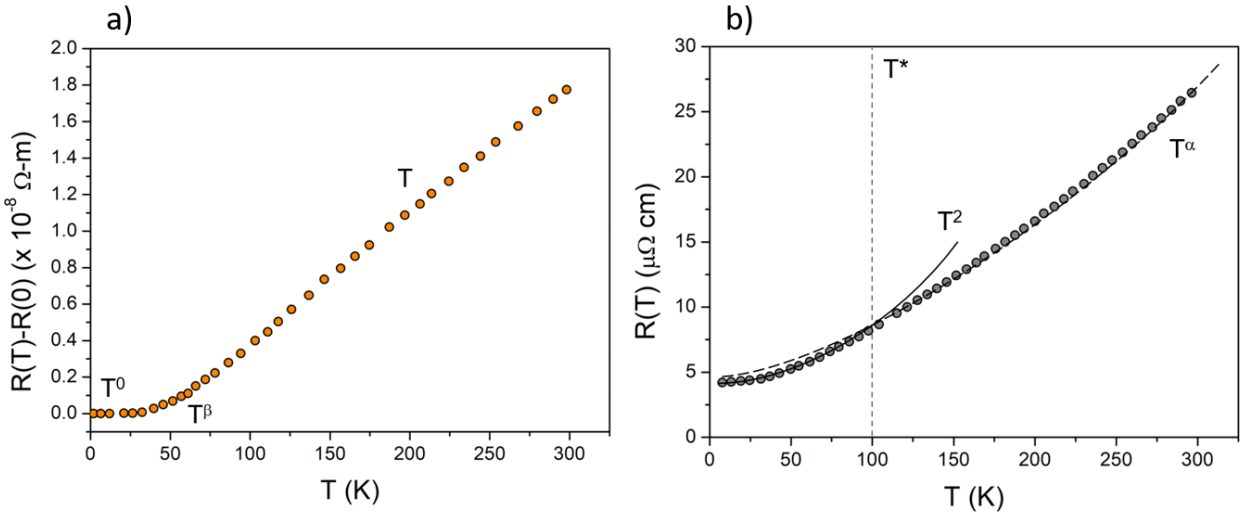

Figure 10: Electrical resistivity as a function of temperature of (a) copper, and (b) NiMnSb. T^{β} ($3<\beta<5$) is the resistivity/T regime of copper in proximity of Θ_R. T^{α} ($1<\alpha<5/3$) is the resistivity/T regime of NiMnSb after the half-metallic/weak-ferromagnet crossover, which occurs at T*. Data are from Ref. [69,96].

A crossover temperature was reported by several studies around 80-100 K. Above such limit, resistivity was found to scale with T^{α} (α=1.35-1.55, depending on the study [69,94]). In such temperature range, phonon-related resistivity should give a contribution linear contribution with T, as prescribed by the Bloch-Grüneisen model. Also, spin diffusion would be accounted with a $T^{5/3}$ contribution, as predicted by Ueda and Moriya (Equation 14). Spin waves would also contribute with a linear T term, as in Equation 11. Thus, the total exponent on temperature should be a combination of those of the various contributions, which are comprised between 1 and 5/3. Accordingly, an experimental exponent of 1.35 [94] was observed. Below 80-100 K, resistivity starts to decrease slower, as the trend was experimentally found to be proportional to T^2. This coincides with an electron scattering essentially caused predominantly by spin waves, as demonstrated by Ueda and Moriya (Equations 13 and 16). As at such temperatures, the phonon contribution is negligible, the trend of resistivity can be ultimately caused by spin waves and spin-flip scattering ($R_{\uparrow\downarrow}$). Since in NiMnSb, the presence of a half-metallic band gap hinders spin-flip phenomena, the T^2 dependency is coherently related only to electron-magnon interactions. Such behavior was also found for other half-metallic ferromagnets, being thus considered typical of such class of materials [97].

2.1.4 Co-based Heusler alloys in spintronic applications

Considerable performances have been obtained using half-metallic Heusler alloys as ferromagnetic films in MTJs. For the Co_2MnSi (3)/ MgO (2.5)/Co_2MnSi (3) (thickness in nm) MTJ, TMR ratios of 1910% and 354% were measured at 4 K and RT, respectively [98]. A steep reduction of TMR ratio was reported when the temperature is increased above 100 K, which was attributed to spin fluctuations at the interface with MgO.

This may be caused possibly by the formation of small fractions of atomically disordered phase in proximity of the MgO barrier [54]. The Co_2FeAl (5)/ $MgAl_2O_4$ (1.2)/ Co_2FeAl (5) MTJ achieved a TMR ratio of 342% at RT [46]. The $MgAl_2O_4$ barrier was used instead of MgO to improve the lattice matching while maintaining coherent tunneling. The synthesis of highly ordered $Co_2FeAl_{0.5}Si_{0.5}$ films in the $Co2FeAl_{0.5}Si_{0.5}$ (30)/ MgO (1.8)/ $Co_2FeAl_{0.5}Si_{0.5}$ (5) MTJ led to ratios of 386% at RT and 832% at 9 K [47]. Sputtered polycrystalline films have been used in a Co_2FeAl (2)/ MgO (1.95)/ $Co_{0.75}Fe_{0.25}$ (5) MTJ, achieving 175% ratio at RT [99]. The rather small figure of merit is mainly due to the film's interfacial smoothness. Such value is however still comparable with the state of the art perpendicular CoFeB/ MgO/ CoFeB junction, which at RT achieved 124% TMR ratio [35].

Perpendicular Heusler-based MTJs have also been characterized. Although the cubic $L2_1$ crystalline structure is not suited for strong magnetic orientations, perpendicular anisotropy can be induced by introducing tetragonal $D0_{22}$ distortion, or by interfacial coupling. A Co_2FeAl (1)/ MgO (1.8)/ $Co_{0.2}Fe_{0.6}B_{0.2}$ (1.4) junction with a TMR ratio of 53% at RT [100]. Here, the perpendicular magnetization was introduced by interface coupling with MgO. The insertion of a 0.1 nm thick CoFe layer between MgO and $Co_{0.2}Fe_{0.6}B_{0.2}$ was found to enhance the ratio up to 91%. The magnetoresistance ratio improved up to 132% after further refinement [101].

Having been mentioned such successes in practical applications, the discovery of new half-metallic Heusler alloys is crucial, as they will open more possibilities for crystal matching with insulator barriers, and tailoring of magnetic properties. Co_2VAl and Co_2VGa were reported to be half-metallic with 100% spin-polarization by several ab-initio calculations [102,103]. Single phase bulk samples were successfully synthesized, showing lattice parameters of 5.7798 Å and 5.7920 Å, respectively [49]. Neutron diffraction measurements assessed that the $L2_1$ crystalline ordering of Co_2VGa is almost perfect [104], making the alloy quite suitable for in-device applications. Both magnetic and electrical conductivity characterizations suggested the existence of a half-metallic band gap in such compound [105]; however, a direct measurement of its degree of spin-polarization is still lacking. On the other hand, combined pressure-dependent magnetization measurements and ab-initio simulations indicated a non-perfect half-metallicity for Co_2VAl, probably caused by a phase separation between the ordered $L2_1$ and a disordered BCC phase [49]. The series of Co_2TiSi, Co_2TiGe and Co_2TiSn compounds was also extensively studied. The suggested half-metallicity and high T_C combined with constant Seebeck coefficient was found to be of important interest for spin caloric applications. The measurement of electric transport and magnetic properties overall suggested the occurrence of half-metallicity for all the three alloys. The comparison between the calculated density of states, which presents a band-gap in the minority spin sub-band, and the curves obtained by hard X-rays photoelectron spectroscopy (HAXPES) were found to be rather similar, indicating that the electronic structure of experimental samples might be similar [50].

Concerning Co_2ZrSn and Co_2HfSn, they are predicted to be half-metallic ferromagnets by ab-initio calculations [106]. The first experimental measurements on magnetic properties from early 1970s already reported magnetic moments of 1.51 and 1.55 μ_B, respectively. Such values are associated with lattice parameters of 6.082 Å and 6.218 Å, respectively, obtained by neutron diffraction [107]. Since the Slater-Pauling rule of thumb for ferromagnetic compounds would suggest a magnetic moment of 2.0 μ_B assuming a perfect half-metallicity [25], considerable interest has been attracted by such alloys as their HMF behavior is object of debate. Another open point of discussion is the rather remarkable scattering of literature data concerning structural and magnetic properties. In fact, on the one hand, almost every first principle calculation agrees on the existence of a half-metallic density of states at absolute zero, and on a consequent theoretical magnetic moment of 2.0 μ_B [51–53,106,108]. On the other hand, experimental measurements range from 1.34-2.00 μ_B and 1.50-2.00 μ_B for Co2ZrSn [80,107–112] and Co_2HfSn [53,80,107,109,110,113], respectively. Such data are associated with equally scattered values of lattice parameter of 6.226-6.251 Å for Co_2ZrSn, and of 6.218-6.236 Å for Co_2HfSn (see same Ref. as above). Interestingly, in 1973 Ziebeck et al. measured a magnetization of 1.51 μ_B for Co_2ZrSn having a lattice parameter of 6.249 Å (measured by neutron diffraction) [107]; whereas, in 2006 Zhang et al. obtained an extremely similar magnetization value of 1.56 μ_B for a sample having an extremely different lattice parameter of 6.226 Å [112]. Such specimens were nevertheless

synthesized following two extremely different routes: arc melting followed by annealing in the first case, and melt spinning in the second. Such difference, as well as the great dispersion of literature data, is with all probability to be attributed to dissimilar processing routes which ultimately lead to extremely non-reproducible samples. An explanation was proposed in 2017 by Kushwaha et al. [114], who synthesized Co_2ZrSn in different stoichiometry both in form of single crystals and as polycrystalline bulk specimens. The structural and magnetic properties Co_2ZrSn in its various compositional range were measured, eventually finding a linear dependency of magnetization and lattice parameter on the concentration of Co. The degree of disorder in the lattice was also estimated by XRD diffraction, finding that the reduction of magnetization was linearly proportional to the occupancy factor of the Co-site. Such result, which is straightforwardly linked to Co vacancy defects, was also linked to a linear shrinking of the lattice parameter as the occupancy decreased inside the samples. Although such outcomes provided an explanation to the scattering of literature data clarifying the role of defects on several properties of Co-based Heusler alloys, the effect on half-metallicity was not taken into account. The effect on lattice disorder on the electronic and half-metallic properties of Co_2ZrSn is therefore a subject of discussion. Concerning Co_2HfSn, similar explanations have been provided; nevertheless, samples with high degree of crystalline ordering have recently been obtained more easily, making the investigation of its half-metallic properties simpler [52,53]. As far as the transport properties are concerned, literature data are extremely scarce. This is disappointing since the generation of spin-polarized currents via spin-Seebeck effect can play a major role in spintronic and spin-caloric devices [54].

3. Aim and structure of this work

The aim of this work is to provide qualitative and quantitative explanations on the effect of crystalline disorder on the half-metallic, electronic, transport, structural and magnetic properties of Co-based Heusler alloys. To achieve this, two major case-studies will be considered: Co_2ZrSn and Co_2HfSn. The choose of these alloys was due to the following reasons:

- The scattering of data present in the literature suggest that atomic disorder have a dramatic impact on the properties of these two compounds. Thus, the understanding of the nature of such dispersion can be useful to provide explanations on their structure-properties relationship.
- The comparison between the magnetic properties calculated at absolute zero for pristine cells and experimental results suggest that Co-sites disorder plays the most prominent role in determining the empirical behavior of these materials. This allows us to concentrate our focus to defects which mainly involve Co atoms.
- The congruent solidification of the $L2_1$ phase directly from the melt makes the study of the crystalline properties of such compounds rather easy. In fact, the absence of phase transformations, order-disorder, or martensitic transitions typical of other Co-based Heusler alloys allows to straightforwardly link macroscopic process parameters (e.g. cooling rate) to microscopic features (e.g. lattice parameter) [115].
- The alloys were already synthesized following multiple routes such as arc-melting, melt-spinning, Sn flux solidification etc. Such versatility consent to tailor the synthesis procedure as a function of the specimen's specific requirements.
- The peculiar trends of transport properties like the Seebeck coefficient, which was demonstrated to be rather high for such class of materials [116], encourage further developments for applications as spin-voltage generators or spin-current injectors.
- The combination of high T_C with a rather easy solidification behavior would allow such alloys to play a major role as perspective high performance materials in building high performance MTJs once a systematic understanding of their electronic structure will be achieved.

This study will be structured as follows.

In Chapter 1, the principle behind spintronics and spintronic devices were briefly introduced. An overview on random access memories and on the performances of current state-of-the art semiconductor-only based microelectronic memory devices compared with those of spintronic-based was also provided.

In Chapter 2, the most promising innovative materials in spintronics were presented. The focus was concentrated on Heusler alloys, which are the subject of this work.

In Chapter 4, it will be shown an overview on the experimental and computational methods.

In Chapter 5, a general characterization of the most prominent magnetic and transport properties of Co_2ZrSn and Co_2HfSn will be provided. The two alloys were synthesized by arc melting followed by annealing. Such route led to small quantities of secondary phases to be present in the specimens, which contribution had to be later taken into account. The magnetic properties of both alloys from 2 K to 550 K (well above T_C) will be presented and discussed in the framework of the Wohlfarth model of itinerant magnetism. The occurrence of a crossover from a low-T localized Bloch-type magnetism to a high-T Stoner-type behavior will be highlighted and linked to a change in electron scattering mechanism, which is considered to be an indicator of half-metallicity at low temperatures [69]. The fitting of the magnetization curves with the Edwards-Wohlfarth model allowed to extract information on the shape of the DOS at the Fermi level as a function of the temperature, indicating a rather flat profile. The electronic transport properties (Seebeck coefficient, electrical conductivity, and power factor) will be also presented. A linear increase (in absolute value) from RT to T_C followed by a linear plateau up to 800 K will be observed, indicating a rather drastic change of the DOS at the Curie point. This was confirmed by the estimation of electric conductivities (σ), which trends consist in a linear decrease before T_C, followed by a shallow increase above.

In Chapter 6, Co_2HfSn will be investigated more in depth. The effect of rapid solidification and Spark Plasma Sintering (SPS) on the structural and microstructural properties will be shown in detail. Such processing route allowed to obtain monophasic samples with a quite high crystalline ordering, which was assessed via Rietveld refinement of XRD patterns. The transport properties were measured in such single phase specimens, allowing to analyze the behavior of the pure Co_2HfSn compound without the presence of spurious phases. The trend of electric conductivity at low temperature shown a comparable crossover already observed in magnetic measurements, displaying a trend which is extremely similar to other half-metallic Heusler compounds. The thermal conductivity was also estimated, and the electronic and lattice contribution independently discussed. The thermoelectric figure of merit zT was consequently reported.

In Chapter 7, a more complicated case study on Co_2ZrSn will be presented. Several samples were synthesized with different processing routes, each involving different cooling rate, and thus diverse degree of crystalline disorder. The degree of disorder of the $L2_1$ structure was determined with XRD-based methods, leading to a quantitative estimation of the concentration of Co-vacancy defects in the specimens. A linear correlation between the occupancy factor of the Co site (χ_{Co}) and the lattice parameter will be highlighted, similarly to what already discovered by Kushwaha et al. [114]. The transport properties were measured for all samples, finding trends which are directly linked to the value of χ_{Co} of each specimen. The analysis of the electric conductivity and magnetization at low temperature allowed to suggest that half-metallicity is directly influenced by the Co-site occupancy, as specimens with higher χ_{Co} were also those in which both the magnetization and the half-metallic/ ferromagnetic crossover was closer to those predicted for the pristine compound. The thermal conductivity was analyzed both in terms of microstructural and electric conductivity difference. The thermoelectric figure of merit zT was then estimated and compared.

In Chapter 8, the result of ab-initio calculations will be exposed both for Co_2ZrSn and Co_2HfSn. The investigation of the pristine cells showed that both compounds are predicted to be half-metallic ferromagnets with a magnetization of 2.0 μ_B at absolute zero, which is almost entirely located on Co atoms. Two different functional were used to verify which is the degree of error on simulated data given by slightly different computational parameters. The phonon, elastic and thermal properties were also calculated for perfect supercells. Such data will be compared with those experimentally obtained in the framework of the Slack's model for lattice thermal conductivity. The calculation of transport properties gave results in high agreement with those measured empirically. Last, the DOS and band structure were simulated for supercells containing different types and concentrations of punctual defects. In particular, for both Co_2ZrSn and Co_2HfSn, Co vacancy, Zr/Hf antisites, Sn antisite, Co/Zr swap, Co/Hf swap and Co/Sn swap defects were investigated. The effect of off-stoichiometry in two diverse configurational entropy forms was also simulated. For each defect, the effects on half-metallicity, electronic properties and magnetization will be discussed, as well as their formation energy with respect to the pristine compounds.

Finally, in Chapter 9, some final remarks will be provided in order to summarize the content of the whole work.

By studying such debated cases, an investigation method generally valid for all the other potential half-metallic compounds can be proposed. Since direct evidence on the DOS shape can be extracted only from extremely expensive experimental techniques such as spin-resolves photoelectron spectroscopy, the gathering of indirect evidence from magnetic and transport properties measurements can easily be considered crucial. It is also essential to stress that the effectiveness of ab-initio simulations drastically increase when the outcomes are compared with experimental data, and strikingly decrease when no confirmation with real samples is present.

4. Materials and methods

As mentioned before, in this work a combination of experimental techniques and DFT calculations were used to investigate the properties of Co_2HfSn and Co_2ZrSn alloys. More detailed information about the implied experimental procedures and apparati, as well as the ab-initio simulations' parameters, will be provided in this section.

4.1 Experimental methods

Polycrystalline samples of Co_2HfSn and Co_2ZrSn were synthesized with different techniques, as arc-melting, and melt-spinning followed by spark-plasma sintering (SPS). Specimens were also annealed under vacuum atmosphere. Characterization techniques involved structural and microstructural investigation techniques like X-rays diffraction (XRD), scanning electron microscopy (SEM) combined with energy dispersion spectroscopy (EDS), and electron backscattered diffraction (EBSD). The functional properties were also evaluated, implying the use of SQUID and vibrating-samples magnetometer (VSM) measurements, and of a physical properties measurement system (PPMS) to investigate low temperature transport properties. High temperature transport properties were obtained with a 4-probes and 2-probes Van der Paw geometry resistivity and Seebeck coefficient testers, as well as laser flash analysis (LFA) for thermal conductivity.

4.1.1 Arc melting

In the arc-melting technique, an electric arc of plasma is triggered between a conductive needle and a water-cooled copper crucible on which the metallic elements (or alloys) to be melted are positioned. The application of a high voltage inside an Ar-filled inert chamber triggers the arc, which is subsequently projected on the reactants. Temperatures up to 3300 K are achievable with this technique. An Edmund Bühler (Edmund Bühler GmbH, Bodelshausen, Germany) furnace was used to prepare all the arc-melted samples in this work.

The main advantages of such preparation procedure are the large versatility and high achievable ceiling temperature, making such route ideal for alloys containing elements with high melting point such as Zr and Hf. Speed is also another crucial advantage, as a well-trained operator can effectively synthesize, using the specific instrument described above, up to six or eight different alloys per day, depending on the desired mass.

Despite such favorable features, several disadvantages are to be taken into account. First, it has to be considered that such procedure dies not involve any control temperature, or cooling-speed control, as only an estimation of the applied voltage is indicated. Typical cooling speeds of arc-melting are of the order of $10^1 – 10^2$ K/s. The lack of control of cooling speed is a huge drawback when alloys with a great degree of thermal expansion, like Co_2ZrSn and Co_2HfSn, are prepared, as the fractures and crack formation is often unavoidable in these cases. Another hindering aspect is the fact that, being this technique based on melting, elements' immiscibility in the liquid phase are to be considered, restricting the number of alloys which can be synthesized. Difficulties also arise when two or more reactants have greatly different melting (or boiling) points (such as Zr and Sn, or Hf and Sn), usually requiring the preparation of pre-alloys.

4.1.2 Melt spinning

Melt-spinning is a rapid-solidification technique capable to easily reach cooling speeds of $10^4 – 10^5$ K/s. Here, reactants are melted by means of an induction coil and the liquid subsequently sprayed on a rotary water-cooled copper wheel, ultimately forming metallic ribbons or flakes. The angular velocity of the wheel is proportional to the cooling speed. An Edmund Bühler (Edmund Bühler GmbH, Bodelshausen, Germany) melt-spinning apparatus was used to prepare all the rapidly solidified samples in this work.

Rapid-solidification synthesis can be used for different reasons, the most common of which is microstructural refinement. It is known in fact from basic metallurgy that the driving force of nucleation given by the degree of undercooling with respect to the temperature of the phase transformation, while crystalline growth is governed by diffusion laws. Thus, the high cooling rate typical of melt-spinning leads to high an ΔT, which maximize the nucleation rate, hinders grain growth, thus leading to a fine microstructure. Another important

reason is the increase of the solubility of elements inside alloys. In fact, due to the great quenching efficiency, rapid solidification is suitable for obtaining at RT stoichiometry available only at high temperatures. Other achievable results are obtaining metastable structures and amorphous alloys.

4.1.3 Spark plasma sintering

After mechanical alloying or rapid solidification synthesis, samples are typically obtained as powder, ribbons, or flakes. Such forms are often unsuitable for several characterization techniques that need bulk and dense samples, such as transport properties determination. Sintering is a metallurgical process in which powders are pressed and heated without reaching their melting point. The simultaneous heat and compaction fuse small particles into a dense bulk. The sintering process involve the optimization of several parameters as the ceiling temperature, dwelling time, heating and cooling speed, and applied pressure. Among these, ceiling temperature and applied pressure are perhaps the most important, as they straightforwardly determine the final density and phase composition according to the system's phase diagram. Dwelling time is often used as a factor to favor diffusion processes, while heating and cooling ramps are important to avoid the formation of thermal expansion induced cracks or fractures.

Spark plasma sintering (SPS) is a technique in which metal powders are inserted inside a graphite mold, which is positioned in a pressing machine. An electric field is applied to the mold while simultaneously pressing, inducing the densification of the material. The use of plasma as a source of heat allows to reach high ceiling temperatures; however, the actual involvement of plasma in the process is still uncertain. All the sintered samples were processed with a Fuji (Kobe, Japan) 515 S machine at CNRS (Thiais, France).

4.1.4 X-rays diffraction

Diffraction of X-rays is one of the primary techniques for the investigation of crystalline structures. A complete dissertation on the principles behind XRD is not the purpose of this work; however, a quite extensive analysis on how such technique can be used to determine the degree of disorder in Heusler structures is provided in Section 7. From powder diffraction patterns several properties can be extracted, such as the relative abundance of phases, lattice parameters, crystal size and preferential orientations, etc. The most widespread mean to obtain such data from XRD patterns is perhaps a procedure called Rietveld refinement, in which a theoretical pattern is calculated based on basic crystallographic information of sample's constituent phases. An iterative refinement process aimed to obtain the best possible fit between the experimental points and the simulated pattern is then performed. Finally, when a satisfactory fit is reached, it becomes possible to assume that the modelled properties coincide with the real ones, allowing us to extract information from XRD measurements. Being the Rietveld refinement a full-pattern analysis, it is considered more reliable than results obtained from those extracted by the linearization of single peak's features like intensities or width.

In order to avoid contributions from preferential orientations, all XRD patterns were collected from fine powders in the Bragg-Brentano geometry. In such configuration, samples are positioned flat between the X-rays source and detector. Patterns are collected in reflection mode, with both the source and detector synchronously moving scanning the whole desired 2-theta range. All XRD measurements were performed with a X'Pert Pro diffractometer (PANalytical B.V., Almelo, The Netherlands) with a Cu kα radiation source, while the Rietveld refinements were carried out using the MAUD software [117].

4.1.5 Scanning electron microscopy – Energy dispersion spectroscopy

Imaging techniques like the scanning electronic microscopy (SEM) are an extremely powerful way to rapidly and effectively determine microstructural features of metallic samples, as well as their elementary composition if coupled with spectroscopic techniques like energy dispersion spectroscopy (EDS). In SEM, electrons are extracted from a source material, which can be a tungsten filament, a LaB_6 crystal, or other. Such electrons are accelerated and collimated by several magnetic coils, and finally directed on the specimen. At this point, incident particles interact with the target's atom in several ways, the most important of which are by elastic or non-elastic collisions. In the first process, electrons are scattered back without losing much energy in a way

which is proportional to the sample's local average atomic number. In the second process, incident particles cause the extraction of secondary electrons from target's atoms with a mechanism which is proportional to superficial morphological features. The specimen's surface is point-by-point scanned with the electron beam, while a detector simultaneously collects the intensity of backscattered (BSE) and secondary (SE) electrons arriving from the sample, allowing to obtain an image of its surface. Depending on the used detector (BSE or SE) one can obtain images which highlights compositional (BSE) or morphological (SE) properties. Image's resolution depends on several factors, both sample-dependent and instrumental. Sample-dependent factors are essentially related on how deep the electron beam penetrates in the specimen, while instrumental factors largely depend on how much the beam is well collimated.

SEM instruments can be equipped with EDS probes, which are essentially X-ray fluorescence spectrometers able to determine elementary compositions. Relative atomic or weight abundances are easy to obtain, typically in the form of punctual, or area spectra. Linear scans or bi-dimensional maps are also common. Absolute abundances are much more complicated to determine, usually implying the use of reference analytical standards. The error intrinsically associated with EDS quantifications is typically in the order of magnitude of 1% at. (atomic percent), while the spatial resolution is approximately 1 μm.

4.1.6 Electron backscattered diffraction

For samples with extremely low surface roughness (i.e., less than 100 nm), the contribution of crystalline orientations on backscattered electrons intensity becomes non-negligible. In fact, in highly polished samples, one can distinguish between grains in BSE images, as crystals will scatter more or less electrons depending on their orientation. By tilting the sample with a sufficient angle (typically 70°), backscattered electrons will start to form coherent patterns, named Kikuchi lines [118], which can be collected by apposite probes. Since the Kikuchi lines are essentially diffraction patterns, they strongly depend on crystal orientation, and are also typical of the phase's space group. By collecting point-by-point such Kikuchi lines, it is possible to obtain a map (often also improperly called "image") of the orientation of each individual grain exposed on sample's surface, being also able to assign them to each constituent phase. Other properties, such as microstrain, lattice deformation, grains' size and geometrical shape, grain geminates, etc. are possible to be quantified with such technique.

The spatial resolution of electron backscattered diffraction (EBSD) is extremely high, potentially reaching 20-50 nm. For this reason, it is strongly recommended for the study of samples with extremely fine microstructures, such as nanostructured alloys. Also, penetration depth of the electron beam is extremely small due to the tilted sample, allowing to effectively investigate sample's surface without possible interferences from the inside of the bulk. All EBSD analysis were performed with a TESCAN S9000G FESEM equipped with an Oxford Instruments Symmetry S3 probe.

4.1.7 Magnetic measurements

Evidence on half-metallicity can be deduced from magnetization measurements at low-T. Superconducting quantum interference devices (SQUID) are extremely sensitive magnetometers based on superconducting coils containing Josephson junctions able to detect extremely weak magnetic fields. When coupled with cryogenic refrigeration lines, such instrumentation is able to measure field as low as 10^{-14} T down to 2-3 K. Being this sensitive, depending on their intrinsic magnetization, small mass of sample is required, as signal saturation is highly probable even for weak ferromagnets. Due to its superconductor-based functioning principle, for temperatures higher than RT, SQUID starts to be unsuitable; thus, a vibrating-sample magnetometer (VSM) was used for T > 400 K. In VSM, the sample is placed between two electromagnets, which cause the specimen's magnetic moment to align with the external field. As the sample is moved up and down, its magnetic dipole moment generates a field that changes as a function of time. The oscillating magnetic field generates an electric signal in VSM detecting coils, which is proportional to specimen's magnetization. The vibrational movement is often induced using piezoelectric materials. All SQUID measurements were performed with a Quantum Design (San Diego, CA, U.S.A.) MPMS3 in the field interval 0 ±70 kOe, between 2 K and 400 K; whereas, between 300 and 550 K, a furnace-equipped VSM magnetometer (Lake Shore

Cryotronics, OH, U.S.A.) in the field interval 0 ± 17 kOe, under constant Ar gas flux, was used at INRIM (Turin, Italy).

4.1.8 Transport properties

The determination of electronic transport properties above RT was performed on two-electrodes, two-thermocouples instrumental configuration. Here, a rectangular shaped bar is positioned between two electrodes, both containing heating coils. All the experimental arrangement is contained inside a furnace which progressively heat the sample. When the set temperature is reached, the electrode heaters generate the needed ΔT, which is measured by two lateral contacting thermocouples. One of the two thermocouple leads is used to measure the electromotive force generated by the specimen. For the measurement of the electrical conductivity above RT, a four-terminal direct current technique was used in order to minimize the effect of parasitic contact or wire resistances. A constant direct current is applied to the sample. The resulting voltage drop over a portion of length of the specimen is again measured using one of the two thermocouples wire. High temperature electronic transport properties were measured with the equipment described in Ref. [119,120] at CNR (Padova, Italy) and CNRS (Thiais, France), respectively.

Electrical conductivities and Hall coefficients below RT were measured in physical properties measurement system (PPMS) down to 3 K. As far as the first measurement is concerned, the experimental set-up is essentially the same as described above, with the exception that the sample is not heated up in a furnace, but cooled down inside the PPMS cryogenic liquid-He refrigeration chamber. As far as Hall resistivity is concerned, a magnetic field has to be also applied. When a charge particle is placed in a field, it will experience a Lorentz force proportional to its mobility and on field's intensity. The Lorentz force is stronger when the direction of motion is perpendicular to the direction of the magnetic field, causing charged particles to accumulate at one edge of the sample. Such charge accumulation generates an electric field, which leads to a potential difference called Hall voltage. By taking into account the specimen's thickness, the Hall coefficient can be then calculated. All low-T electronic transport properties were measured in a Quantum Design (San Diego, CA, U.S.A.) PPMS system at CNRS (Thiais, France)

Thermal conductivity can be calculated by multiplying sample's thermal diffusivity by its density and specific heat. Thermal diffusivity can be measured with laser flash analysis (LFA), which is currently one of the most widespread thermophysical investigation technique. In LFA, the analysis consists of a pulse heating the front side of a sample surface with a short laser pulse, and then measuring the time evolution of the back surface temperature using an infrared detector. The determination of specific heat capacity was performed using by comparing differential scanning calorimetric (DSC) tracks of Co_2ZrSn and Co_2HfSn with those of a standard sapphire reference, and subtracting the contribution of the empty sample holder. Thermal diffusivities were measured on a Netzsch (Selb, Germany) 427 and 457 analyzers at CNR (Padova, Italy) and Université Paris-Saclay (Île-de-France, France); whereas, heat capacities were tested on a Perkin Elmer (Waltham, MA, U.S.A.) DSC 8000 calorimeter. High temperature DSC tracks, used for the measurement of samples' melting points, were performed on a Kep Technologies Setaram (Mougins, 06250, Sophia-Antipolis, France) Type 31 HT-DTA calorimeter.

4.2 DFT calculations

In principle, solving the Schröedinger equation would allow to predict any experimental result; however, except for few simple systems, this can only be solved numerically with the introduction of several approximations. As such calculations use only basic crystallographic data of the system to be investigated and fundamental physical constants, therefore being independent from experimental results, they are called first-principles or ab-initio calculations. These are usually performed by computer codes, which implement several methods, such as density functional theory (DFT), self-consistent field (SCF), and projector augmented wave (PAW).

4.2.1 Density functional theory

In DFT, energy is seen as a functional (namely, a higher-order function) of the charge density. This means that energy is considered a function of charge density, which is itself a function of atomic positions. According to Schröedinger equation, the energy of a system containing electrons and nuclei can be entirely calculated by solving the eigenvalue (E) from the eigenfunction (Ψ) using the Hamiltonian operator ($\hat{H}$), as formulated in Equation 20.

$$\hat{H}\Psi = E\Psi \tag{20}$$

$$\hat{H} = T_N + T_e + V_{NN}(\bar{R}) + V_{ee}(\bar{r}) + V_{eN}(\bar{r}) \tag{21}$$

The Hamiltonian operator in Equation 21 consists of several terms. T_N and T_e are the kinetic energies of nuclei and electrons, respectively, while V_{NN}, V_{ee}, and V_{eN} are the potential energies from the nucleus-nucleus, electron-electron, and electron-nucleus interactions, respectively. $\bar{R}$ and $\bar{r}$ are vectors which specify the positions of nuclei and electrons, respectively. Being this equation difficult to solve for systems containing many electrons and nuclei, the Born-Oppenheimer approximation allowed to simplify the Hamiltonian as in Equation 22.

$$\hat{H} = T_e + V_{ee}(\bar{r}) + V_{ext}(\bar{r}, \bar{R}) \tag{22}$$

Here, the motion of nuclei is considered independent from that of electrons; in fact, being nuclei much heavier and slower than electrons, they can be considered fixed, so that T_N is approximated to zero. Also, since nuclei's position does not change, V_{NN} becomes constant and can be neglected. In Equation 22, V_{ext} is the potential energy from electron-nucleus interaction, or external potential.

The calculation of V_{ext} remained problematic until 1964, when Hohenberg and Kohn [121], proposed their two theorems. The first theorem stated that V_{ext} is a unique functional of electron density, apart from an additive constant, implying that electron density uniquely determines the Hamiltonian operator. The second theorem indicates that the energy of the system achieves the lowest value in the ground state only if the electron density used in the calculation is the true density of the ground state. This implies that the total energy of the ground state can be calculated from the minimization of the functional of electron density.

Although V_{ext} can be obtained in theory using such theorems, T_e and V_{ee} remain unknown until, in 1965, Kohn and Sham [122] proposed an approach to approximate them. They described a system of N non-interacting electrons formulating a single wave function of N orbitals ϕ_i. In such description, kinetic energy and electron densities are formulated as in Equation 23 and 24, respectively.

$$T_s[\rho] = -\frac{1}{2}\sum_{i}^{N}\langle\Phi_i|\nabla^2|\Phi_i\rangle \tag{23}$$

$$\rho(r) = \sum_{i}^{N}|\Phi_i(r)|^2 \tag{24}$$

It is important to note that $T_s[\rho]$ is not the true kinetic energy, but the one of a system of non-interacting electrons that reproduces the true ground state density. As far as the potential energy term is concerned, the classical Coulomb interaction, or Hartree energy, can be separated from V_{ee}, and defined as in Equation 25. At this point, the energy functional can be arranged as in Equation 26 by introducing the exchange-correlation

term, described in Equation 27. E_{exc} is essentially the error that is committed by using a non-interacting kinetic energy, and by treating electron-electron interactions only with classical physics.

$$V_H[\rho] = -\frac{1}{2}\int \frac{\rho(r_1)\rho(r_2)}{|r_1 - r_2|} dr_1 dr_2 \tag{25}$$

$$E[\rho] = T_s[\rho] + V_{ext}[\rho] + V_H[\rho] + E_{exc}[\rho] \tag{26}$$

$$E_{exc}[\rho] = (T[\rho] - T_s[\rho]) + (V_{ee}[\rho] - V_H[\rho]) \tag{27}$$

The Schröedinger equation can be therefore rewritten as the Kohn-Sham equation, which Hamiltonian operator consists in four terms: the kinetic energy, the external potential, the Hartree potential V_H, and the exchange-correlation energy with respect to the electron density $\rho(r)$. Given the exact value of E_{exc}, the Kohn-Sham approximation is able to provide the exact ground state $E[\rho_0(r)]$.

It is easy to deduce that, for this reason, the evaluation of E_{exc} is crucial in solving the Kohn-Sham equation, which outcome is essentially determined by how accurately the exchange-correlation term is calculated. The exchange interaction is the effect which result when two indistinguishable particles with either remaining unchanged (symmetric) or changing signs (anti-symmetric) [123]; whereas, correlation is the interaction of one electrons with all the other electrons in a system which influence its motion [124]. The two main approximations used to calculate E_{exc} are the local density approximation (LDA), and the generalized gradient approximation (GGA).

On the one hand, LDA describes the system as a homogenous electron gas [125], approximating E_{exc} as a an integral over a local function of the charge density. For systems in which the density varies slowly, LDA gives good predictions, reliably describing properties like ground-state geometries, vibrational frequencies, elastic moduli, and phase relative stabilities. Despite this, properties like binding energies are often somewhat unreliable. LDA can be considered as the zero-order approximation in terms of the density and its derivatives in the expansion of the charge density matrix. By including the first order gradient term in the expansion, the so-called gradient expansion approximation (GEA) is obtained. However, this method yields to certain unphysical properties in the exchange-correlation hole [126], which is the conditional probability that describes electrons' mutual positions. On the other hand, in GGA, a functional form that ensures the normalization of the exchange-correlation hole is used, retaining the analytical properties of LDA. The GGA approximation describes E_{exc} as a functional of the local value of the electronic density and its gradient. Compared to LDA, GGA improve the reliability of atomic and binding energies, energy barriers, and structural energy differences [127]. One of the most widespread GGA-based functional is the Perdew-Burke-Ernzerhof (PBE), which rather relative simplicity is sufficient to produce results which accuracy is typically better than LDA-based and other GGA functionals.

4.2.2 Self-consistent field

The self-consistent field (SCF) is an iterative numerical method to solve the Kohn-Sham equation, aimed to obtain the exact value of the total energy [128]. In a first glance, the initial input density is guessed and used to determine V_H and E_{exc}. The Hamiltonian operator is then constructed and used to solve Kohn-Sham approximation eigenvalue. The diagonalization of the Hamiltonian result in a set of occupied single particle orbitals (Φ_n) from which the output density can be constructed. Since the output and input densities are equal only if the ground state electron density has been found, they are compared and the cycle repeated (using the output as a new input) if their difference is larger than a set predetermined value. The cycle repeats until the difference between output and input densities becomes negligible.

4.2.3 Plane waves and pseudopotentials

According to the Bloch theorem, wave functions must be composed of a phase factor and a periodic function, as in the following equation:

$$\Psi_{nk}(r) = e^{ikr} u_{nk}(r) \tag{28}$$

With u(r) a periodic function which periodicity is coherent with that of the examined crystal, n the band index, and k the wave vector in the first Brillouin zone. Applying the Fourier transform on u(r) will result in a sum of plane waves, as in Equation 29, which result in the wave function of Equation 30.

$$u_{nk}(r) = \frac{1}{\sqrt{\Omega}} \sum_{G} C_{Gnk} e^{iGr} \tag{29}$$

$$\Psi_{nk}(r) = \frac{1}{\sqrt{\Omega}} \sum_{G} C_{Gnk} e^{i(G+k)r} \tag{30}$$

Where G is the reciprocal lattice vector, C_{Gnk} the coefficient of the Fourier transform and Ω the lattice primitive cell volume (that is also the normalization factor). The sampled k values are called k-points. Based on the system's symmetry, irreducible k-points can be sampled using a grid in the first Brillouin zone. The integration of the square of the wave function determines the charge density, and ultimately solve the Kohn-Sham equation. In Equations 29 and 30, the $C_{Gnk}e^{i(G+k)r}$ plane wave term is the essential to estimate more complex wave functions; so that, it is serves as basis set function.

Since they are extremely efficient to implement alongside efficiently evaluable Hamiltonians by using fast Fourier transforms, plane waves are often used as basis set functions. Although in theory only a sum of infinite plane waves fully describes the real wave function, basis set chosen with a proper cutoff energy are sufficient to give a reliable approximation, as low-energy wave function are more important than those with high energy. Nevertheless, it has to be said that since wave functions of the atomic cores oscillates rapidly, large set of plane waves would be required to describe core orbitals or valence electrons close to the core region. This can be solved with the used of pseudopotential approximation that replaces the exact potentials with smoother pseudopotentials which are more easily describable with a smaller set of plane waves. Being the pseudopotential essentially identical to the real potential in the valence region, and since the vast majority of physical and chemical properties of crystal almost exclusively depends on valence electrons, pseudopotentials are commonly used in DFT calculations to solve the Kohn-Sham equation.

4.2.4 Projector augmented wave method

Although the use of pseudopotentials leaves the description of atomic potentials sufficiently distant from the nucleus unaltered, the exact wave function near the nucleus is lost, which can create problems in the calculation of some physical properties. An approximation that can be applied to solve the pseudopotential problem is the projector augmented plane wave (PAW) method [129].

In the PAW method, the wave function is divided in two regions: the augmentation sphere, which is centered in the nucleus, and the bonding region, which describes the valence part. Although for the bonding region a pseudo wave function is still used, for the near-nucleus portion an all-electron wave function is used instead. As two wave functions are used, two separate energy cutoffs are needed. Ultimately, both wave functions match at the boundaries of the spheres.

Inside the augmentation sphere, the true wave function is expanded in a number of partial waves Φ_i, each of them corresponding to a smooth partial wave Φ'_i, as in Equation 31 and 32. These are identical outside the augmentation sphere.

$$|\Phi_i\rangle = \left(1 + \hat{T}_R\right)|\Phi_i'\rangle \tag{31}$$

$$\hat{T}_R|\Phi_i'\rangle = |\Phi_i\rangle - |\Phi_i'\rangle \tag{32}$$

In the augmentation region, the pseudo wave function can be expanded into pseudo partial waves, each multiplied by a coefficient c_i, thus being numerically easier to calculate.

4.2.5 Calculation of thermal properties

The calculation of thermal properties was performed with the Phonopy code in the harmonic approximation [130]. This is a versatile code, able to post-process the majority of DFT outputs of different codes, either by density functional perturbation theory (DFPT) or finite displacement method (FDM). The capability of Phonopy ranges from simple calculations of phonon bands and phonon density of states to the estimation of thermal properties, irreducible representations of normal modes, non-analytical-term correction, atomic modulations, mean square displacements, dynamic structure factors, and mode Grüneisen parameters.

Phonopy's workflow is also rather straightforward. From the unit cell relaxed structure, defective supercells of desired dimensions are created, in which atoms are displaced from the "pristine" position based on the symmetry of the investigated crystal. Force constants are then calculated using the energy of the displaced structures, using a DFT code.

4.2.6 Calculation of transport properties

Transport properties were calculated using the BoltzTraP2 code [131], which implements smoothed Fourier interpolation algorithm for electronic bands. Starting from a DFT-calculated band structure, for each band, the code writes the quasi-particle energies and their derivatives as Fourier sums. The transport properties are then calculated in the rigid-band approximation (RBA), which assumes that changing the temperature, or doping a system, does not change the band structure. In the following we will suppress the orbital index.

BoltzTraP2 is also often associated with the constant relaxation time approximation (CRTA), in which the Seebeck coefficient and Hall coefficient become independent of the scattering rate. With such method, they can be obtained on an absolute scale as a function of doping and temperature in a single scan. The CRTA in combination with the RBA, which makes the group velocities independent of the chemical potential and temperature, also has a computational advantage as it makes the transport distribution function independent of temperature and doping. The main limitation of the CRTA method is that the electrical and the electronic term thermal conductivity are delivered as dependent on the relaxation time parameter.

Furthermore, for ferromagnetic materials, in which the band structure profoundly changes as a function of temperature, the RBA approximation limits the reliability of such calculations for temperatures below the Curie point, below which it can be assumed that the material's electronic structure remains unaltered.

5. Magnetic and electronic transport properties of Co_2HfSn and Co_2ZrSn

The magnetic properties are discussed in terms of the Edwards-Wohlfarth [132,133] model of weak itinerant ferromagnetism using Arrott-plots [134] and checking the functional dependence of the magnetization around T_C. Experimental indications of half-metallicity are found by analyzing the magnetization dependence on temperature in both alloys. A shift from a high-temperature $M \sim T^2$ regime (Stoner law) to a low-temperature $M \sim T^{3/2}$ regime (Bloch law) was observed, and it has been attributed to a variation of the spin-flip mechanism (Stoner excitations in the first case, and transverse spin waves in the second one), suggesting the potential presence of the half-metallic band gap, as found in other HMF Heusler alloys [69,94,135].

5.1 Materials and methods

The pure elements were weighted in the appropriate stoichiometric quantities and melted in the arc furnace (Edmund Bühler GmbH, Bodelshausen, Germany). Due to the large difference in the melting points of Zr/Hf and Sn, two pre-alloys were synthesized for each system, namely CoZr and CoSn for Co_2ZrSn, and CoHf and CoSn for Co_2HfSn, to guarantee a better homogenization of the melt. Pre-alloys were melted together several times in order to obtain homogeneous samples. The ingots were wrapped in tantalum foils, sealed in evacuated quartz tubes, and annealed at 800 °C for 6 days. X-ray diffraction (XRD) investigation was performed in Bragg–Brentano configuration with a X'Pert Pro diffractometer (PANalytical B.V., Almelo, The Netherlands) using a Cu-Kα radiation as the X-ray source. For the XRD analysis, the samples were crushed in thin powders to remove the effect of possible preferred crystallographic orientations. The Rietveld refinements of the XRD patterns were performed with the MAUD software [117]. The surface analysis was executed by Scanning Electronic Microscopy (SEM) with an EVO 50 microscope (Carl Zeiss Microscopy GmbH, Jena, Germany) equipped with an Inca Energy 250 Energy Dispersion Spectrometer (EDS) in backscattered electrons (BSE) mode on mechanically polished surfaces. The XRD and SEM-EDS investigations were performed on both the as-cast and annealed specimens. Hardness measurements were performed on the annealed samples with a microhardness tester (Buehler, Lake Bluff, IL, USA) using a load of 4.9 N. The length of the indent diagonals and crack length were measured using a DMLM optical microscope (Leica, Wetzlar, Germany). The error associated with the mechanical properties was calculated using the standard t-student type formula for independent measurements, or $Er = SD \cdot t/n^{1/2}$ (where Er is the obtained error, SD is the standard deviation, t is the tabulated t-student value relative to a confidence interval of 95%, and n is the number of independent measurements). The densities of the two alloys were measured by weighting ingots of known volume and by the Archimedes principle using a pycnometer. Static magnetic properties were measured by means of a SQUID magnetometer (QD MPMS3) in the field interval 0 ±70 kOe, between 2 K and 400 K, and by a furnace-equipped VSM magnetometer (Lakeshore) in the field interval 0 ± 17 kOe, between 300 K and 550 K, under constant Ar gas flux. Low and high temperature measurements were observed to match on the temperature interval 300-400 K, common to the two magnetometers. Small regular prism-shaped samples were used for magnetic measurements. The Seebeck coefficient and electrical conductivity were measured on bar-shaped annealed samples (12x2x2 mm^3) under He flow between room temperature and 778 K by using a custom test apparatus described in ref. [119]. Furthermore, in order to assess the thermal stability of the alloys, the properties were measured upon heating and cooling.

5.2 Structural, microstructural and mechanical characterization

The XRD patterns of both annealed alloys are shown in Figure 11. Figure 12 a,b) and Figure 12 c,d) show the backscattered SEM images of annealed Co_2ZrSn and Co_2HfSn ingots, respectively, where the gray contrast suggests the homogeneous distribution of two secondary phases immersed in the main phase. Table 1 shows the results of the Rietveld refinement of the XRD patterns shown in Figure 11 and the EDS elemental compositions of the phases observed in Figure 12, which are all related to the annealed samples, together with the results of the same investigations performed on the as-cast alloys. As reported in Table 1, both the Rietveld

refinement and the EDS measurements indicate that phase 1 and 4 correspond to the Co_2ZrSn and Co_2HfSn Heusler structures, respectively, and they represent the main component of each alloy.

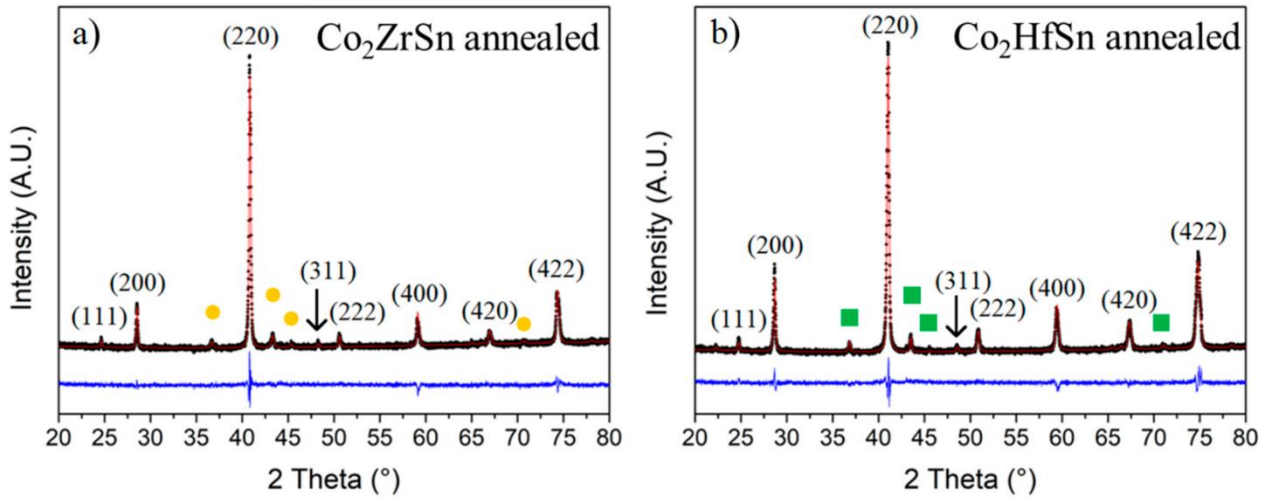

Figure 11: XRD patterns and Rietveld refinements of the Co_2ZrSn (a) and Co_2HfSn (b) annealed alloys. Black: experimental, red: calculated, blue: difference. The signals of the secondary phases are highlighted with coloured shapes (orange circles for Co_2Zr and green squares for Co_2Hf).

In the case of Co_2ZrSn alloy, phases 2 and 3 are found to be the binary compounds Co_2Zr and CoSn, respectively, while in the Co_2HfSn specimen, phases 3 and 5 are the binary compounds CoSn and Co_2Hf, respectively. Ziebeck et al. [107] also reported the presence of secondary phases, together with the Heusler phase even after annealing.

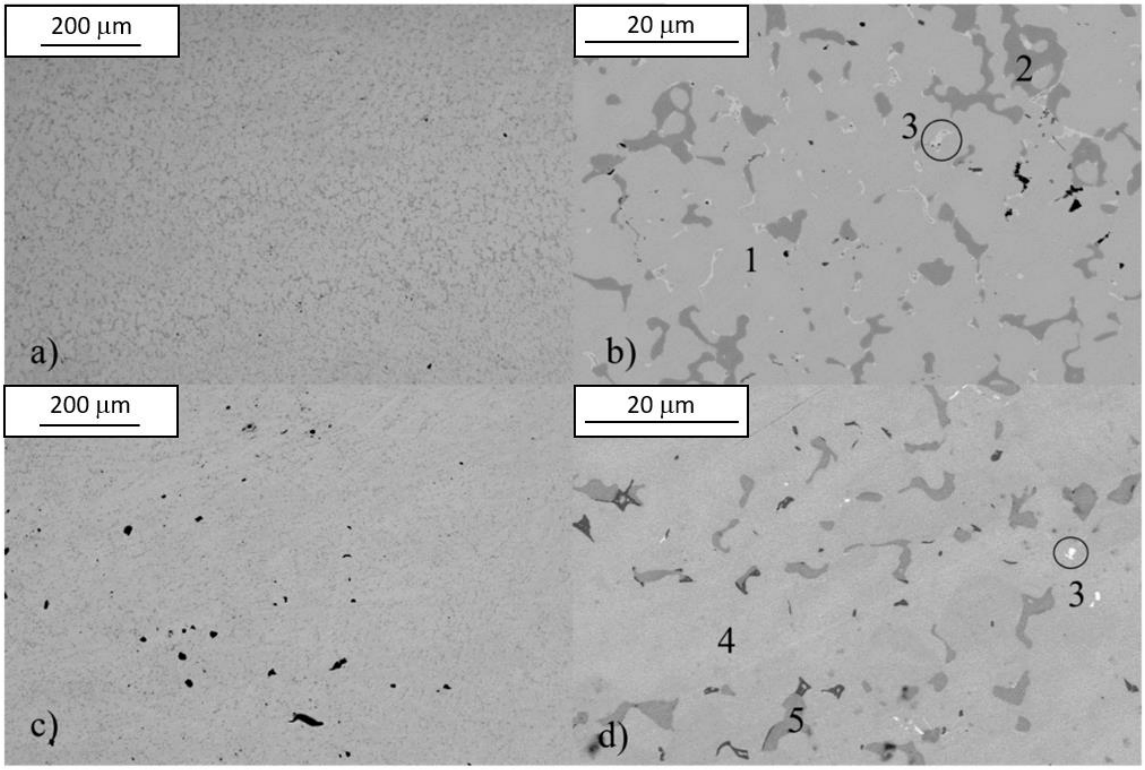

Figure 12: Backscattered electrons SEM images of the Co_2ZrSn (a,b) and Co_2HfSn (c,d) annealed alloys. In accordance with the results of the Rietveld refinement of the XRD patterns, the observed phases are the $L2_1$-type Co_2ZrSn Heusler (1), the C15-type Co_2Zr (2), CoSn (3), the $L2_1$-type Co_2HfSn Heusler (4), and the C15-type Co_2Hf (5).

Average EDS measurements at low magnifications indicated that the overall composition of the specimens slightly deviates from the nominal stoichiometry. The average atomic compositions of the samples resulted to be 53% Co, 25% Zr, and 22% Sn for the Co_2ZrSn sample, and 51% Co, 25% Hf, and 24% Sn for the Co_2HfSn alloy, indicating slight Sn depletion and Co excess, with consequent formation of the observed secondary phases.

Co_2ZrSn As Cast							
Elemental composition (at. %)			Label	Phase	Structure	*a* (Å)	Abundance (wt. %)
Co	Zr	Sn					
45	28	27	1	Co_2ZrSn	$L2_1$	6.2338	88%
65	21	13	2	Co_2Zr	C15	6.9174	12%
58	-	42	3	CoSn	B35	-	-
Co_2ZrSn Annealed							
Elemental composition (at. %)			Label	Phase	Structure	*a* (Å)	Abundance (wt. %)
Co	Zr	Sn					
46	27	27	1	Co_2ZrSn	$L2_1$	6.2458	88%
66	19	15	2	Co_2Zr	C15	6.9212	12%
58	-	42	3	CoSn	B35	-	-
Co_2HfSn As Cast							
Elemental composition (at. %)			Label	Phase	Structure	*a* (Å)	Abundance (wt. %)
Co	Zr	Sn					
45	27	28	4	Co_2HfSn	$L2_1$	6.2101	93%
65	26	9	5	Co_2Hf	C15	6.9024	7%
56	-	44	3	CoSn	B35	-	-
Co_2HfSn Annealed							
Elemental composition (at. %)			Label	Phase	Structure	*a* (Å)	Abundance (wt. %)
Co	Zr	Sn					
47	26	27	4	Co_2HfSn	$L2_1$	6.2157	93%
66	25	9	5	Co_2Hf	C15	6.8915	7%
55	-	44	3	CoSn	B35	-	-

Table 1: Composition, prototype–structure, cell parameters, and relative abundances of the different phases in the Co_2ZrSn and Co_2HfSn samples. The structure of the phase 3, CoSn, is shown as reported in the Co-Sn phase diagrams [136].

As reported in Table 1, the Rietveld analysis allowed quantifying the amount of secondary phases in the samples, which is 12% wt. for Co_2Zr (2) and 7% wt. for Co_2Hf (5). Concerning phase 3 (CoSn), its abundance is too small to be calculated with the Rietveld refinement (so its quantity will be considered negligible). The relative amount of the secondary phases does not change after annealing; however, slight variation of the phases atomic composition and lattice parameters can be observed. The lattice parameters found for the as-cast alloys are 6.2338 Å and 6.2101 Å for Co_2ZrSn and Co_2HfSn, respectively. After annealing, the values of the lattice parameters become 6.2458 Å for Co_2ZrSn and 6.2157 Å for Co_2HfSn, which are very close to the equilibrium values reported by Ziebeck et al. [107] (i.e., 6.249 Å and 6.218 Å for Co_2ZrSn and Co_2HfSn, respectively). The unaltered phases' relative abundance before and after the annealing treatment, as well as the small changes in their elementary composition and in lattice parameters suggest that the Heusler phases 1 and 4 crystallize congruently from the melt with small impurities of secondary compounds Co_2Zr and Co_2Hf (2

and 5 respectively) and traces of CoSn (3), which are due to the slight deviation of the prepared samples from the nominal stoichiometry. Thus, these alloys can be easily processed by direct solidification of the melt.

As reviewed by Ponton et al. [137], when the surface of a material is indented, the cracks that propagate from the imprint can be of two different classes: halfpenny type and Palmqvist type. It is known that the halfpenny cracks propagate both on the surface (radial direction) and deeply below (median direction) the imprint. For this reason, they are also called radial-median cracks. Conversely, the Palmqvist type is shallower and includes cracks that do not propagate directly below the indentation, but only in the radial direction. It is possible to distinguish between the two typologies of cracks by performing a light polishing of the surface of the sample after indentation. After the procedure, if the cracks remain visible and always connected to the inverted pyramid of the indent, the behavior can be classified as halfpenny; whereas, a small detachment should be visible in case of cracks of the Palmqvist type, or, alternatively, only the indenter imprint should be observed in case of very shallow cracks [138–140]. It was also generally observed that fairly shallow Palmqvist-type cracks are expected for hard metallic materials [138].

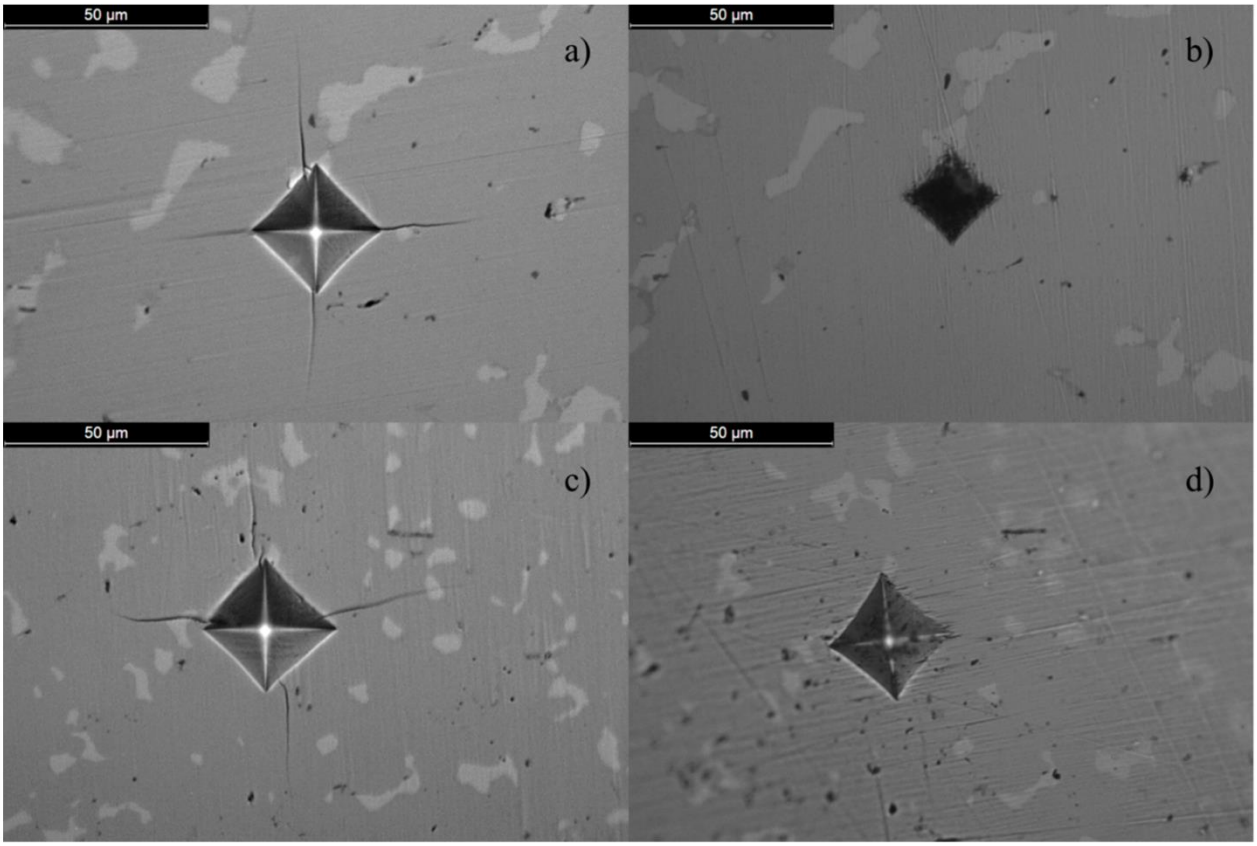

Figure 13: Examples of Vickers indentations on the Co_2ZrSn (a,b) and Co_2HfSn (c,d) alloys before (a,c) and after (b,d) light polishing.

As expected, significant cracks have been observed after the first indentation, which has been used to determine the hardness, as reported in Table 2. After light polishing of the surface using a 3 µm diamond paste, the radial cracks were no longer visible, indicating that these are extremely shallow. In Figure 13, as an example, one of the several indentations performed for each alloy is shown before and after the polishing treatment. No secondary cracks propagated from the Vickers imprint, which indicates that the whole load was transferred to the radial cracks, allowing an accurate estimation of the fracture toughness (K_{IC}). The same result was observed for all the other indentations. Several polishing cycles were performed until the Vickers imprints disappeared, and also in these cases, no median cracks were observed. It is possible to distinguish between the two types of cracks from the ratios *c/a* or *l/a* (where *c* is the length of the cracks from the center of the indent to their tip, *a* is half of the indentation diagonal, and *l* is the length of the crack measured from the corner of the indent).

Being $c = a + l$, it turns out that *c/a* and *l/a* are linked by the following relationship $l/a = (c/a) - 1$. According to Refs. [138] and [141], when $c/a \leq 2.5$ (or $l/a \leq 1.5$), the crack should be classified as Palmqvist. Other studies [142,143] fix the upper limit of Palmqvist cracks for values of *l/a* around 2.5 (or $c/a \leq 3.5$). The l/a ratio was calculated for both the alloys and the values obtained are lower than 1.5 in all the cases (see Table 2).

Alloy	**Hardness (HV)**	***l/a***	**K_{IC} (MPa·m$^{1/2}$)**
Co_2ZrSn	903 ± 31	1.42	2.07 ± 0.23
Co_2HfSn	899 ± 26	1.41	2.06 ± 0.14

Table 2: Average values of *l/a* ratios, Vickers hardness, and fracture toughness K_{IC} for the Co_2ZrSn and Co_2HfSn alloys.

In agreement to the micrographic observations, the cracks can be described as Palmqvist-type, so the fracture toughness K_{IC} can be evaluated using the Shetty–Wright–Mincer–Clauer equation [137,144], which in the case of a standard Vickers indenter is:

$$K_{IC} = 0.0319 \frac{P}{a \cdot l^{1/2}} \tag{33}$$

where *P* is the applied load. As reported in Table 2, the two alloys exhibit similar mechanical properties, showing a rather high hardness for metallic compounds and a fracture toughness comparable to those of ceramics [145]. These values are close to those generally exhibited by Heusler alloys [146].

5.3 Magnetic properties

Figure 14 shows the hysteresis loops, M(H), obtained by SQUID measurements at selected temperatures between 2 K and 400 K for Co_2HfSn (a) and Co_2ZrSn (b) alloys. Both samples clearly show a non-saturating high-field behavior, which becomes increasingly apparent at high temperatures. The low-field region of the hysteresis loops for Co_2HfSn and Co_2ZrSn alloys is highlighted in more detail in Figure 1c and 1d, respectively. A symmetric hysteresis loop is observed in both samples, with coercive field values at T = 2 K of 16 Oe for Co_2HfSn and 7 Oe for Co_2ZrSn, which gradually decreases with increasing temperature down to about 7 Oe and 2 Oe, respectively, at T = 400 K. The non-saturating high-field trend of the M(H) curves is highlighted in Figure 14e and Figure 14f for Co_2HfSn and Co_2ZrSn alloys, respectively. High temperature magnetic properties obtained by the VSM are shown in Figure 15 in the range around T_C. Combining SQUID and VSM measurements, it was possible to obtain the complete magnetization curve as a function of temperature under constant field (H = 5 kOe), as shown in for both alloys. The magnetization curves obtained by SQUID and VSM measurements match satisfactorily.

From the values of coercive fields, it is possible to suggest a weak itinerant ferromagnetic behavior for both alloys. In weak itinerant ferromagnets, the electrons responsible for ferromagnetism participate in the electrical conduction and the unbalance between spin-up and spin-down carriers is small. In Wohlfarth's simple model of weak itinerant ferromagnetism, the following relationship is obtained under equilibrium conditions for free magnetic energy [132,133]:

$$\frac{H}{M} = \alpha(T) + \beta(T)M^2 + O\{M^4\} \tag{34}$$

with M(H,T) the magnetization, and α, β the temperature dependent coefficients. This expression is valid when the following two conditions are simultaneously satisfied:

- $M(H,T) \ll Nn\mu_B$, where *N* is the number of atoms concurring to provide electrons to the conduction band, *n* the number of electrons per atom in the conduction band, μ_B is the Bohr magneton;

- b) $T \ll T_F$, where T_F is the Fermi temperature of the electron gas. In our case, the maximum magnetization is $M_{max} \cong 0.1\, Nn\mu_B$, and T is always well below T_F for both alloys.

In the present case, the terms in higher even powers of magnetization (M^{2j}, where j = 2,3,4, …) may be considered negligible, because the leading factor in the coefficient of these terms is of the type $\rho'^{2j}_F/\rho'^{4j+1}_F$, where ρ_F and ρ'_F are, respectively, the density of states and its derivative at the Fermi energy [132]; these coefficients are estimated to be very small for $j \leq 2$, when the DOS ρ(E) does not show a highly structured behaviour around the Fermi energy.

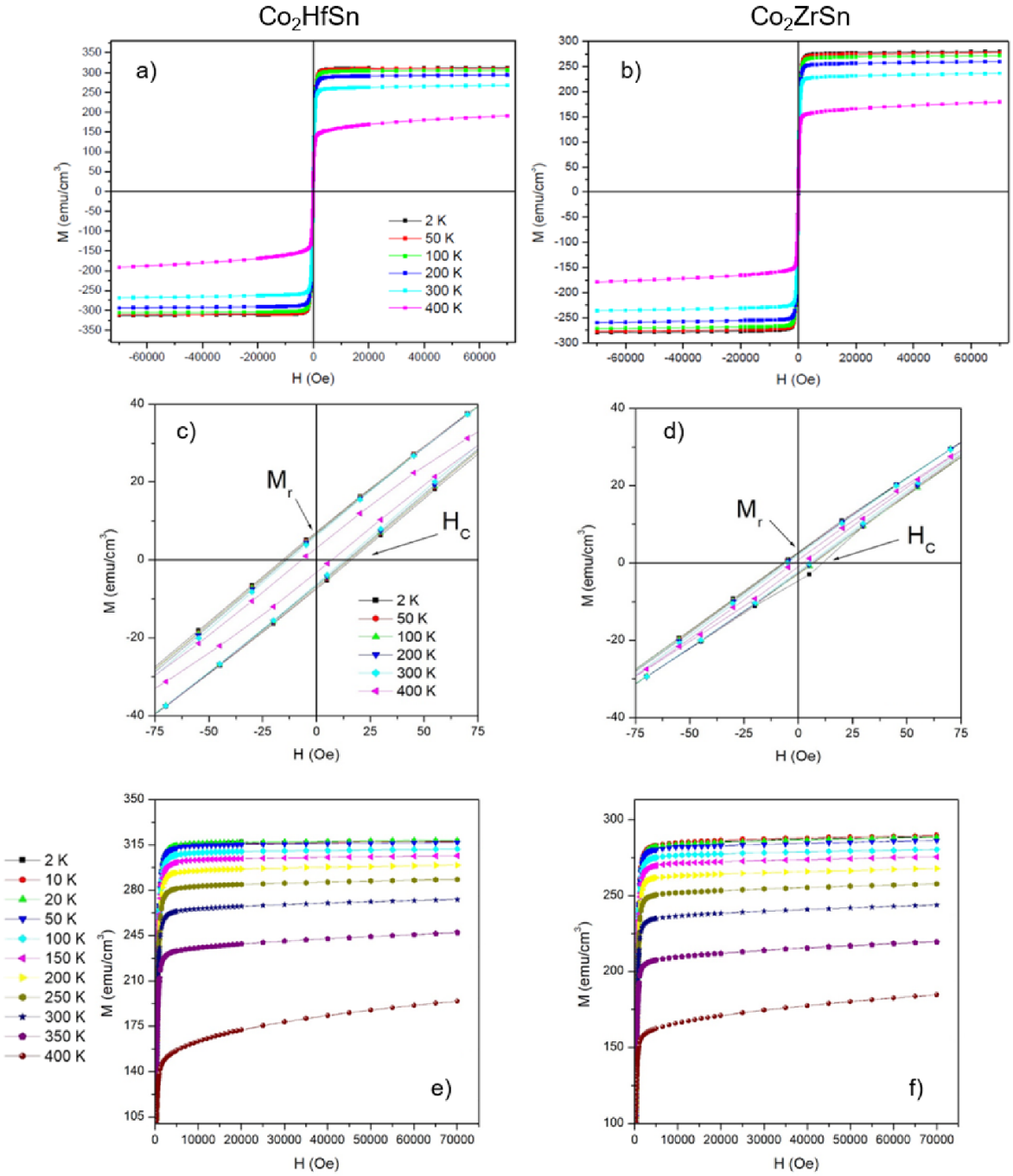

Figure 14: SQUID magnetization results. a-b) Hysteresis loops of Co_2HfSn and Co_2ZrSn, c-d) Low-field details Co_2HfSn and Co_2ZrSn, e-f) High-field details Co_2HfSn and Co_2ZrSn at different temperatures.

This model implies that the ferromagnetic order of Co_2HfSn and Co_2ZrSn compounds can be basically described by two temperature-dependent parameters, α and β (see Equation 34). These quantities can be derived from the Arrott plots, as shown in Figure 17.

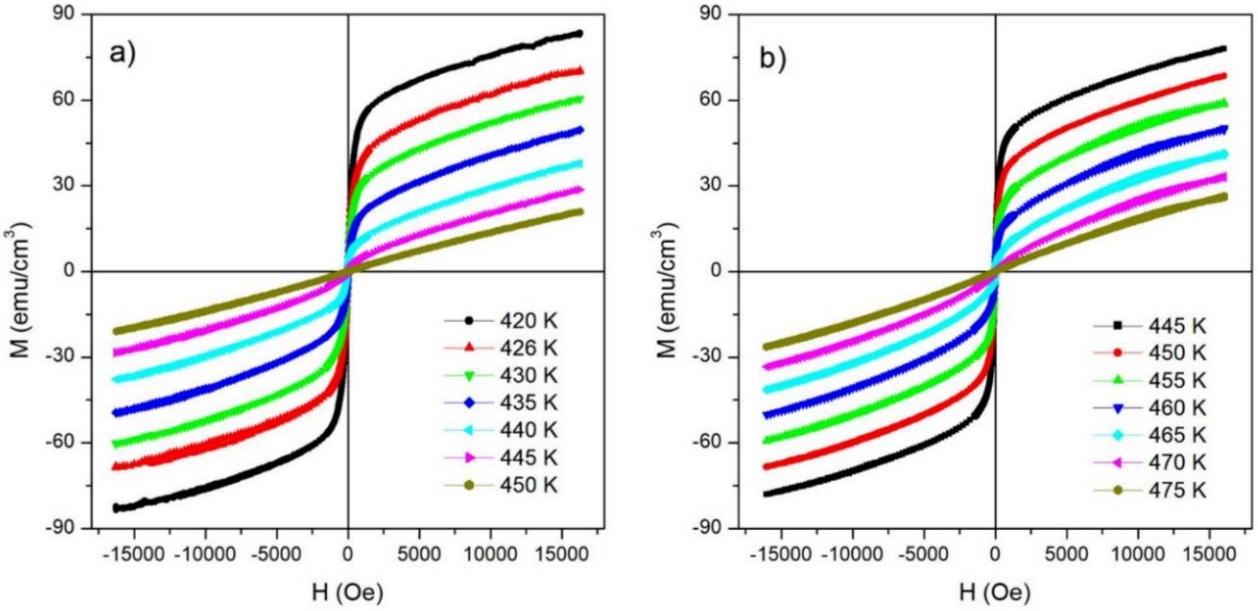

Figure 15: VSM measurements of magnetization in proximity of the Curie temperature in Co_2Hfsn (a) and Co_2ZrSn (b).

In weak itinerant ferromagnetism, Arrott plots directly derive from Equation 34, when $O\{M^4\}$ terms are neglected, so that a linear relationship between M^2 and H/M should be observed at all temperatures, both well below and above T_C (Figure 17).

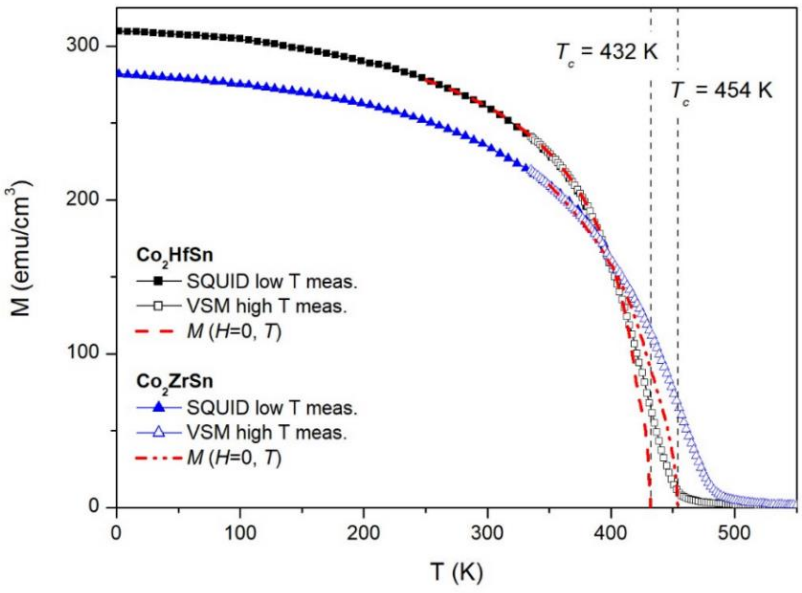

Figure 16: Temperature dependence of magnetization of Co_2HfSn and Co_2ZrSn samples under a constant field of 5 kOe. Full and open symbols refer to SQUID and VSM measurements, respectively. Red dashed lines are the corresponding M(H=0, T) curves. The Curie Temperatures (T_C) are highlighted by the vertical grey dashed lines.

As usual, the low-field regions are excluded by the plot, because the Wohlfarth theory applies to an infinitely extended, ideal single crystal, containing no magnetic domain walls, whereas the low-field regions of the measured M(H) curves are dominated, in real samples, by the presence of multiple magnetic domains arising by effect of surfaces, grain boundaries, defects, magnetic anisotropies, and responsible for the observed magnetic hysteresis. Data shown in Figure 17 are taken for $H \geq 7$ kOe, i.e., well above the closure field of the hysteresis loops, where the sample can be assumed to be in a single-domain state. The observed linearity between M^2 and H/M at all temperatures (Figure 17 a,b) strongly suggests that both compounds are indeed weak itinerant ferromagnets. It should be remarked that in all ferromagnetic materials the linearity between M^2 and H/M can usually be observed near to the Curie temperature, being derived from the general Landau's theory of magnetic phase transitions [133,134], but it is hardly found elsewhere.

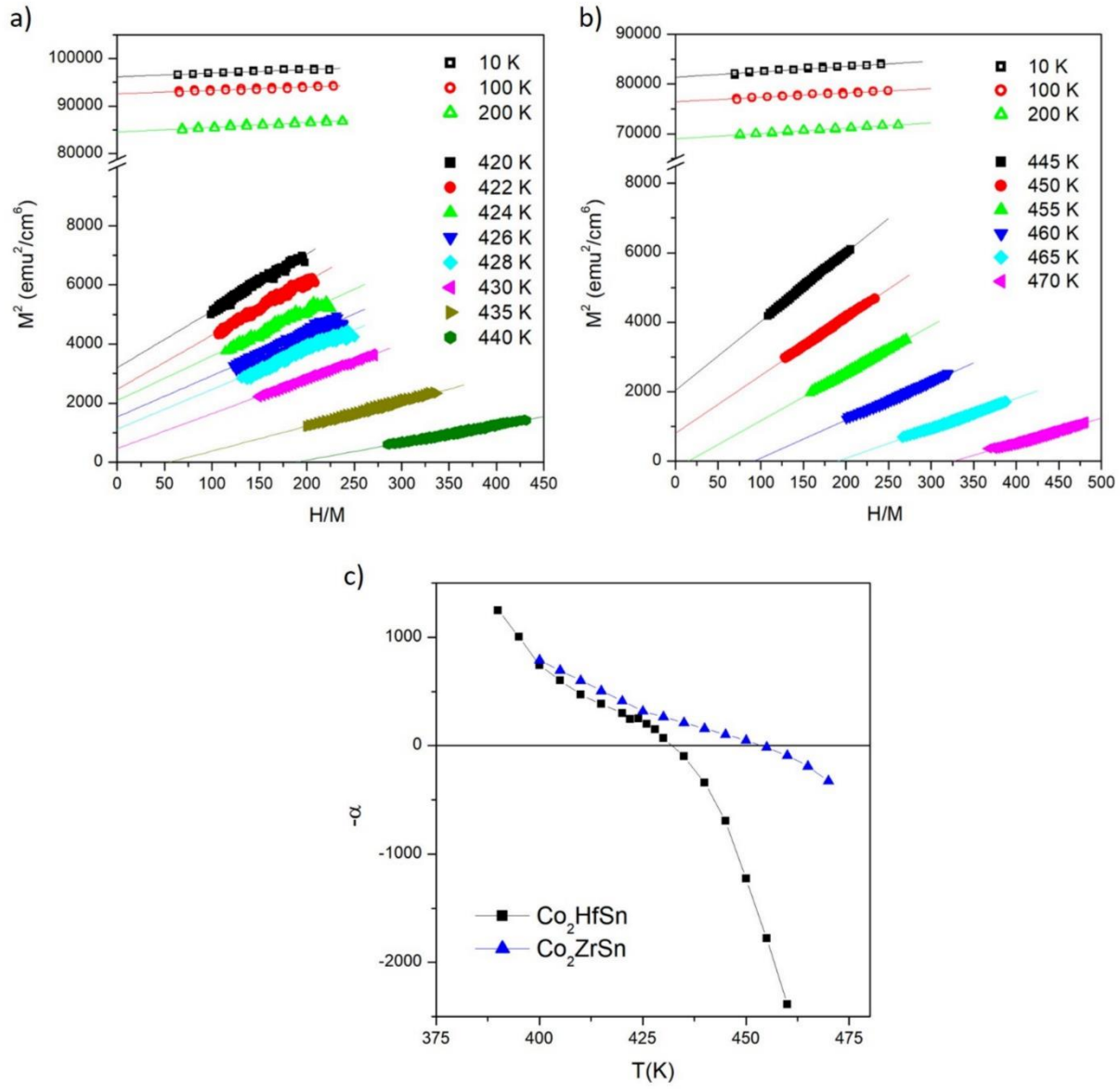

Figure 17: Arrott plot of a) Co_2HfSn, b) Co_2ZrSn alloys, and c) -α parameter as a function of temperature around T_C.

The trend of the parameter -α(T) as a function of temperature is shown in Figure 17c. It should be noted that information about T_C can be obtained either from the graphs in panels a), b) of Figure 17 (the linear extrapolation of the high-field data is expected to pass through the origin at $T = T_C$) or from the change of sign of the parameter -α(T) observed in Figure 17c. The latter method allows a more accurate estimate of the transition temperature, resulting in $T_C = 432$ K and $T_C = 454$ K for Co_2HfSn and Co_2ZrSn, respectively. The

theoretical zero-field magnetization for $T \leq T_C$ is $(H = 0, T) = \sqrt{-\alpha(T)/\beta(T)}$. This curve is shown in Figure 16 (red dashed line). The effect of applying a constant magnetic field (H = 5 kOe) during measurements is negligible at low temperatures (i.e., $(H = 5\ kOe, T) \cong M(H = 0, T)$) whereas it becomes increasingly apparent when T approaches to T_C and obviously for $T > T_C$. As a matter of fact, the magnetization curve at 5 kOe obtained using the SQUID magnetometer (i.e. up to 400 K) can be safely taken as representative of the behaviour of the ideal spontaneous magnetization.

The data reported in Arrott plots are well described (even in proximity of the ferromagnetic-paramagnetic transition) by using the mean-field values for the exponents of H/M and M, as appearing in Equation 34 (i.e., 1 and 2, respectively) [53,133]. Slightly different values of the critical exponents (1.02-1.03 and 2.10-2.12, respectively) were recently found in Co_2HfSn by exploiting accurate magnetization measurements performed using a SQUID magnetometer around T_C [53]. A further method to prove that the mean field model is able to describe the magnetic properties of Co_2HfSn and Co_2ZrSn samples at high temperatures, is to verify the functional dependence of M on H near T_C. According to Equation 35, at T_C the behavior of M with H is predicted to be:

$$M(H) = \frac{1}{\beta^{\frac{1}{3}}(T_C)} H^{1/3} \tag{35}$$

The $M(H^{1/3})$ curves are reported in Figure 18 for temperatures around T_C. All curves are basically linear and almost parallel to each other, as indicated by the theory, the coefficient β being almost constant there.

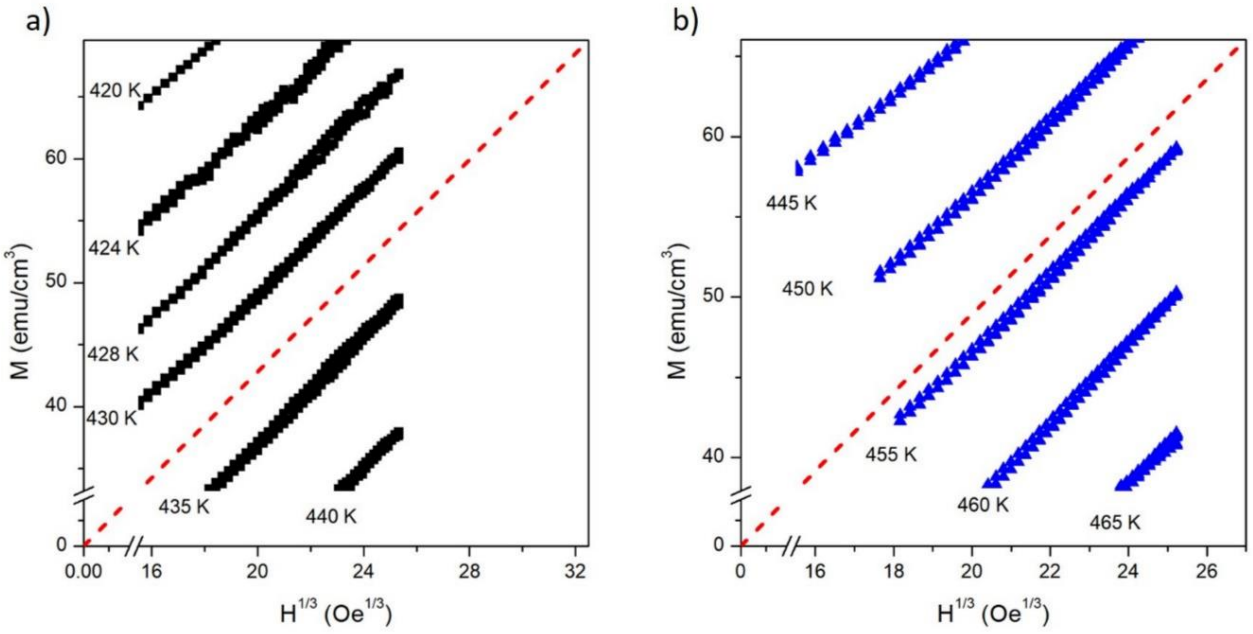

Figure 18: Symbols: experimental magnetization dependence on $H^{1/3}$ around T_C of Co_2HfSn (a) and Co_2ZrSn (b). Dashed straight lines: behavior of $M(H^{1/3})$ predicted at $T = T_C$.

The inverse initial susceptibility $\chi_0^{-1} = (\lim_{H\to 0} \frac{dM}{dH})^{-1}$ is reported as a function of $T > T_C$ in Figure 19a,b (full symbols). In the mean field model of weak itinerant ferromagnetism, $\chi_0^{-1}(T) \equiv \alpha(T)$, as directly derived from Equation 34. The quantity α(T) obtained from the Arrott plots is also shown in Figure 19a,b (open symbols). Experimental and predicted results are in rather good agreement well above T_C, while close to the Curie temperature the inverse magnetic susceptibility is substantially lower than the theoretical prediction, indicating that the M(H) curves are steeper than predicted by the model. This can be checked by directly looking at experimental and calculated M(H) isotherms (Figure 19c,d). The theoretical curves are easily obtained in analytical form by solving Equations 36 and 37.

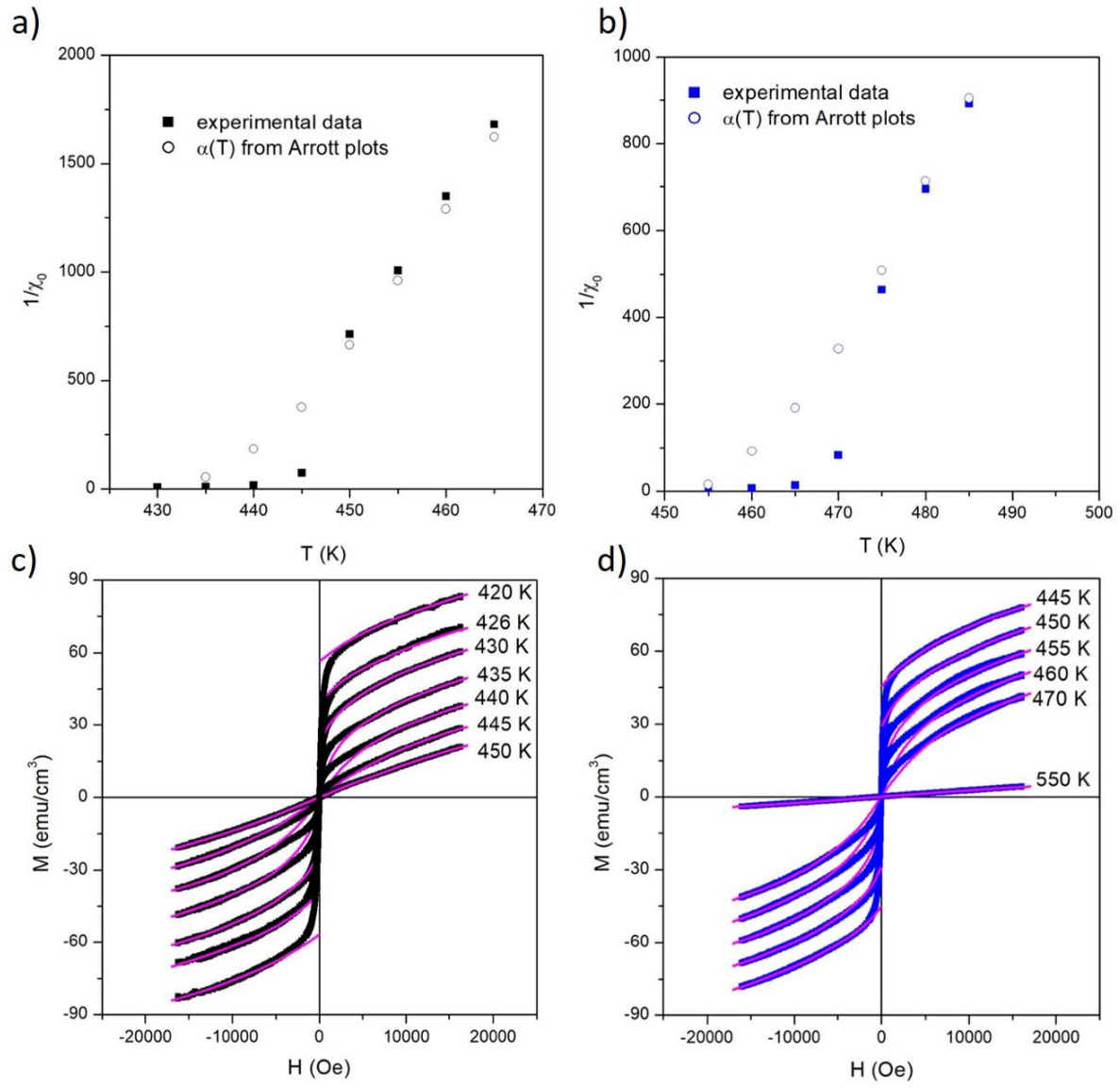

Figure 19: Upper row: inverse of the zero-field magnetic susceptibility (χ_0^{-1}) as a function of temperature in Co_2HfSn (a) and Co_2ZrSn (b). Full symbols: experiment, open symbols: theory. Lower row: comparison between experimental and calculated M(H) isothermal magnetization curves of Co_2HfSn (c) and Co_2ZrSn (d). Full symbols: experiment, lines: theoretical M(H) curves.

Equation 34 is a simple algebraic equation of the third order in M when terms in powers of M higher than M^2 in the right-hand term are negligible, and can therefore be solved in a straightforward way. The solutions under T_C (where $\alpha < 0$) are:

- If $\Delta = \frac{H^2}{4\beta^2} + \frac{\alpha^3}{27\beta^3} < 0$ (low fields)

$$M(H,T) = 2\sqrt{\frac{-\alpha}{3\beta}}\cos\left[\frac{1}{3}atan\left(\frac{\sqrt{\frac{(-\alpha)^3}{27\beta} - \frac{H^2}{4}}}{H}\right)\right] \quad (36)$$

- If $\Delta = \frac{H^2}{4\beta^2} + \frac{\alpha^3}{27\beta^3} > 0$ (high fields)

$$M(H,T) = \sqrt[3]{\frac{H}{2\beta} + \frac{1}{\beta}\sqrt{\frac{H^2}{4} + \frac{\alpha^3}{27\beta}}} + \sqrt[3]{\frac{H}{2\beta} - \frac{1}{\beta}\sqrt{\frac{H^2}{4} + \frac{\alpha^3}{27\beta}}} \quad (37)$$

The two solutions perfectly match for $\Delta = 0$. The solution above T_C (where $\alpha > 0$) is the same as Equation 37. It should be noted that the temperature dependence of M(H,T) is contained in the α and β parameters only.

The curves drawn using the $\alpha(T)$ and $\beta(T)$ values derived from the Arrott plots, with no adjustable parameters, are shown in Figure 19c,d. For both compounds, all theoretical curves appear to be superimposed to the corresponding experimental results at high magnetic fields. This confirms that terms in high powers of magnetization (M^{2j}, where j = 2,3,4, …) in Equation 34 are not required in order to describe the present experimental results. As it will be discussed later, this is related to the shape of the electronic density of states around the Fermi level.

Below T_C, the agreement between theory and experiment is to be expected only at high fields, when the sample is in a single-domain state. In particular, the theory predicts the existence of a finite value of the spontaneous magnetization M(H,T) for $H \rightarrow 0$, whereas the presence of magnetic domains in a real sample leads to a much lower remanence value, which is very close to zero in the temperature range considered in Figure 19c,d. This explains the observed deviation between theory and experiment below about 7 kOe.

Well above T_C the agreement between theory and experiment is very good. In this case, both experimental and theoretical curves appear to be perfectly superimposed over the entire magnetic field range, including the low field region. A deviation is observed in both compounds for temperatures slightly higher than T_C; in particular, the experimental curves turn out to be steeper than predicted by the model. This behavior reflects the discrepancy of χ_0^{-1} and α values around T_C put in evidence by Figure 19a,b. One possible origin of this behavior is the presence of slight fluctuations in the composition of samples, which could entail a non-uniform transition temperature T_C in different regions of the material. In this case, the higher slope of the experimental curves for temperatures just above T_C could derive from a residual ferromagnetic contribution of regions where the magnetic transition has not yet occurred. In this regard, it should be mentioned that as far as the composition of Heusler phases are concerned, SEM-EDS analysis of samples indicated deviations from the ideal stoichiometry, of the order of a few percent, as reported Section 5.1.

5.3.1 Magnetization at low temperature

The temperature dependence of the magnetization measured under a magnetic field of 5 kOe (basically coincident with the spontaneous magnetization, as remarked before) is shown in Figure 20. In both compounds, the magnetization is accurately fitted by a law of the type $M_s = M_s(0) \cdot (1 - AT^2)$ up to T ≈ 230 K (left panels). However, at low temperatures, the M(T^2) curve deviates upwards from a straight line, as shown in the two insets of Figure 20; in Co_2ZrSn the deviation is stronger and takes place below about 70 K, whilst in Co_2HfSn it is observed below about 30 K. At low temperatures, the magnetization can be instead fitted by the Bloch law, $M_x = M_s(0) \cdot (1 - BT^{3/2})$, as shown in Figure 20 (right panels). These results are in good agreement with the calculated DOS (see Section 8) and with the possible half-metallic character of these Heusler alloys. In itinerant ferromagnets, the linear dependence of magnetization on the square of temperature arises by effect of spin flipping excitations of electrons (Stoner excitations); however, in HMFs, spin-flip processes are inhibited at low temperatures by the spin-flip energy E_{flip}, so that transverse spin wave excitation, resulting in the Bloch law, becomes the dominant mechanism of magnetization reduction [69,94]. This effect can be pictured as the prevalence of localized (Heisenberg-type) ferromagnetism at very low temperature (as expected for half metals when spin-flip processes are inhibited) followed by a gradual transition to standard itinerant ferromagnetism, when Stoner excitations begin to play an important role.

The observed crossover between Bloch and Stoner laws for M(T) is in agreement with the theoretical prediction that the Fermi energy is in the gap of the minority electron sub-band. In Co_2ZrSn, the crossover

temperature is higher than in Co_2HfSn, suggesting a higher spin-flip energy, as actually predicted by calculations (Section 8). In Co_2HfSn, the much weaker deviation of M(T) away from the T^2 law is compatible with a Fermi energy still located in the minority electron gap, but very close to its upper edge, so that spin-flip processes begin to take place at very low temperatures. The picture emerging from the present analysis for Co_2HfSn agrees with the results of simulations (see Section 8), where the Fermi level was found to be remarkably close to the edge of the conduction band. It should be remarked that in the region where spin-flip effects dominate, the quantity $\Delta M/M = [M_s\,(0) - M_s\,(T\text{^}2\,)]/M_s\,(0) = AT^2/M_s\,(0)$ turns out to have basically the same slope ($A/M_s(0) \approx 1.70 \cdot 10^{-6}K^{-2}$) in both alloys, indicating that the densities of electronic states around the Fermi level are similar in the two compounds [147], in qualitative agreement with the calculated DOS.

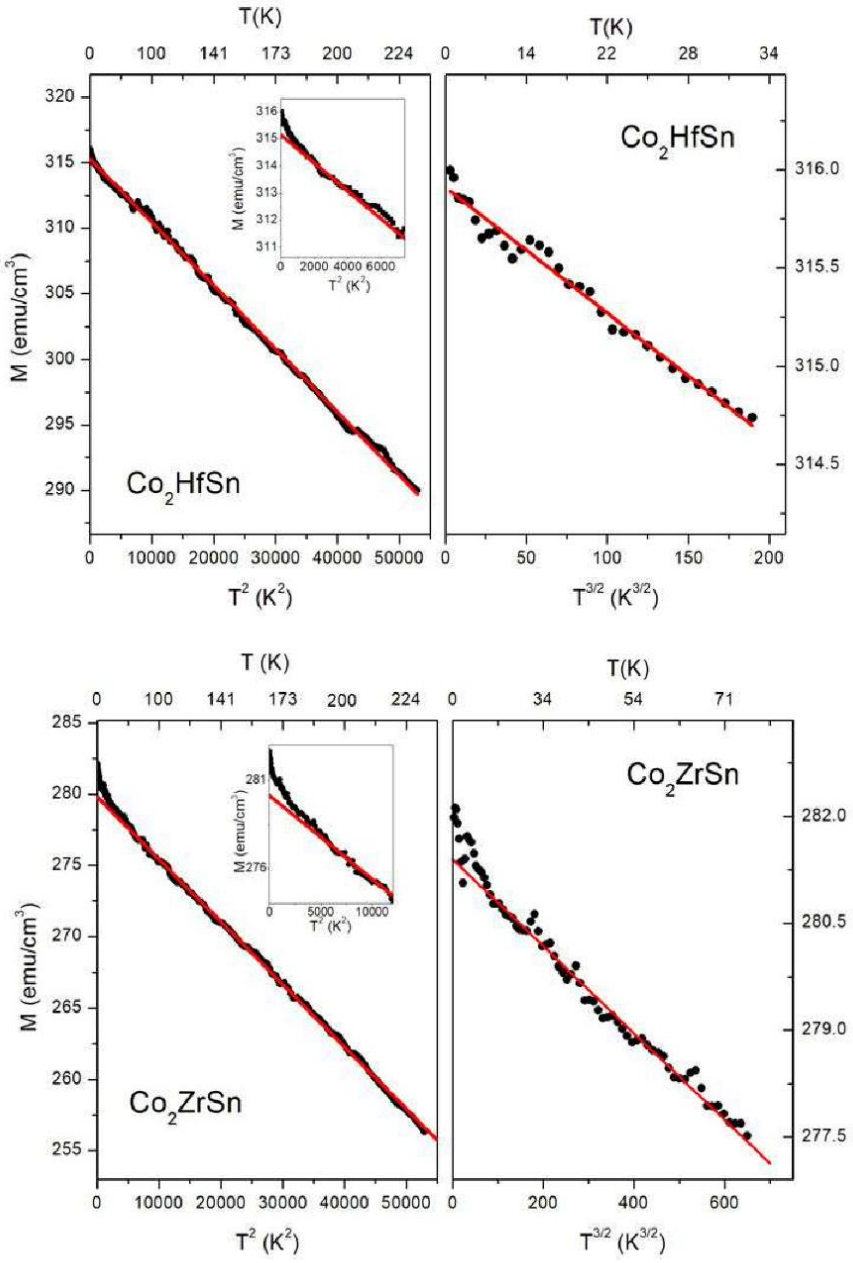

Figure 20: Left panels: Plot of spontaneous magnetization M_s as a function of T^2 in Co_2HfSn (up) and Co_2ZrSn (down). Insets show the deviation from the T^2-law. Right panels: plot of M_s as a function of $T^{3/2}$ at low temperatures in Co_2HfSn (up) and Co_2ZrSn (down).

As far as the magnetic moments per formula unit are concerned, based on the Slater-Pauling rule for half-metallic Heusler alloys as well as ab-initio calculations (Section 8), values of $\mu = 2.00\ \mu_B$ are expected for these compounds. Magnetic moments of $\mu = 2.01\ \mu_B$/f.u. for Co_2HfSn and 1.80 μ_B/f.u. for Co_2ZrSn result from extrapolation to T = 0 K of the overall experimental data. These values are in agreement with the experimental values of μ reported in different papers, ranging from 1.50 to 2.00 μ_B/f.u. in Co_2HfSn [53,80,107,109,110,113] and from 1.34 to 2.00 μ_B/f.u. in Co_2ZrSn [80,107–112,148]. However, the effect of the relative amount of impurities present in the samples used in our measurements (see Section 5.2) should also be taken into account. The intermetallic compounds Co_2Hf and Co_2Zr are known to be standard Pauli paramagnets, characterized by very low susceptibility values [108,149,150]. A calculation done using these susceptibility values shows that the contribution of the magnetic impurities is completely negligible at all temperatures, resulting in a magnetization at 70 kOe which is lower than the measured value by about three orders of magnitude. Considering the presence of the impurity phases, the values per formula unit would become: $\mu = 2.15\ \mu_B$/f.u. for Co_2HfSn and 2.05 μ_B/f.u. for Co_2ZrSn. Deviations from stoichiometry and secondary phases are rarely taken into consideration in the literature on the considered alloys. However, the type and fraction of spurious non-Heusler compounds can strongly affect the experimental value of magnetic moment per unit formula, and can be deemed responsible for the very scattered experimental values of μ found in the literature as shown above. The occurrence of secondary phases in Co_2ZrSn and Co_2HfSn samples has already been reported in literature also by Yin et al. [115], who extensively investigated formation enthalpies and other thermodynamic properties of a large number of Co-based Heusler compounds.

5.4 Transport properties

The trends of the electrical conductivity (σ), Seebeck coefficient (S), and power factor (PF) of annealed Co_2ZrSn and Co_2HfSn ingots as a function of the temperature are shown in Figure 21. The transport properties were measured imposing a cyclic ramp of temperature in order to ensure the thermal stability of the samples and the reproducibility of the results under thermal cycling. Since no hysteresis is observable between heating and cooling, it is confirmed that the specimens are stable, and the outputs are reproducible. Values previously obtained for Co_2TiSn [50] are reported for comparison. It should be noted that the values measured in this work refer to samples containing metallic secondary phases (i.e., Co_2Zr and Co_2Hf) [151], which likely tend to increase the electrical conductivity and lower the absolute value of the Seebeck coefficient with respect to the corresponding single-phase materials.

The Seebeck coefficient of both alloys is shown in Figure 21a as a function of temperature. It is negative as in the case of Co_2TiSn [50], indicating that the major charge carriers are electrons (n-type). At 298 K, the values of *S* are −9 μV/K and −13 μV/K for Co_2ZrSn and Co_2HfSn alloys, respectively. The absolute values of S of two alloys show a linear increase from room temperature to T_C. At higher temperatures, the values of *S* settle on a plateau at approximately −34 μV/K and −38 μV/K for Co_2ZrSn and Co_2HfSn samples, respectively. As reported for Co_2TiSn and other types of compounds [50,152,153], a linear increase of Seebeck coefficient followed by a constant value above the Curie temperature can be related to a steady position of the Fermi level over an extended range of temperature.

Figure 21a shows that the electrical conductivities of Co_2ZrSn and Co_2HfSn are quite similar to each other. At room temperature (298 K), electrical conductivities values of 4196 S/cm and 4476 S/cm are measured for Co_2ZrSn and Co_2HfSn, respectively. Since for this class of compounds, the Curie point can be determined measuring the point at which σ changes its slope [50], T_C values of 465 K and 426 K have been obtained for Co_2ZrSn and Co_2HfSn, respectively. The electrical conductivity decreases almost linearly as a function of the temperature until T_C is reached, where it exhibits the lowest value, namely 2982 S/cm for Co_2ZrSn and 3046 S/cm for Co_2HfSn. After T_C, the electrical conductivities show a slight increase with the temperature, until values of 3235 S/cm and 3267 S/cm are observed for Co_2ZrSn and Co_2HfSn, respectively, at 778 K. Considering these trends, it is possible to observe that the materials show metallic-like behavior at temperatures lower than T_C, whereas the electrical conductivities switch to a semiconductor-like behavior at higher temperatures. This is a consequence of the ferromagnetic–paramagnetic transition, which strongly influences the electronic DOS of the alloys. These results are in good agreement with those reported by De Souza et al. [154].

The behavior of the power factor (PF = $S^2\sigma$) as a function of temperature is similar for the two alloys, as shown in Figure 21c. Between room temperature and T_C, the PF of the two alloys increases as a function of temperature. Above T_C, the PF values for both alloys reach a plateau, which is maintained up to 778 K. The observed behavior strongly reflects the trend of the Seebeck coefficient, which actually gives the main contributions to PF. At room temperature, values of 0.026 $mW \cdot m^{-1} \cdot K^{-2}$ and 0.068 $mW \cdot m^{-1} \cdot K^{-2}$ are observed for S, while at 778 K, they show a plateau value of 0.38 $mW \cdot m^{-1} \cdot K^{-2}$ and 0.47 $mW \cdot m^{-1} \cdot K^{-2}$ for Co_2ZrSn and Co_2HfSn samples, respectively. In most of the thermoelectric materials, the temperature dependence of the power factor shows a peak value in a narrow temperature range (approximately 100 K) [155], leading to a less efficient conversion when large temperature gradients are imposed. In the case of Co_2ZrSn and Co_2HfSn alloys, the extension of the power factor plateau across a wider temperature range (200–300 K) would allow obtaining optimal conversions also when temperature gradients of hundreds of degrees are used.

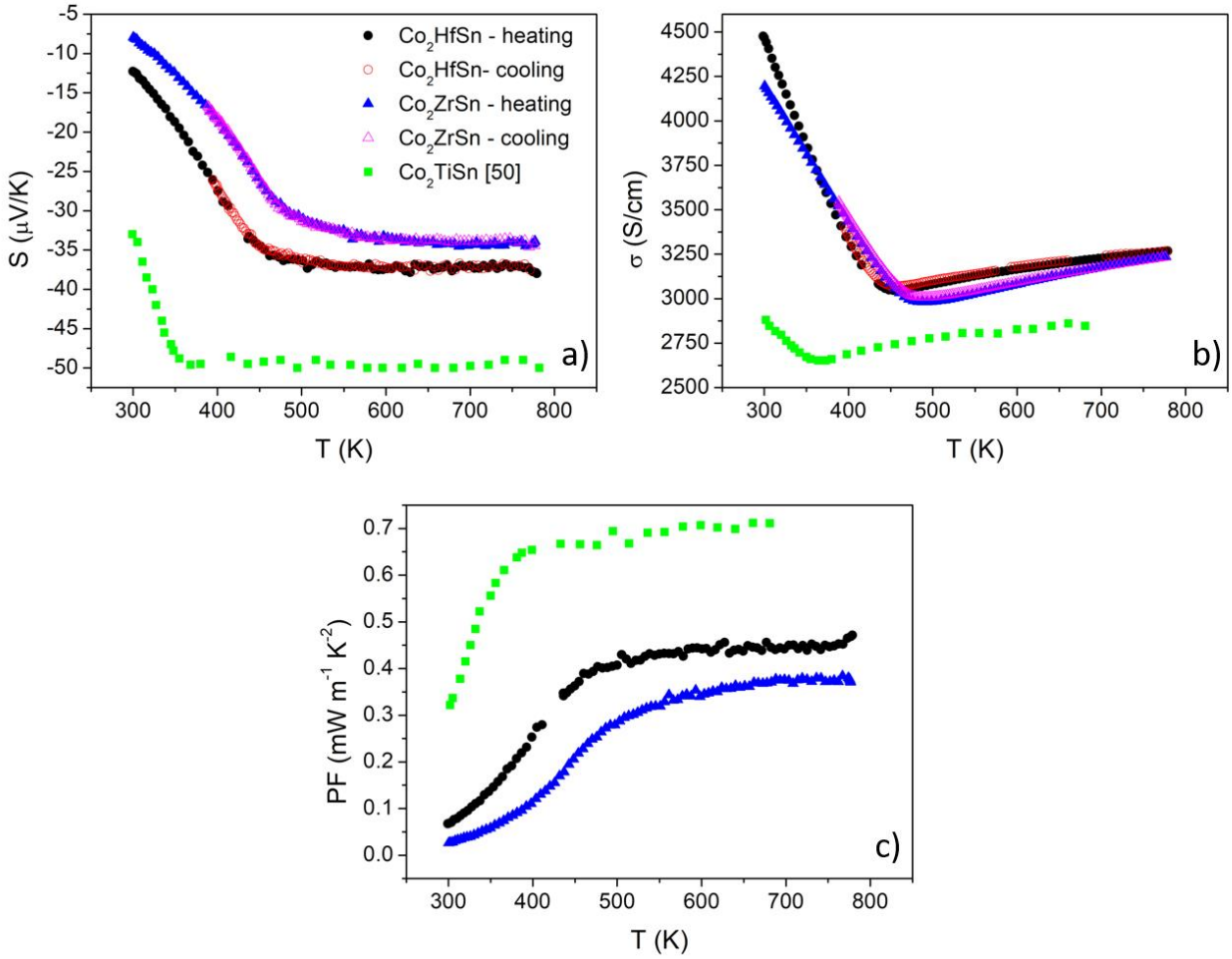

Figure 21: Seebeck coefficient (a), electrical conductivity (b), and power factor (c) of the Co_2ZrSn and Co_2HfSn alloys. The transport properties of Co_2TiSn are shown as a comparison [50].

In the case of homogeneous solid solutions, the thermoelectric properties can be modulated on the basis of the fraction of the substituting elements. For example, the substitution effects are deeply known for the Fe_2VAl and Fe_2VAl-related FH compounds [156–159]. In fact, it is known that in multi-substituted Fe-based FH alloys, where the V atoms are replaced with isoelectronic elements (Nb and Ta), the thermoelectric performances result generally enhanced. The implementation of these strategies on the Co-based FH alloys would be a considerable step forward in the application of this class of materials. Potentially, isoelectronic substitution of X in Co_2XSn (X = Ti, Zr, Hf) might lead to a complete solubility over the whole compositional range, such as in (Zr,Hf)NiSn half-Heusler compound, or to partial solubility in a limited compositional range, such as in (Ti,Zr)NiSn and (Ti,Hf)NiSn half-Heusler alloys [160].

As far as the Seebeck coefficient is concerned, Co_2TiSn shows the highest absolute value of about 50 μV/K after T_C, while for Co_2HfSn and Co_2ZrSn compounds, values equal to 38 μV/K and 34 μV/K, respectively, can be observed. However, when the electrical conductivity is taken into account, Co_2TiSn is the compound with the lowest σ, while Co_2Hf and Co_2ZrSn display similar values of 3153 S/cm and 3214 S/cm, respectively. This leads to power factor values of 0.71 $mW \cdot m^{-1} \cdot K^{-2}$, 0.47 $mW \cdot m^{-1} \cdot K^{-2}$ and 0.38 $mW \cdot m^{-1} \cdot K^{-2}$ for Co_2TiSn, Co_2HfSn, and Co_2ZrSn compounds, respectively. All these values are quite high for metallic materials. Considering Co_2TiSn and Co_2HfSn, which respectively show the largest Seebeck coefficient and electrical conductivity in the series, as end members, we could expect that if Ti is progressively substituted by Hf, the absolute value of the Seebeck coefficient would decrease, while the electrical conductivity would increase. the substitution of Ti with Hf would shift the Curie temperature at higher values, similarly to Co_2TiZ (Z = Si, Ge, Sn), where a fine tuning of T_C can be achieved by substituting the Z atom [50]. As already mentioned, an increasing value of T_C is useful in spintronics and spin-caloritronics applications, where it is desirable to have ferromagnetic materials even at high temperatures.

5.5 Conclusions

In this section, the structural, mechanical, magnetic, and electronic transport properties of the Co_2ZrSn and Co_2HfSn Heusler compounds synthesized by arc melting with subsequent annealing have been exposed. The almost invariance of the relative abundances of phases after annealing reflects that the equilibrium is reached directly by solidification of the melt. The presence of small quantities of secondary phases, as previously reported by other studies [107], can be explained by the observed slight deviation of the samples from the nominal stoichiometry. The two alloys show high hardness (about 900 HV) and fracture toughness typical of ceramics (about 2 $MPa \cdot m^{1/2}$).

Both alloys can be considered as weak itinerant ferromagnets over most of the investigated temperature intervals and are well described by the Edwards-Wohlfarth model, neglecting high-power terms of magnetization. This simple mean-field approach is able to explain the magnetic behaviour of both compounds over a wide range of temperatures and applied magnetic fields. The agreement between the experimental *M(H)* curves and the ones predicted by the model without making use of terms in higher powers of magnetization indicates that basically smooth profiles of the density of states are expected in proximity of the Fermi level for both compounds. The temperature dependence of spontaneous magnetization at low temperatures confirms the existence of a crossover from localized ferromagnetism to standard itinerant ferromagnetism. This can be related to a change in spin-flip mechanism possibly due to the presence of a half-metallic band gap at low temperatures as already observed for other Heusler compounds [69,94,161].

The transport properties of Co_2ZrSn and Co_2HfSn were measured for the first time [116]. The Seebeck coefficient values are negative for both the alloys across the entire range of temperature explored (i.e., from room temperature up to 778 K), indicating an n-type behavior where electrons are the major charge carriers. For both the alloys, the absolute value of the Seebeck coefficient increases almost linearly between room temperature and the Curie temperature and shows a constant plateau after T_C instead of the typical peak shape. No sign of hysteresis was shown after thermal cycling, indicating the good thermal stability of the alloys in the considered temperature range. Concerning the electrical conductivities, both the compounds are found to behave similar to metals before T_C, and similar to semiconductors after T_C; furthermore, the values of σ set in almost constant plateaus at temperatures sufficiently higher than the Curie point. The power factor of the alloys also exhibits a quite linear increase, followed by a constant ceiling, reflecting the trends of the Seebeck coefficients that are the dominant contributors to the power factor.

Taking into account the information available in the literature for the Co_2TiSn compound, we ordered the transport properties of the Co_2XSn (X = Ti, Zr, Hf) family of Heusler compounds. While Co_2ZrSn and Co_2HfSn show larger electrical conductivities, Co_2TiSn shows a larger absolute value of the Seebeck coefficient. Thus, Co_2TiSn shows the largest power factor in the series. The possible effects of the substitution of Ti with Hf on the electronic transport properties were considered beneficial both for the enhancement of transport properties and for the tuning of T_C for spintronic applications.

6. Transport properties and half-metallicity of Co_2HfSn obtained by rapid solidification and sintering

In this section we investigated the electronic and thermal transport properties of the Co_2HfSn Heusler alloy, spotlighting its potential for spintronic and spin-injection applications. The rapid solidification process notably expands the stability domain of the Heusler phase, paving the way for consistent single-phase sample preparation and untainted compound characterization. In fact, the presence of secondary phases is known to be a major preparation issue with Heusler alloys [115]. In fact, previous samples obtained by arc-melting and annealing (see Section 5) were found to include a small but non-negligible amount of Co_2Hf secondary phase. The fast quenching rate also favors microstructure refinement, enhancing the thermoelectric figure of merit. Quantitative information on such microstructure has been obtained from electron backscattered diffraction (EBSD) analysis, as well as SEM-EDS. The thermoelectric properties were measured in Co_2HfSn to assess its potential as a thermoelectric material and to better establish its electronic ground state. The electrical conductivity at low temperature has shown a peculiar behavior, consisting in a low-T σ/T^2 regime, followed by a $\sigma/T^{1.40}$ above 75 K. This has been explained, similarly to other Heusler compounds [69,94], by considering a change in the electronic scattering mechanisms induced by a crossover from a half-metallic to an itinerant ferromagnetic state. The figure of merit zT of Co_2HfSn was experimentally estimated here for the first time [52].

6.1 Materials and methods

The elemental metals (Co 99.97 %, Hf 99.7 %, Sn 99.97 % purity) were weighted in appropriate stoichiometric quantities and melted in an Edmund Buhler GmbH (Bodelshausen, Germany) arc-furnace. The sample was melted several times to ensure homogeneity. The alloy was then re-melted in a boron nitride crucible and injected onto a rotary copper wheel (20 m/s speed) using an Edmund Buhler GmbH melt-spinning apparatus. The rapidly solidified material was hand-grinded into powder and subsequently sintered by spark plasma sintering (SPS) with a Fuji 515 S equipment. Graphite molds lined with graphite paper were used to obtain pellets 8–10 mm in diameter and approximately 2.5 mm thick. After several trials, good sintering conditions were determined to be 1373 K for the temperature, 66 MPa for the pressure, and 1 min for the dwell time, reaching a relative density of 95 % with respect to the theoretical one. The structural properties of the samples were analyzed by X-rays diffraction (XRD) in Bragg-Brentano geometry using a PANalytical X'Pert Pro diffractometer. The XRD patterns were refined with the Rietveld method using MAUD software [117]. Microstructural characterizations have been obtained by Scanning Electron Microscopy (SEM) using a TESCAN Vega 4 equipped with an Oxford Instruments energy dispersion spectroscopy (EDS) Ultim Max 40 probe. The electron backscattered diffraction analysis was performed on a flat sample polished down to 40 nm with a TESCAN S9000G FESEM equipped with an Oxford Instruments Symmetry S3 EBSD probe. The electrical resistivity (four-probes, Van Der Pauw geometry) and Seebeck coefficient were measured on a bar-shaped sample obtained from a sintered pellet, using a custom apparatus described in detail in Ref. [120], with a thermal gradient of $\Delta T \sim 2$ K. An 8 mm wide, 2 mm thick cylindrical disk was used for the measurement of the thermal diffusivity between 300 K and 800 K on a Netzsch LFA 427 laser flash, whereas the specific heat capacity (Cp) was obtained on a PerkinElmer DSC 8000 calorimeter. The Hall effect and the electrical resistivity below room temperature were collected with a Quantum Design physical properties measurement system, PPMS (DC mode, Van Der Pauw geometry), from 2 K to 300 K, and, in the latter case, by varying the magnetic field between 7 and -7 T.

6.2 Structural and microstructural characterization

Figure 22a shows the experimental XRD pattern (open circles) of a pulverized sample taken from a sintered pellet. This is juxtaposed with the fitted pattern (red line) obtained through Rietveld refinement and the difference between experimental and calculated patterns (blue line). The XRD analysis reveals that the sample is monophasic, with only the $L2_1$ Co_2HfSn Heusler phase detected. On the other hand, SEM analysis, Figure 22b, shows small impurities of C15-type Co_2Hf Laves phase. These impurities are present in such small

quantities that they fall below the detection threshold of the XRD technique. The good quality of the fit confirm that this compound effectively crystalizes in the ordered $L2_1$ structure.

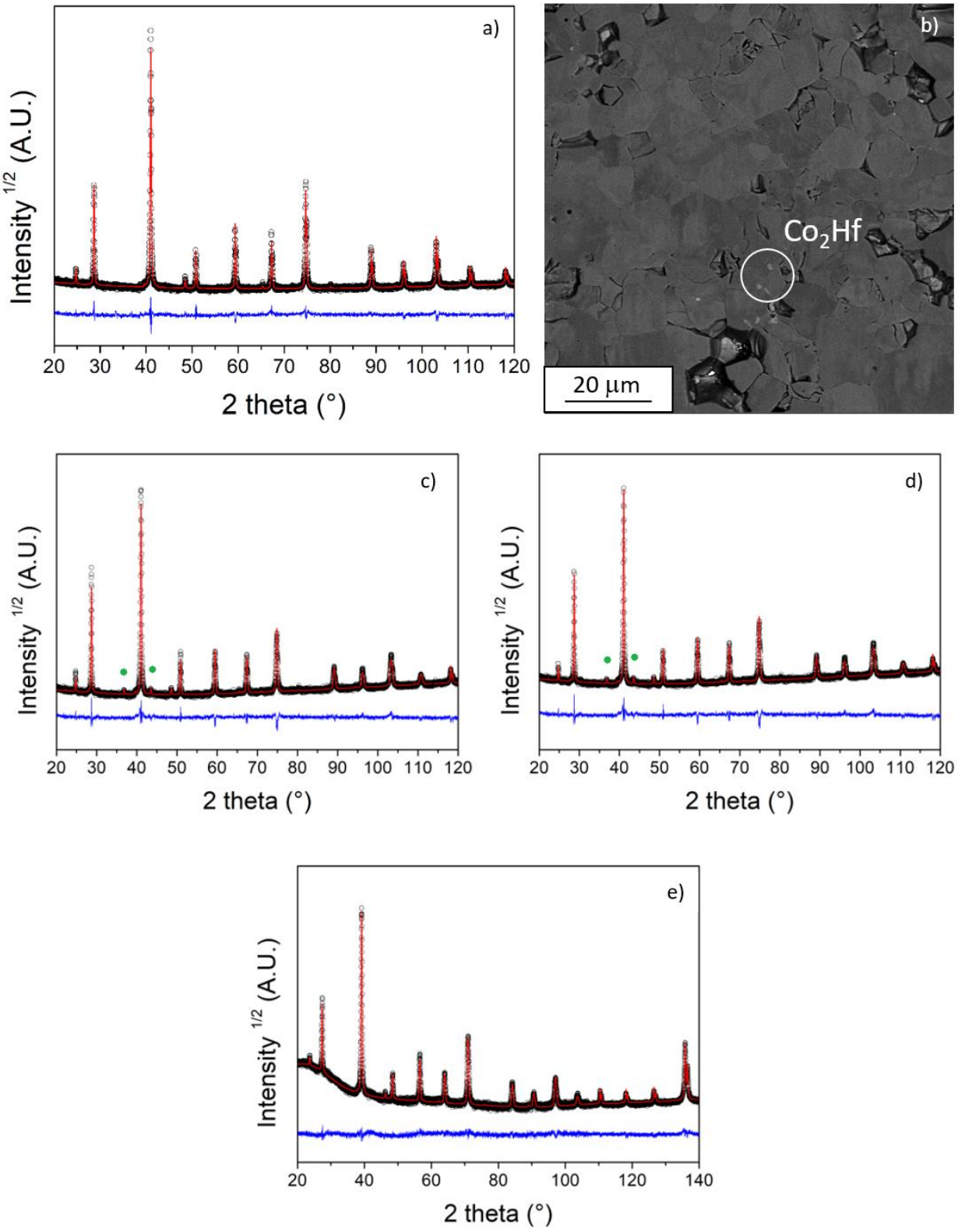

Figure 22: (a) XRD analysis of the sintered Co2HfSn sample; (b) SEM image (backscattered electrons) of the sintered sample. Rietveld refinement of XRD patterns of arc melted as-cast (a), annealed (1273 K, 6 days) (b), melt-spun Co_2HfSn (b). The high background intensity in c) at low angles is due to the amorphous material of the sample holder.

The lattice parameter (*a*) of the Co_2HfSn compound was determined to be 6.2211 Å, slightly different from the value of 6.2157 Å, previously reported for the non-monophasic sample in Section 2. This variation underscores the significant influence that different processing methods exerts on the structural properties of the Heusler phase.

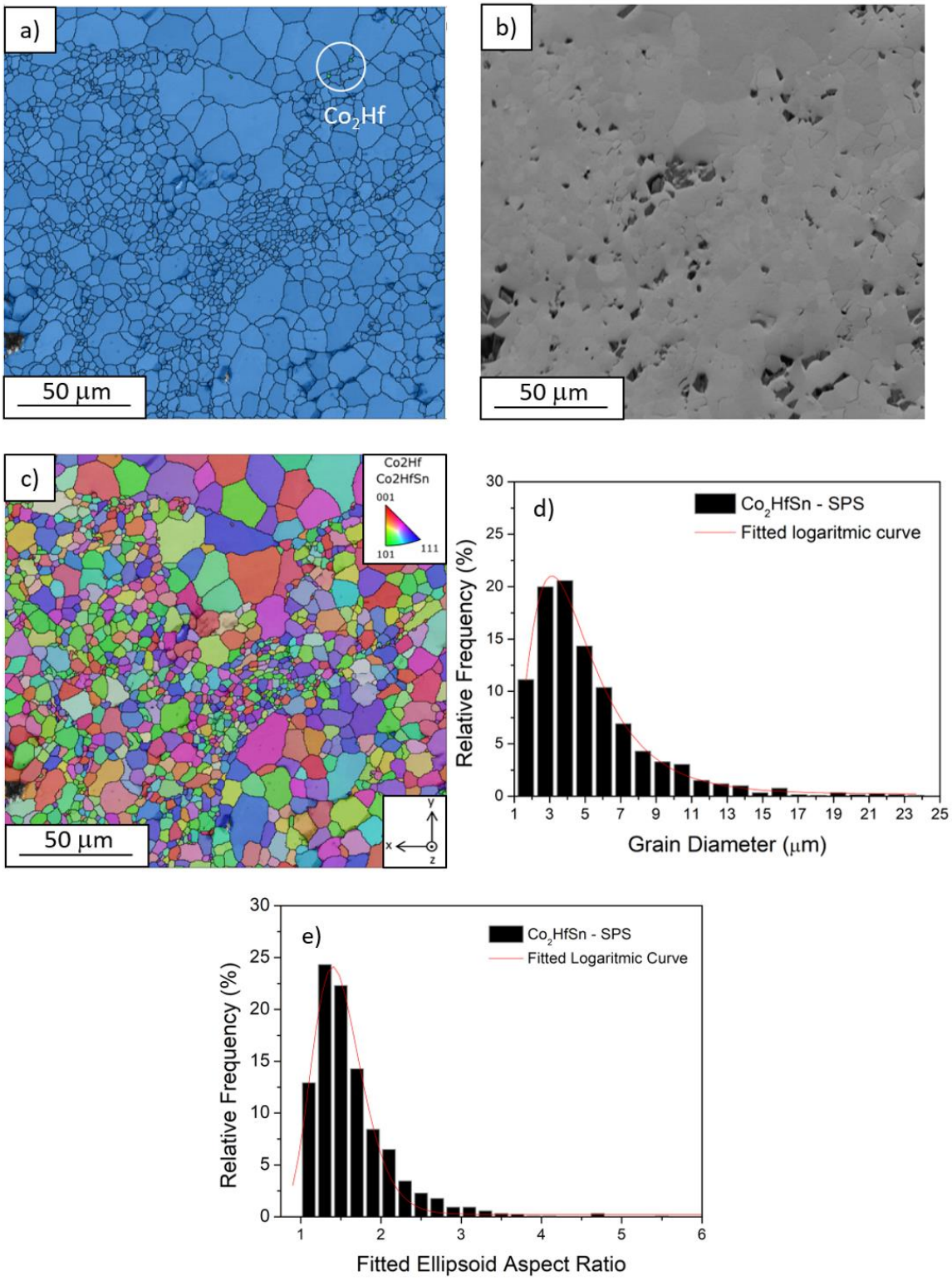

Figure 23: FESEM micrographs of the sintered Co_2HfSn sample, obtained with different detectors: (a) EBSD map (light blue: Co_2HfSn, green: Co_2Hf); (b) backscattered electron detector; (c) EBSD grains orientation map along the *z* direction; (d) grain size distribution of the Co_2HfSn Heusler phase (histogram: experimental distribution, red line: logarithmic fit); (e) fitted ellipsoid aspect ratio.

Results of the Rietveld analysis of XRD patterns of the arc melted as-cast, annealed and melt-spun Co_2HfSn alloy can be found in Figure 22c,d,e. A weight percentage of 2 % of Co2Hf secondary phase was found in the as-cast specimen, and the same quantity was detected after annealing at 1273 K for 6 days. Furthermore, after the rapid solidification process, the melt-spun material was observed to be fully monophasic. This suggests that the fast cooling rate enhances the experimentally achievable compositional range for the Heusler phase.

EDS measurements on the sintered pellet revealed atomic relative abundances (at. %) of 48%, 25%, 27% of Co, Hf and Sn, respectively, suggesting the presence of a monophasic Heusler phase with the aforementioned composition in the sample. The small impurities of secondary phases displayed an atomic composition of 66% Co, 29% Hf, 4% Sn, which is consistent with findings reported in Section 2. To gain a comprehensive understanding and obtain quantitative data on the microstructure resulting from the selected processing method, an EBSD analysis has been performed on polished sintered pellets. As it can be noticed from Figure 23a, the sample appears basically monophasic, as only the Heusler phase (light blue) was identified. Small grains of Co_2Hf (green) were also found; however, their relative abundance is estimated to be lower than 0.25%. Therefore, the presence of this secondary phase will be deemed negligible in subsequent discussions. SEM images, Figure 23b, also reveals the presence of porosities of various sizes in the sample; nevertheless, a relative density of 95% (10.8 g/cm^3) was measured compared to the theoretical value for the bulk material (11.4 g/cm^3). In Figure 23c, an EBSD grain orientation map is presented, where individual grains are color-coded based on their orientation relative to a specified axis. For this representation, the map corresponds to the z-axis, aligning with the pressure direction during the SPS process. Given the random color distribution across the entire sample area, it is evident that the sintered pellet does not display any preferential grain orientation. Additionally, Figure 23a and 19c further highlight that the grains are predominantly equiaxed, with a peak-distribution of the ellipsoid aspect ratio of 1.41 (Figure 23e). This suggests the presence of nearly spherical grains. One crucial parameter that can be quantified through EBSD analysis is the grain size distribution, as shown in Figure 23d. From the figure, it is possible to note that the resulting average grain size is around 5 μm, suggesting a relatively fine microstructure.

6.3 Transport properties

The electronic transport properties of Co_2HfSn are shown in Figure 24. The Seebeck coefficient was measured from 300 K up to 800 K, both during heating (empty black circles connected by the back line) and cooling (empty red circles) cycles, to ensure the absence of hysteresis. In Figure 24a, it is possible to observe a trend that is both qualitatively and quantitatively coherent to that already reported previously [116]. At room temperature, the *S* value stands at -13 μV/K and it then exhibits a linear increase in absolute value, rising at a rate of approximately 0.20 $\mu V/K^2$ up to 426 K, identified as the T_C [116]. Beyond this temperature, the Seebeck coefficient stabilizes, settling at a plateau value of about -41 μV/K up to 800 K. The negative value of *S* indicates that electrons are the dominant charge carriers.

The electrical conductivity (σ) between 300 K and 800 K is reported in Figure 24b. At room temperature, σ stands at 4718 S/cm, then it decreases almost linearly at a rate of about -13.57 $S\,cm^{-1}K^{-1}$, bottoming out at 3300 S/cm. Beyond this point, σ starts to weakly rise at a rate close to 0.56 $S\,cm^{-1}K^{-1}$, reaching a value of 3496 S/cm at 800 K. Since T_C for such compounds can be determined by measuring the temperature at which σ changes its slope [50], for this sample a T_C of 426 K is estimated from Figure 24b. As previously reported [116], the linear decrease of σ below T_C indicates the metallic behaviour of the alloy in the ferromagnetic state. Conversely, a weak increase of σ is observed in the paramagnetic state above T_C. As the power factor is largely dominated by S, similar patterns emerge in Figure 24a and c.

Figure 24d delineates the trend of σ from room temperature down to 2 K. Here, a noticeable variation in the σ vs T trend is evident: from a parabolic pattern below 75 K to a nearly linear behaviour above this threshold. This peculiar behaviour, previously observed also in other Heusler compounds, was explained by the transition from a low-temperature half-metallic state to a at high-temperature conductive state [69,94]. The half-metallic state, because of the absence of a minority-spin density of states at the Fermi level, renders the spin-flip electron scattering unfeasible, leading to the observed pattern [107,162]. Conversely, at elevated temperatures, multiple

electronic scattering mechanisms come into play, including spin waves, phonons, and spin fluctuations. This results in a σ dependency on T with an exponent ranging between 1 and 5/3 [69,161], consistent with the exponent value of 1.40 derived from the fit of our experimental data. An extensive overview on the model used to explain such behavior, and on the electrical resistivity of half-metallic Heusler alloys has been provided in Section 2.1.3. It should be noted that, similarly to other half-metallic Heusler compounds [69], Co_2HfSn exhibits a regime shift in magnetization (M) analogous to σ, with a crossover temperature around 30 K [51]. As far as magnetization is concerned, this regime change is again ascribed to a transition from a low-temperature half-metallic state to a high-temperature conductive state [69,94,116,163].

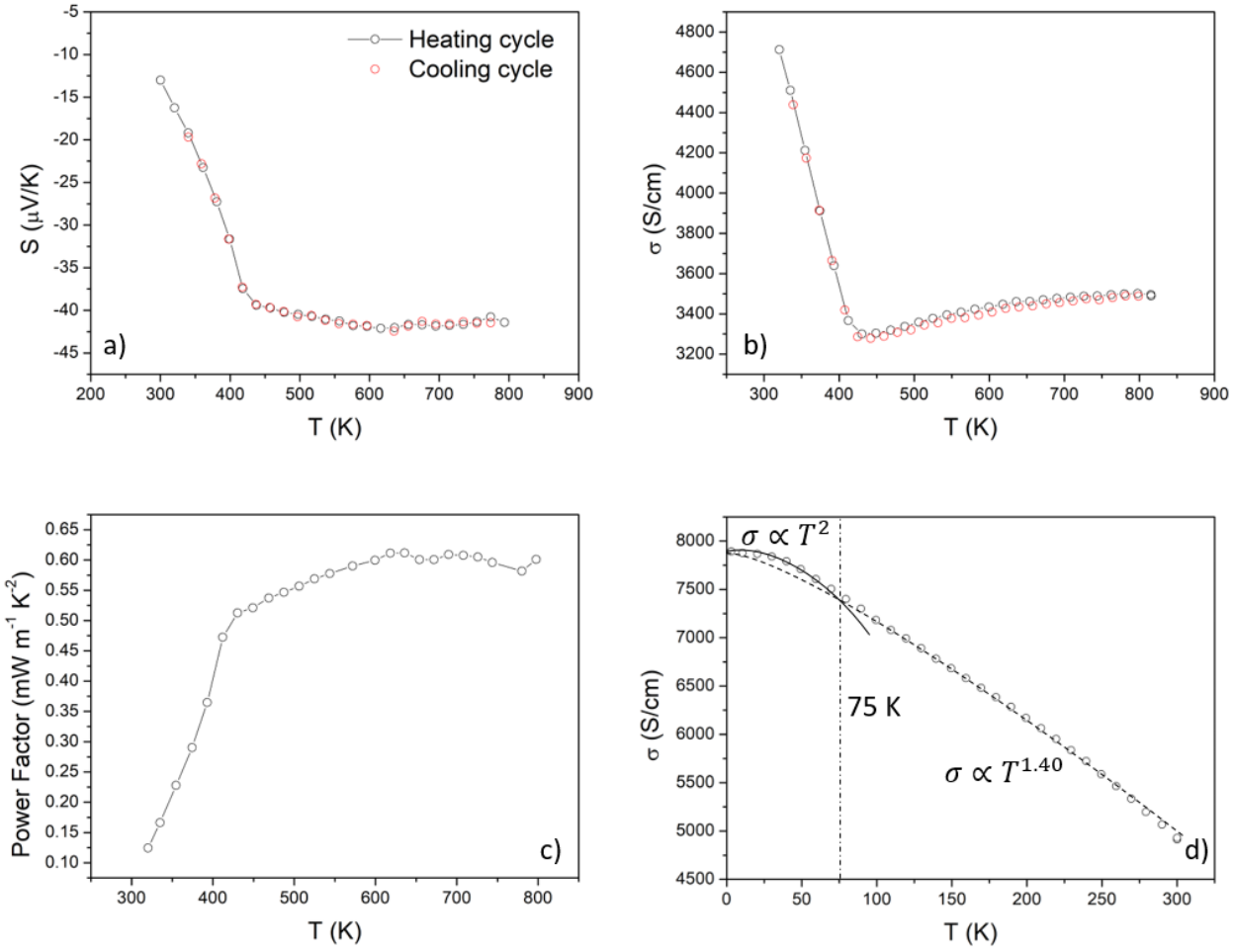

Figure 24: Electronic transport properties of sintered Co_2HfSn. Seebeck coefficient (a), electrical conductivity (b) and power factor (c) between 300 K and 800 K (the black lines connecting the open black circles are a guide to the eye). Low temperature electrical conductivity between 2 K and 300 K (d) (open circles represent experimental values, the continuous and dashes lines are fitting curves).

The Hall resistivity and charge carrier concentration were also measured from 2 to 300 K. An anomalous contribution (Figure 25c) was observed between no-field conditions and 1 T. However, at higher magnetic fields (H) only the ordinary contribution is evident, as illustrated in Figure 25a. Values of Hall resistivity (R_H) between 1 and 7 T are remarkably consistent, as evident when comparing the slopes of the respective lines in Figure 25a, all converging to a value of approximately $5.8 \cdot 10^{-10}$ m^3/C. The charge carrier concentration (n) was calculated as a function of T using the R_H values, according to the relation $n = (R_H e)^{-1}$, where e is the electron charge, and results are shown in Figure 25b. Here, it is noteworthy that n remains largely unaffected by temperature changes up to room temperature, maintaining a nearly constant value of about $1 \cdot 10^{28}$ m^{-3}, a characteristic value for conductive materials.

The trends of the thermal diffusivity and thermal conductivity, k, as a function of T are reported in Figure 26a and Figure 26b, respectively. In both cases, the variation mirrors that of σ, Figure 24b, with a linear decline from room temperature up to approximately T_C and followed by a linear increase after it. With this data, the electronic, k_{el} (open black squares), and lattice, k_{lat} (open red triangles), contributions to k (filled black circles) were calculated, and they are illustrated in Figure 26b.

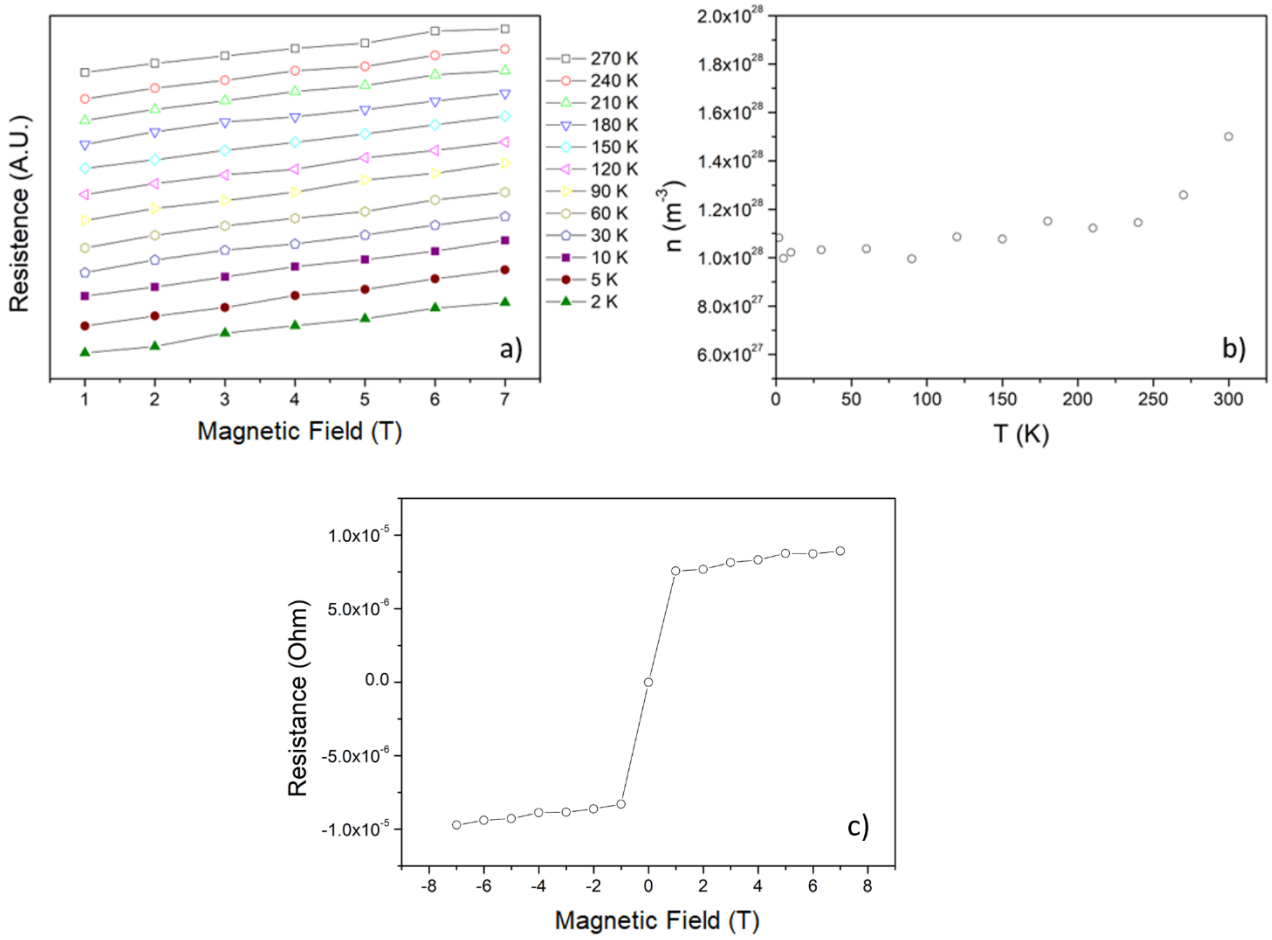

Figure 25: (a) Hall resistivity as a function of magnetic field; (b) charge carrier concentration as a function of temperature; (c) Hall resistivity at 300 K for sintered Co_2HfSn.

The Wiedemann-Franz ($k_{el} = L\sigma T$) law was employed, with $L = 1.5 + exp\left[-\frac{|S|}{116}\right]$ WΩK^{-2} the Lorentz number as proposed by Snyder et al. [164] and $k_{lat} = k - k_{el}$. From Figure 26b, one can discern that, below approximately 700 K, the main contribution to k is given by the lattice component. However, above this temperature, the electronic component becomes increasingly dominant. The specific heat capacity (C_p) is reported as a function of temperature in Figure 26c, revealing a peak at T_C, and then maintaining with a rather constant value (~ 0.48 Jg^{-1}K^{-1}, or 200.2 JK^{-1} per mole of formula unit) within the examined temperature range. This pattern is coherent with observations for other similar compounds reported in the literature [165]. The kink at T_C in k_{lat} arises from an incomplete compensation of the diffusivity dip by the C_p peak and it can be considered as an artefact. Lastly, from the measured electronic and thermal transport properties, the thermoelectric figure of merit ($zT = \frac{S^2\sigma}{k}T$) was estimated as a function of temperature and illustrated in Figure 26d. The trend closely follows those of PF and S, with a minimum value of 3.4·10^{-3} at 300 K and peaking at 4.0·10^{-2} at 800 K.

A comparison with the previous spurious annealed sample (see Section 5) is possible by comparing Figure 24 and Figure 21. It can be noted that the elimination of the Co_2Hf secondary phase had a beneficial effect both

on the Seebeck coefficient and on the electrical conductivity. In fact, an increase of approximately 7% can be seen in the case of S after T_C (from -38 μV/K for the annealed to -41 μV/K for the sintered specimen); whereas σ was enhanced by the 8% at T_C (3046 S/cm and 3300 S/cm for the annealed and sintered samples, respectively). The preparation of single phase alloys is thus crucial for the optimization of transport properties.

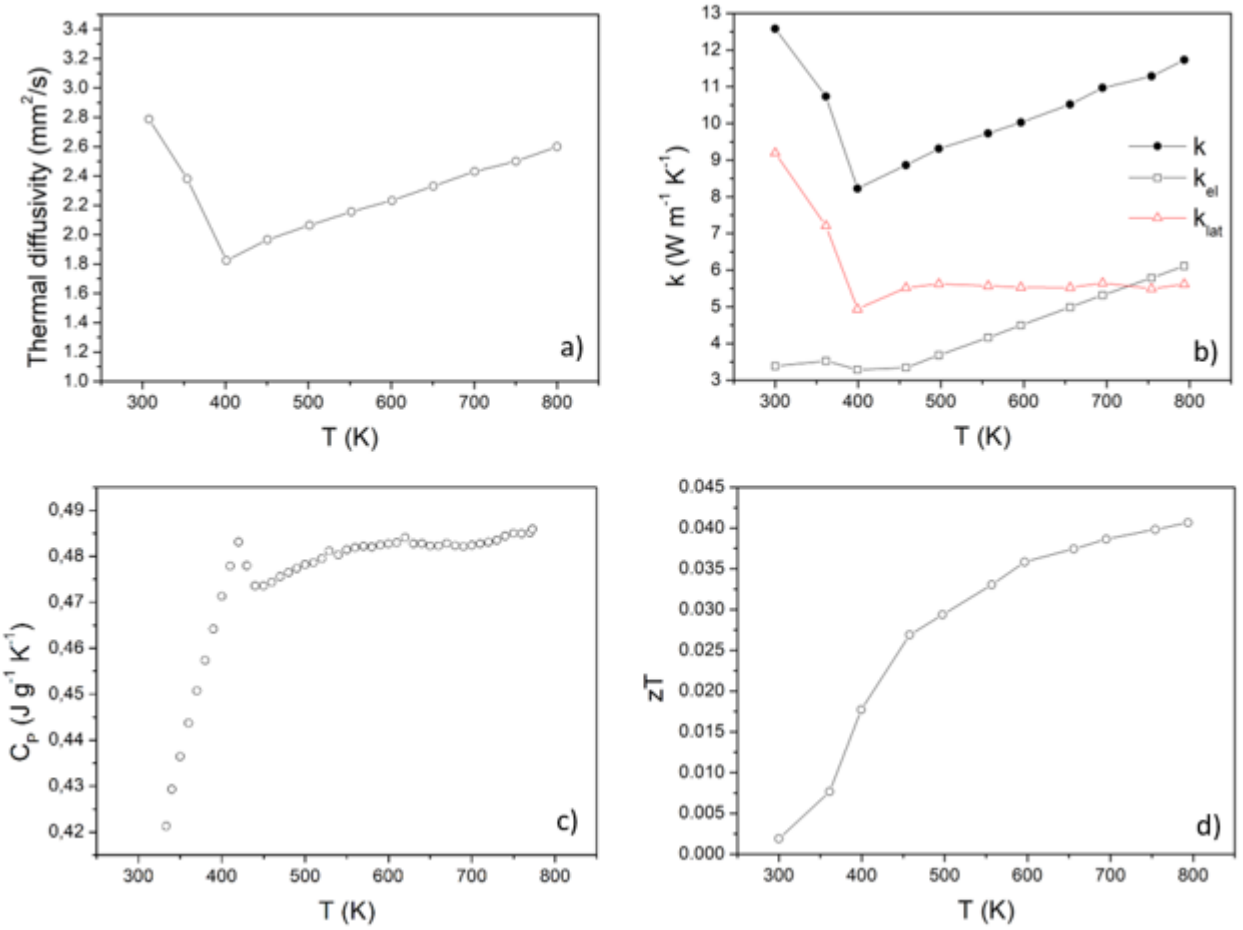

Figure 26: Experimental values as a function of temperature of thermal diffusivity (a), thermal conductivities k (filled black circles), k_{el} (open black squares) and k_{lat} (open red triangles) (b), specific heat capacity (c) and thermoelectric figure of merit, zT, (d) for sintered Co_2HfSn.

6.4 Conclusions

The Co_2HfSn Heusler compounds was synthesized by rapid solidification (melt-spinning) followed by spark-plasma sintering. This method enabled the preparation of a monophasic and stoichiometric sample with a fine microstructure and represents an advancement with respect to the multiphase sample containing off-stoichiometric Heusler compound reported previously. Quantitative information on the phases, grain size and stoichiometry were obtained by means of several techniques such as XRD, SEM-EDS and EBSD, giving an extensive characterization of the metallurgical characteristics of samples prepared following such processing route.

Transport properties were measured from 300 K up to 800 K and, with electric conductivity measurements extending down to 2 K. Around 75 K, a change of regime of σ vs T was observed. A shift from a low-T σ/T^2 proportionality to a high-T $\sigma/T^{1.40}$ correlation occurred, which was explained in terms of different electron scattering mechanisms. In fact, as reported for other compounds [69,94], the variation of resistivity is explainable as the consequence of the presence of a half-metallic state at low temperatures (below 75 K), where the half-metallic band gap is responsible for the hindering of spin-flip scattering. On the contrary, in the high-temperature (above 75 K) conductive state, several electron scattering mechanisms are possible, making the

exponent of the σ/T dependency being comprised between 1 and 5/3 [107,161,162]. Coherently, an exponent value of 1.40 was experimentally observed.

The Hall resistivity was also measured from 2 to 300 K, showing anomalous properties at low fields, and ordinary behavior at higher H with relatively constant values along the whole investigated temperature range. From the R_H data, the charge carrier concentration was estimated, resulting in values rather independent from T around $1 \cdot 10^{28}$ m^{-3}, which are typical of conductive materials. Having S, σ, and k, the thermoelectric figure of merit zT was experimentally estimated here for the first time, being equal to 0.040 at its maximum value at 800 K.

7. The role of Co-vacancy defects and atomic ordering on the transport, magnetic, and half-metallic properties of Co_2ZrSn Heusler alloy

In this chapter, the formation of point defects in Co_2ZrSn samples processed by different routes is investigated from the experimental point of view. Since the cooling rate is responsible for the existence of various degrees of disorder and defect concentrations inside the Heusler structure [166,167], the use of various synthesis procedures allowed to obtain samples with diverse lattice ordering. Specifically, specimens were prepared by arc-melting, arc-melting followed by annealing, rapid solidification (melt-spinning) followed by spark-plasma sintering (SPS). Analysis of the XRD patterns by two independent models evidenced the presence of vacancies on then Co site as the main defect (Figure 27), leading to different occupancy values of this crystallographic site in the investigated samples. The effect of the vacancies on the transport properties, magnetism, and half-metallicity of Co_2ZrSn, is studied.

The results of the transport (Seebeck coefficient, electrical conductivity, thermal conductivity, Hall coefficient, charge carrier concentration and zT) and magnetic characterizations show a strong structure-properties correlation in Co_2ZrSn, which is reflected also in its half-metallicity.

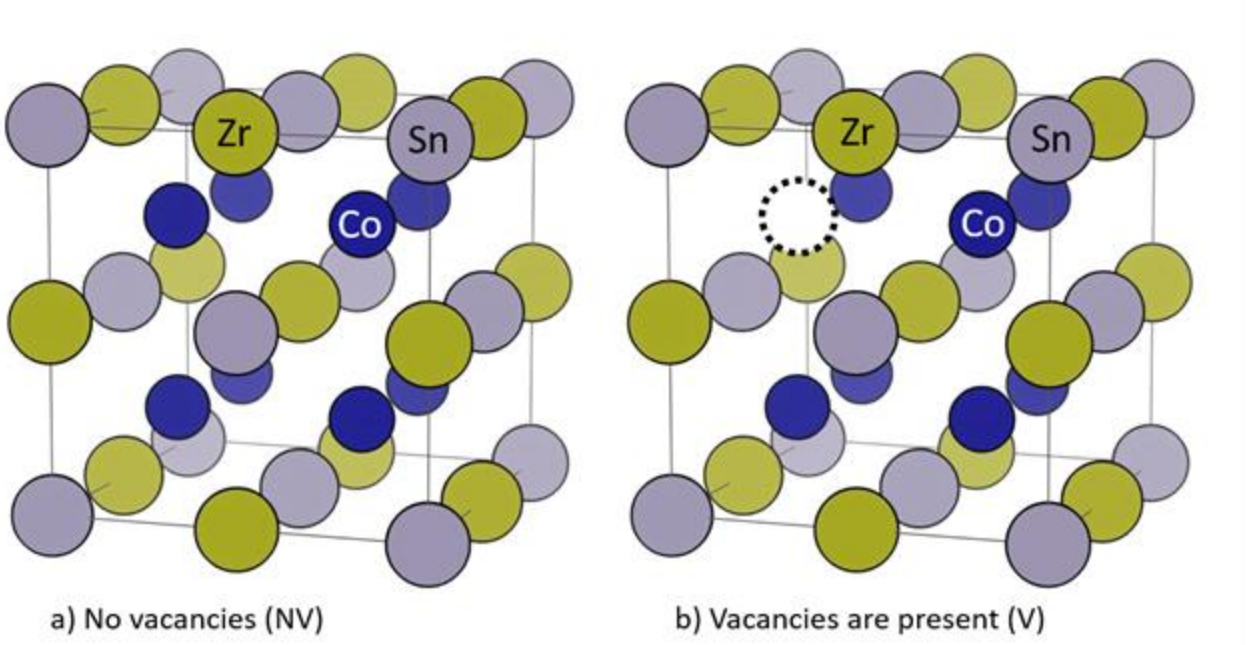

Figure 27: Depiction of pristine vacancy-free (a) and vacancy-defective (b) Heusler structures.

In this chapter, a review of the $L2_1$ structure crystallographic properties will be initially presented, in order to guide the subsequent interpretation of the experimental results.

7.0.1 The crystallography of the $L2_1$ Heusler phase

A schematic depiction of the $L2_1$ Heusler phase is presented in Figure 27. The fundamental properties of such family of intermetallic compounds were already discussed in Section 2; however, it is important to remind once again that in Co_2ZrSn, atom sites occupy the 8c Wyckoff positions (0.25, 0.25, 0.25) sitting in tetrahedral sites, while Zr and Sn occupy the 4a (0, 0, 0) and 4b (0.5, 0.5, 0.5) Wyckoff positions, respectively, being located in octahedral sites. As shown in Figure 11, the XRD pattern of an Heusler compound shows three peculiar peaks at low angles, namely (111), (200), and (220). It is known from the literature [114] that the intensity of the (111) reflex is associated with the ordering of the octahedral positions (in this case, the sites of Zr and Sn), while that of (200) is related to the order of the 8c tetrahedral site (Co site). The intensity of main peak, (220), is often regarded as independent from the crystalline order. This simple rule of thumb, despite

being undoubtedly useful, must be analyzed and understood more in depth if one's objective is to extract correct information from XRD patterns.

In the following section, a comparison between two similar, and simultaneously deeply different Heusler systems will be performed, namely Co_2ZrSn and Fe_2VAl. Despite sharing the same crystal structure, such compounds are not as similar as they appear. Among all differences, three main dissimilarities can be highlighted:

- Functional properties: as discussed previously, Co_2ZrSn is an itinerant ferromagnet at room temperature, showing high electrical conductivity, and low S. Also, as it will be discussed in the next section, a charge carrier concentration of 10^{28} m^{-3} was measured for such compound. On the other hand, Fe_2VAl is a semiconductor, displaying comparatively significantly lower σ and dramatically higher S. The charge carrier concentration was estimated around 10^{26} m^{-3}.
- Solidification pattern: Co_2ZrSn solidifies congruently in the $L2_1$ ordered structure directly from the melt. On the contrary, Fe_2VAl shows an order-disorder transition from a high-T B2 structure to a ordered low-T $L2_1$ Heusler structure.
- Composition: the crystallographic structural factors, F(hkl), of each XRD peak highly depend on the average atomic number of the atoms occupying the sites included in the considered (hkl) plane. As peak intensities, I(hkl), are proportional to F(hkl), it is easy to understand that the atomic number of the constituent elements plays a huge role in determining the shape of a compound's XRD pattern. On the one hand, on Co_2ZrSn, the lightest element (Co) occupies the 8c site. On the other hand, in Fe_2VAl, it is the heaviest element (Fe) which is located in 8c. As it will be shown, such difference will be remarkably important in the investigation of their structural properties via x-rays diffraction.

For both alloys, the F(hkl) of the (111), (200), and (220) peaks were simulated using the PowderCell simulation software package [168] in the following conditions:

- Pristine: perfect $L2_1$ system, in which the occupancy of each site is equal to 1.
- 8c-vacancy: the occupancy of the 8c site was reduced to 0.75. This is equivalent to simulate the effect of the removal of one Co (in Co_2ZrSn) and Fe (in Fe_2VAl) atom from the unit cell, namely obtaining a $Co_{1.75}ZrSn$ alloy.
- Anti-sites: the effect of anti-site defects in the 8c site was simulated by keeping the total site occupancy at a value of 1, while setting the partial occupancies to 0.75 for Co and Fe (in Co2ZrSn and Fe2VAl, respectively) and to 0.25 for the anti-site element. Several anti-sites were simulated, namely:
    - Zr anti-site (Co_2ZrSn): 0.75 Co; 0.25 Zr
    - Sn anti-site (Co_2ZrSn): 0.75 Co; 0.25 Sn
    - V anti-site (Fe_2VAl): 0.75 Fe; 0.25 Al
    - Al anti-site (Fe_2VAl): 0.75 Fe; 0.25 Al

  Additionally, an anti-site defect of an extrinsic element was also simulated, as:
    - Al anti-site (Co_2ZrSn): 0.75 Co; 0.25 Al
    - Sn anti-site (Fe_2VAl): 0.75 Fe; 0.25 Sn

The simulation of such systems allowed us to observe the peak intensity trend as a function of the type of defect. The average atomic number in the 8c site (Z_{8c}) was selected as a quantitative parameter to discriminate between the different defects.

Observing the two systems from the compositional point of view, it is possible to note that in Co_2ZrSn intrinsic anti-site defects always involve an increase of Z_{8c}, as both Zr and Sn have higher Z than Co. On the other hand, in Fe_2VAl, intrinsic anti-site defects always imply a decrease of Z_{8c}, as both V and Al have lower Z than Fe. As it will be shown later, this difference will be crucial. The simulation of hypothetical extrinsic Al and Sn anti-sites in Co_2ZrSn and Fe_2VAl, respectively, was aimed to investigate which is the effect of an anti-site defects which behaves oppositely in determining Z_{8c}. It is clear that, in real samples, Al defects in Co_2ZrSn and Sn defects in Fe_2VAl, can only occur as a consequence of doping or undesired contaminations during the preparation process. The F(hkl) and relative peak intensities of the (111), (200), and (220) peaks in Co_2ZrSn

and Fe_2VAl are reported in Table 3. Being (220) the main peak, its relative intensity is assumed being equal to 1.

Co_2ZrSn									
Defect	χ_{8c}	Z_{8c}	F(111)	F(200)	F(220)	F_{111}/F_{220}	F_{200}/F_{220}	I_{111}/I_{220}	I_{200}/I_{200}
Pristine	1.00 Co	27	38.84	123.66	438.26	0.09	0.28	1.55	8.67
Vac.	0.75 Co	20.25	38.84	168.77	397.81	0.10	0.42	1.89	19.59
Zr-AS	0.75 Co; 0.25 Zr	30.25	38.84	102.22	458.30	0.08	0.22	1.42	5.41
Sn-AS	0.75 Co; 0.25 Sn	32.75	38.84	83.27	475.55	0.08	0.18	1.32	3.34
Al-AS	0.75 Co; 0.25 Al	23.50	38.84	149.03	415.81	0.09	0.36	1.73	14.01
Fe_2VAl									
Defect	χ_{8c}	Z_{8c}	F(111)	F(200)	F(220)	F_{111}/F_{220}	F_{200}/F_{220}	I_{111}/I_{220}	I_{200}/I_{200}
Pristine	1.00 Fe	26	34.33	57.58	243.69	0.14	0.24	4.00	6.21
Vac.	0.75 Fe	19.5	34.33	15.95	206.81	0.17	0.08	5.52	0.66
V-AS	0.75 Fe; 0.25 V	25.25	34.33	51.58	237.89	0.14	0.22	4.20	5.20
Al-AS	0.75 Fe; 0.25 Al	22.75	34.33	35.09	223.81	0.15	0.16	4.75	2.72
Sn-AS	0.75 Fe; 0.25 Sn	32	34.33	99.52	282.00	0.12	0.35	2.99	13.76

Table 3: Crystallographic features of (111), (200), (220) XRD reflexes in various Co_2ZrSn and Fe_2VAl $L2_1$ Heusler systems. χ_{8c} is the occupancy of the 8c site, Z_{8c} is the average atomic number of atoms occupying the 8c site in the unit cell, F_{hkl}/F_{220} and I_{hkl}/I_{220} are the structural factor and peak intensity ratios, respectively, of the (hkl) plane with respect to the main peak (220) expressed in percentage.

The trends of F(hkl) and their ratios F_{111}/F_{220} and F_{200}/F_{220} as a function of Z_{8c} are reported for both alloys in Figure 28. Observing F(220), the main reflex, it is possible to see that both in Co_2ZrSn and Fe_2VAl the value increase as a function of Z_{8c}. As far as F(111) is concerned, it remains constant as the average atomic number in the 8c site varies (namely, as defects are introduced in 8c). This is coherent with the rule established by the literature saying that the (111) peak is unrelated to the disorder in the 8c position [114]. Considering now F(200), the first important difference between Co_2ZrSn and Fe_2VAl can be observed. In fact, as in Co_2ZrSn F(200) decreases with the increasing Z_{8c}, in Fe_2VAl this declines as Z_{8c} grows. The implication of this opposite trend becomes evident considering the structural factor ratios of (111) and (200) with respect to (220), as shown in Figure 28c,d). In case of Co_2ZrSn, F(200)/F(220) decrease with Z_{8c}; however, the most important thing to note is the mutual position of the defective systems with respect to the pristine system (which average atomic number in 8c is highlighted by the dashed grey line). It is easy to see that the introduction of vacancies implies an increase of F(200)/F(220), as well as the introduction of anti-site defects with atoms which atomic number is less than 27 (i.e. Al anti-sites). On the other hand, intrinsic anti-site defect always have the opposite effect of decreasing F(200)/F(220). This makes possible to undeniably distinguish between Co vacancies and intrinsic anti-site defects, since their effect on the crystallographic structural factors is diametrically opposite. It is also possible to predict that with such method, it would be extremely difficult to quantify the effect of anti-site defects with atomic number lower than 27; nevertheless, being such elements not present in the un-doped compound's composition, this drawback is deemed marginal.

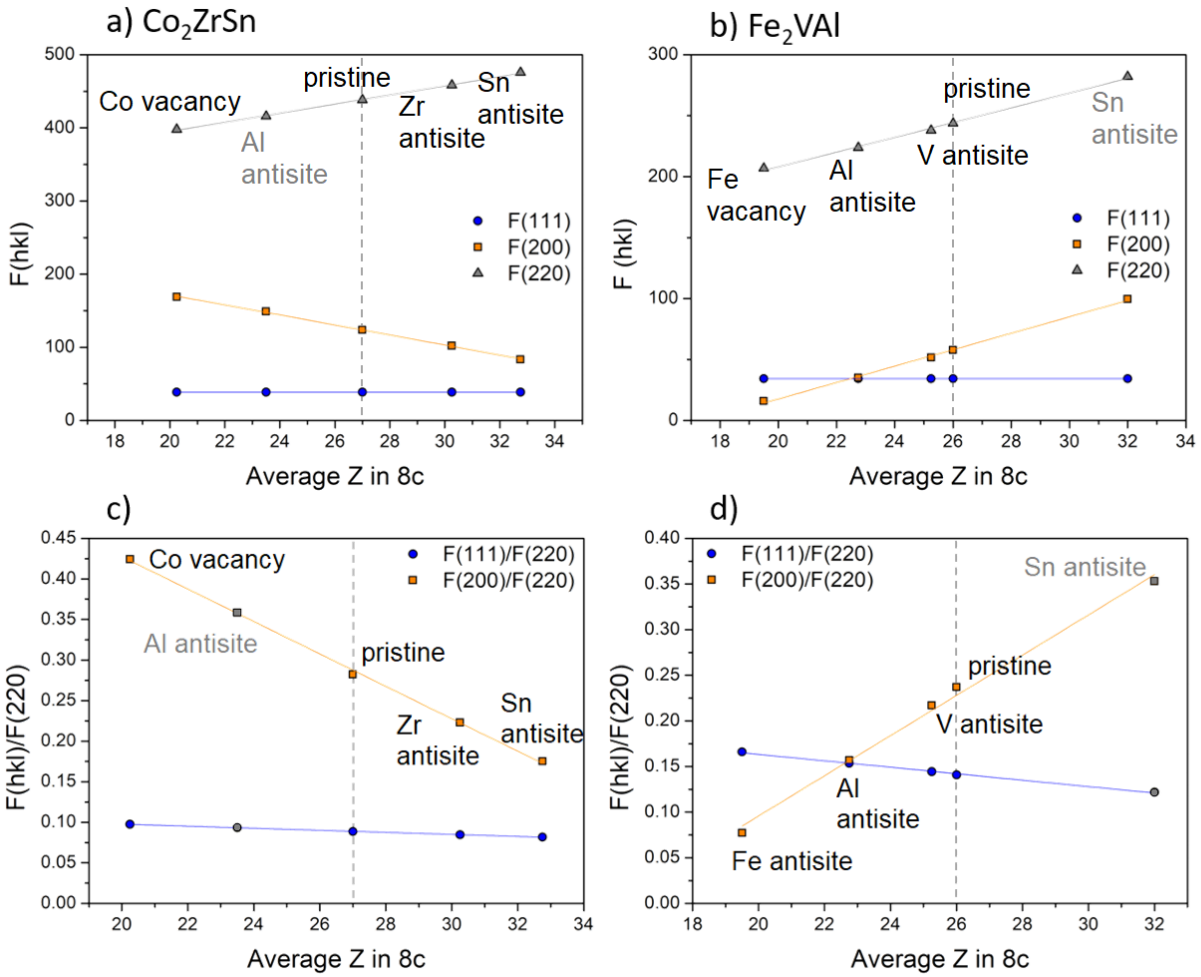

Figure 28: Structural factors of (111), (200), (220) XRD reflexes of (a) Co_2ZrSn, and (b) Fe_2VAl. Structural factor ratios of the (111) and (200) peaks with respect to that of the main peak (220) of (c) Co_2ZrSn, and (d) Fe_2VAl. The extrinsic anti-sites are indicated in grey color.

Considering now Fe_2VAl, it can be seen firstly how F(200)/F(220) increase with the increasing Z_{8c}. Secondly, contrariwise to Co_2ZrSn, in this case all the intrinsic defects have the same effect on F(200)/F(220). In fact, since both Al and V have lower atomic number than Fe, and since their effect on the (200) reflex is the same of Fe vacancies (which implies a lowering of Z_{8c} as well), it is impossible to unanimously distinguish between vacancies and anti-sites solely based on the analysis of the (200) reflex. On the other hand, in Fe_2VAl, extrinsic anti-sites with elements having higher Z than Fe would be easier to spot, as (see Sn anti-site) their effect on the F(200)/F(220) is opposite to those of intrinsic defects.

Since in crystallography XRD peak intensities are directly related to their relative structure factors, from F(hkl) values it is possible to straightforwardly obtain the intensity of each peak in the XRD pattern as a fraction of that of the main peak (220), which is by definition to be equal to 1 (or 100%). The intensity of the (111) and (200) peaks with respect to that of (220) of Co_2ZrSn and Fe_2VAl are shown in Table 3, while their trends as a function of Z_{8c} are illustrated in Figure 29.

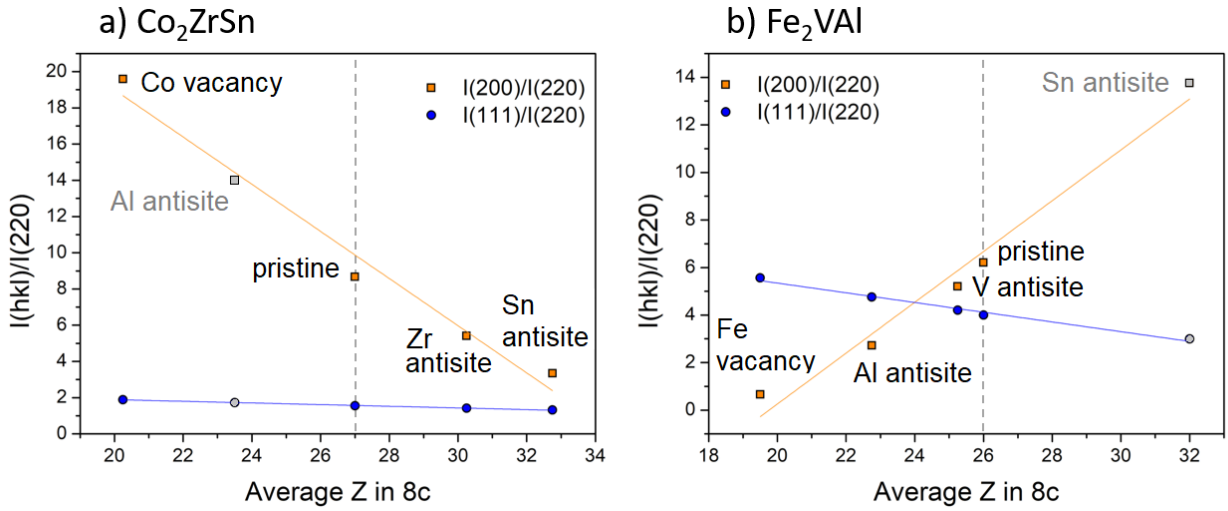

Figure 29: Intensities of the (111) and (200) peaks with respect to that of the main peak (220) of (a) Co_2ZrSn, and (b) Fe_2VAl. The extrinsic anti-sites are indicated in grey color.

Being peak intensities and structural factors directly related, it is possible to see how Figure 29 and Figure 28c-d essentially show the same evidence, with the only difference that I(hkl)/I(220) data can be interpreted also under the quantitative aspect. In Co_2ZrSn, taking the pristine compound as a reference, it can be seen how Co vacancies is the only intrinsic defect implying an increase of I(200)/I(220), while intrinsic anti-sites all lead to its decrease. Quantitatively, a relative intensity of 8.67% is expected for the pristine system, while a 19.59% is predicted when χ_{8c} is 0.75. As already shown for F(hkl), the intensity of the (111) reflex show little to none change as a function of the defect inserted in the 8c site. On the other hand, in Fe_2VAl, the intensity of the (200) peak always decreases with respect to the pristine system as a consequence of the introduction of intrinsic defects, making it impossible to distinguish between Fe vacancies and Al/V anti-sites. The substitution of Fe with elements with atomic number higher than 26 would lead to an increase of the (200) peak intensity, leading to a well recognizable effect. Also in this case, the intensity of the (111) remains approximately constant, being scarcely useful in identifying defects in 8c.

The same analysis can also be performed simulating the effect of defects involving the octahedral sites (4a and 4b), and it is reported in Appendix B. From such study, it will be possible to see that the introduction of defects in 4a and 4b has little to no effect on the intensity of (200), being instead determinant for that of (111), as already established by the literature.

Having been clarified the situation related to intensities, peak positions can now be analyzed. Concerning Co_2ZrSn, single crystal XRD patterns have been collected by Kushwaha et al. [114] for samples synthesized with increasingly lower Co content, effectively producing specimens with increasingly higher concentration of Co vacancies. The same samples were also analyzed with powder diffraction, obtaining analogous values. In Figure 30a, the results obtained in such study are reported. It is possible to see how the lattice parameter was found to linearly decrease as a function of Co occupancy (χ_{Co}). The same behavior was also observed for the magnetic moment, enforcing the evidence obtained by ab-initio calculations according to which the DOS of Co_2ZrSn is at the Fermi level essentially determined by Co atoms. The experimental and calculated data which will be exposed in the next sections will overall confirm such outcomes, finding that the Co_2ZrSn lattice shrinks as atoms are removed from the 8c sites, and expands when bulkier elements (such as Zr and Sn) are substituted to Co atoms in 8c.

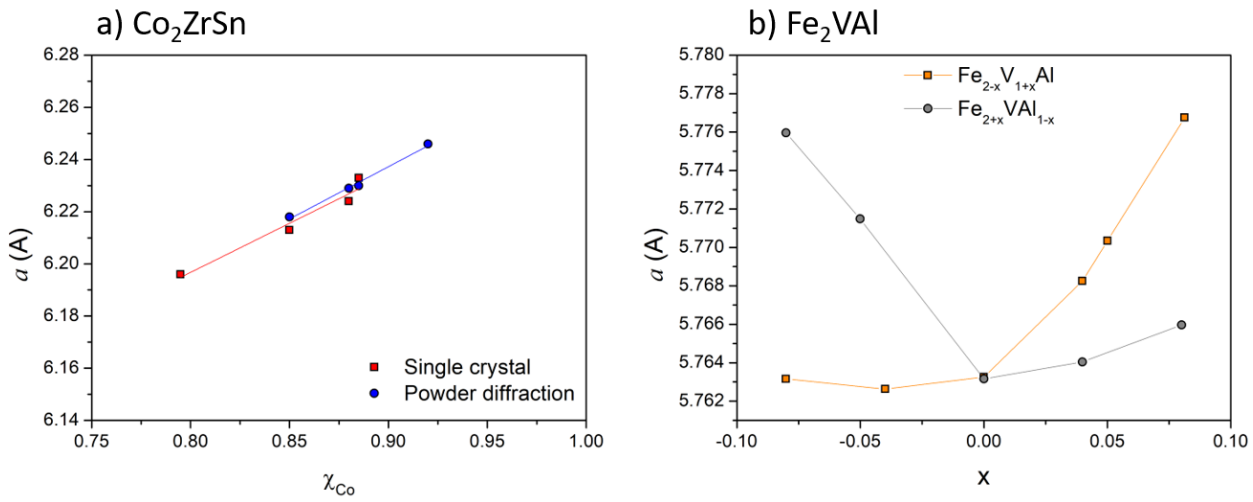

Figure 30: Lattice parameter as a function of composition of (a) Co_2ZrSn, and (b) Fe_2VAl. Data of (a) are from Ref. [114], while data from (b) are from Ref. [169].

On the other hand, in Fe_2VAl, the situation is overall more complicated. From ab-initio calculations, one is expected to find the same trend of Co_2ZrSn; however, experimental evidence show that the lattice parameter expands as a result of both depletion and enrichment of Fe in 8c, as depicted in Figure 30b. This was later modeled by considering the charge associated with defects and correcting the calculations taking charge transfer phenomena into account. This correction was not deemed necessary for Co_2ZrSn in the literature because of two main reasons. First, calculated data were found to satisfactorily match experimental evidence without further computational corrections. Second, as already mentioned before, the charge carrier concentration of Co_2ZrSn is typical of a metallic compound, being two orders of magnitude higher than that of the semiconductive Fe_2VAl. Such higher carrier density is responsible for a higher electronic delocalization across the lattice; hence, the removal of one atom in such dispersed system do not create strong charges as in insulant ionic solids or semiconductors. This leads again to an easier interpretation of XRD data for Co_2ZrSn than in Fe_2VAl, as the change of *a* can be unambiguously related to vacancies or anti-sites defects in the first case, while this being not entirely possible in the latter.

7.1 Materials and methods

Elemental metals (Co 99.97%, Zr 99.90%, Sn 99.97% purity) were weighted in the appropriate stoichiometric quantity and melted in an Edmund Buhler GmbH (Bodelshausen, Germany) arc-furnace several times to ensure homogeneity. Subsequently, a part of the so obtained as cast alloy was wrapped in a Ta foil, sealed in an evacuated quartz tube, and annealed for 6 days at 1000°C. Another part of the as cast alloy was re-melted inside a boron nitride crucible and injected onto a rotary copper wheel (20 m/s speed) using an Edmund Buhler melt-spinning apparatus. The rapidly solidified alloy was hand-grinded into powder and then sintered by spark plasma sintering in a Fuji 515 S sinter machine, using graphite molds lined with graphite paper. Several pellets with a diameter of 8-10 mm and thicknesses approximately of 2.5 mm were obtained under the optimal sintering conditions, which were found to be 1223 K as ceiling temperature kept for 1 minute (1.5 K/s as both heating and cooling rate), and 66 MPa of pressure. The samples were crushed into powder and analyzed by X-rays diffraction (XRD) in Bragg-Brentano geometry with a PANalytical X'Pert Pro diffractometer. The Rietveld refinement procedure was performed using the MAUD code [117]. Other portions were polished down to 40 nm roughness and characterized with a TESCAN Vega 4 Scanning electronic microscope (SEM) equipped with an Oxford Instruments energy dispersion spectroscopy (EDS) Ultim Max 40 probe. The electron backscattered diffraction analysis (EBSD) was performed with a TESCAN S9000G Field-Emission SEM (FESEM) equipped with an Oxford Instruments Symmetry S3 EBSD probe.

The Seebeck coefficient and electrical resistivity of the as cast, annealed and spark plasma sintered (SPS) alloys were measured on bar-shaped specimens using the instrumentations described in Ref [119,120].

Thermal diffusivities were collected by laser flash technique with Netzsch (Selb, Germany) 427 and 457 analyzers; whereas, heat capacities were tested on a Perkin Elmer (Waltham, MA, USA) DSC 8000 calorimeter. The electrical resistivity and Hall coefficients below room temperature were analyzed with a Quantum Design (Darmstadt, Germany) physical properties measurement system, PPMS (DC mode, Van Der Pauw geometry), from 2 K to 300 K. In the latter case, the magnetic field was varied between 7 and -7 T. Static magnetic properties were measured with a Quantum Design MPMS3 SQUID magnetometer, and with the abovementioned PPMS system in the field interval of 0 ± 7 T. For higher temperatures (300-550 K), a VSM magnetometer (Lakeshore) was used in a field interval of 0 ± 17 kOe.

7.2 Vacancies and Co-site ordering characterization in the Heusler lattice

The amount of vacancy defects present in the Heusler lattice can be quantified using the Rietveld method by letting the total Co occupancy free of converge to the best value during the refinement process. In order to understand how accurate and reproducible this procedure is, a comparison with a second set of Rietveld analysis in which the Co occupancy was fixed at a value of 1 (namely, a defect-free structure) was performed. The Rietveld refinements of powder XRD patterns of arc-melted (as cast), annealed, and melt spun sintered (SPS) specimens are shown in Figure 31 for both the defective (V) and non-defective (NV) models. In all specimens the $L2_1$ Heusler was found to be the main phase with small amounts of Co_3Sn_2 impurities, which peaks are highlighted by the arrows.

Non-defective (NV)					
Parameter	As cast	Annealed	SPS + An.	SPS	Melt spun
R_{exp} %	1.6625	1.3718	1.4068	1.4688	1.4092
R_b %	2.6493	1.8876	2.515	2.5885	1.9589
χ	1.6580	1.9106	2.4103	2.4007	1.6377
Defective (V)					
Parameter	As cast	Annealed	SPS + An.	SPS	Melt spun
R_{exp} %	1.6625	1.3718	1.4068	1.4688	1.4092
R_b %	2.4385	1.7388	2.3811	2.4586	1.8633
χ	1.4177	1.7036	2.2014	2.3656	1.6273
ΔR_b	0.2108	0.1488	0.1339	0.1299	0.0956
$\Delta\chi^2$	14.49	10.83	8.67	1.46	0.64

Table 4: R and χ factors of the Rietveld analysis of non-defective (NV) and defective (V) Co_2ZrSn samples.

It is possible to note that, generally speaking, the Rietveld refinements both in the non-defective and defective conditions fit the experimental XRD pattern quite well. Nevertheless, a more careful observation allows to notice that a rather important discrepancy between the experimental and calculated patterns occur in correspondence of the peak associated with the (200) plane.

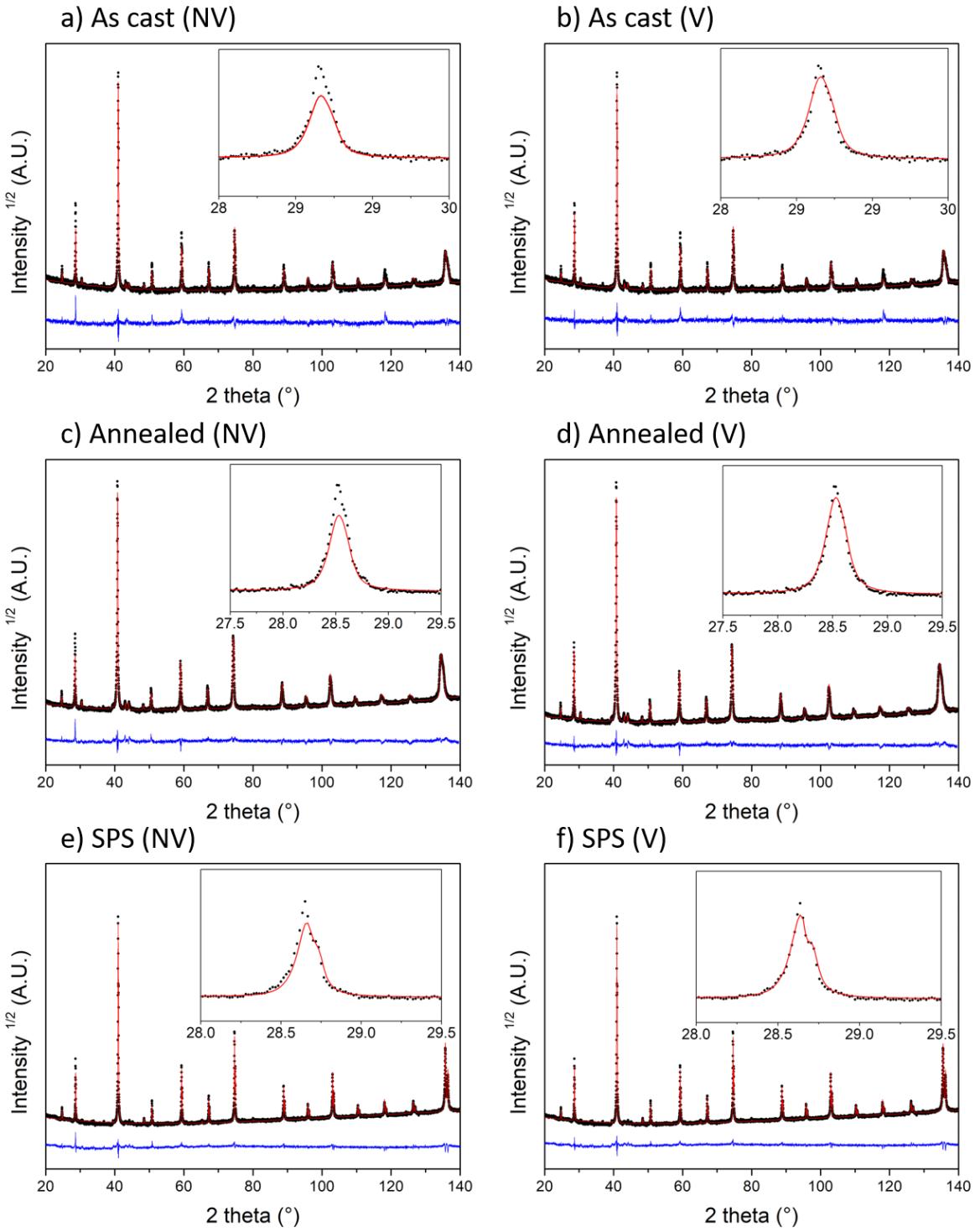

Figure 31: Rietveld refinements of the XRD patterns for the as cast (a), annealed (c) and sintered (e) samples, assuming a pristine non defective Heusler structure (NV), and for the as cast (b), annealed (d) and sintered (f) samples, assuming a defective Heusler structure containing vacancies on the Co-site (V).

As reported by Mahat et al. [170], the intensity of the (200) peak is linked to the order of atoms in the tetrahedral position, namely Co. Similarly, the (111) reflex is an indicator of octahedral positions ordering (Zr, Sn), while the main peak (220) is independent from the ordering state [171]. This was also highlighted in Section 4.0.1 based on crystallographic simulations. Accordingly, it can be stated that the more the Rietveld refinement is able to accurately fit the intensity of the (200) peak, the more the description of the ordering of Co-site in the Heusler structure will be correct.

As it can be noted in the insets of Figure 31, the refinement is qualitatively better in the defective model, where the Co occupancy was not fixed at a value of 1 and was let free to converge during the process. From a quantitative point of view, a complete review of the convergence parameters and accuracy figures of merit in Rietveld analysis is not the purpose of this study; however, in 2006 B.H. Toby [172] effectively reviewed the topic, allowing us to remind to that work for more detailed information. In summary, three parameters can be considered for determining the quality of a Rietveld refinement: R_{exp}, R_b and χ^2. R_{exp} is a parameter which solely depends on the quality of the XRD measurement, accounting for background noise, signal/noise ratio and linearity of the baseline. The lower R_{exp}, the better is the pattern quality. As far as R_b is concerned, it quantifies the difference between the calculated fit and the experimental pattern based on the intensity of each point of the diffractogram. The closer R_b is to R_{exp}, the better is the refinement. χ^2, often called the "goodness of fit" parameter, is a composite value which takes into account the least square difference between the calculated and experimental profiles. During the refinement process, χ^2 starts out large when the model is poor and decreases as the model produces better agreement with the data. The closer χ^2 is to 1, the better is considered the model; however, it should be noted that this should never drop below such value.

In Table 4 the R_{exp}, R_b, and χ^2 factors are provided for both the defective and non-defective analysis. The XRD characterization was also performed (see Appendix A) on the rapidly solidified (melt spun) material prior to the sintering process, and for a portion of sintered alloy subsequently annealed at 1000°C for 6 days (SPS + An.). Since the smaller are R_{exp}, R_b, and χ^2 the better is the quality of the analysis, if the defective refinement resulted in lower values than the non-defective, then it would be possible to safely conclude that the occupancy of Co-sites is not 1, and that the Heusler structure is better described when the presence of Co vacancies is taken into account.

As far as the convergence parameters of the Rietveld refinements are concerned, the difference of χ^2 between the NV and V models was calculated as in Equation 38, whereas; ΔR_b was calculated simply as the difference between the R_b% of NV and V models.

$$\Delta\chi^2 = \frac{\chi^2_{NV} - \chi^2_V}{\chi^2_{NV}} \cdot 100 \tag{38}$$

The results of the Rietveld refinement are reported for each sample in Table 5. Considering the results obtained applying the V model, the most defective sample of the series was observed to be the arc-melted specimen (As cast), which presented the lowest Co site occupancy of 0.82, leading to a nominal $Co_{1.64}ZrSn$ formula unit. The same sample after annealing (Annealed) was found with an increased occupancy of Co sites, equal to 0.88, bringing the formula unit to $Co_{1.76}ZrSn$. On the other hand, the alloy synthesized by rapid solidification (melt-spun) was observed to be the closest to the pristine stoichiometry, having χ_{Co} of 0.96 and a $Co_{1.92}ZrSn$ stoichiometry. This is because the rapid cooling allows to expand the solubility limit of Co inside the Heusler compound, allowing to force the stoichiometry towards the nominal one. As the rapidly solidified powder is subjected to the heat treatment involved in the spark plasma sintering process (see Section 4.3), a shift towards more stable conditions begins, resulting in a slight decrease of χ_{Co} to a value of 0.94 ($Co_{1.88}ZrSn$) for the SPS specimen. When the so obtained SPS sample was subsequently annealed for an extensive period (SPS + An.), Co occupancy kept decreasing as the Heusler compound's composition shifts towards the thermodynamically favorite stoichiometry, leading to a χ_{Co} of 0.91 ($Co_{1.82}ZrSn$), which is extremely close to what observed for the Annealed alloy. On the other hand, considering the NV, no difference in Co occupancy was estimated, as this model, by definition, does not take into account deviations from the pristine stoichiometry.

Aiming to evaluate which model best describes this set of samples, as it is possible to see from Table 4, both R_b and χ^2 of the V model are lower than those of NV, indicating that the model that takes into account the presence of vacancy defect describes the experimental samples better than the one which do not consider the presence of such defects. Overall, the V model was observed to generally being more reliable to describe the experimental XRD patterns, with values of χ^2 better than NV up to 14.49%. As it is possible to note from Figure 32a, $\Delta\chi^2$ and ΔR_b increase as the concentration of vacancies inside the specimen becomes higher. This

is to be expected, as for specimens having stoichiometry close to the pristine (i.e. melt-spun and SPS), V and NV are extremely similar. Coherently, as the samples become more and more defective (or, as χ_{Co} become increasingly lower than 1), NV begins to fit the experimental data less effectively, thus amplifying $\Delta\chi^2$ and ΔR_b. In fact, $\Delta\chi^2$ was calculated being 0.64% and 1.46%, respectively for the melt-spun and SPS specimens, which are the least defective. The more defective SPS+An. and Annealed samples show higher $\Delta\chi^2$ around 9-11%. The most defective sample, the As-cast, present the highest $\Delta\chi^2$ of 14.49%, indicating that the V model is considerably better in describing such sample. From Figure 32a it is also possible to note how the increase in goodness of fit is rather linear with the increasing χ_{Co}, ideally reaching a $\Delta\chi^2$ equal to zero when χ_{Co} approaches 1. This would happen for an ideal pristine sample, for which the NV and V models would coincide. Analogous considerations are applicable for ΔR_b, which shows a linear trend as a function of χ_{Co}.

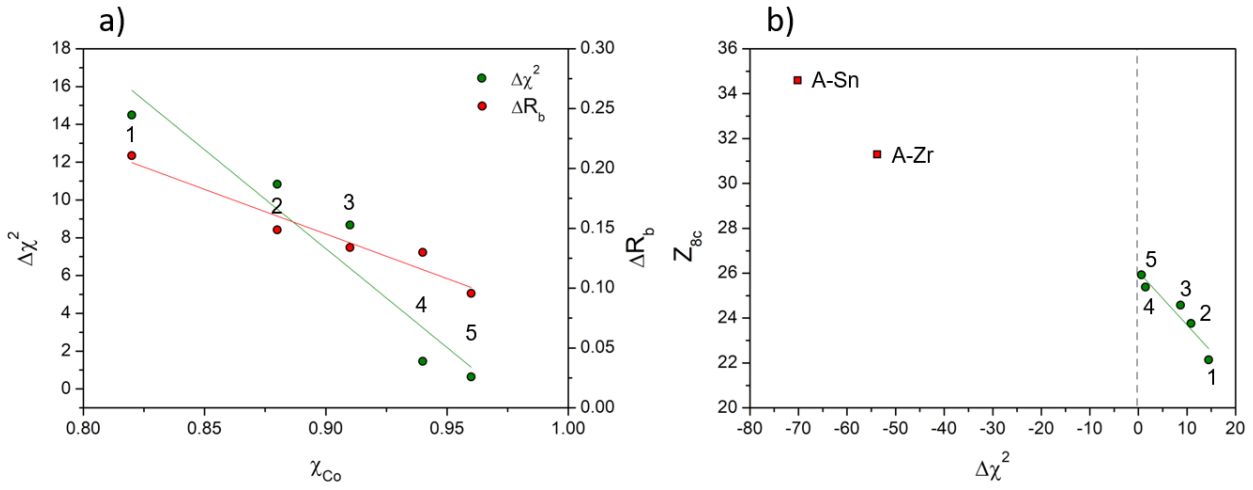

Figure 32: (a) $\Delta\chi^2$ as a function of χ_{Co}, and (b) $\Delta\chi^2$ as a function of Z_{8c} of all Rietveld refinements. Sample numeration: 1- As-cast, 2- Annealed, 3- SPS+An., 4: SPS, 5: melt-spun.

Two additional Rietveld refinements were performed, as an example, for the As-cast sample imposing Zr and Sn anti-sites as the only defect present in the alloy. An arbitrary 0.33 occupancy factor was assigned to Zr and Sn as initial conditions. Such two models, which will be labeled as A-Zr and A-Sn, respectively, were first computed in their fixed initial conditions. Then, the Zr and Sn occupancy was unlocked and the models let free to converge to the optimal occupancy values. As already explained, the introduction of elements with atomic number higher than 27 in the 8c site have the effect to decrease the intensity of the (200) peak; in fact, as noticeable from Figure 33, the quality of fit on the (200) peak dramatically decrease with respect to NV. Unsurprisingly, as soon as Zr and Sn occupancies are let free to converge, the refinement rapidly brings such values at zero, ultimately returning outcomes which are analogous to NV. At this point, if the total Co occupancy is unlocked as well, the refinement becomes as the V model.

Considering the A-Zr and A-Sn models from the quantitative aspect, when compared with A-cast's NV, $\Delta\chi^2$ of -54% and -70% are obtained. The minus sign is indicative of the fact that in these cases, the defective model is less reliable than the non-defective, as the fit on the intensity and profile of the (200) peak is worsened after that defects are introduced in the refinement. $\Delta\chi^2$ of A-Zr and A-Sn was in fact calculated as follows:

$$\Delta\chi^2 = \frac{\chi^2_{NV} - \chi^2_{A-Zr/Sn}}{\chi^2_{NV}} \cdot 100 \qquad (39)$$

This is also shown in Figure 32b, where Z_{8c} is plotted as a function of $\Delta\chi^2$. Here, it is possible to note that, again, $\Delta\chi^2$ tends to be almost zero for an average atomic number in 8c of 27, which would be satisfied for a pristine sample. Considering the V model, $\Delta\chi^2$ becomes increasingly positive for samples with stoichiometry further from the ideal Co_2ZrSn, meaning that the V model progressively better describes highly defective specimens (see Equation 38). On the other hand, $\Delta\chi^2$ of A-Zr and A-Sn are negative (Equation 39), meaning

that such models are worse than NV in fitting the experimental values. Additionally, their absolute $\Delta\chi^2$ values of 53% (A-Zr) and 70% (A-Sn) are way far from being acceptable to describe our set of samples.

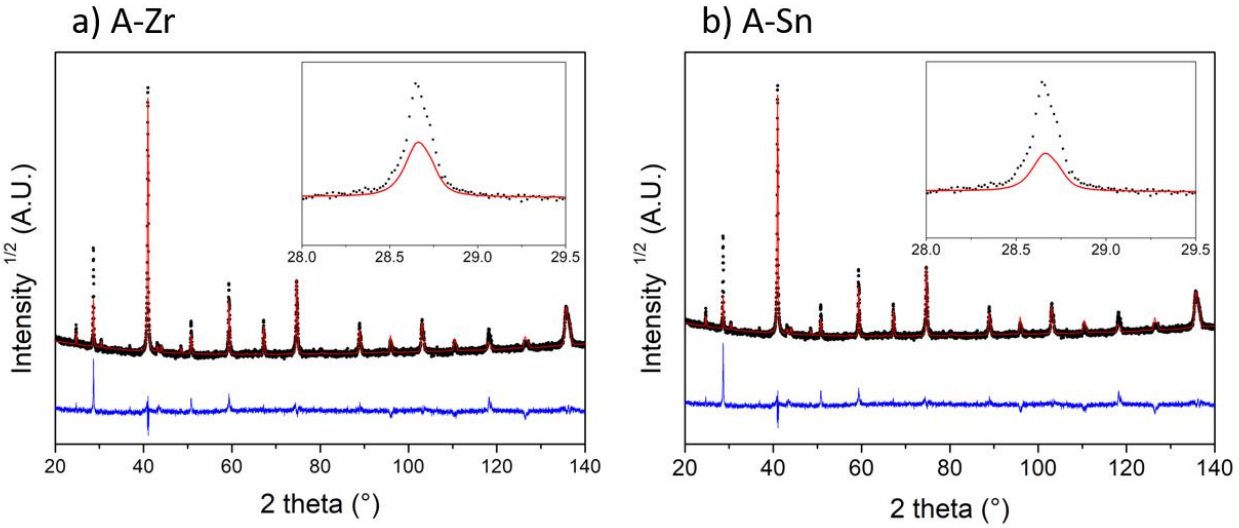

Figure 33: Rieteveld refinement of the As-cast sample XRD pattern in the (a) A-Zr, and (b) A-Sn model assuming a 0.33 anti-site occupancy in the 8c sub-lattice as initial condition.

In Figure 34a, the lattice parameter (*a*) of Co_2ZrSn specimens were plotted as a function of the Co occupancy (χ_{Co}). As the NV and V only differ for peaks' intensities, the lattice parameters obtained from both models are identical. Considering Figure 34a, the first aspect to notice is that *a* scales linearly with χ_{Co} similarly to what already found by Kushwaha et al. [114], who obtained extremely comparable results in a previous study (see Figure 30). The linear shrinking of the *a* with the decreasing χ_{Co} is compatible with the progressive increasing of the vacancy concentration, as also previously reported for single crystal samples. Such trend is impossible to explain considering other types of defects, as intrinsic anti-sites with Zr and Sn always involve atoms with an atomic radius larger than Co, leading to a lattice expansion. Such statement was confirmed by ab-initio calculations performed on several defective Co_2ZrSn systems, which will be explained more in detail in Section 8.

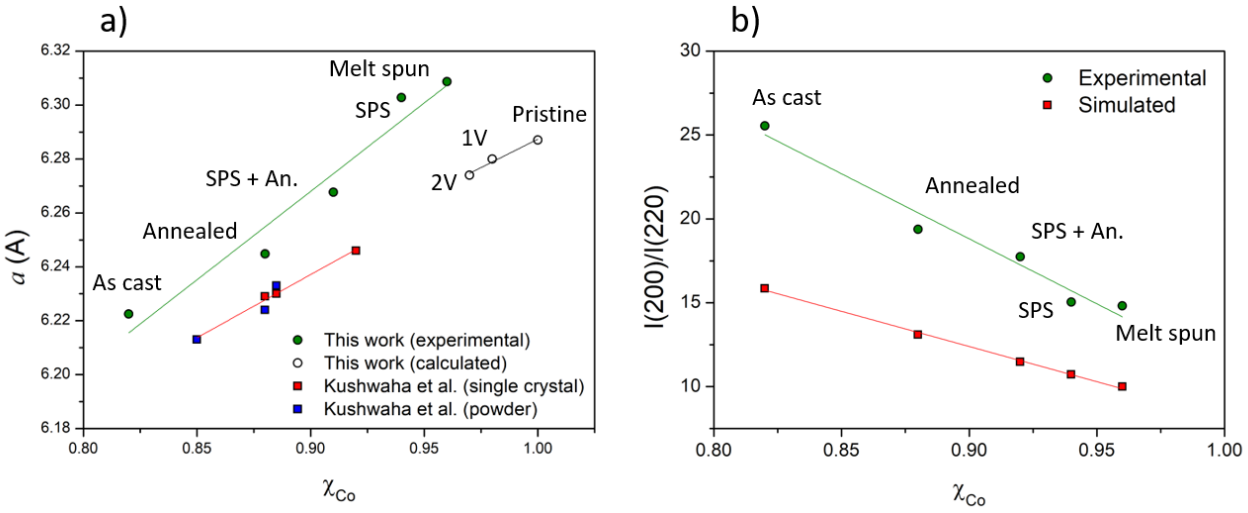

Figure 34: Lattice parameter (a) and I(200)/I(220) (b) as a function of χ_{Co} for the various Co_2ZrSn samples. The simulated I(200)/I(220) values for a single and infinite Co_2ZrSn crystal are also reported. Data of Kushwaha et al. are from Ref. [114]. Calculated data will be discussed in Section 8.3.2.

The disorder in the 8c site was also evaluated without the use of the Rietveld refinement method, by measuring the experimental I(200)/I(220) ratios for the various samples (see Table 5). In Figure 34b, the trend of I(200)/I(220) are reported as a function of χ_{Co}, showing again a linear trend which is coherent to what expected from the theory. In fact, as highlighted in Figure 29, I(200)/I(220) increases with the increasing vacancy concentration in 8c, coherently to what found experimentally. Also, by extrapolating the trend at a χ_{Co} of 1, a I(200)/I(220) of 11.06 is observed, which is extremely close to the 8.67 predicted for a perfect and infinite Co_2ZrSn crystal. Overall, the experimental and simulated I(200)/I(220) trends as a function of χ_{Co} are in good agreement, leading to the same conclusions deduced from Rietveld refinements, and indicated vacancies as the most important defect affecting the sites of Co.

	As cast	Annealed	SPS + An.	SPS	Melt spun
a (Å)	6.2225	6.2448	6.2677	6.3028	6.3087
χ_{Co}	0.82	0.88	0.91	0.94	0.96
% wt. Co_3Sn_2	4.3	3.7	< 2.0	< 2.0	< 2.0
I(200)/I(220)%	25.54	19.38	17.74	15.04	14.82

Table 5: Lattice parameter (*a*), Co occupancy (χ_{Co}), abundance of Co_3Sn_2 secondary phase expressed in weight %, 200/220 peak area ratio for the Co_2ZrSn specimens obtained by different processing routes.

As noticeable from Table 5, having the SPS and melt spun alloys approximately the same Co occupancy, they present accordingly almost identical I(200)/I(220) values. Being the heat treated samples the closest to the thermodynamic conditions, it is reasonable to state that the presence of vacancies or, more in general, Co-site disorder is thermodynamically favored as the equilibrium conditions for the Heusler compound possibly involve the occurrence of a certain amount of defects (see Section 8). This can be better understand considering the processing route of the sintered specimen. During the melt-spinning process, cooling rates between 10^4 and10^5 K/s are reached, allowing to obtain alloys in metastable conditions [173]. The melt spun material was found to be the least defective, presenting a χ_{Co} of 0.96 and thus the largest lattice parameter. This is because the rapid cooling allows to expand the solubility limit of Co inside the Heusler compound, allowing to force the stoichiometry towards the nominal one. As the rapidly solidified powder is subjected to the heat treatment involved in the spark plasma sintering process (see Section 4.3), a shift towards more stable conditions begins, resulting in a slight decrease of χ_{Co} and thus *a*. Being the difference of χ_{Co} small, extremely similar values of I(200)/I(220) ratio are measured for such two specimens. When the so obtained SPS sample was subsequently annealed for an extensive period (see SPS + An. specimen), the Co occupancy kept decreasing as the Heusler compound composition shifts towards the thermodynamically favorite stoichiometry. The usual associated shrinking of lattice parameter is again reported. Here, a noticeable reduction of the I(200)/I(220) ratio is also observed. Similarly, the arc melted as cast sample, which was subjected to a typical cooling rate between 10 and 10^2 K/s, is located on the edge of *a* and χ_{Co} values range.

7.3 Microstructural and texture analysis

In Figure 35, electron backscattered images of the as cast, annealed, and sintered samples are presented. Having the specimens been polished down to a 40 nm mesh, Heusler phase grains with different orientations appear with different gray tones due to backscattered electron diffraction. Additionally, the secondary Co_3Sn_2 is highly recognizable and is mainly located at the grain boundaries of the Heusler phase. In the case of the sintered sample, the amount of secondary phase is significantly lower than in the as cast and annealed samples, in agreement with the results of the Rietveld refinement of the XRD patterns reported in Table 5.

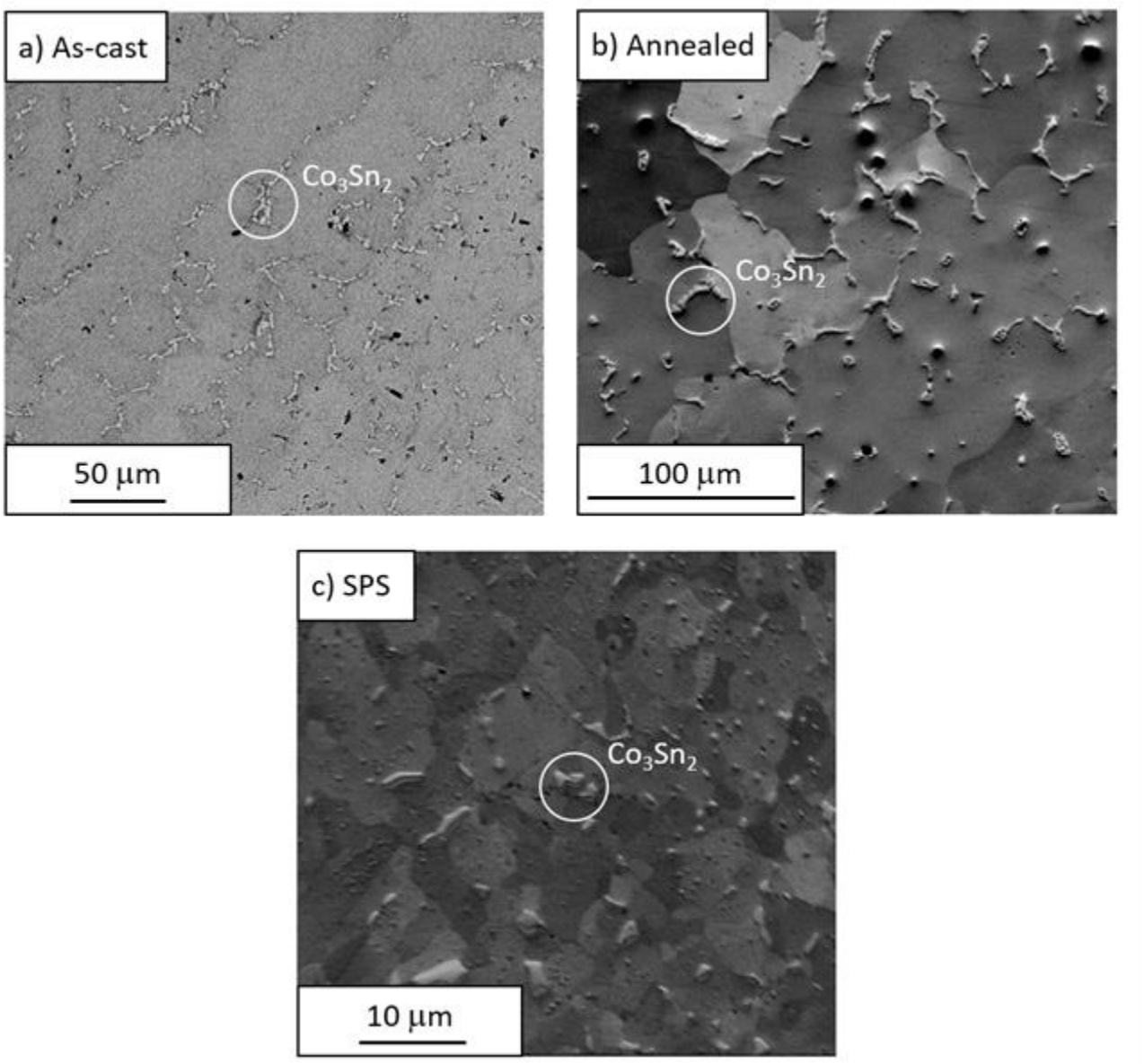

Figure 35: SEM backscattered images of the as cast (a), annealed (b), and sintered (c) Co_2ZrSn samples.

EDS spectra revealed an average atomic composition equal to 49% Co, 24% Zr, 26% Sn for all samples (considering an intrinsic error of the EDS technique approximately of 1% for each element). Spot spectra on the various phases shown a composition of the secondary phases approximately of 61% Co, 4% Zr, 35% Sn, confirming the presence of an intermetallic Co_3Sn_2 compound as suggested by XRD patterns (see Figure 31).

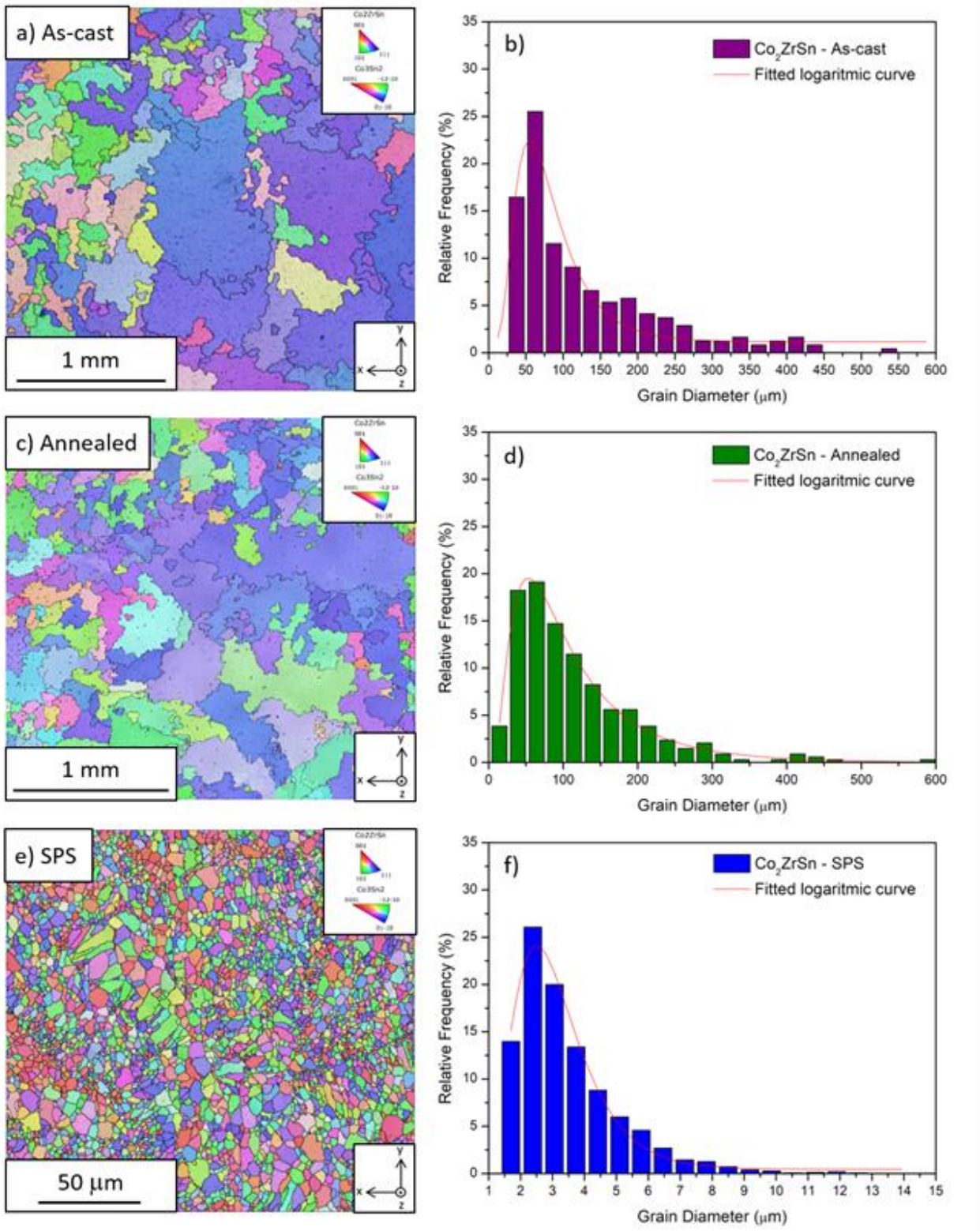

Figure 36: EBSD grain orientation maps (along the *z* direction) of the as cast (a), annealed (c) and sintered (e) samples. Grain size distributions of the as cast (b), annealed (d) and sintered (f) samples.

The stoichiometry of such phase is approximately the same in all specimens with percentages of Zr fluctuating between 3 and 4%. The composition of the Heusler phase in the different samples is reported in Table 6. As it can be noticed, compositions measured by EDS satisfactorily match the stoichiometry calculated from Co occupancy values resulting from Rietveld refinements. Further speculations solely based on EDS data are difficult to assess, as the intrinsic error relative to the EDS technique in such sample is on the order of

magnitude of 1%; nevertheless, two observations can still be made. First, it is noticeable that the average value of Co composition increases as both χ_{Co} and a (see Table 5) increase, as to be expected. Secondly, it is important to note that in the as cast and SPS samples, the standard deviation on the atomic percentages is higher than the technique's intrinsic error, suggesting a slight non-homogeneity of such samples. On the contrary, the atomic relative abundances of the Heusler phase in annealed specimens (Annealed and SPS +An.) are less dispersed, suggesting an increase of homogeneity derived from the heat treatment.

Sample	χ_{Co}	Phase stoichiometry	EDS elemental composition (at. %)		
			Co	Zr	Sn
As cast	0.82	$Co_{1.64}ZrSn$	46.5 ± 2.0	26.5 ± 2.0	28.0 ± 2.0
Annealed	0.88	$Co_{1.76}ZrSn$	47.0 ± 1.0	26.0 ± 1.0	27.0 ± 1.0
SPS	0.94	$Co_{1.88}ZrSn$	48.0 ± 1.5	25.5 ± 1.5	26.5 ± 1.5
SPS + An.	0.91	$Co_{1.82}ZrSn$	48.0 ± 1.0	26.0 ± 1.0	26.0 ± 1.0
Melt spun	0.96	$Co_{1.92}ZrSn$	49.0 ± 1.5	25.0 ± 1.5	26.0 ± 1.5

Table 6: Co occupancy (χ_{Co}), phase stoichiometry (calculated from χ_{Co}), and EDS elemental composition of the Heusler phase for various samples processed by different techniques.

Quantitative information on grain size, shape, and preferential orientations can be extracted from the analysis by EBSD technique. In Figure 36a,c,e, the EBSD grain orientation maps are presented. Here, each grain is colored based on its orientation with respect to a certain considered axis, which is in this case *z*, or the direction of the applied pressure during the sintering process. Since grains appeared randomly colored along the whole investigated area, it is possible to conclude that no preferential orientation is present in the samples. Additionally, grains appear qualitatively equiaxial, presenting an average ellipsoid aspect ratio of approximately 1.5 in all the specimens (see Appendix A), indicating rather circularly shaped crystals. From EBSD maps, grain size distributions were calculated and reported in Figure 36b,d,f. Having been subjected to a considerably faster cooling rate during the rapid solidification process, it is not a surprise that the lowest average grain size is shown by the sintered alloy, showing an average value between 2 μm and 3 μm. Being the cooling rate during the arc-melting lower, the as cast sample present considerably larger grains with an average diameter of about 55 μm. This value was not found to change after the annealing period. The effect of the microstructure refinement on transport properties will be discussed more in detail in Section 7.4.

7.4 Transport properties

The Hall resistivity was measured in a ± 7 T range between 3 and 300 K for all the as cast, annealed, and sintered samples, allowing to obtain the trend of the charge carrier concentration. In Figure 37a,b, the Hall resistivity of the annealed specimen is shown as an example (see Appendix A for those of the as cast and sintered specimens). A strong anomalous contribution was found at low fields, Figure 37a, while above ± 1 T an ordinary behaviour is observed with the resistivity that scales linearly with field, Figure 37b. As the resistance was found to have approximately the same slope as a function of the field at various temperatures, rather constant Hall coefficients (R_H) of $4.77 \cdot 10^{-10}$ m^3/C, $6.05 \cdot 10^{-10}$ m^3/C, and $6.53 \cdot 10^{-10}$ m^3/C were found for as cast, annealed, and sintered samples, respectively. The charge carrier concentration (n) as a function of T was calculated starting from R_H values ($n = (R_H \cdot e)^{-1}$, where e is the electron charge) and is reported in Figure 37c. For all the specimens the values of *n* remain rather constant in the whole temperature range. The average charge carrier concentration between 3 and 300 K is $1.28 \cdot 10^{28}$ m^{-3}, $1.05 \cdot 10^{28}$ m^{-3}, and $9.87 \cdot 10^{27}$ m^{-3} for the as cast, annealed, and sintered samples, respectively, indicating a typical conductive behaviour. From the same set of measurements, the electron mobility, μ, was obtained, showing at room temperature larger values for the sintered (1.97 $cm^2V^{-1}s^{-1}$) and annealed (1.91 $cm^2V^{-1}s^{-1}$) samples with respect to the as cast specimen (1.24 $cm^2V^{-1}s^{-1}$). At 2 K, values of 2.70 $cm^2V^{-1}s^{-1}$, 3.39 $cm^2V^{-1}s^{-1}$ and 1.66 $cm^2V^{-1}s^{-1}$ were obtained for the sintered, annealed and as cast samples, respectively.

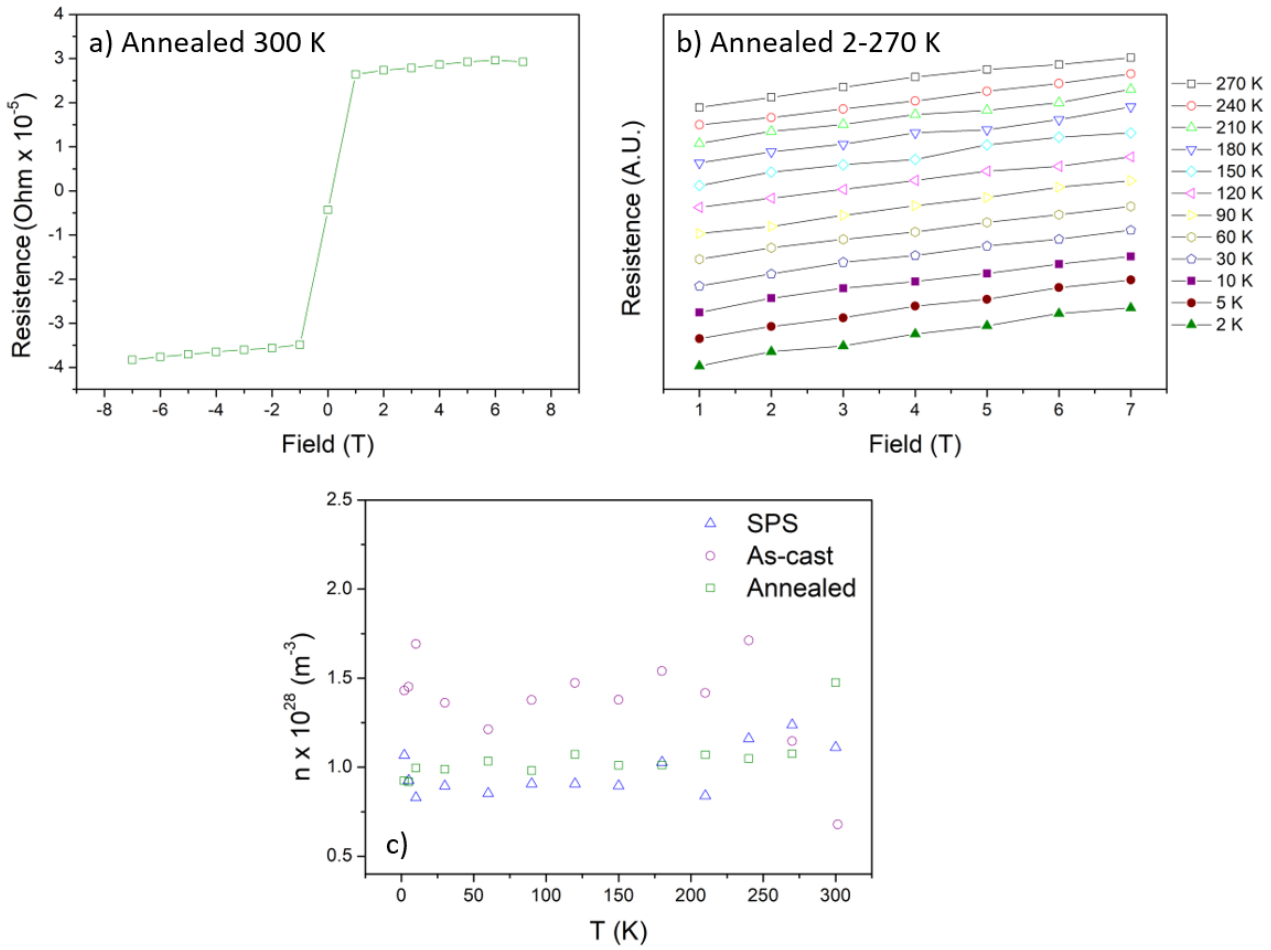

Figure 37: Hall resistivity of the annealed sample measured at 300 K (a). Hall resistivity as a function of the applied magnetic field measured in the temperature range between 3 and 270 K for the annealed sample (b). Charge carrier concentration of the as cast, annealed, and sintered specimens (c).

Figure 38 shows the temperature dependence of the electronic transport properties of the as cast, annealed, and sintered samples. The Seebeck coefficient was measured between 300 and 800 K, Figure 38a, showing a similar behaviour for all the samples. As previously reported [116], |S| shows a linear increase from room temperature to approximately T_C, followed by a plateau above the Curie point. Coherently with what already reported, the negative values of S indicate that the material is n-type, having electrons as main charge carriers. The absolute values of S for the different measured samples are inversely proportional to the carrier concentration and are directly proportional to the Co-site occupancy, suggesting that a higher vacancy concentration decrease |S|. Concerning the electrical conductivity, Figure 38b, it decreases almost linearly from room temperature to a minimum value and subsequently weakly rises. For this type of compounds, the temperature at which σ changes its slope corresponds to the Curie point, T_C, where the transition from ferromagnetic to paramagnetic behaviour occurs [50]. According to this method, the annealed sample shows a slightly different value of T_C with respect to the as prepared ones (i.e. as cast and sintered), probably due to the observed composition fluctuations of the Heusler phase in the different samples, as reported in Section 4.3. In fact, as already reported [52,114], even small compositional inhomogeneity can have an effect on T_C, leading to the remarkable scattering of data observed in literature [80,107–112,148]. Between 300 K and 400 K (before T_C), the annealed and sintered samples show similar values and trends of the electrical conductivity due to the very close values of electron mobility and carrier concentration at 300 K. In the same temperature range, the electrical conductivity of the as cast sample is lower than the other two samples since the decrease of electron mobility (- ~50%) prevails with respect to the increase of the carrier concentration (+ ~20%). Above the Curie

point, the values of electrical conductivity scales with Co-site occupancy, showing the lowest values for the most defective sample (i.e. as cast).

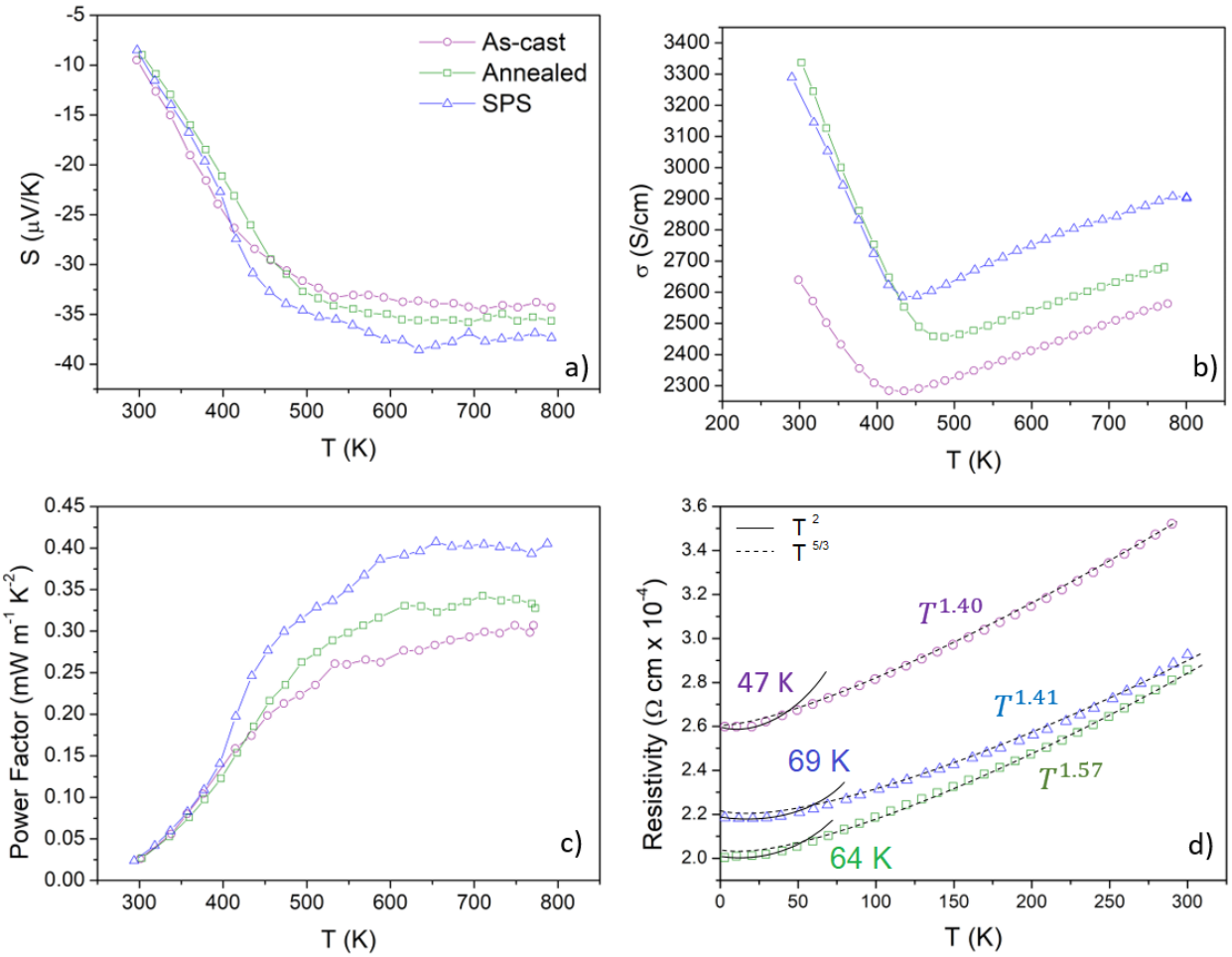

Figure 38: Seebeck coefficient (a), electrical conductivity (b) and power factor (c) measured between 300 K and 800 K. Electrical resistivity (d) measured between 2 K and 300 K.

Due to the square dependence on S, the power factor ($PF = S^2\sigma$) shows a trend similar to the one of the Seebeck coefficient, consisting of a rather linear increase until T_C followed by a plateau, as shown in Figure 38c. At 773 K, values of 0.296 mW $m^{-1} K^{-2}$, 0.338 mW $m^{-1} K^{-2}$, and 0.400 mW $m^{-1} K^{-2}$ were obtained for the as cast, annealed, and sintered samples, respectively. These values scale with the Co-site occupancy, indicating that the overall electronic transport properties are strongly influenced by the vacancy concentration.

Figure 38d shows the electrical resistivity as a function of temperature between 2 K and 300 K. A change of the dependence of R on T was found around 50-70 K for all the samples. At lower temperature the dependence is parabolic, while increasing the temperature σ becomes proportional to T^x. In particular, the as cast, annealed, and sintered samples show a regime change from parabolic to T^x (with x equal to 1.40, 1.57 and 1.41, respectively) at 47 K, 64 K and 69 K, respectively. This behavior was reported for other Heusler compounds (both bulk and thin films) and was interpreted as the crossover from a low-T half-metallic state to a conductive ferromagnetic one at higher temperatures [69,94,161,174]. In fact, it was reported that at low temperatures the presence of a half-metallic state, which is associated with the absence of a minority-spin density of states at the Fermi level, impedes the occurrence of spin-flip electron diffusion, thus causing the reduction of electrical conductivity [161,162]. Contrariwise, at higher temperatures the occurrence of several electron scattering mechanisms is possible, such as spin waves, phonon, and spin fluctuations. Since spin waves and phonons contribute with a linear proportionality of σ on T to the total electrical conductivity, and since spin fluctuations

concur with a $T^{5/3}$ dependency, the value of the resulting temperature exponent at high-T is expected to be between 1 and 5/3 [69,95], as indeed experimentally observed in this work for all the specimens. An extensive overview on the model used to explain such behavior, and on the electrical resistivity of half-metallic Heusler alloys has been provided in Section 2.1.3. Overall, such trend of electrical resistivity is not incompatible with the presence of a half-metallic gap at low temperatures. It has to be noted that the same crossover at low-T was found also in the trend of magnetization (M) on temperature for Co_2ZrSn, Co_2HfSn [52] and other Heusler compounds [69,94,161,175], being again linked to the presence of the same half-metallic state below a certain T. For Co_2ZrSn, the previously obtained crossover temperature by the measurement of M/T was around 70 K [51], which is consistent with the values found in this work both from the characterization of electrical conductivities, Figure 38d, and of that of magnetic properties (see Section 5.5).

Considering both the low and high T profile of the electrical conductivity, several observations can be made. Comparing the as cast and annealed samples, the latter shows significantly larger values than the former over the entire range of temperatures. Being these two specimens microstructurally identical (Figure 36), the difference of σ can be linked to compositional effects, showing that the increase of Co-site occupancy has a beneficial effect on electrical conductivity. When the annealed and sintered samples are taken into account, their electrical conductivities are very similar between room temperature and 450 K, while at higher temperature the sintered sample shows larger values than the annealed one. Conversely, between 2 K and 300 K, σ of the annealed sample becomes larger with respect to the sintered one. According to the different χ_{Co} values in the two samples, the electrical conductivity of the SPS specimen (χ_{Co} = 0.94) is expected to be significantly larger than the annealed (χ_{Co} = 0.88) over the whole temperature range. However, the microstructure of the two specimens, Figure 36, show a larger grain boundary density for the SPS sample with respect to the annealed. Since the charge carrier scattering due to grain boundaries is dominant at lower temperature [176], the larger values of σ observed for the annealed sample between 2 K and 300 K can be explained in terms of lower grain boundary density. At higher temperature, where the grain boundary scattering is less effective, the larger values found for the sintered specimen can be interpreted in terms of lower vacancy concentration (i.e. larger χ_{Co}). This interpretation agrees with the fact that the electronic properties of Co_2ZrSn almost exclusively depend on Co atoms as a direct consequence of its density of states at the Fermi level [51].

From thermal diffusivity values, the thermal conductivity, k, was obtained (Figure 39) by multiplying them by the respective sample densities (8.22 g/cm^3 for as cast and annealed, 7.89 g/cm^3 for sintered) and the Co_2ZrSn phase specific heat capacity, C_P. The trends of k as a function of T are quite similar to those of σ, as a linear decrease from 300 K to T_C is followed by a linear increase above the Curie point. This trend is analogous to that reported for the similar Co_2HfSn Heusler alloy [52]. The electronic contribution to the thermal conductivity, k_{el}, was calculated using the Wiedemann-Franz law ($k_{el} = L\sigma T$, with $L = 1.5 + exp\left[-\frac{|S|}{116}\right]$ WΩK^{-2} as proposed by Snyder et al. [164]). The lattice contribution, k_{lat}, was estimated as $k_{lat} = k - k_{el}$ and is reported in Figure 39e. Since the annealed and sintered samples have comparable values of σ, the corresponding k_{el} were found to be similar as well; whereas, the as cast sample, which exhibits the lowest σ, shows the lowest k_{el} contribution, accordingly. As far as k_{lat} is concerned, the as cast and annealed specimens present close values while the SPS sample has the lowest k_{lat}. In the case of the SPS sample, the lowest values of k can be interpreted in terms of a finer microstructure, and lower density with respect to the as cast and annealed. However, the decrease in density is only about 4% while the decrease of k and k_{lat} at 300K are about 20% and 30%, respectively, suggesting a significant effect of the larger grain boundary density on phonon scattering.

The thermoelectric figure of merit zT was estimated on the basis of the measurement of all the involved transport properties. Overall, the sintered sample was found to have the highest zT in the whole investigated temperature range as a consequence of the higher S, σ, and of the lower k. The annealed specimen exhibited larger values of S and σ than the as cast sample as a consequence of the χ_{Co} increase induced by the heat treatment; however, the higher value of thermal conductivity, due the coarser microstructure with respect to the sintered sample, causes a decrease of the thermoelectric conversion efficiency. At last, the as cast specimen

was found to have the worst figure of merit because of the lowest S and σ and the largest value of thermal conductivity due to the more defective structure (i.e. lowest χ_{Co}) and the coarser microstructure, respectively. At 300 K, similar values of zT (~ $0.75 \cdot 10^{-3}$) were found for all the samples, while at 800 K zT values of $2.18 \cdot 10^{-2}$, $2.52 \cdot 10^{-2}$, and $3.39 \cdot 10^{-2}$ were observed for the as cast, annealed, and SPS samples, respectively.

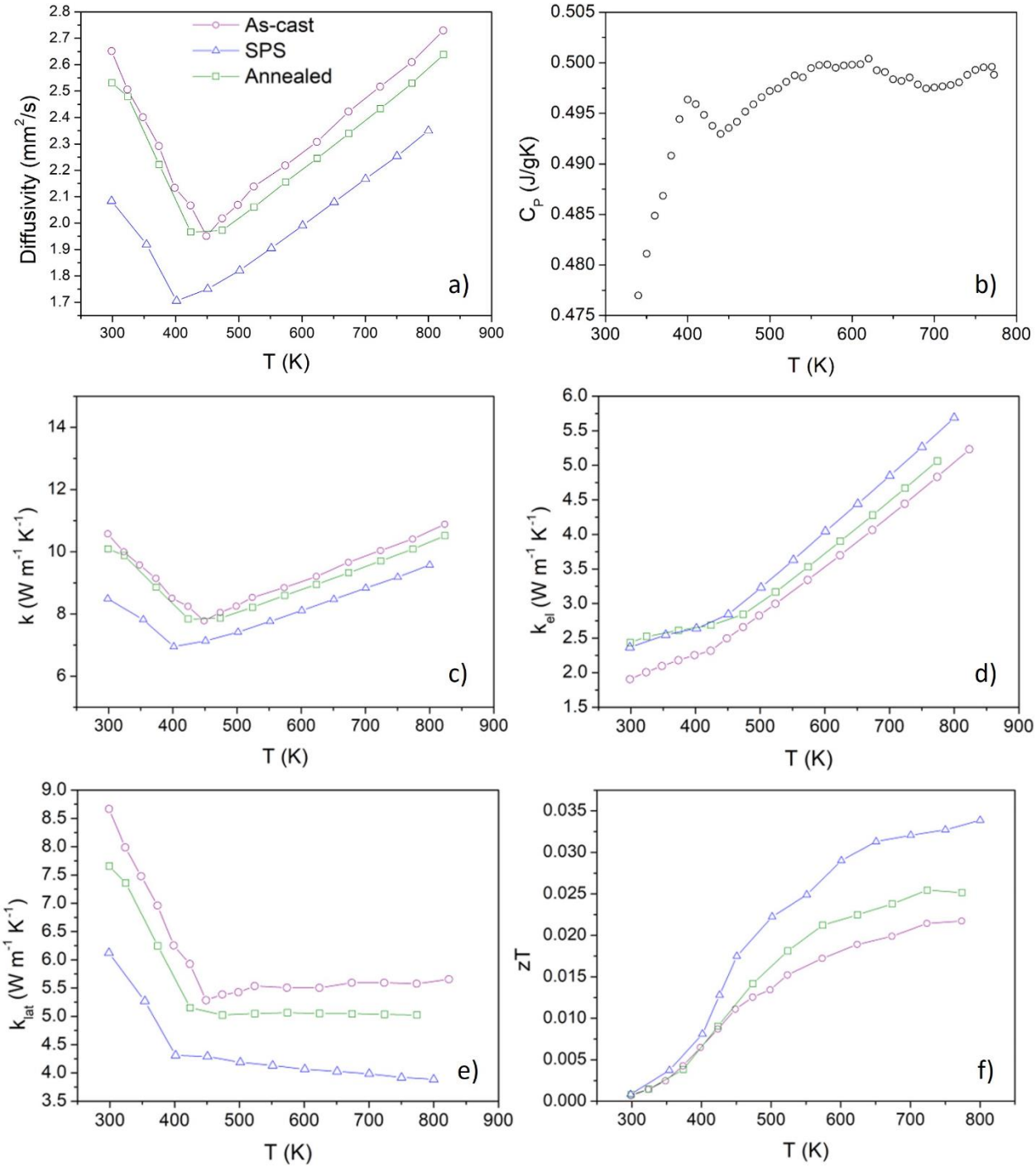

Figure 39: Thermal diffusivity (a), specific heat capacity C_P (b), conductivity k (c), electronic contribution to thermal conductivity k_{el} (d), lattice contribution to thermal conductivity k_{lat} (e), thermoelectric figure of merit zT (f) of as cast, annealed, and sintered samples.

7.5 Magnetic properties

The magnetization curves M(H) measured at 20 K on as cast, annealed, and sintered Co_2ZrSn samples are shown in Figure 40a. All M(H) curves exhibit a small hysteresis (coercive fields of the order of 3-4 Oe). The saturation magnetization at 20 K was found to increase as a function of χ_{Co} as reported in Table 5 for the measured specimens. The magnetization of a pure Co_3Sn_2 sample at the same temperature is also shown for comparison. Considering the low amount of such a secondary phase in the measured Co_2ZrSn samples, it can be safely concluded that the contribution to the overall magnetic signal of the Co_3Sn_2 phase is negligible. Therefore, the values of the saturation magnetization of all Co_2ZrSn specimens can be referred as related to the Heusler compound only. These results agree with previous findings by Kushwaha et al. [114], stating that in Co_2ZrSn, Co-occupancy has a dramatic effect on the magnetic properties. In particular, the increase of vacancies' concentration was found to significantly lower the saturation magnetization, as shown here.

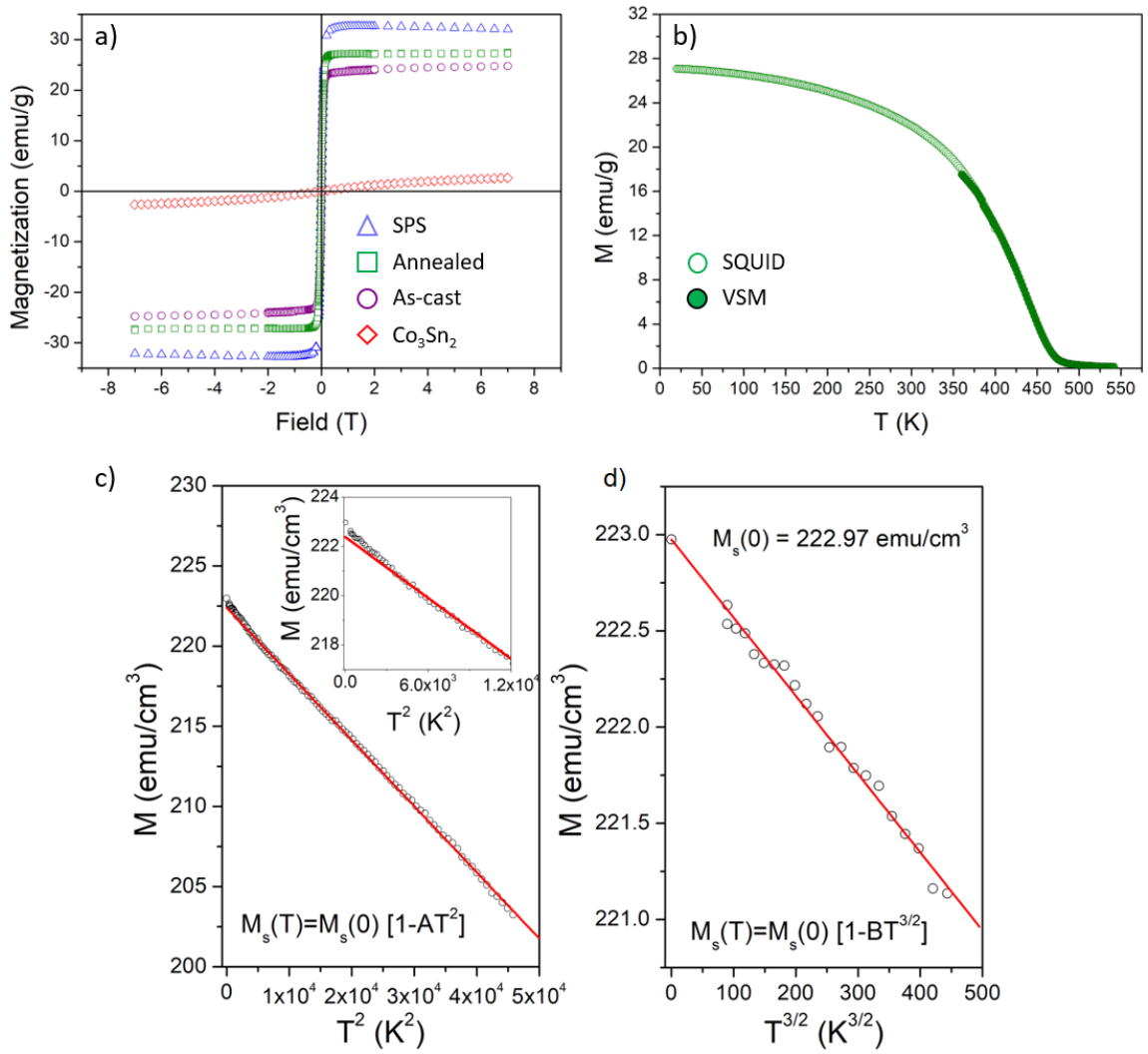

Figure 40: Hysteresis curves at 20 K of as cast, annealed, sintered Co_2ZrSn samples, and pure Co_3Sn_2 phase (a). Temperature dependence of magnetization under constant field of 5 kOe of annealed Co_2ZrSn (b). Spontaneous magnetization as a function of T^2 (c) and $T^{3/2}$ (d). Inset of (c) shows the deviation from T^2 regime.

Considering the magnetic moment at low temperature exhibited by the various samples, it can be noted how such value essentially follows those of Co occupancy. As highlighted in Figure 41, the dependency of μ on χ_{Co} is linear and qualitatively agrees with the results reported by Kushwaha et al. [114]. This confirms that the

magnetic moment is mainly located on Co atoms, as suggested by ab-initio calculations. The effect of the Co vacancy defects on the half-metallicity of Co_2ZrSn will be discussed more in detail in Section 5.

The annealed alloy, which is the closest to the thermodynamic stability due to the extended heat treatment, was selected for further investigations. The low and high temperature magnetic properties were measured respectively with SQUID and VSM, allowing to obtain a complete magnetization curve as a function of temperature, Figure 40b, under a constant field of 5 kOe (this value has been selected in order to avoid spurious effects on magnetization related to the presence of magnetic domains). The curves obtained using the two instruments match satisfactorily. The overall behavior of the M(T) shows the degradation of magnetic order by effect of the increasing temperature and allows to get an estimation of the Curie temperature. However, the presence of a constant applied field smears out the transition region. The Curie temperature more accurately derived by the Arrott plot method and was estimated to be 448 K, which is close to the previously measured value of 454 K [51].

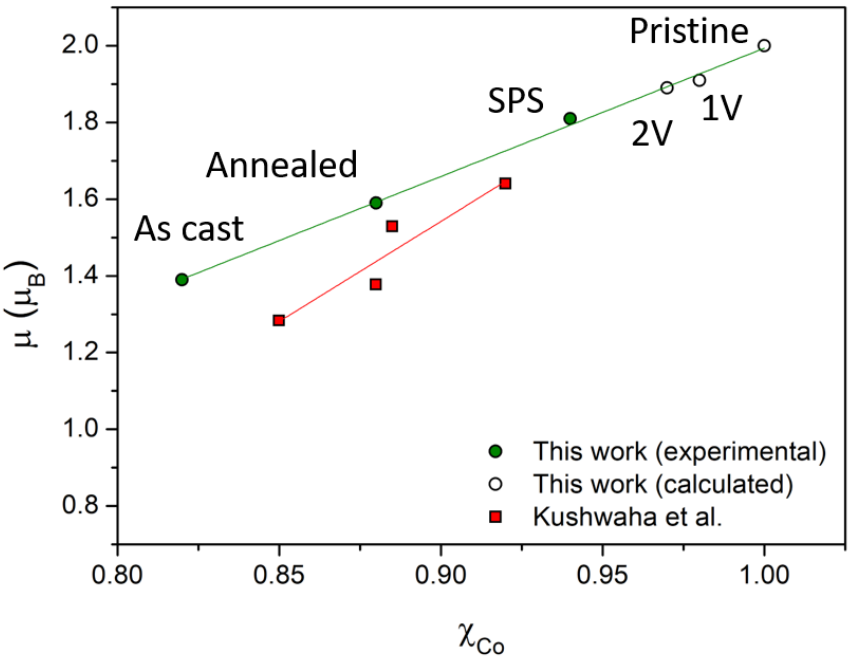

Figure 41: Saturation magnetization as a function of Co-occupancy of the experimentally obtained Co_2ZrSn as cast, annealed, and sintered samples. Literature data are from Ref. [114]. Calculated data will be discussed in Section 8.3.2.

The behavior of magnetization at low temperatures was found to be accurately fitted by the expression $M_s = M_s(0)(1 - AT^2)$, as shown in Figure 40c. Such a quadratic law holds up to more than 200 K. At the lowest temperatures however, the M/T^2 curve was found to deviate upwards, as shown in the inset of Figure 40(c), making the previous law unsuitable for the description of the magnetization for $T \rightarrow 0$ K. This deviation starts to occur at approximately 58 K. Below such a temperature, the magnetization is instead best fitted by the Bloch law $M_x(T) = M_s(0)\left(1 - BT^{3/2}\right)$, indicating Bloch-type localized magnetism, as shown in Figure 40(d). This result is similar to the one reported previously and is coherent with the trends of electrical conductivities presented in Section 4.4. In fact, as already demonstrated for other Heusler compounds [51,69,94,161], such a crossover from a low-T, Bloch-type localized magnetism to a high-T Stoner-type itinerant magnetism can be linked to a crossover from a half-metallic state (where collective spin-wave excitations predominate) to a conductive ferromagnetic state (where the decay of magnetization is caused also by spin fluctuations), as already discussed for low-T electrical resistivity. The crossover temperature of 58 K determined here is also coherent with the one of 64 K independently assessed by the resistivity measurements.

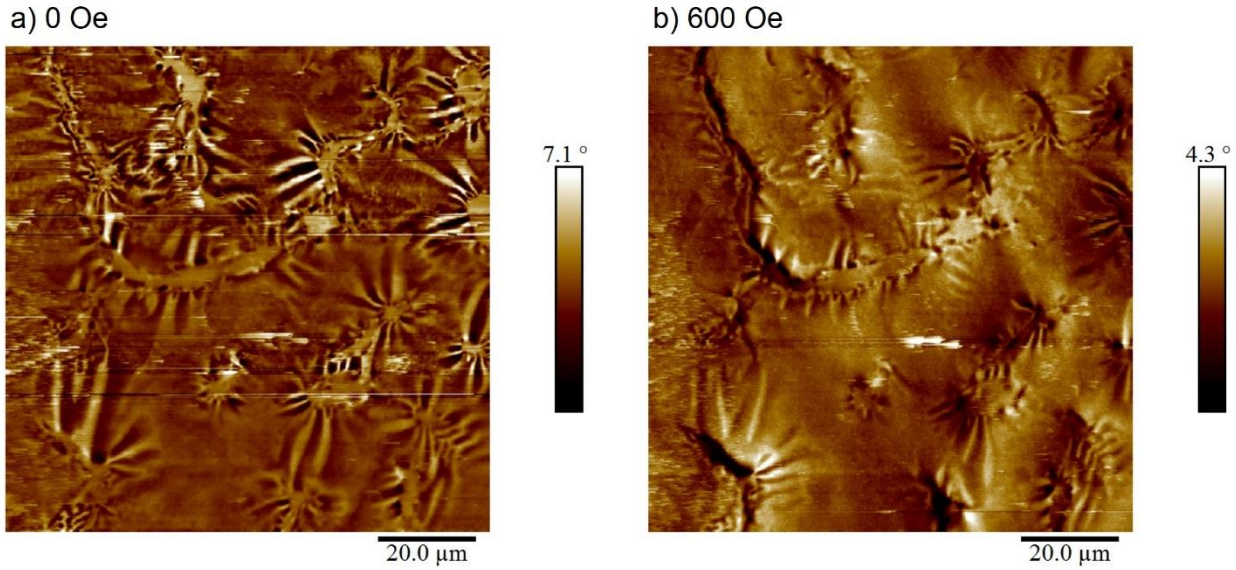

Figure 42: Magnetic force microscopy images of annealed Co_2ZrSn at an external field of (a) 0 Oe, and (b) 600 Oe.

The domain structure of the annealed sample was studied by magnetic force microscopy (MFM), as shown in Figure 42. In zero field conditions, peculiar domain structures are formed in proximity of the Co_3Sn_2 inclusions. The same structures are observed at 600 Oe; however, the alignment of the magnetic domains as a consequence of the introduction of the external field reduces the observed contrast. Such images corroborate the results indicating a weak ferromagnetic behavior at room temperature, also showing that defects like grain boundaries and secondary phase inclusion play a prominent role in determining the magnetic properties. Such particular stripes-shaped pattern of magnetic domains has size of approximately 20 µm, which is comparable with those of secondary phase crystals. This result emphasizes once more the importance of obtaining single-phase and nearly defect less samples, encouraging the rapid-solidification processing route.

7.6 Conclusions

In this chapter, the effect of the Co vacancy defect on the structural, transport, and magnetic properties Co_2ZrSn have been extensively discussed. Samples with various concentrations of defects were obtained by different processing methods (arc melting, annealing, melt spinning, SPS), each involving diverse cooling rate and thermal treatments. Such samples were characterized by XRD followed by accurate Rietveld analysis of the measured patterns, allowing to quantify the number of vacancies in every specimen by fitting the Co-site occupancy in the structure. The degree of structural disorder in the Co sub-lattice was independently estimated by measuring the areas of the 200 and 220 reflections, leading to a trend which is coherent with that obtained with the Rietveld refinement. Overall, the lattice parameter was found to linearly decrease with the increasing of Co vacancy concentration, as well as the order of the Co sub-lattice. The effect of processing on the microstructure was evaluated by SEM-EDS and EBSD analysis. Rapid solidification with subsequent sintering was found to be the most effective route in refining the microstructure as well as in minimizing the vacancy concentration and, consequently, enlarging the stability field of the Heusler phase. This allowed the preparation of samples with an amount of secondary phases below the XRD detection limit.

The Seebeck coefficients were found to follow the trend of Co occupancy, with the specimens with higher χ_{Co} presenting the highest values of S. The electrical conductivity was found to depend both on vacancy concentration and grain boundary concentration. Grain boundary scattering is dominant at lower temperature, while at higher temperature the role of occupancy and point defects prevails. The low-T resistivity showed a change of regime in proximity of 50-70 K. Below such temperature, a $R \propto T^2$ trend was measured for all the samples; whereas, at higher T, a T^x ($1 < x < 5/3$) proportionality of R is reported. In Co-based Heusler compounds, this behaviour was found to be linked to a crossover from a low-T half-metallicity to a high-T

conductive ferromagnetic state, as the spin-flip electron diffusion is hindered by the half-metallic gap at low temperatures. The Hall resistivity and charge carrier concentration were also measured, giving values of the order of 10^{-10} m^3/C and 10^{28} m^{-3}, respectively, that are typical of conductive metallic materials. As expected, the absolute values of S show an inverse proportionality with respect to the carrier concentration The thermal conductivity and the thermoelectric figure of merit zT were experimentally quantified for the various samples. The first was found to be sensitive to microstructure refinement. The second revealed to be mainly sensitive to Co-site occupancy, as the least defective (and highest ordered) samples presented progressively higher zT. The values of the magnetic moment showed a linear dependency on χ_{Co}. A crossover from a low T half-metallic to a high T conductive state was found by measuring the magnetization as a function of temperature. As already reported in previous studies for similar Heusler alloys [51,69], this is the result of spin-flip fluctuations being impossible in systems where half-metallicity is present. The crossover temperature was found to be consistent with those obtained by the measurement of electrical conductivities.

8. The half-metallic, electronic, magnetic, transport, phonon, and thermal properties of pristine and defective Co_2ZrSn and Co_2HfSn compounds studied by ab-initio calculations

In this chapter, several properties of Co_2ZrSn and Co_2HfSn alloys will be investigated by ab-initio calculations with the aim of rationalizing and organizing the experimental results in a coherent and consistent framework.

The electronic structure, transport, and thermal properties of the pristine compounds will be calculated. The electronic density of states and band structures will be analyzed using two different functionals to determine the effect of computational parameters on the results. It will be shown that both the alloys are half-metallic ferromagnets at absolute zero, in which nevertheless the Fermi level lies quite close to the edge of the conduction band. The transport properties resulted in quite good agreement with the experimental values, suggesting that the electronic structure of actual samples is potentially rather similar to those calculated. The phonon density of states (pDOS) and thermal properties were simulated in the harmonic approximation. These results will be used in the framework of the Slack model [177] to estimate di lattice thermal conductivity k_{lat}.

The density of states of defective Co_2ZrSn and Co_2HfSn supercells will be also calculated to estimate the effect of various point defects on their half-metallic properties. Being the DOS at the Fermi level predominantly determined by Co atoms, the effort will be focus on defects involving the Co site. Co vacancy will be found to have the lowest formation energy among all defects, presumably being the most abundant in real specimens. Such defect, despite being responsible for a significant lowering of the magnetic moment, was not found to introduce levels inside the half-metallic band gap of both alloys, ultimately preserving their half-metallicity if present in sufficiently diluted concentrations.

8.1 Computational details

Ab-initio calculations were performed using Vienna Ab Initio Simulation Package (VASP) [163] with projector augmented plane (PAW) method [129], Perdew-Burke-Ernzhof (PBE) [127] and Perdew-Burke-Ernzhof optimized for solids (PBEsol) [178] functionals with Co, Hf_pv, Sn_d potentials [179]. Single cells with 15x15x15 and 24x24x24 Monkhorst-pack k-points meshes were used for ionic relaxation cycles and single-point energy calculations, respectively, for the calculation of the electronic structures of pristine compounds. For the calculation of transport properties, the post-processing was performed with the BoltZTraP2 code [131]. A 2x2x2 supercell (128 atoms in total) sampled with a 7x7x7 Monkhorst-pack [180] k-point grid was used for both the vacancy simulations and phonon calculations. In the first case, one and two Co atoms were removed from the core of the supercell, bringing the system to a total of 127 and 126 atoms, respectively. The phonon calculations were performed on a pristine supercell. The post-processing data treatment for the calculations of phonon and thermal properties were performed in the harmonic approximation with the Phonopy code [130]. The energy cutoff was always set at 500 eV. Gaussian and tetrahedron type smearing were respectively used for ionic relaxation cycles and single-point energy calculations.

8.2 Pristine Co_2HfSn and Co_2ZrSn compounds

The study of the pristine cells is aimed to set a baseline for the interpretation of experimental results. By comparing measured values with data obtained for the ideal alloys, the magnitude of the deviation of real samples from the perfectly ordered case can be deduced. The use of two slightly different functionals is aimed to better understand whether such variations are due to actual physical effects, or to intrinsic errors due to the computational method.

8.2.1 Electronic and magnetic properties

The total energy of the calculated cubic unit cell as a function of the lattice parameter is reported in Figure 43 for both compounds. Minimum energy values are reached for lattice parameters of 6.2498 Å and 6.1641 Å for Co_2HfSn with PBE and PBEsol, respectively, while 6.2843 Å and 6.2029 Å are obtained for Co_2ZrSn with

PBE and PBEsol, respectively. Experimental lattice parameters of 6.2157 Å for Co_2HfSn and 6.2458 Å for Co_2ZrSn, obtained at room temperature as shown in Section 2, are inside the calculated values. Formation energies (ΔE_{form}) per formula unit starting from the constituent elements (α-Co, α-Hf, α-Zr, β-Sn) of -1.60 eV/f.u. and -1.61 eV/f.u. were obtained using PBE functional for Co_2HfSn and Co_2ZrSn, while, for PBEsol, ΔE_{form} values turned out equal to -1.76 eV/f.u. and -1.74 eV/f.u., respectively.

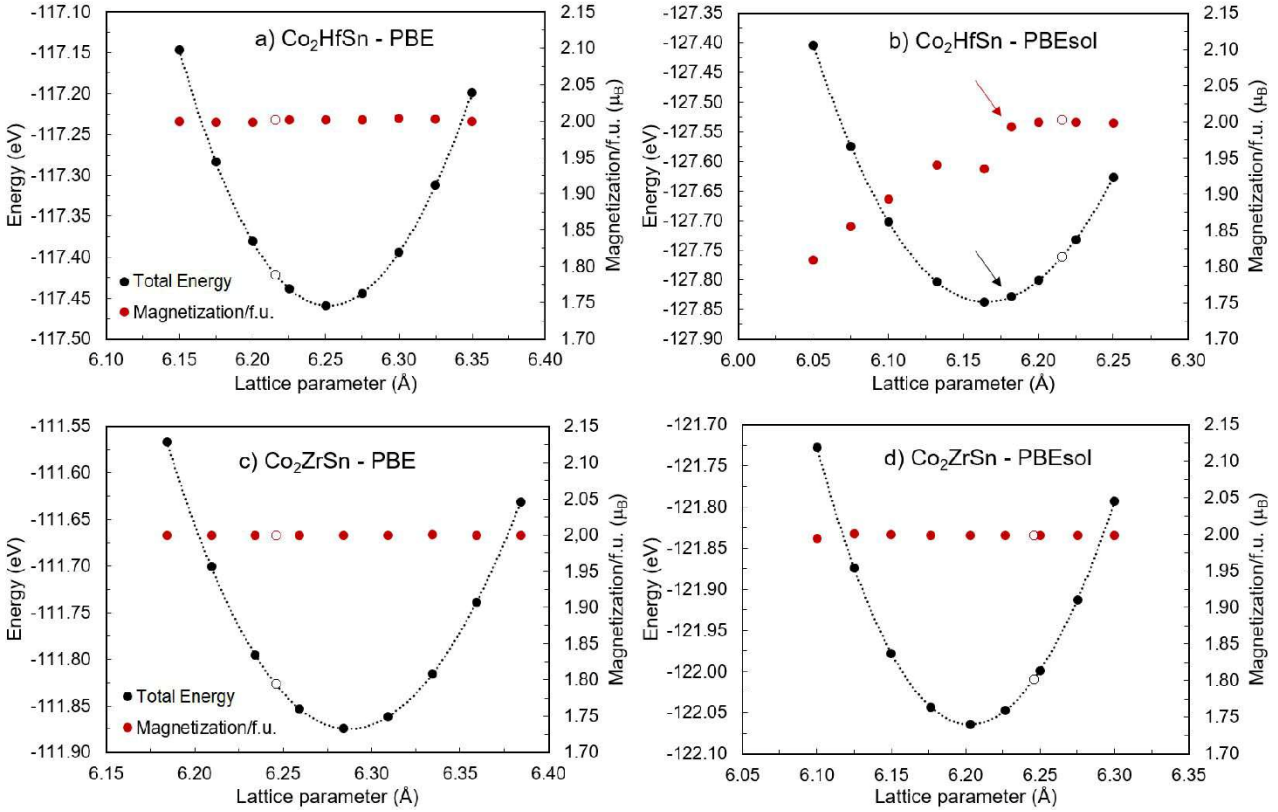

Figure 43: Total energy (black dots) and magnetization per formula unit (red dots) as a function of lattice parameter *a* (each point corresponds to results of a DFT calculation with fixed lattice parameter). a), b) Co_2HfSn computed with PBE and PBEsol, respectively. c), d) Co_2ZrSn computed with PBE and PBEsol, respectively. Empty circles are used for calculations performed imposing experimental lattice parameter values (Section 2). Near-equilibrium cell in Co_2HfSn-PBEsol is highlighted by arrows.

The magnetization per formula unit were also calculated as a function of the lattice parameter and results are also reported in Figure 43. For both alloys and functionals, the magnetization is generally not very sensitive to variations of a. An exception is Co_2HfSn when computed with PBEsol (Figure 43b) in which fluctuations up to 0.20 μ_B are observed within a range of 0.2 Å. In particular, it is notable how magnetization suddenly increases from 1.93 μ_B in the equilibrium cell (which lies at the minimum of the curve) to 2.00 μ_B in a near-equilibrium cell (highlighted by arrows), that has a lattice parameter of 6.1821 Å. Total energies and magnetic moments were also calculated imposing the above mentioned experimental lattice parameters and are indicated with empty circles in Figure 43. All magnetization values per formula unit are close to 2 μ_B.

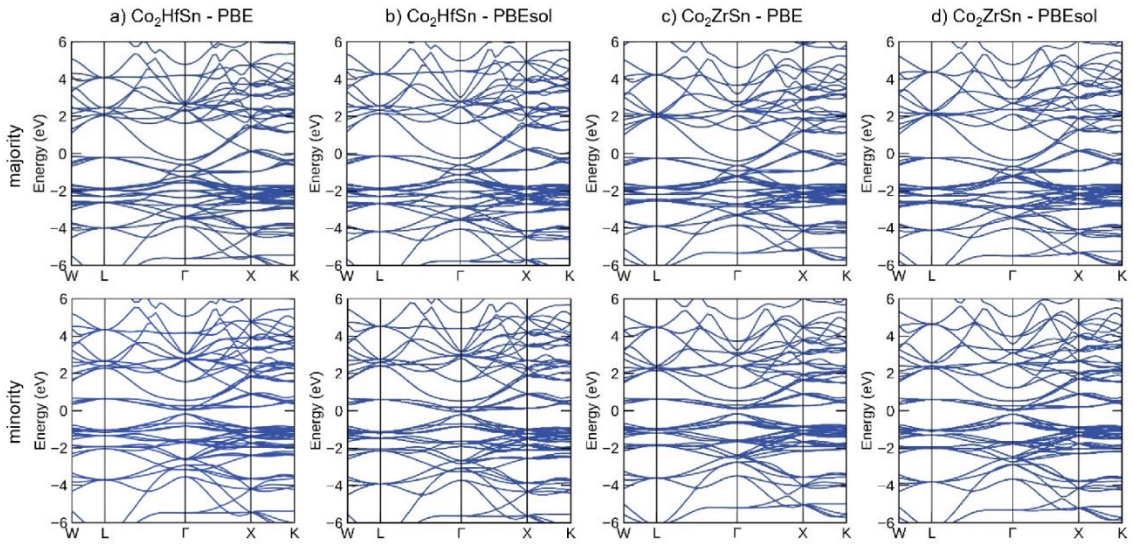

Figure 44: Band structure diagrams of Co_2HfSn alloy calculated with a) PBE, b) PBEsol functionals and Co_2ZrSn alloy with c) PBE, d) PBEsol functionals.

Calculated band structure diagrams are shown in Figure 44. It can be noted that band gaps in the minority sub-bands are direct and centred on the Γ point, while majority spin bands crossing the Fermi level are partially filled. This can be observed even more clearly from density of states diagrams, reported in Figure 45. Comparable profiles were obtained with the two functionals, both for valence and conduction levels, in majority and minority spin sub-bands. As expected for weak itinerant ferromagnets [181], majority and minority sub-bands are approximately specular and slightly shifted relative to each other. Band gaps in the minority spin sub-bands of 0.34 eV and 0.30 eV are observed for Co_2ZrSn when PBE and PBEsol are used, respectively, and the Fermi energy (E_F) is observed inside the gap.

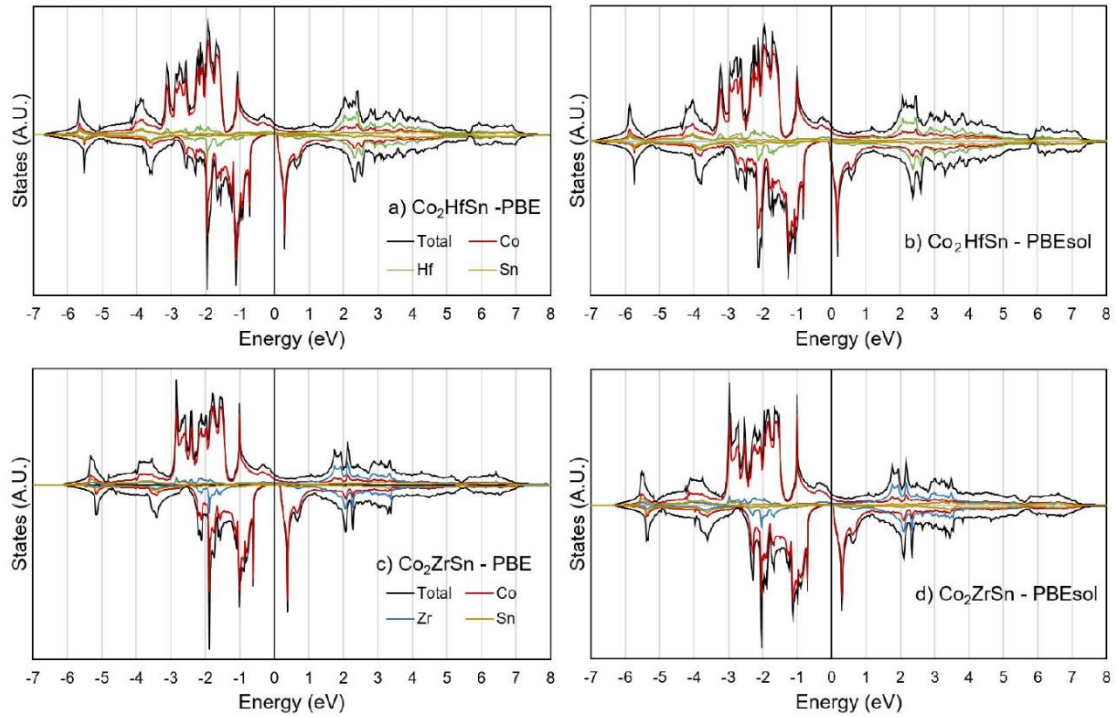

Figure 45: Total and projected density of states diagrams for the fully relaxed structures of Co_2HfSn alloy calculated with a) PBE, b) PBEsol functional and of Co_2ZrSn alloy calculated with c) PBE, d) PBEsol.

In Co_2HfSn, a band gap of 0.30 eV is obtained for PBE calculations and E_F is also observed inside the minority gap; however, when PBEsol functional is used, the Fermi energy is observed slightly outside the band gap for the minority spin sub-band. This implies that at 0 K a few electrons with minority spins have enough energy to be in the conduction band, with consequences on the calculated magnetic properties. The steep slope of the minority DOS near the Fermi energy is also particularly important as minor variations in the position of E_F can significantly change the balance between majority and minority electrons at 0 K.

Values of approximately 2 μ_B (see Figure 43) for the calculated magnetization were found in all cases, apart from Co_2HfSn computed with PBEsol, in which a 1.93 μ_B value was obtained for the fully relaxed cell. Thus, except for this latter case, the alloys are observed to follow the Slater-Pauling rule. Comparing Figure 45a with Figure 45b, and Figure 45c with Figure 45d, it can be noted that the PBEsol functional systematically locates Fermi energy of alloys closer to the conduction band. In Co_2HfSn, the position of the E_F is slightly inside the minority conduction band, causing the above-mentioned deviation from Slater-Pauling rule. The same shift of Fermi level towards the conduction band can be observed in the Co_2ZrSn DOS (Figure 45c and Figure 45d) when comparing PBE and PBEsol results; however, in this case, E_F is always inside the band gap and the resulting magnetization does not change from 2.00 μ_B.

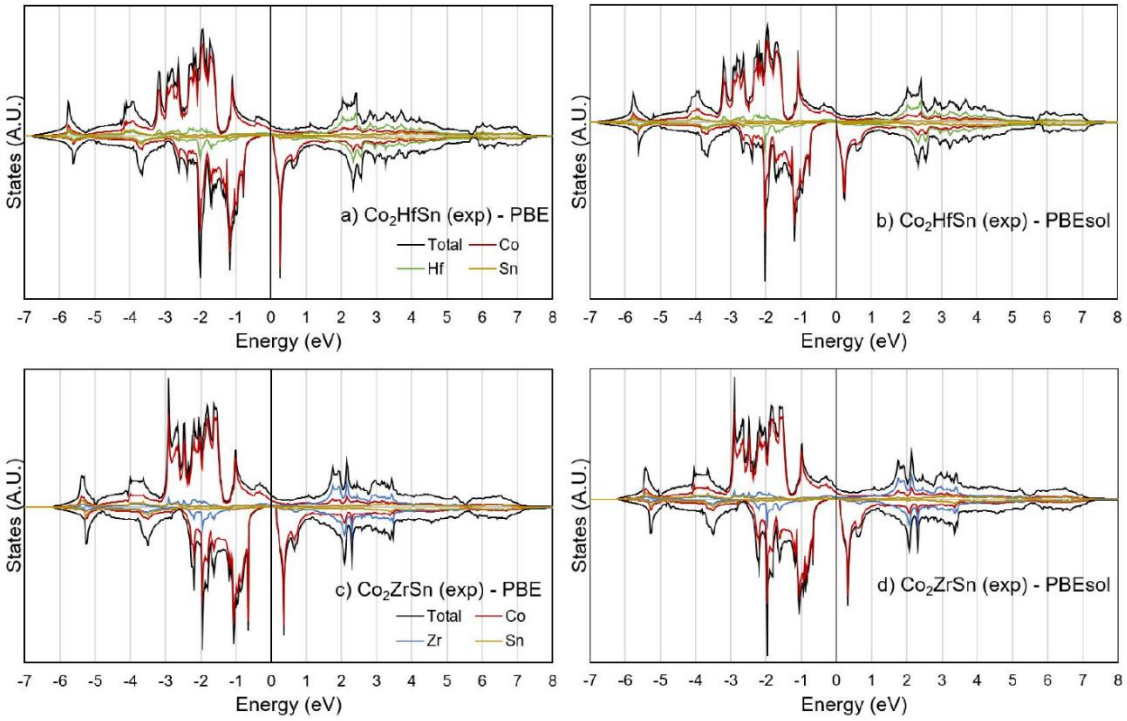

Figure 46: Total and projected density of states diagrams calculated imposing experimentally obtained lattice parameters (Section 2) of Co_2HfSn alloy with a) PBE, b) PBEsol functional and Co_2ZrSn alloy calculated with c) PBE, d) PBEsol.

Furthermore, as it can be noted from Figure 43b, the magnetic moment in the case of Co_2HfSn-PBEsol is also highly sensitive to small lattice parameter variations. In fact, it is noticeable how it rapidly increases up to 2.00 μ_B when increasing a. Increasing the fixed lattice parameter in the calculation also corresponds to a shift of the Fermi energy towards lower energies, i.e. from the conduction band to the gap in the minority sub-band. Hence, the PBEsol results for Co_2HfSn are underestimating the lattice parameter and the magnetic moment, while the position of the Fermi level is overestimated with respect to the minority band gap. This becomes evident considering the DOS diagrams shown in Figure 46 calculated using the previously mentioned experimental lattice parameters (empty circles in Figure 43). In all cases, the calculated DOS does not significantly differ from those reported in Figure 45 as well as calculated magnetic moment values, with the exception of Co_2HfSn-PBEsol (Figure 46b). In this case, Fermi energy is inside the half-metallic band gap in the minority spin sub-

band and, accordingly, magnetic moment value here is 2 μ_B as in the other cases. Band-gap values for Co_2HfSn are here of 0.32 eV and 0.27 eV when calculated with PBE and PBEsol, respectively, while for Co_2ZrSn they are 0.36 eV and 0.30 eV, respectively, with PBE and PBEsol.

Spin-flip energy (E_{flip}), defined as the energy of the limit of minority-spin conduction band subtracted to E_F, is another important parameter that can be used to evaluate half-metallicity. For the equilibrium cells in Co_2ZrSn, E_{flip} are equal to 0.18 eV and 0.08 eV for calculations with PBE and PBEsol functionals, respectively. In Co_2HfSn, E_{flip} is 0.10 eV for PBE, while, for PBEsol, E_F intersects the conduction band 0.08 eV above the highest limit of the band gap. Using experimental lattice parameters, spin-flip energies are for Co_2HfSn respectively of 0.06 eV and 0.01 eV with PBE and PBEsol, while for Co_2ZrSn they are 0.16 eV and 0.12 eV with PBE and PBEsol, respectively. In all cases, Co_2ZrSn compound shows the largest E_{flip}.

As noticeable from projected DOS diagrams (Figure 45 and Figure 46), in all cases, densities of states near Fermi level are dominated by Co contribution. Also, magnetization values are due almost exclusively to Co atoms, as expected. This information suggests that tuning of half-metallic and conductive properties can be effectively achieved acting almost exclusively on Co sites. Simultaneously, this indicates that defects involving Co-sites are potentially the main disruptors of half-metallicity in real samples. Also, since the Fermi level was found to dangerously shift towards the conduction band as the lattice parameter change, *a* can also be considered an important player in achieving effective half-metallic specimens regardless of the Co sublattice's ordering role.

Co_2HfSn					
	E_g (eV)	ΔE_{form}/f.u. (eV)	μ/f.u. (μ_B)	T_C (K)	*a* (Å)
PBE	0.30	-1.60	2.00	-	6.2498
PBEsol	(0.22)	-1.76	1.93	-	6.1641
Exp.	-	-	2.01-2.15 1.50-1.99*	432 430 [53]	6.2157 6.218 [107]
Co_2ZrSn					
	E_g (eV)	ΔE_{form}/f.u. (eV)	μ/f.u. (μ_B)	T_C (K)	*a* (Å)
PBE	0.34	-1.61	2.00	-	6.2843
PBEsol	0.30	-1.74	2.00	-	6.2029
Exp.	-	-	1.80-2.05 1.34-1.81$^{\$}$	454 448 [112]	6.2458 6.249 [107]

Table 7: Band gap (E_g) of the relaxed structures, formation energy (ΔE_{form}) per formula unit, magnetic moment in number of Bohr magnetons per formula unit (μ), Curie temperature (T_C) and cell parameter (*a*) for Co_2HfSn and Co_2ZrSn alloys. Band gap of Co_2HfSn with PBEsol is indicated in brackets because the Fermi energy is not inside the minority band gap. μ values are reported both in the limit of neglected presence of secondary phases, and as they are considered Pauli paramagnets. * Ref [53,80,107,109,110,113]; $^{\$}$ Ref. [80,107–112,148]. Values without reference are this section and Section 2.

A collection of relevant data reported in this study, together with a selection of previously reported results in literature is presented in Table 7. As it can be noticed, calculated data are generally in agreement with experimental values. In all cases, the half-metallic character of the investigated compounds has been confirmed by the present calculations, apart from Co_2HfSn when computed with PBEsol. The reason for this discrepancy has already been discussed and is essentially related to the underestimation of the equilibrium lattice parameter of the unit cell when using this exchange-correlation functional for such system. This is also confirmed by the calculation performed using the experimental lattice parameters in Figure 46.

8.2.2 Transport properties

Building on the VASP output files obtained previously, transport properties were calculated using the BoltzTraP2 code between absolute zero and the Curie temperature. In fact, calculations beyond the Curie transition are not deemed reliable. This is because, at T_C, the compound undergoes a transition from ferromagnetic to paramagnetic, causing the electronic density of states to experience significant and unpredictable shifts (DFT calculations are, by definition, performed at 0 K). A charge carrier concentration of $1.0 \cdot 10^{28}$ m^{-3} for both alloys, consistent with experimental results, was chosen for the simulations.

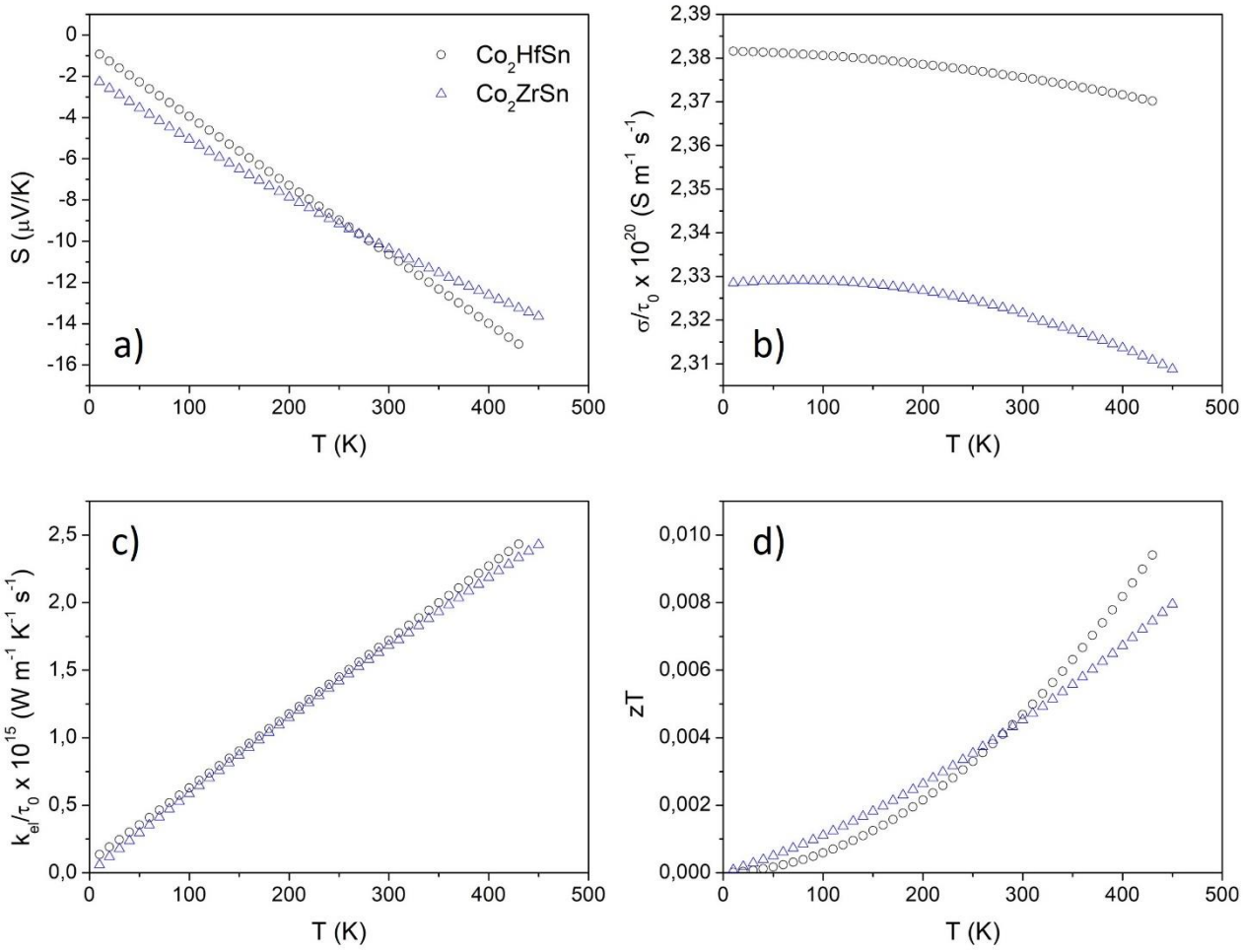

Figure 47: Seebeck coefficient (a), electrical conductivity (b), electronic thermal conductivity (c), figure of merit zT (d) calculated for the pristine Co_2HfSn and Co_2ZrSn. τ_0 is the relaxation time.

The Seebeck coefficient dependency on T are reported in Figure 47a, confirming an n-type behaviour throughout the temperature range, in agreement with the experimental observations. At 300 K, a calculated values of -10.6 μV/K and -10.3 μV/K were obtained respectively for Co_2HfSn and Co_2ZrSn, which are reasonably coherent with the experimental ones (-13.0 μV/K for Co_2HfSn and -9.0 mV/K for Co_2ZrSn). The electrical conductivity, Figure 47b, and the derived electronic contribution to the thermal conductivity, Figure 47c, show temperature dependences similar to those observed experimentally. The figure of merit zT was also calculated, Figure 47d, and it turned out equal to $4.7 \cdot 10^{-3}$ and $4.55 \cdot 10^{-3}$ at 300 K for Co_2HfSn and Co_2ZrSn, respectively. While the first closely matches the experimental value of $3.3 \cdot 10^{-3}$, the latter slightly overestimates the experimental Co_2ZrSn figure of merit which is $0.75 \cdot 10^{-3}$. This can be due to a higher contribution of k_{lat}, which is not taken into consideration in calculations. The Hall resistivity was also computed, obtaining for Co_2HfSn a value of $9.2 \cdot 10^{-10}$ m^3/C at 300 K, which is close to the experimental value of $5.8 \cdot 10^{-10}$ m^3/C. For Co_2ZrSn, the calculated R_H value at 300 K is $5.58 \cdot 10^{-10}$ m^3/C, which agrees with the measured $6.05 \cdot 10^{-10}$ m^3/C

of the annealed sample. Comparing the two alloys, it is possible to note how all the calculated transport properties are both qualitatively and quantitatively similar, effectively showing that the density of states of the two compounds are not deeply different.

Another possible consideration can be made by comparing the calculated and experimental from RT to T_C. As already mentioned, the fundamental principle on which the BoltZTraP2 is built around (the "frozen band" approximation), is based on the assumption that the DOS remains constant (or "frozen") in the entire simulated temperature range. From here, the electrons population in the valence and conduction bands is calculated using the Boltzmann theory, thus deriving the electronic transport properties. As far as the Seebeck coefficient is concerned, not only the experimental trends are linear as well as those computed using BoltZTraP2, but also simulated and measured data are in quantitative agreement as shown before. Considering σ, quantitative comparisons are made difficult by the presence of the relaxation time τ_0, which is difficult to estimate; however, the simulated trends are again in good agreement with the experimental. Insomuch, it can be suggested that the real DOS of such compounds could present a similar behavior of those calculated; namely, their initial half-metallic shape does not dramatically change while raising the temperature.

8.2.3 Phonon and thermal properties

The phonon band structure and density of states of the pristine Co_2HfSn and Co_2ZrSn compounds are reported in Figure 48. Among the 48 total modes, it is possible to note from the phonon dispersion diagram, Figure 48a, that the lowest frequency vibration approach 0 THz at the Γ point. These are acoustic modes, which consist of in-phase oscillation of all atoms and are composed by one longitudinal and two transverse modes. The two transverse modes are degenerate from W to L, and from W to L to Γ. At higher frequencies are located the optical modes, 45 in total, consisting of out-of-phase vibrations of the atoms in the supercell. It is possible to note that in the region between 0 and 3 THz, a significant overlap between the acoustic and optic modes occurs in each investigated k-point except for Γ. This high extent of overlap is present also between optical-optical modes in the higher region of the diagram. Finally, a small band gap of approximately 0.08 THz (for both alloys) separates at 5.10 THz for Co2HfSn and 5.89 THz for Co2ZrSn the set of higher frequency optical modes. In Figure 48c-d, the phonon densities of states (pDOS) are shown. For Co_2HfSn, the low-frequency region (0 to 4 THz) is predominantly governed by Hf-related vibrations, as heavier atoms typically vibrate at lower frequencies. This is followed by Sn-related vibrations between 4 and 5 THz and, lastly, the modes involving Co atoms manifest as expected at high frequencies beyond 5 THz. In Co_2ZrSn, the low frequency vibrations (below 3.8 THz) are instead dominated by the contribution of Sn atoms, while Co atoms are the main contributors in the middle section (from 3.8 to 5.8 THz). The high frequency optical modes above the band gap are formed prevalently by motions of Zr.

The thermal properties derived in the harmonic approximation are reported in Figure 48e-f. The Helmoltz free energies (red circles) decrease with increasing temperature and their values at 0 K are 10.98 kJ/mol and 11.35 kJ/mol for Co_2HfSn and Co_2ZrSn, respectively. The non-null values at 0 K are due to atomic oscillations occurring also at the absolute zero (Zero Point Energy). On the contrary, entropy (blue circles), as expected, increases as a function of T and is zero at 0 K. The heat capacity at constant volume (C_V, green circles) witnesses a sharp ascent with temperature up to approximately 200 K, where a plateau is reached for both alloys. At low temperatures, the C_V's trajectory follows approximately the Debye model, showcasing a T^3 dependence behaviour. With 4 atoms in the alloys' formula unit, the heat capacity limit should be 12R, or 99.8 J/molK. When calculated beyond the Curie point to 1000 K, the C_V is 99.3 J/molK for both alloys, in good agreement with the12R theoretical value and with those in the literature [106]. As reported previously, experimental values of 200.2 J/molK and 159.96 J/molK were obtained as C_P from 300 to 800 K for Co_2HfSn and Co_2ZrSn, respectively. Considering that for incompressible substances with constant density like solids, the heat capacity at constant volume and pressure are approximately the same, there is a notable divergence between the calculated and experimental figures. This discrepancy can be attributed to the harmonic approximation under which the calculations were performed. It is plausible that anharmonic effects, which exceed this approximation, are evident in the sample even at 300 K [182]. Moreover, given that this compound

undergoes a ferromagnetic-paramagnetic transition, it is important to consider magnetic excitations. Such excitations often contribute significantly to the heat capacity around T_C [183] and to the entropy.

In order to estimate the lattice component of the thermal conductivity k_{lat}, a model proposed by Slack [177] has been satisfactorily used for the study of other Heusler compounds [184]. According to this model, the lattice thermal conductivity is given by:

$$k_{lat} = 3.1 \cdot 10^{-6} \frac{M\theta_D \delta}{\gamma^2 n^{2/3} T} \tag{40}$$

where θ_D is the Debye temperature in K, δ is the cubic root of the volume in Å^3, n is the number of atoms in the primitive unit cell, M is the average atomic mass in atomic unit, and γ the Grüneisen parameter.

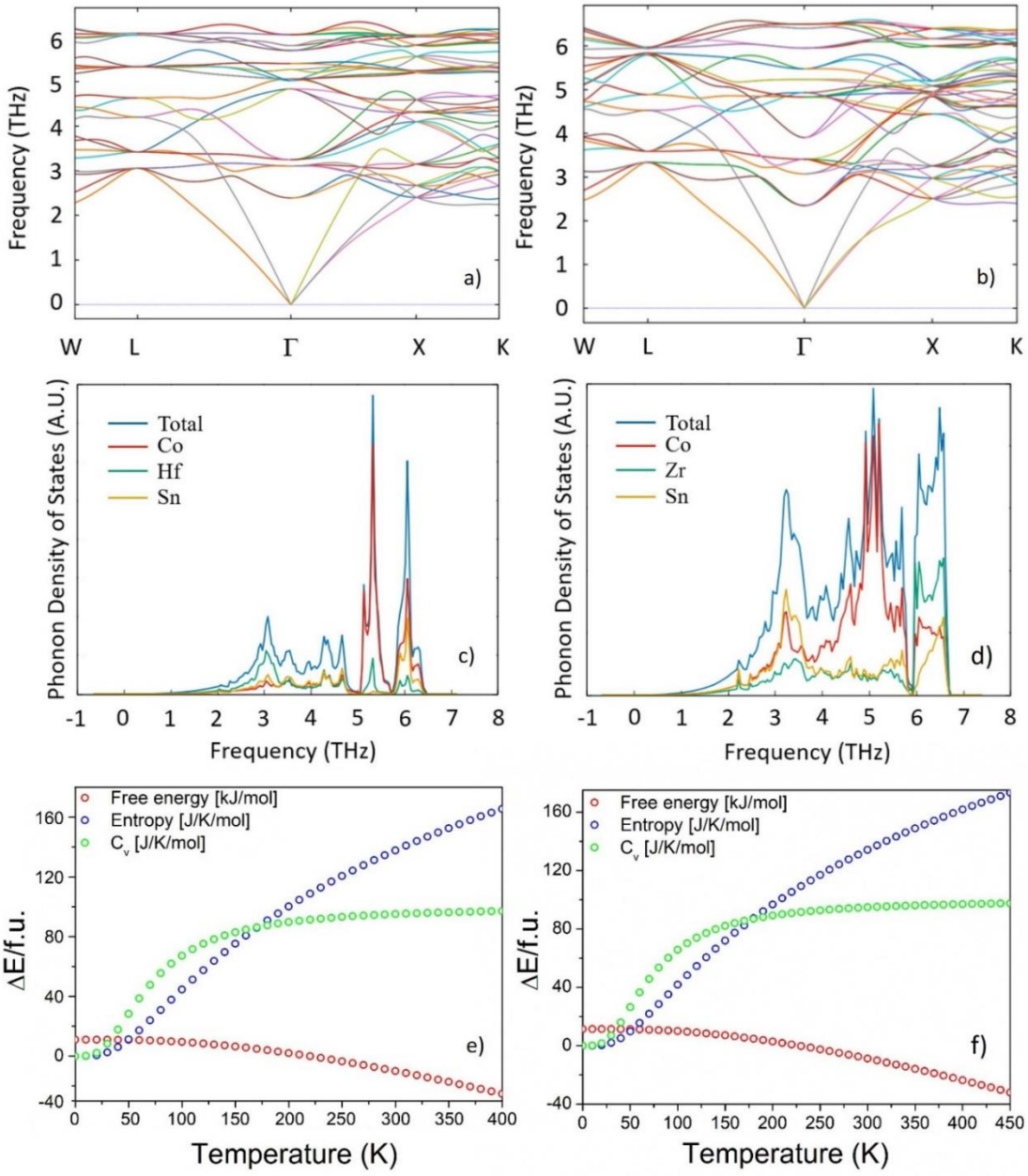

Figure 48: Phonon band structures (each colour corresponds to a different vibrational mode) of (a) Co_2HfSn and (b) Co_2ZrSn; phonon density of states of (c) Co_2HfSn and (d) Co_2ZrSn; thermodynamic properties of (e) Co_2HfSn and (f) Co_2ZrSn as a function of temperature. Each quantity is referred to moles of formula unit.

In Equation 24, θ_D and γ are calculated from the longitudinal and transverse sound velocities, which are derived from the elastic moduli. The longitudinal (ν_L) and transversal (ν_T) propagation velocities inside a material are:

$$\nu_T = \sqrt{\frac{G}{\rho}} \quad ; \quad \nu_L = \sqrt{\frac{B + 4/3G}{\rho}} \tag{41; 42}$$

where ρ is the density, and B, G the bulk and shear moduli, respectively. The average sound wave velocity is then given by:

$$\nu_A = \left[\frac{1}{3}\left(\frac{1}{\nu_L^3} + \frac{2}{\nu_T^3}\right)\right]^{-1/3} \tag{43}$$

The Debye temperature is estimated as follows:

$$\theta_D = \frac{h}{k_B}\left(\frac{3n}{4\pi V}\right)^{1/3} \nu_A \tag{44}$$

Where h and kB are the Planck and Boltzmann constants, n the number of atoms in the unit cell, and V the cell volume. The Grüneisen parameter γ is calculated from the relation proposed by Belomestnykh [185]:

$$\gamma = \frac{9 - 12\left(\frac{\nu_T}{\nu_L}\right)^2}{2 + 4\left(\frac{\nu_T}{\nu_L}\right)^2} \tag{45}$$

Last, the Slack equation for k_{lat} is derived:

$$k_{lat} = 3.1 \cdot 10^{-6} \frac{M\theta_D^3 \delta}{\gamma^2 n^{2/3} T} \tag{46}$$

With δ^3 the volume per atom in Å^3, and M the average atomic number in atomic mass units. The bulk modulus B was determined by fitting the energy-volume curve to the Murnaghan equation of state [186]:

$$E(V) = E_0(V) + \frac{BV}{B'}\left(\frac{(V_0/V)^{B'}}{B' - 1} + 1\right) - \frac{BV_0}{B' - 1} \tag{47}$$

where B' is the derivative of the bulk modulus, V the volume, and V_0 the volume of the fully relaxed cell. The average shear modulus was estimated by Hill [187]:

$$G = \frac{G_V + G_R}{2} \tag{48}$$

with the G_V and G_R the Voigt [188] and Reuss [189] upper and lower bounds, respectively:

$$G_V = \frac{C_{11} - C_{12} + 3C_{44}}{5} \tag{49}$$

$$G_R = \frac{5(C_{11} - C_{12})C_{44}}{4C_{44} + 3(C_{11} - C_{12})} \tag{50}$$

This approach was adopted because there is no exact expression for the polycrystalline average shear modulus in terms of the elastic constants C_{ij}. However, the homogenization scheme proposed in Equation 48 has been found acceptable [186]. The $C_{11} - C_{12}$ difference was obtained by applying of a volume-conserving orthorhombic strain tensor (ε) to the face centered cubic vectors:

$$\varepsilon = \begin{pmatrix} x & 0 & 0 \\ 0 & -x & 0 \\ 0 & 0 & \dfrac{x^2}{1-x^2} \end{pmatrix} \tag{51}$$

where *x* is the distortion parameter for a mechanically stable system, which is an even function of the total energy defined as:

$$\Delta E(x) = \Delta E(-x) = V(C_{11} - C_{12})x^2 + O[x^4] \tag{52}$$

Simultaneously, $C_{44}$was calculated by the application of a volume-conserving monoclinic strain tensor (ε') to the fcc vectors.

$$\varepsilon' = \begin{pmatrix} 0 & x/2 & 0 \\ x/2 & 0 & 0 \\ 0 & 0 & \dfrac{x^2}{4-x^2} \end{pmatrix} \tag{53}$$

In this case, the total energy is related to *x* as follows:

$$\Delta E(x) = \Delta E(-x) = \frac{1}{2} V C_{44} x^2 + O[x^4] \tag{54}$$

According to the Mehl's prescription [190], the distortion parameter *x* was varied between 0 and ± 0.05. Last, the Young's modulus was calculated from B and G:

$$E = \frac{9BG}{3B + G} \tag{55}$$

A summary of the elastic and thermal properties calculated for Co_2HfSn is shown in Table 8. Overall, all the values of the elastic constants and thermal properties are in good agreement with those already available in the literature [106].

	C_{11}-C_{12} (GPa)	C_{44} (GPa)	G_V (GPa)	G_R (GPa)	G (GPa)
Co_2HfSn	118	94	80	76	78
Co_2ZrSn	126	87	78	76	77
	B (GPa)	E (GPa)	θ_D (K)	γ	k_{lat} at 400K (W/mK)
Co_2HfSn	161	201	361	1.72	30.8
Co_2ZrSn	154	197	391	1.69	32.3

Table 8: Calculated elastic constants (C), elastic moduli (B and E), Debye temperature (θ_D), Grüneisen parameter (γ), and lattice thermal conductivity at 400 K (k_{lat}) of Co_2HfSn and Co_2ZrSn.

As it can be noticed from Table 8, the calculated k_{lat} differs significantly from the experimental value reported previously. This discrepancy arises from the assumptions underlying the Slack model. First, when the relative

atomic mass difference of the elements in the alloy exceeds approximately 100%, as in this case, k_{lat} is systematically overestimated by up to an order of magnitude. This has been previously highlighted for other Heusler compounds [184]. Second, the model produces inaccurate results when the acoustic and optical phonon branches overlap, as in the present cases (see Figure 48). This is due to the inability to integrate the acoustic phonon density of states separately from the optical contribution [177]. Third, this model considers only the scattering between acoustic phonons, neglecting all the other scattering phenomena, such as those with impurities, vacancies, dislocations, grain boundaries etc. [177,184]. Last, one important prescription of the Slack model is to evaluate k_{lat} at a temperature sufficiently larger than θ_D [177]. Considering that the paramagnetic transition of Co_2HfSn and Co_2ZrSn occur at approximately 400 K and having the Debye temperatures at 361 K and 391 K, respectively, this request cannot be entirely fulfilled as the elastic moduli were calculated at 0 K in the ferromagnetic state. Setting aside this issue, the k_{lat} values at 700 K are 17.6 W/mK for Co_2HfSn and 16.2 W/mK for Co_2ZrSn, which are considerably closer to the experimental, and comparable with those reported for semiconductive Heusler compounds [184]. Additionally, below T_C one must take into account also magnons' contribution on k_{lat}, which should be more precisely labeled as $k_{lat/mag}$ below the Curie point. Such term makes comparisons between experimental and calculated values not entirely reliable below T_C.

The problem of the overlap between acoustic and optical modes can be partially addressed according to Slack using the derivation of the Debye temperature proposed by Domb and Salter [191]; in fact, one of the main assumptions of the Slack model is that the acoustic modes should be well separated from the optical modes. When this is not possible, as in the present case, the integration of the phonon density of states should be carried out over both the acoustic and optical branches. A solution proposed by Slack is the substitution of θ_D with θ_D'. This quantity was defined by Domb and Salter as [191]:

$$\theta_D' = \frac{h}{k_B}\sqrt{\frac{5\mu_2}{3}} = \frac{h\nu_{MAX}}{k_B}\sqrt{\frac{5I(2)}{3}} \tag{56}$$

where μ_2 and I(2) are the expansion of phonon momentum truncated at the second order, and ν_{MAX} is the maximum frequency of the phonon spectrum defined in terms of force constants. According to Domb and Salter, for the face centered cubic lattice, I(2) can be considered equal to 1/2. This is reported to be still applicable by the authors in case of mixed crystals containing different atoms forming a well-ordered structure. Thus:

$$\theta_D' = \frac{h\nu_{MAX}}{k_B}\sqrt{\frac{5I(2)}{3}} = \frac{h\nu_{MAX}}{k_B}\sqrt{\frac{5}{6}} = 0.9129\frac{h\nu_{MAX}}{k_B} \tag{57}$$

Being ν_{MAX} equal to 6.5 THz for Co_2HfSn and 6.6 THz for Co_2ZrSn (see Figure 48), θ_D' values of 285 K are obtained for both alloys instead of 361 K and 391 K, respectively, calculated with Equation 44. Substituting θ_D' in Equation 40, k_{lat} of 15.1 W/mK and 12.5 W/mK are determined at 400 K for Co_2HfSn and Co_2ZrSn, respectively. If the electronic density of states is considered valid above T_C (as in other studies [106]), at 700 K k_{lat} of 8.6 W/mK and 6.7 W/mK, respectively. This is extremely close to the experimental value shown in Figure 26 and Figure 39.

8.3 Defective Co_2HfSn and Co_2ZrSn compounds

Using 2x2x2 supercells, defective Co_2HfSn and Co_2ZrSn systems were investigated. The nomenclature of such systems is schematically depicted in Figure 49. As suggested by the DOS diagrams, as the density of states at the Fermi level is for both alloys essentially determined by the contribution of Co atoms, the effort was focused on defects involving such site. The effects on the electronic, magnetic, and half-metallic properties of the following defects were analyzed:

- Vacancy: one (1V) and two (2V) Co atoms were removed from a 128 atoms pristine supercell, respectively obtaining the $Co_{1.97}XSn$ (χ_{Co} = 0.984) and $Co_{1.94}XSn$ (χ_{Co} = 0.969) compounds (X = Hf, Zr). For Co_2HfSn only the 1V defect was simulated, while for Co_2ZrSn both 1V and 2V were computed in order to compare the results with the experimental samples.
- Zr/Hf anti-site: the substitution of one Co atom with one of Zr in Co_2ZrSn and one of Hf in Co_2HfSn, respectively leading to Zr anti-site and Hf anti-site defects.
- Sn anti-site: the substitution of one Co atom with one Sn atom.
- Co/Zr swap: in Co_2ZrSn, the mutual position exchange of one Co atom with one of Zr.
- Co/Hf swap: in Co_2HfSn, the mutual position exchange of one Co atom with one of Hf.
- Sn swap: in both alloys, the mutual position exchange of one Co atom with one of Sn.
- Off-stoichiometry: As explained in the previous sections, Co_2HfSn and Co_2ZrSn compounds are experimentally found, in their most stable form (see annealed samples) in composition different from the theoretical 50% Co, 25% Zr/Hf, 25% Sn (at. %) per formula unit. In real samples, the stoichiometry of the Heusler phase is approximately 48% Co, 26% Zr/Hf, 26% Sn. This stoichiometry was recreated in 128-atoms supercells combining an X anti-site (X = Zr in Co_2ZrSn, and X = Hf in Co_2HfSn) and a Sn anti-site defect replacing Co atoms, resulting in an empirical $Co_{62}X_{33}Sn_{33}$ formula unit. The effect of configurational entropy was also considered. A first defect named type 1 was obtained by replacing Co atoms in the (0.375; 0.375; 0.375) and (0.625; 0.625; 0.375) fractional coordinates, which are separated by a relatively close distance equal to $\frac{1}{4}a\sqrt{3}$. Type 2 was instead obtained by replacing Co atoms located in the (0.125; 0.125; 0.875) and (0.625; 0.625; 0.375) sites, being separated by a farther $\frac{1}{2}a\sqrt{3}$ distance.

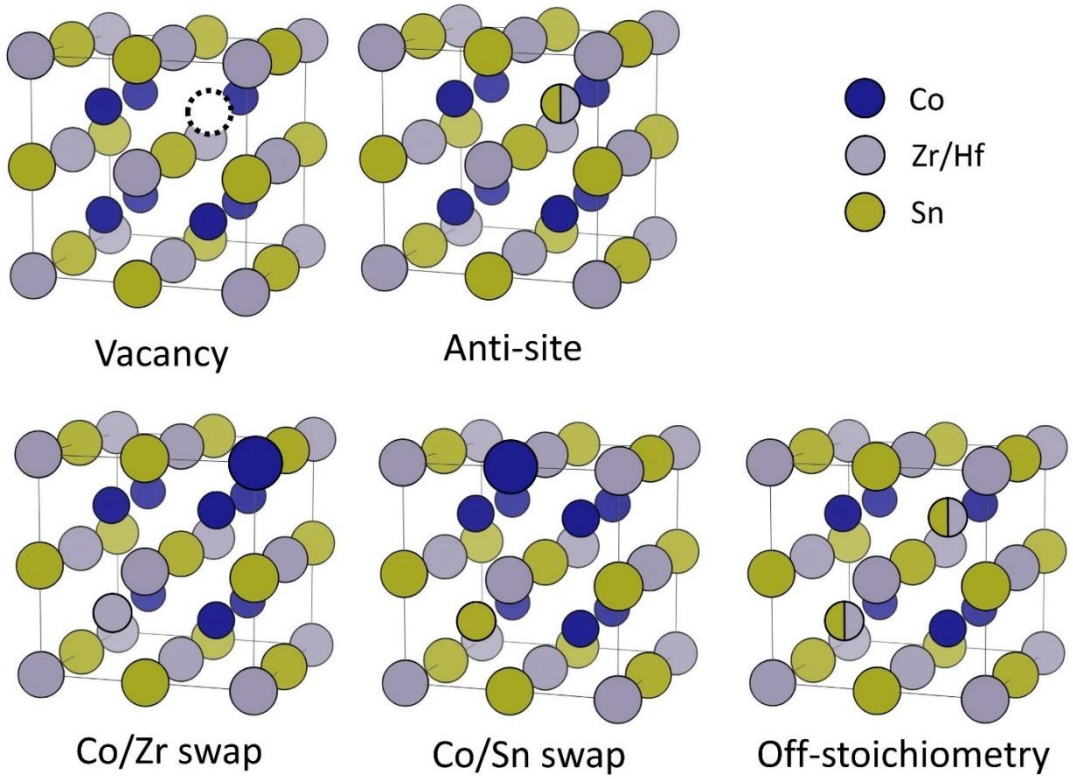

Figure 49: Schematic depiction of the investigated defective Co_2HfSn and Co_2ZrSn systems. The illustrated concentration of defects inside the cells is not indicative of those simulated and are to be taken only as qualitative.

A summary of the lattice parameters, band gaps, spin-flip energies, magnetic moments, and formation energies of the investigated defects is presented in Table 9. It is possible to note that the lowest formation energy was

found for vacancy defects, which formation is endothermic by only 11 equivalent K. It is also the defect which lead to the most significant reduction of magnetic moment. The off-stoichiometry defects are, on the other hand, more endothermic for both alloys; nevertheless, their effect on the magnetic properties is equally dramatic. Being the vacancy and the off stoichiometry the only directly experimentally observed defects, the effort will be focused prevalently on these systems. A review on the effect of all the other defects on the electronic properties of Co_2HfSn and Co_2ZrSn is shown in Appendix B.

Co_2HfSn					
System	*a* (Å)	E_G (eV)	E_{flip} (eV)	μ/f.u. (μ_B)	ΔE_{form} (eV)
Pristine	6.251	0.32	0.084	2.00	-
1V	6.245	0.31	0.084	1.91	0.004
Hf anti-site	6.266	0.34	0.063	2.03	0.074
Sn anti-site	6.268	0.06	0.041	1.97	0.097
Co/Hf swap	6.257	0.27	0.050	2.00	0.107
Co/Sn swap	6.260	0.26	0.023	2.00	0.108
Type 1	6.283	0.14	0.030	2.00	0.171
Type 2	6.283	-	-	1.86	0.175
Co_2ZrSn					
System	*a* (Å)	E_G (eV)	E_{flip} (eV)	μ/f.u. (μ_B)	ΔE_{form} (eV)
Pristine	6.287	0.37	0.181	2.00	-
1V	6.280	0.35	0.181	1.91	0.001
2V	6.274	0.33	0.180	1.89	0.001
Zr anti-site	6.302	0.33	0.084	2.03	0.060
Sn anti-site	6.303	-	-	2.03	0.083
Co/Zr swap	6.294	-	-	1.89	0.112
Co/Sn swap	6.294	0.28	0.120	2.00	0.105
Type 1	6.318	0.11	0.100	2.00	0.150
Type 2	6.318	-	-	1.87	0.149

Table 9: Collection on computed data on defective Co_2HfSn and Co_2ZrSn systems. Formation energies are calculated with respect to the pristine compounds.

8.3.1 Defective Co_2HfSn

A single Co-vacancy defect was introduced in a 128-atoms pristine supercell, resulting in a $Co_{1.97}HfSn$ (χ_{Co} = 0.984) total formula unit. The density of states and band structures of such defect (named 1V) is shown in Figure 50. Comparing Figure 45 and Figure 50, it can be seen that the introduction of the vacancy did not significantly affect the overall shape of the electronic DOS, effectively not leading to a loss of half-metallicity. The most significant effect is however on the magnetic moment; in fact, the removal of one Co atom led to a change from a magnetic moment of 2.00 μ_B in the pristine compound to a value of 1.91 μ_B in 1V. Although no levels were introduced inside the band gap, ultimately leaving the half-metallicity unaltered, a reduction was observed from a E_G of 0.32 eV (pristine) to 0.31 eV (1V). The spin-flip energy remained the same, 0.084 eV, indicating that it is the valence band to shift towards the Fermi level. A small formation energy of 0.004 eV, equivalent to 46.4 K, was calculated, which is also the lowest ΔE_{form} of all defects in Co_2HfSn. This indicates

that the vacancy defect is very likely to be present in real samples. Overall, it is important to note that the reduction of magnetic moment is not straightforwardly associated with a loss of half-metallicity, suggesting that the Slater-Pauling rule must be verified from case to case and not to be taken as a *a priori* way to estimate the half-metallic nature of experimental specimens.

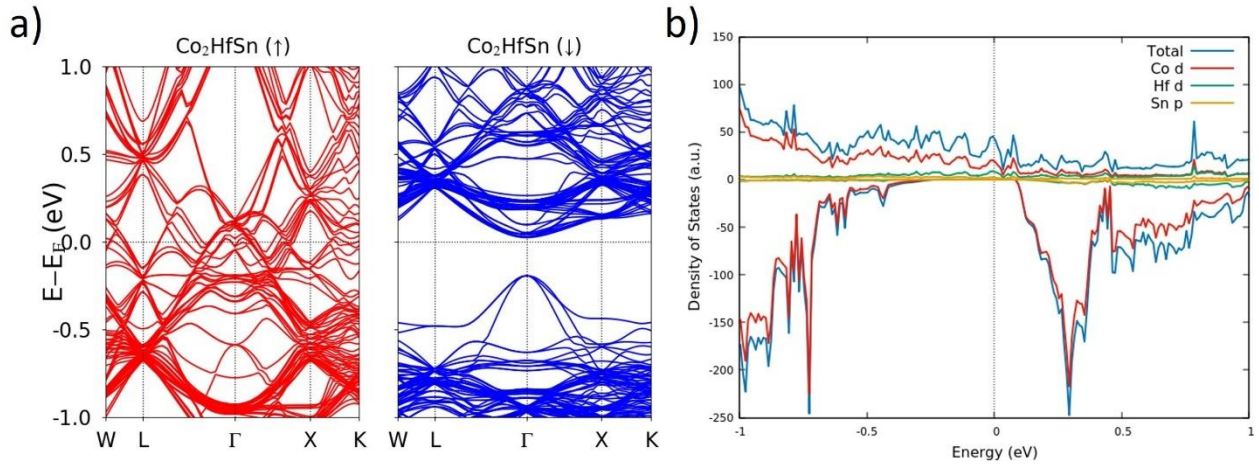

Figure 50: Band structure (a) and density of states diagram (b) of Co_2HfSn 1V defect.

The band structure and density of states of the off-stoichiometry type 1 and type 2 defects are shown in Figure 51. It is immediately noticeable how both defects introduce levels in the minority spin band gap, presenting a large risk for the pursue of half-metallic samples.

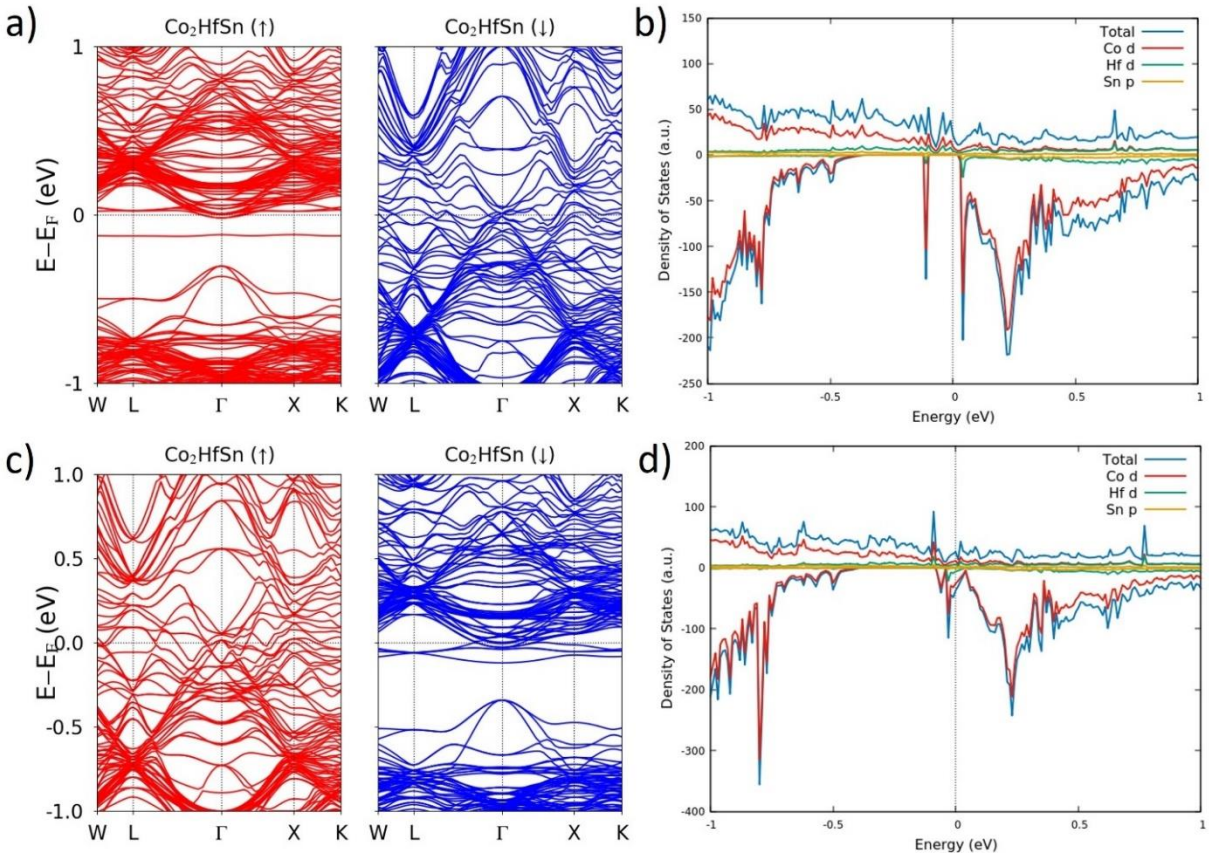

Figure 51: Band structure (a,c) and DOS diagram (b,d) of type 1 and type 2, respectively, defects in Co_2HfSn.

In the type 1 defect, Figure 51a-b, a single energy level is introduced slightly under E_F, reducing E_G down to 0.14 eV and E_{flip} to 0.030 eV. The magnetic moment was calculated to be still 2.00 μ_B.

On the other hand, type 2 introduces a way denser cluster of energy levels located exactly on the Fermi level, effectively destroying the half-metallicity of Co_2HfSn. The spin polarization is reduced from the 100% of the pristine system to a 18.1%. The magnetic moment is also reduced to 1.86 μ_B. As far as formation energies are concerned, both defects have similar ΔE_{form} of 0.171 eV and 0.175 eV for types 1 and 2, respectively. It should be considered that these two systems differ only for the distance of substituted atoms, with type 1 being the close-substituted and type 2 the far-substituted configuration. In real samples, it is highly likely that those defects would be simultaneously present, together with other entropic configurations which were not taken into account here. The extremely similar formation energies effectively encourage such concern.

Summarizing, two main conclusions can be deduced from these calculations on Co_2HfSn. First, it is to be remarked that not all defects lead to a loss of half-metallicity, even if they induce a reduction of the magnetic moment. In fact, although the removal one Co atom effectively led to a reduction of μ, no levels were introduced inside the band gap, with only a slight reduction of E_G being observed. Second, other defects (or the sum of many different types) cause instead the half-metallicity to be disrupted, consequently introducing dense clusters of energy levels in proximity or in correspondence of the Fermi level. This evidence strongly indicates that achieving samples with high degree of crystalline order is crucial for the pursue of good half-metallic properties.

8.3.2 Defective Co_2ZrSn

Having experimental evidence of a linear trend of magnetic moment as a function of χ_{Co}, two different concentrations of the Co vacancy defect were investigated.

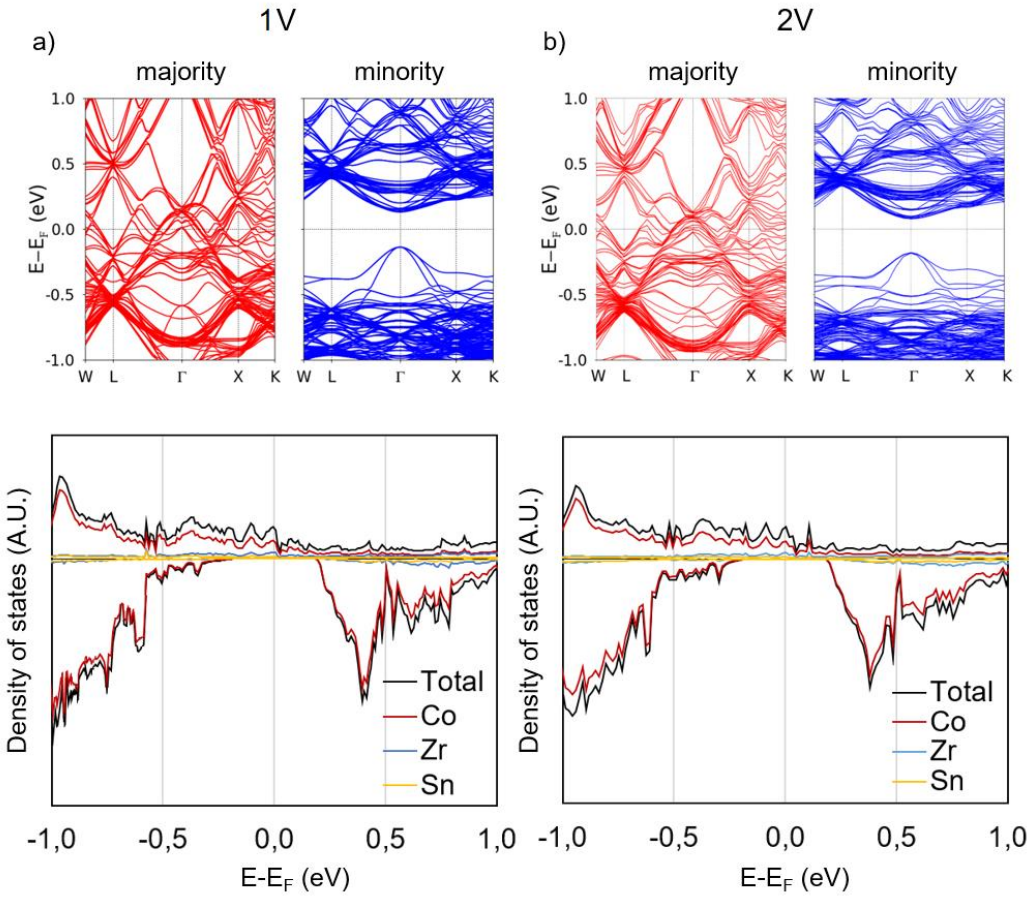

Figure 52: Band structure and density of states in proximity of the Fermi level of 1V (a) and 2V systems (b).

From a 128-atoms supercell, one and two Co atoms were removed obtaining the 1V and 2V systems, which have $Co_{1.97}ZrSn$ (χ_{Co} = 0.984) and $Co_{1.94}ZrSn$ (χ_{Co} = 0.969) formula unit, respectively. The band structure and DOS of 1V and 2V are shown in Figure 52. In both cases, ΔE_{form} is endothermic by only 0.001 eV, which correspond to a temperature of approximately 11 K. Hence, Co vacancy is predicted to be an extremely likely defect also in Co_2ZrSn, as already at 11 K the defect is thermodynamically stable. Being the effective stoichiometry of the 1V and 2V systems extremely similar, their formation energies were also found to be approximately the same with respect to the pristine compound. Figure 52, showing the band structure and DOS of the 1V and 2V defective structures, reveals that the progressive introduction of vacancies, at least for the concentrations considered here, does not cause the appearance of energy states inside the minority-spin band gap, conserving the half-metallicity of the system. At the same time, the calculated band gap energies progressively decrease (0.35 eV for $Co_{1.97}ZrSn$, 1V, and 0.33 eV for $Co_{1.94}ZrSn$, 2V) as the concentration of vacancies inside the supercell grows. Interestingly, E_{flip} remained constant at 0.18 eV for both the defective supercell, showing the same value of the pristine compound. This suggests that in defective systems it is the valence band which shifts towards the Fermi level, while the conduction band remains at the same distance from E_F as in the pristine material. The decrease of the band gap energy when increasing the vacancy concentration agrees with the corresponding decrease of the Seebeck coefficient and increase of the carrier concentration observed experimentally.

	Pristine	1V	2V	SPS	Annealed	As cast
a (Å)	6.287	6.280	6.274	6.3028	6.2448	6.2225
χ_{Co}	1.00	0.98	0.97	0.94	0.88	0.82
μ (μ_B)	2.00	1.91	1.89	1.81	1.59	1.39

Table 10: Calculated and measured properties of various Co_2ZrSn systems.

In Table 10, the values of lattice parameters, Co occupancy, and magnetic moment of all the studied systems (both calculated and experimental) are collected. The mutual relationships between such quantities are reported in Figure 53. The dependency of the lattice parameter from χ_{Co} and μ is linear for both the simulated and measured systems. Such two trends are in qualitative agreement; however, they do not quantitatively match, as the results of calculations is highly dependent on the initial parameters (cutoff energy, convergence algorithm, k-points grid etc.), functional (PBE, PBEsol, Hartee-Fock, hybrids, etc.) and methodology (PAW, LAPW, Thomas-Fermi etc.). The observed trend can be also due to the lattice thermal expansion, as experimental *a* are collected at RT, while those calculated are to be referred at absolute zero. Also, the presence of other defect involving the octahedral sites is not to be excluded in polycrystalline samples. Interestingly, our calculated data are in optimal agreement with the trend defined by single crystal measurements in the literature [114]. This is plausible as DFT calculations are performed on infinite crystals; thus, experimental data obtained from single crystal measurements represent more closely the ideal conditions used in ab-initio simulations. The same considerations can be stated observing the trend of μ as a function of *a* in Figure 53b. Also in this case, the calculated values are in quantitative agreement with those reported from single crystal measurements. Polycrystalline samples analyzed in our work are also agree quantitatively in case of the as-cast and annealed specimens, while the SPS sample slightly deviates from the trend defined by the literature. The reason behind such discrepancy are difficult to assess; however, one can speculate on the fact that the SPS sample, as highlighted in Figure 36, have grain boundary density extremely higher than the other two, being also microstructurally extremely far from a single crystal. Most importantly, the trend of magnetic moment as a function of Co occupancy is the same for experimental and calculated Co_2ZrSn. In fact, values of μ of both synthesized specimens and simulated systems are fitted by the same linear regression as depicted in Figure 53c. Such quantitative agreement allows us to make the following considerations:

- The selected set of computational parameters is highly reliable in estimating the magnetic properties of the Co_2ZrSn compound as a function of Co occupancy.

- In real samples, the magnetic moment is almost exclusively located on Co atoms as predicted by computations.
- Co vacancies are responsible for a linear decrease of the magnetic moment as a function of their concentration in the system. From simulations, this do not coincide with a loss of half-metallicity. The strong agreement between computed and measured values strongly suggest that this is the case also in actual samples.

Such linear trend overall agrees with those reported by Kushwaha et al. [114] both for single crystals and polycrystalline Co_2ZrSn. The change in the DOS of real alloys as a function of temperature is difficultly deducible from DFT calculation, which are performed at 0 K; nevertheless, the experimental evidence of low-T scattering mechanisms compatible with half-metallic systems and the rather good agreement with simulations strongly support the indication of half-metallicity, which is however highly susceptible to defects and lattice disorder.

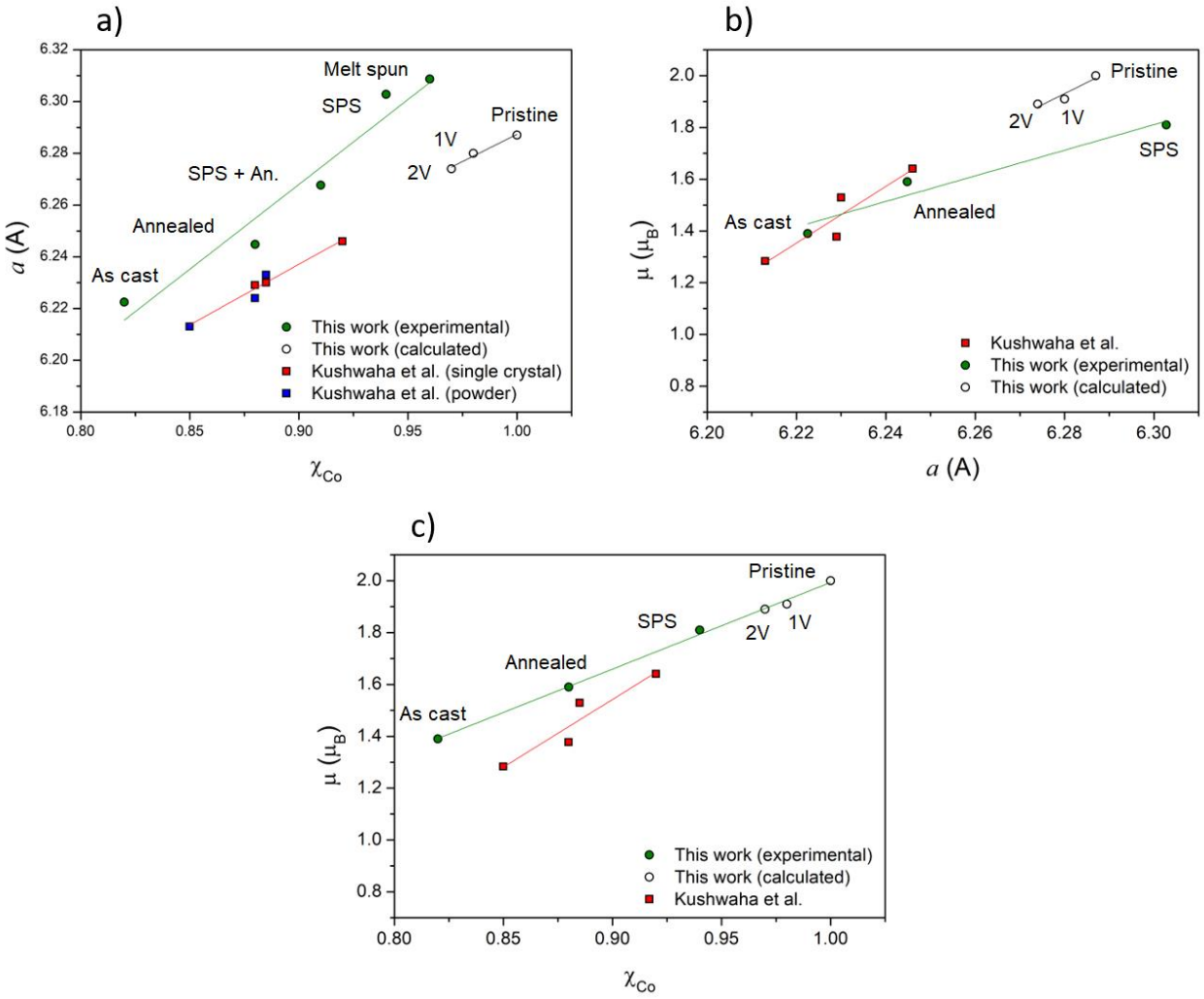

Figure 53: lattice parameter as a function of χ_{Co} (a) and μ (b), and magnetic moment as a function of χ_{Co} (c) for calculated and experimental Co_2ZrSn systems. Literature data are from Ref. [114].

The band structure and DOS of off-stoichiometry defects in Co_2ZrSn are reported in Figure 54. Comparing Figure 51 and Figure 54, it is possible to note the similarity between Co_2ZrSn and Co_2HfSn systems. Type 1 defect is in fact seen to introduce a single state in the minority-spin band gap also in Co_2ZrSn, leading to a significant reduction of E_G from 0.37 eV (pristine) to 0.11 eV. As in Co_2HfSn, the magnetic moment remains at 2.00 μ_B since the emerging energy level is not perfectly superimposed with E_F. Type 2 defect is on the other hand calculated to introduce a denser group of allowed energy levels in correspondence of the Fermi level,

leading to the disappearance of the half-metallic band gap. The magnetic moment is in this case reduced to 1.87 μ_B. Spin-polarization is in this case reduced from the 100% of the pristine system to a 78.4%, which is way higher than the 18.4% of the type 2 in Co_2HfSn. As far as the formation energies are concerned, type 1 and type 2 have similar ΔE_{form} of 0.150 eV and 0.149 eV, respectively. This indicated that off-stoichiometry defects are likely to form independently from their configuration, suggesting that in real samples it is likely to expect combinations of diverse defects.

From Table 9 it is also possible to observe that the defect formation energies of such multiple defects are similar to the sum of the ΔE_{form} of the respective single defects (X anti-site and Sn anti-site). For Co_2HfSn and Co_2ZrSn respectively, the sum is 0.171 eV and 0.143 eV, compared to the calculated values of 0.171-0.175 eV and 0.149-0.150 eV. It shows that forming multiple defects needs the same energy as forming their constituent single defects separately.

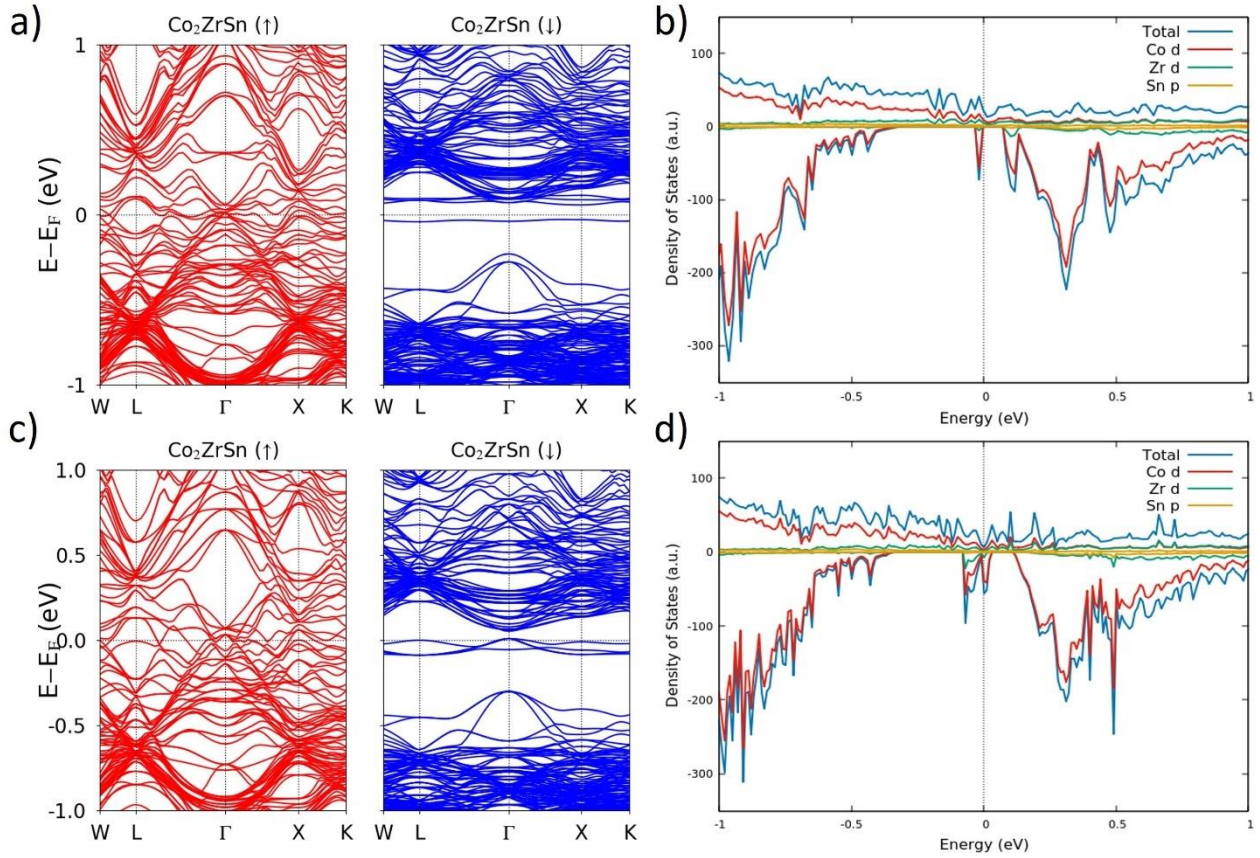

Figure 54: Band structure (a,c) and DOS diagram (b,d) of type 1 and type 2, respectively, defects in Co_2ZrSn.

8.4 Conclusions

The pristine and defective Co_2HfSn and Co_2ZrSn were investigated by DFT calculations. The pristine systems were found to be half-metallic with a magnetic moment of 2.00 μ_B. The use of two different functionals allowed to estimate the numerical reliability of the calculations. The Co_2HfSn compound was found to be not half-metallic when simulated with the PBEsol functional. This was demonstrated to be the result of a rather strong dependency of the Fermi level on the lattice parameter of the considered functional, suggesting that in such systems the conduction band is quite close to E_F. This is also confirmed by the rather small spin-flip energies. When the DOS were calculated imposing the experimentally observed lattice parameters, both compounds were found to be half-metallic. The transport properties were found in agreement with the experimental values. Seebeck coefficient at 300 K quantitatively agrees with measurements, and the trends of the electrical conductivity and k_{el} are correctly reproduced as well. The phonon band structure and density of states indicated a strong overlap between acoustic and optical modes. This made the estimation of k_{lat} based on the Slack's

formula quite difficult, as the limits of such model made quantitative comparisons challenging. Nevertheless, applying the opportune corrections (as proposed by Domb and Salter), a satisfactory match has been achieved.

Calculations on several defective systems were also performed. Overall, defects were found to play an important role on the half-metallic nature of these compounds, as a loss of half-metallicity was reported multiple times. Co vacancy was found to be the most stable defect in both cases; however, although being responsible of a significant lowering of the magnetic moment, such defect was not found to lead to the disappearance of the half-metallic behavior. This also suggested that a magnetic moment lower than 2 μ_B is not straightforwardly linked to non-half-metallic materials and to a reduction of spin-polarization. On the other hand, defects like off-stoichiometry led to the appearance of energy levels in correspondence of the Fermi level, drastically reducing the spin-polarization. Based on such evidence, high crystalline ordering is deemed crucial for applications in spintronics.

9. Final remarks

The series of Co_2TiSn, Co_2ZrSn, and Co_2HfSn Heusler alloys is considered promising for next-generation high performance spintronic MTJs, as they combine high Curie temperature, congruent solidification from the melt, absence of order-disorder or martensitic transitions, good magnetic properties, and high predicted spin-polarization. The effect of the p-type element in the Co_2TiZ (Z= Si, Ge, Sn) family was previously investigated by Barth et al. [50], finding that Sn was overall the best option for occupying the Z site in the $L2_1$ system. As far as the role of the Y element (Y= Ti, Zr, Hf) is concerned, data in the literature are scattered, as values of magnetization of Co_2ZrSn and Co_2HfSn alloys are overall extremely dispersed. A preliminary explanation for such scattering were provided by Kushwaha et al. [114] who synthesized the Co_2ZrSn compound as a single crystal in different stoichiometry and measured the magnetic properties. The linear dependence of the magnetic moment from the Co content in the samples indicated that Co vacancies play a significant role in determining the properties of the compound.

Our investigation started with the characterization of the magnetic properties. Hysteresis loops showed a weak ferromagnetic behavior for both the compounds and Curie temperatures higher than 400 K. The nature of their ferromagnetism was found to be well described by the Edwards-Wohlfarth model for itinerant ferromagnets. Deviations from such formula were found to be present mainly at low fields, where the theory presents its intrinsic limitations. The fit between experimental and modeled data was found to be consistent also when the ${\rho'}_F^{2j}/{\rho'}_F^{4j+1}$ approximation was considered. In such hypotheses, the terms with exponents higher than 2 in Equation 5 are neglected since the derivative of the density of states is assumed to be negligible at the Fermi level, predicating a flat profile. In such approximation, the model was found to fit the experimental data quite well, suggesting that, at 2 K, in such alloys the DOS in proximity of E_F is almost zero. This was verified by ab-initio calculations which shown a rather flat profile of the density of states at E_F both in the minority-spin band, where a half-metallic band gap is present, and in the majority-spin band, where the derivative of the total DOS is small. The magnetization behavior as a function of temperature shown also interesting features. At low temperatures, the M/T trends of both compounds were observed to be extremely similar to that of the NiMnSb Heusler alloy, which half-metallicity was experimentally demonstrated in previous studies [69]. While decreasing the temperature, a crossover from a high-T $M_s = M_s(0) \cdot (1 - AT^2)$ Stoner-type itinerant ferromagnetism to a low-T $M_x = M_s(0) \cdot (1 - BT^{3/2})$ Bloch-type localized magnetism was measured. The shift from an itinerant to a localized behavior was linked to the fact that the electronic conduction at low T is hindered by the presence of a half-metallic band gap, as predicted by the theory. In such scheme, as in the HMF state spin-flip diffusion is impossible due to the presence of the band gap, the electron scattering mechanism is subjected to a change, so that the main scattering route are spin-waves and electron-phonon interactions. Once the temperature is raised sufficiently, spin-flip diffusion becomes possible as electrons have now sufficient energy to overcome the band gap, consequently changing their conduction mechanism and M/T dependency. Interestingly, also the profile of the electrical conductivity of both alloys was found to be analogous to that of NiMnSb. The same crossover from a low-T to a high-T regime was found approximately at the same T independently measured for the magnetization with the SQUID magnetometer. The R/T trends were found extremely coherent with those of NiMnSb and with the model proposed by Hordequin et al. [94]. In such framework, resistivity is assumed to be the sum of several independent contributions. At high-T, electronic scattering can occur according to many terms, such as magnon, and phonon-related, which collectively cause a R/T^x dependency, with $1 < x < 5/3$. In HMF materials, such as NiMnSb, at low-T the spin-flip conduction is impossible, thus causing the electrical conductivity to decrease more drastically following a R/T^2 dependency, which is due to the contribution of thermally excited spin-waves as explained by Ueda et al. [95]. As modeled by Ueda and Moriya [95], and later applied by Hordequin et al. [94] and Turban et al. [69] on the half-metallic NiMnSb Heusler compound, such low-T behavior is not explainable via the Bloch-Grüneisen model of electron scattering in normal metals, being instead compatible with the presence of a half-metallic band gap in the DOS. This behavior was observed for both for Co_2HfSn and Co_2ZrSn, also showing crossover points around 40-70 K, which agree with those estimated measuring the magnetization. Such

experimental evidence is not incompatible with the presence of a half-metallic band gap at low-T in these alloys.

As far as the magnetic moment at 2 K is concerned, calculations for the pristine system predicts a value of 2.00 μ_B in agreement with the Slater-Pauling rule. For Co_2HfSn and Co_2ZrSn this was not always the case experimentally, as in the literature relatively scattered values ranging approximatively from 1.50 μ_B to 2.00 μ_B can be found. Our work demonstrated that such dispersed values are due to the sum of the effect of secondary phases and lattice disorder inside the samples. In fact, for specimens synthesized via arc melting followed by annealing, non-negligible amounts of secondary phases (Co_2Hf, Co_2Zr, CoSn, and Co_3Sn_2) were always detected. A reliable processing route able to avoid the formation of such impurities was found to be the rapid solidification (melt spinning) followed by spark plasma sintering (SPS). Single phase samples were reliably obtained following such procedure. The rapid solidification was also found in case of Co_2ZrSn to provide more solubilization of Co inside the $L2_1$ lattice, noticeably increasing the crystalline order. For samples containing 7-11% of secondary phases, the magnetic moments were found to be comprised between 2.0-2.1 μ_B and 1.8-2.0 μ_B for Co_2HfSn and Co_2ZrSn, respectively. In this case, the lower limits were estimated assuming the spurious phase giving the same magnetic contribution of the Heusler phase, while the upper limit indicates the case in which such phases give a negligible contribution to the magnetization. Since the values of Co_2HfSn were found to be quite well centered on the value predicted by the theory and from the Slater-Pauling model, further attention was later dedicated to the less straightforward case of Co_2ZrSn.

The transport properties were measured both as a convenient tool to collect evidence on the DOS shape and half-metallic properties, and as a crucial characterization in key of potential spin-injection applications. The charge carrier concentration was found to be in the order of 10^{28} m^{-3}, typical of conductive materials. The Seebeck coefficient was observed in both cases to be negative and to linearly increase in absolute value until T_C, settling in a constant plateau afterwards. The electrical conductivity shown a linear decrease from RT to T_C, followed by a shallow linear increase above the Curie point. A rather similar trend was found for the thermal conductivities, which electronic and lattice contributions were estimated separately using the Wiedemann-Franz equation. An independent estimation of k_{lat} was attempted by means of DFT calculations in the framework of the Slack's model. Such procedure was hindered by the several limitations of the Slack equation, which was found to be less reliable for systems in which the difference of atomic mass of the constituting elements exceeds 100%, and when, as in the present cases, the optical and acoustic phonon modes are strongly overlapped. In addition, the model is deemed reliable for temperatures way higher than the Debye T, θ_D. Since in our case θ_D is extremely close to T_C, and since considerations based on DFT calculations cannot be safely performed above the Curie point, the application of the Slack model for k_{lat} was found to be difficult. Nevertheless, if this limit is ignored, and if the correction proposed by Domb and Salter are applied, values in agreement with those experimentally measured can still be observed. The thermoelectric figure of merit zT was estimated for the two alloys for the first time. The profile was found to be resemblant of those of the Seebeck coefficient, highlighting the strong dependency of zT from S. The absolute value was found to be in the order of 10^{-3} at 300 K, which is sufficient for spin-injection purposes.

The effect of Co occupancy and lattice disorder was studied in the case of Co_2ZrSn. The alloy was synthesized following different processing routes, each involving diverse cooling rates, and consequently distinctive crystalline order. As mentioned before, the rapid solidification was found to give single phase specimens which Heusler phase's formula unit is closer to the ideal Co_2ZrSn. Sample obtained with procedures involving slower cooling rates, or annealing, shown progressively lower occupancy on the Co site in the $L2_1$ lattice, accompanied by the presence of secondary phases. The Co site occupancy was quantified for each sample by Rietveld refinement of XRD patterns. In general, most of the structural, electronic, and magnetic properties were observed to follow trends which linearly depends on χ_{Co}, implying that Co vacancies play a crucial role in determining the DOS of Co_2ZrSn. The magnetic moment at 2 K was measured for the as cast, annealed, and sintered specimens, finding a linear μ/χ_{Co} trend. Such behavior was quantitatively confirmed by DFT calculations performed on Co_2ZrSn systems in which different Co vacancy concentrations were introduced.

Overall, the magnetic moment was found to linearly scale with the concentration of Co vacancies inside the Heusler phase.

In Co_2ZrSn, the trends of transport properties were rationalized in terms of a compositional and a microstructural contribution. As far as the Seebeck coefficient is concerned, the compositional contribution alone is sufficient to explain its behavior. In fact, greater absolute values of S were found for samples having progressively higher χ_{Co}. The trend of the electrical conductivity from RT to 800 K was explained as a combination of both terms. On the one hand, at 300 K, where electrons are effectively scattered at grain boundaries, the annealed sample was found to have the highest σ, as the relatively low grain boundary density is accompanied by a sufficiently high χ_{Co}. The sintered specimen, despite having slightly higher χ_{Co}, shows also way higher density of grain boundaries which hinder electron diffusivity. The as cast alloy, despite having the same microstructure of the annealed, present also by far the lowest χ_{Co}, consequently presenting the lowest σ. On the other hand, at 800 K electron scattering at grain boundaries becomes negligible, thus implying that the trend of σ is describable only considering the compositional term. Indeed, at such temperature, the higher χ_{Co}, the larger the electrical conductivity shown by the samples. Such consideration can be assumed valid starting from 500 K, where the conductivity of the annealed sample considerably decreases with respect to that of SPS. Last, the microstructural contribution was found sufficient to well explain the behavior of thermal conductivity, since samples showing finer grains were found to have the lowest k.

Ab-initio simulations were performed on pristine supercells. Both systems were calculated using two different functionals in order to evaluate the stability of the results from the computational parameters. In all cases, the compounds were found half-metallic with 100% spin-polarization at absolute zero, with the only exception of Co_2HfSn when computed with the PBEsol functional. In this case, the Fermi level was observed to slightly intersect the edge of the conduction band, leading to a conductive state. Calculations performed at different fixed values of lattice parameters indicated that such functional tend to locate E_F in positions which are extremely dependent on even small variations of *a*, highlighting that for such systems, where the Fermi energy is very close to the edge of the conduction band, the choose of the initial computational parameters highly determines the final outcomes. Simulations performed imposing the experimentally measured lattice parameters resulted in half-metallic ground states with 100% spin-polarization in all cases. The transport properties and phonon density of states were also determined. When the experimental charge carrier concentration is selected, the computed values of Seebeck coefficient, electrical conductivity, k_{el}, and zT are in very good agreement with the measured values, indicating that the calculated DOS is overall resemblant of those of real samples. The phonon band structure showed that the acoustic and optical modes are strongly overlapped, hindering the integration as separate contribution, and thus making the calculation of k_{lat} based on the Slack's formula difficult as mentioned above. The thermal properties were in rather good agreement with the experimental.

The effects of multiple defects were also investigated by ab-initio calculations in both alloys. In all cases, the most stable defect was determined to be the Co vacancy, having equivalent formation energies under 100 K with respect to the pristine compound. This indicates that vacancies are likely the most common defect in real samples, as already suggested by experimental evidence. A non-negligible shrinking of the band gap was found as a result of increasingly higher concentrations of Co vacancies inside perfect supercells; however, no energy levels were introduced inside the gap, conserving at least at 0 K, their half-metallic properties. The magnetic moment was found to decrease consequently to the removal of Co atoms, showing that a reduction of μ is not always indicative of a loss of half-metallicity. In Co_2ZrSn, the reduction of magnetic moment as a function of the vacancy concentration was observed to be linear and quantitatively coherent with the experimental results, furtherly corroborating previous considerations. The measured stoichiometry of real specimens, which slightly deviates from the ideal 50% Co, 25% Hf/Zr, 25%Sn in annealed alloys, was reproduced in calculations in two different entropic configurations. All configurations were found to introduce levels in the band gap of both alloys, effectively deteriorating half-metallicity. The spin-polarization was calculated to be reduced from 100% of the ideal compounds to approximately 18% and 78% in off-stoichiometric Co_2HfSn and Co_2ZrSn supercells, respectively. The formation energy of such complex defects was estimated to be about equal to those of the

single defects of which they are composed, indicating that they are not thermodynamically unfavored with respect to the simultaneous occurrence of these. Other defects were investigated for both systems, suggesting that the appearance of levels inside the half-metallic gap is not uncommon as a result of the introduction of some sort of deviation from perfect crystalline order, and thus indicating that the study of processing route able to provide highly ordered and defectless samples is to be greatly looked after.

In conclusion, the present study contributed to clarify the electronic and magnetic properties of Co_2HfSn and Co_2ZrSn alloys, also investigating the effect of defects and crystalline disorder on such properties with a combination of experiments and ab-initio calculations. The methodology used in this work was found to effectively give self-consistent and coherent results and can potentially be applied to the study of similar materials. All the experimental outcomes were successfully rationalized in the framework of already existing physical models, and/or strongly supported by first-principles simulations. As strong evidence of the presence of a half-metallic gap at low temperatures were collected for the bulk material, further developments of this work would be the synthesis of these compounds as thin-films with the subsequent direct measurement of the spin-polarization and TMR ratio.

10. Bibliography

1. Popper, K. *Conjectures and refutations: The growth of scientific knowledge*; routledge, 2014;
2. Fuller, R.B.; Kuromiya, K. *Critical path*; Macmillan, 1981;
3. Hanson, R. Economics of the singularity. *iEEE Spectr.* **2008**, *45*, 45–50.
4. Buchanan, M. The law of accelerating returns. *Nat. Phys.* **2008**, *4*, 507.
5. Turchin, P. *History \& mathematics: Historical dynamics and development of complex societies*; Editorial URSS, 2006;
6. Flamm, K. Has Moore's law been repealed? an economist's perspective. *Comput. Sci. \& Eng.* **2017**, *19*, 29–40.
7. Gargini, P.; Balestra, F.; Hayashi, Y. Roadmapping of nanoelectronics for the new electronics industry. *Appl. Sci.* **2021**, *12*, 308.
8. Moore, S.K. A better way to measure progress in semiconductors. *node is nonsense," IEEE Spectr.* **2020**.
9. Williams, F.C.; Kilburn, T. Electronic digital computers. *Nature* **1948**, *162*, 487.
10. Bhatti, S.; Sbiaa, R.; Hirohata, A.; Ohno, H.; Fukami, S.; Piramanayagam, S.N. Spintronics based random access memory: a review. *Mater. Today* **2017**, *20*, 530–548.
11. Fusari, G. Dispositivi di memoria per sistemi embedded, le opportunità della MRAM. *Elettron. Oggi* **2023**, *514*, 48–50.
12. Mordor, I. *MRAM Market Size & Share Analysis - Growth Trends & Forecasts (2024 - 2029)*; Mordor Intelligence, 2024;
13. Åkerman, J. Toward a universal memory. *Science (80-.).* **2005**, *308*, 508–510.
14. Thomson, W. XIX. On the electro-dynamic qualities of metals:—Effects of magnetization on the electric conductivity of nickel and of iron. *Proc. R. Soc. London* **1857**, 546–550.
15. Sbiaa, R. Magnetoresistive read heads: fundamentals and functionality. *Dev. Data Storage Mater. Perspect.* **2011**, 97.
16. Reig, C.; Cardoso, S.; Mukhopadhyay, S.C. Giant magnetoresistance (GMR) sensors. *Smart Sensors, Meas. Instrum.* **2013**, *6*, 1–301.
17. Chappert, C.; Fert, A.; Van Dau, F.N. The emergence of spin electronics in data storage. *Nat. Mater.* **2007**, *6*, 813–823.
18. Miyazaki, T.; Tezuka, N. Giant magnetic tunneling effect in Fe/Al2O3/Fe junction. *J. Magn. Magn. Mater.* **1995**, *139*, L231--L234.
19. Julliere, M. Tunneling between ferromagnetic films. *Phys. Lett. A* **1975**, *54*, 225–226.
20. Hirohata, A.; Sukegawa, H.; Yanagihara, H.; Žutić, I.; Seki, T.; Mizukami, S.; Swaminathan, R. Roadmap for emerging materials for spintronic device applications. *IEEE Trans. Magn.* **2015**, *51*, 1–11.
21. Bowen, M.; Barthélémy, A.; Bibes, M.; Jacquet, E.; Contour, J.P.; Fert, A.; Wortmann, D.; Blügel, S. Half-metallicity proven using fully spin-polarized tunnelling. *J. Phys. Condens. Matter* **2005**, *17*, L407.
22. Jourdan, M.; Minár, J.; Braun, J.; Kronenberg, A.; Chadov, S.; Balke, B.; Gloskovskii, A.; Kolbe, M.; Elmers, H.-J.; Schönhense, G.; et al. Direct observation of half-metallicity in the Heusler compound Co2MnSi. *Nat. Commun.* **2014**, *5*, 3974.

23. Liu, H.; Honda, Y.; Matsuda, K.; Arita, M.; Uemura, T.; Yamamoto, M. Highly Spin-Polarized Tunneling in Epitaxial Magnetic Tunnel Junctions with a Co2MnSi Electrode and a MgO Barrier with Improved Interfacial Structural Properties. *Jpn. J. Appl. Phys.* **2012**, *51*, 93004.

24. Jin, Y.; Kharel, P.; Valloppilly, S.R.; Li, X.-Z.; Kim, D.R.; Zhao, G.J.; Chen, T.Y.; Choudhary, R.; Kashyap, A.; Skomski, R.; et al. Half-metallicity in highly L21-ordered CoFeCrAl thin films. *Appl. Phys. Lett.* **2016**, *109*.

25. Galanakis, I.; Dederichs, P.H.; Papanikolaou, N. Slater-Pauling behavior and origin of the half-metallicity of the full-Heusler alloys. *Phys. Rev. B* **2002**, *66*, 174429.

26. Wang, D.; Nordman, C.; Daughton, J.M.; Qian, Z.; Fink, J. 70\% TMR at room temperature for SDT sandwich junctions with CoFeB as free and reference layers. *IEEE Trans. Magn.* **2004**, *40*, 2269–2271.

27. Ikeda, S.; Hayakawa, J.; Lee, Y.M.; Matsukura, F.; Ohno, Y.; Hanyu, T.; Ohno, H. Magnetic tunnel junctions for spintronic memories and beyond. *IEEE Trans. Electron Devices* **2007**, *54*, 991–1002.

28. Daughton, J.M. Magnetoresistive memory technology. *Thin Solid Films* **1992**, *216*, 162–168.

29. Zhu, J.-G. Magnetoresistive random access memory: The path to competitiveness and scalability. *Proc. IEEE* **2008**, *96*, 1786–1798.

30. Tsymbal, E.Y.; Mryasov, O.N.; LeClair, P.R. Spin-dependent tunnelling in magnetic tunnel junctions. *J. Phys. Condens. Matter* **2003**, *15*, R109.

31. Slonczewski, J.C. Current-driven excitation of magnetic multilayers. *J. Magn. Magn. Mater.* **1996**, *159*, L1--L7.

32. Schrag, B.D.; Anguelouch, A.; Xiao, G.; Trouilloud, P.; Lu, Y.; Gallagher, W.J.; Parkin, S.S.P. Magnetization reversal and interlayer coupling in magnetic tunneling junctions. *J. Appl. Phys.* **2000**, *87*, 4682–4684.

33. Shi, J.; Tehrani, S.; Scheinfein, M.R. Geometry dependence of magnetization vortices in patterned submicron NiFe elements. *Appl. Phys. Lett.* **2000**, *76*, 2588–2590.

34. Nishimura, N.; Hirai, T.; Koganei, A.; Ikeda, T.; Okano, K.; Sekiguchi, Y.; Osada, Y. Magnetic tunnel junction device with perpendicular magnetization films for high-density magnetic random access memory. *J. Appl. Phys.* **2002**, *91*, 5246–5249.

35. Ikeda, S.; Miura, K.; Yamamoto, H.; Mizunuma, K.; Gan, H.D.; Endo, M.; Kanai, S.; Hayakawa, J.; Matsukura, F.; Ohno, H. A perpendicular-anisotropy CoFeB--MgO magnetic tunnel junction. *Nat. Mater.* **2010**, *9*, 721–724.

36. Karthik, S. V; Takahashi, Y.K.; Ohkubo, T.; Hono, K.; Gan, H.D.; Ikeda, S.; Ohno, H. Transmission electron microscopy study on the effect of various capping layers on CoFeB/MgO/CoFeB pseudo spin valves annealed at different temperatures. *J. Appl. Phys.* **2012**, *111*.

37. Zhao, W.S.; Zhang, Y.; Devolder, T.; Klein, J.-O.; Ravelosona, D.; Chappert, C.; Mazoyer, P. Failure and reliability analysis of STT-MRAM. *Microelectron. Reliab.* **2012**, *52*, 1848–1852.

38. Sbiaa, R. Magnetization switching by spin-torque effect in off-aligned structure with perpendicular anisotropy. *J. Phys. D. Appl. Phys.* **2013**, *46*, 395001.

39. Fang, L.; Liu, J.; Ju, S.; Zheng, F.; Dong, W.; Shen, M. Experimental and theoretical evidence of enhanced ferromagnetism in sonochemical synthesized BiFeO3 nanoparticles. *Appl. Phys. Lett.* **2010**, *97*.

40. Diao, Z.; Panchula, A.; Ding, Y.; Pakala, M.; Wang, S.; Li, Z.; Apalkov, D.; Nagai, H.; Driskill-Smith, A.; Wang, L.-C.; et al. Spin transfer switching in dual MgO magnetic tunnel junctions. *Appl. Phys. Lett.* **2007**, *90*.

41. Valenzuela, S.O.; Tinkham, M. Direct electronic measurement of the spin Hall effect. *Nature* **2006**, *442*, 176–179.

42. Bishnoi, R.; Ebrahimi, M.; Oboril, F.; Tahoori, M.B. Architectural aspects in design and analysis of SOT-based memories. In Proceedings of the 2014 19th Asia and South Pacific Design Automation Conference (ASP-DAC); 2014; pp. 700–707.

43. Garcia, V.; Bibes, M.; Bocher, L.; Valencia, S.; Kronast, F.; Crassous, A.; Moya, X.; Enouz-Vedrenne, S.; Gloter, A.; Imhoff, D.; et al. Ferroelectric control of spin polarization. *Science (80-.).* **2010**, *327*, 1106–1110.

44. Barnes, S.E.; Ieda, J.; Maekawa, S. Rashba spin-orbit anisotropy and the electric field control of magnetism. *Sci. Rep.* **2014**, *4*, 4105.

45. Galanakis, I.; H Dederichs, P. Half-metallicity and Slater-Pauling behavior in the ferromagnetic Heusler alloys. *Half-Metallic Alloy. Fundam. Appl.* **2005**, 1–39.

46. Scheike, T.; Sukegawa, H.; Inomata, K.; Ohkubo, T.; Hono, K.; Mitani, S. Chemical ordering and large tunnel magnetoresistance in Co2FeAl/MgAl2O4/Co2FeAl (001) junctions. *Appl. Phys. Express* **2016**, *9*, 53004.

47. Tezuka, N.; Ikeda, N.; Mitsuhashi, F.; Sugimoto, S. Improved tunnel magnetoresistance of magnetic tunnel junctions with Heusler Co2FeAl0. 5Si0. 5 electrodes fabricated by molecular beam epitaxy. *Appl. Phys. Lett.* **2009**, *94*.

48. Wurmehl, S.; Fecher, G.H.; Kandpal, H.C.; Ksenofontov, V.; Felser, C.; Lin, H.-J.; Morais, J. Geometric, electronic, and magnetic structure of Co2FeSi: Curie temperature and magnetic moment measurements and calculations. *Phys. Rev. B* **2005**, *72*, 184434.

49. Kanomata, T.; Chieda, Y.; Endo, K.; Okada, H.; Nagasako, M.; Kobayashi, K.; Kainuma, R.; Umetsu, R.Y.; Takahashi, H.; Furutani, Y.; et al. Magnetic properties of the half-metallic Heusler alloys Co2VAl and Co2VGa under pressure. *Phys. Rev. B* **2010**, *82*, 144415.

50. Barth, J.; Fecher, G.H.; Balke, B.; Graf, T.; Shkabko, A.; Weidenkaff, A.; Klaer, P.; Kallmayer, M.; Elmers, H.-J.; Yoshikawa, H.; et al. Anomalous transport properties of the half-metallic ferromagnets Co2TiSi, Co2TiGe and Co2TiSn. *Philos. Trans. R. Soc. A Math. Phys. Eng. Sci.* **2011**, *369*, 3588–3601.

51. Difalco, A.; Barrera, G.; Palumbo, M.; Castellero, A.; Baricco, M.; Tiberto, P.M.; Allia, P. Itinerant magnetism, electronic properties and half-metallicity of Co2ZrSn and Co2HfSn Heusler alloys. *J. Alloys Compd.* **2022**, *918*, 165464.

52. Difalco, A.; Winning, I.G.; Palumbo, M.; Baricco, M.; Castellero, A.; Alleno, E. Transport properties of Co2HfSn Heusler alloy obtained by rapid solidification and sintering. *Solid State Sci.* **2024**, 107455.

53. Rahman, A.; Rehman, M.U.; Zhao, H.; Liu, W.; Wang, J.; Lu, Y.; Ruan, K.; Dai, R.; Wang, Z.; Tao, X.; et al. Itinerant magnetism in the half-metallic Heusler compound Co 2 HfSn: Evidence from critical behavior combined with first-principles calculations. *Phys. Rev. B* **2021**, *103*, 94425.

54. Hirohata, A.; Lloyd, D.C. Heusler alloys for metal spintronics. *MRS Bull.* **2022**, *47*, 593–599.

55. Boona, S.R.; Myers, R.C.; Heremans, J.P. Spin caloritronics. *Energy \& Environ. Sci.* **2014**, *7*, 885–910.

56. Ji, Y.; Strijkers, G.J.; Yang, F.Y.; Chien, C.L.; Byers, J.M.; Anguelouch, A.; Xiao, G.; Gupta, A. Determination of the spin polarization of half-metallic CrO 2 by point contact Andreev reflection. *Phys. Rev. Lett.* **2001**, *86*, 5585.

57. Siratori, K.; Iida, S. Magnetic Property of Mnx Cr1- x O2. *J. Phys. Soc. Japan* **1960**, *15*, 210–211.

58. Serrate, D.; De Teresa, J.M.; Ibarra, M.R. Double perovskites with ferromagnetism above room

temperature. *J. Phys. Condens. Matter* **2006**, *19*, 23201.

59. Žutić, I.; Fabian, J.; Sarma, S. Das Spintronics: Fundamentals and applications. *Rev. Mod. Phys.* **2004**, *76*, 323.

60. Furdyna, J.K. Diluted magnetic semiconductors. *J. Appl. Phys.* **1988**, *64*, R29--R64.

61. Dietl, T.; Ohno, o H.; Matsukura, a F.; Cibert, J.; Ferrand, e D. Zener model description of ferromagnetism in zinc-blende magnetic semiconductors. *Science (80-.).* **2000**, *287*, 1019–1022.

62. Zhao, K.; Chen, B.; Zhao, G.; Yuan, Z.; Liu, Q.; Deng, Z.; Zhu, J.; Jin, C. Ferromagnetism at 230 K in (Ba 0.7 K 0.3)(Zn 0.85 Mn 0.15) 2 As 2 diluted magnetic semiconductor. *Chinese Sci. Bull.* **2014**, *59*, 2524–2527.

63. Watanabe, K. Magetic Properties of Clb-Type Mn Base Compounds. *Trans. Japan Inst. Met.* **1976**, *17*, 220–226.

64. De Groot, R.A.; Mueller, F.M.; Van Engen, P.G.; Buschow, K.H.J. New class of materials: half-metallic ferromagnets. *Phys. Rev. Lett.* **1983**, *50*, 2024.

65. Kirillova, M.M.; Makhnev, A.A.; Shreder, E.I.; Dyakina, V.P.; Gorina, N.B. Interband Optical Absorption and Plasma Effects in Half-Metallic XMnY Ferromagnets. *Phys. status solidi* **1995**, *187*, 231–240.

66. Hanssen, K.; Mijnarends, P.E. Positron-annihilation study of the half-metallic ferromagnet NiMnSb: Theory. *Phys. Rev. B* **1986**, *34*, 5009.

67. Hanssen, K.; Mijnarends, P.E.; Rabou, L.; Buschow, K.H.J. Positron-annihilation study of the half-metallic ferromagnet NiMnSb: Experiment. *Phys. Rev. B* **1990**, *42*, 1533.

68. Soulen Jr, R.J.; Byers, J.M.; Osofsky, M.S.; Nadgorny, B.; Ambrose, T.; Cheng, S.F.; Broussard, P.R.; Tanaka, C.T.; Nowak, J.; Moodera, J.S.; et al. Measuring the spin polarization of a metal with a superconducting point contact. *Science (80-.).* **1998**, *282*, 85–88.

69. Turban, P.; Andrieu, S.; Kierren, B.; Snoeck, E.; Teodorescu, C.; Traverse, A. Growth and characterization of single crystalline NiMnSb thin films and epitaxial NiMnSb/MgO/NiMnSb (001) trilayers. *Phys. Rev. B* **2002**, *65*, 134417.

70. Beretta, D.; Neophytou, N.; Hodges, J.M.; Kanatzidis, M.G.; Narducci, D.; Martin-Gonzalez, M.; Beekman, M.; Balke, B.; Cerretti, G.; Tremel, W.; et al. Thermoelectrics: From history, a window to the future. *Mater. Sci. Eng. R Reports* **2019**, *138*, 100501.

71. Heusler, F.; Starck, W.; Haupt, E. Magnetisch-chemische studien. *Verh. Dtsch. Phys. Ges* **1903**, *5*, 219–232.

72. Kübler, J.; William, A.R.; Sommers, C.B. Formation and coupling of magnetic moments in Heusler alloys. *Phys. Rev. B* **1983**, *28*, 1745.

73. Ishida, S.; Akazawa, S.; Kubo, Y.; Ishida, J. Band theory of Co2MnSn, Co2TiSn and Co2TiAl. *J. Phys. F Met. Phys.* **1982**, *12*, 1111.

74. Fujii, S.; Ishida, S.; Asano, S. A half-metallic band structure and Fe2MnZ (Z= Al, Si, P). *J. Phys. Soc. Japan* **1995**, *64*, 185–191.

75. Brown, P.J.; Neumann, K.-U.; Webster, P.J.; Ziebeck, K.R.A. The magnetization distributions in some Heusler alloys proposed as half-metallic ferromagnets. *J. Phys. Condens. Matter* **2000**, *12*, 1827.

76. Geiersbach, U.; Bergmann, A.; Westerholt, K. Structural, magnetic and magnetotransport properties of thin films of the Heusler alloys Cu2MnAl, Co2MnSi, Co2MnGe and Co2MnSn. *J. Magn. Magn. Mater.* **2002**, *240*, 546–549.

77. Kämmerer, S.; Thomas, A.; Hütten, A.; Reiss, G. Co2MnSi Heusler alloy as magnetic electrodes in

magnetic tunnel junctions. *Appl. Phys. Lett.* **2004**, *85*, 79–81.

78. Schmalhorst, J.; Kämmerer, S.; Sacher, M.; Reiss, G.; Hütten, A.; Scholl, A. Interface structure and magnetism of magnetic tunnel junctions with a Co 2 Mn Si electrode. *Phys. Rev. B* **2004**, *70*, 24426.

79. Graf, T.; Felser, C.; Parkin, S.S.P. Simple rules for the understanding of Heusler compounds. *Prog. solid state Chem.* **2011**, *39*, 1–50.

80. Van Engen, P.G.; Buschow, K.H.J.; Erman, M. Magnetic properties and magneto-optical spectroscopy of Heusler alloys based on transition metals and Sn. *J. Magn. Magn. Mater.* **1983**, *30*, 374–382.

81. Krenke, T.; Duman, E.; Acet, M.; Wassermann, E.F.; Moya, X.; Mañosa, L.; Planes, A. Inverse magnetocaloric effect in ferromagnetic Ni--Mn--Sn alloys. *Nat. Mater.* **2005**, *4*, 450–454.

82. Kainuma, R.; Imano, Y.; Ito, W.; Sutou, Y.; Morito, H.; Okamoto, S.; Kitakami, O.; Oikawa, K.; Fujita, A.; Kanomata, T.; et al. Magnetic-field-induced shape recovery by reverse phase transformation. *Nature* **2006**, *439*, 957–960.

83. Felser, C.; Hirohata, A. *Heusler alloys*; Springer, 2015;

84. Wurmehl, S.; Fecher, G.H.; Kroth, K.; Kronast, F.; Dürr, H.A.; Takeda, Y.; Saitoh, Y.; Kobayashi, K.; Lin, H.-J.; Schönhense, G.; et al. Electronic structure and spectroscopy of the quaternary Heusler alloy Co2Cr1- xFexAl. *J. Phys. D. Appl. Phys.* **2006**, *39*, 803.

85. Alijani, V.; Winterlik, J.; Fecher, G.H.; Naghavi, S.S.; Felser, C. Quaternary half-metallic Heusler ferromagnets for spintronics applications. *Phys. Rev. B* **2011**, *83*, 184428.

86. Galanakis, I. Orbital magnetism in the half-metallic Heusler alloys. *Phys. Rev. B* **2005**, *71*, 12413.

87. Dunlap, R.A.; Jones, D.F. Mössbauer-effect study of Sn-impurity-site hyperfine fields in the Heusler alloys Co 2 Mn Z (Z= A l, G a, S i, G e, S n). *Phys. Rev. B* **1982**, *26*, 6013.

88. Plogmann, S.; Schlathölter, T.; Braun, J.; Neumann, M.; Yarmoshenko, Y.M.; Yablonskikh, M. V; Shreder, E.I.; Kurmaev, E.Z.; Wrona, A.; Ślebarski, A. Local moments in Mn-based Heusler alloys and their electronic structures. *Phys. Rev. B* **1999**, *60*, 6428.

89. Mahmoud, N.T.; Khalifeh, J.M.; Hamad, B.A.; Mousa, A.A. The effect of defects on the electronic and magnetic properties of the Co2VSn full Heusler alloy: Ab-initio calculations. *Intermetallics* **2013**, *33*, 33–37.

90. Galanakis, I.; Özdo\ugan, K.; Akta\cs, B.; \cSa\cs\io\uglu, E. Effect of doping and disorder on the half metallicity of full Heusler alloys. *Appl. Phys. Lett.* **2006**, *89*.

91. Mavropoulos, P.; Galanakis, I.; Popescu, V.; Dederichs, P.H. The influence of spin--orbit coupling on the band gap of Heusler alloys. *J. Phys. Condens. Matter* **2004**, *16*, S5759.

92. Dowben, P.A.; Skomski, R. Finite-temperature spin polarization in half-metallic ferromagnets. *J. Appl. Phys.* **2003**, *93*, 7948–7950.

93. Chioncel, L.; Katsnelson, M.I.; de Groot, R.A.; Lichtenstein, A.I. Nonquasiparticle states in the half-metallic ferromagnet NiMnSb. *Phys. Rev. B* **2003**, *68*, 144425.

94. Hordequin, C.; Ristoiu, D.; Ranno, L.; Pierre, J. On the cross-over from half-metal to normal ferromagnet in NiMnSb. *Eur. Phys. J. B-Condensed Matter Complex Syst.* **2000**, *16*, 287–293.

95. Ueda, K.; Moriya, T. Contribution of spin fluctuations to the electrical and thermal resistivities of weakly and nearly ferromagnetic metals. *J. Phys. Soc. Japan* **1975**, *39*, 605–615.

96. Chowdhury, A.; Bhattacharjee, S. Experimental investigation of change in sheet resistance and Debye temperatures in metallic thin films due to low-energy ion beam irradiation. *J. Phys. D. Appl. Phys.* **2013**, *46*, 435304.

97. Suzuki, K.; Tedrow, P.M. Resistivity and magnetotransport in cro 2 films. *Phys. Rev. B* **1998**, *58*, 11597.

98. Liu, H.; Honda, Y.; Taira, T.; Matsuda, K.; Arita, M.; Uemura, T.; Yamamoto, M. Giant tunneling magnetoresistance in epitaxial Co2MnSi/MgO/Co2MnSi magnetic tunnel junctions by half-metallicity of Co2MnSi and coherent tunneling. *Appl. Phys. Lett.* **2012**, *101*.

99. Wen, Z.; Sukegawa, H.; Kasai, S.; Inomata, K.; Mitani, S. Tunnel magnetoresistance and spin-transfer-torque switching in polycrystalline Co 2 FeAl full-Heusler-alloy magnetic tunnel junctions on amorphous Si/SiO 2 substrates. *Phys. Rev. Appl.* **2014**, *2*, 24009.

100. Wen, Z.; Sukegawa, H.; Kasai, S.; Hayashi, M.; Mitani, S.; Inomata, K. Magnetic tunnel junctions with perpendicular anisotropy using a Co2FeAl full-Heusler alloy. *Appl. Phys. Express* **2012**, *5*, 63003.

101. Wen, Z.; Sukegawa, H.; Furubayashi, T.; Koo, J.; Inomata, K.; Mitani, S.; Hadorn, J.P.; Ohkubo, T.; Hono, K. A 4-Fold-Symmetry Hexagonal Ruthenium for Magnetic Heterostructures Exhibiting Enhanced Perpendicular Magnetic Anisotropy and Tunnel Magnetoresistance. *Adv. Mater.* **2014**, *26*, 6483–6490.

102. Miura, Y.; Shirai, M.; Nagao, K. Ab initio study on stability of half-metallic Co-based full-Heusler alloys. *J. Appl. Phys.* **2006**, *99*.

103. Kandpal, H.C.; Fecher, G.H.; Felser, C. Calculated electronic and magnetic properties of the half-metallic, transition metal based Heusler compounds. *J. Phys. D. Appl. Phys.* **2007**, *40*, 1507.

104. Umetsu, R.Y.; Kobayashi, K.; Kainuma, R.; Yamaguchi, Y.; Ohoyama, K.; Sakuma, A.; Ishida, K. Powder neutron diffraction studies for the L21 phase of Co2YGa (Y= Ti, V, Cr, Mn and Fe) Heusler alloys. *J. Alloys Compd.* **2010**, *499*, 1–6.

105. Yu, L.; Li, Z.; Zhu, J.; Liu, H.; Zhang, Y.; Cao, Y.; Xu, K.; Liu, Y. Electrical and magnetic transport properties of Co2VGa half-metallic Heusler alloy. *Materials (Basel).* **2022**, *15*, 6138.

106. Raiâ, M.Y.; Masrour, R.; Hamedoun, M.; Kharbach, J.; Rezzouk, A.; Hourmatallah, A.; Benzakour, N.; Bouslykhane, K. Stability, magnetic, electronic, elastic, thermodynamic, optical, and thermoelectric properties of Co2TiSn, Co2ZrSn and Co2HfSn Heusler alloys from calculations using generalized gradient approximation techniques. *J. Mater. Sci. Mater. Electron.* **2022**, *33*, 20229–20256.

107. Ziebeck, K.R.A.; Webster, P.J. A neutron diffraction and magnetization study of Heusler alloys containing Co and Zr, Hf, V or Nb. *J. Phys. Chem. Solids* **1974**, *35*, 1–7.

108. Kanomata, T.; Amako, Y.; Ida, Y.; Adachi, Y.; Osaki, T.; Eto, T.; Nishihara, H.; Shigeta, I.; Imada, S.; Doi, M. Magnetic properties of ferromagnetic Heusler alloy Co2ZrSn. *J. Phys. Chem. Solids* **2022**, 110635, doi:https://doi.org/10.1016/j.jpcs.2022.110635.

109. Terada, M.; Fujita, Y.; Endo, K. Magnetic properties of the Heusler alloys M2XSn (M= Co or Ni, X= Zr, Nb or Hf). *J. Phys. Soc. Japan* **1974**, *36*, 620.

110. Skolozdra, R. V; Stadnyk, Y. V; Gorelenko, Y.K.; Terletskaya, E.E. Influence of vacancies on the magnetic and electrical properties of Heusler phases Me'Co2-xSn (Me'= Ti, Zr, Hf). *Sov. physics. Solid state* **1990**, *32*, 1536–1538.

111. Ślebarski, A.; Jezierski, A.; Neumann, M.; Plogmann, S. Influence of vacancies on the electronic structure of CoZrSn Heusler alloys. *Eur. Phys. J. B-Condensed Matter Complex Syst.* **1999**, *12*, 519–523.

112. Zhang, W.; Qian, Z.; Sui, Y.; Liu, Y.; Su, W.; Zhang, M.; Liu, Z.; Liu, G.; Wu, G. Magnetism and Hall effect of the Heusler alloy Co2ZrSn synthesized by melt-spinning process. *J. Magn. Magn. Mater.* **2006**, *299*, 255–259.

113. Baggio-Saitovitch, E.; Butz, T.; Vasquez, A.; Vincze, I.; Wagner, F.E.; Endo, K. Hyperfine fields in Co-based Heusler alloys. *Le J. Phys. Colloq.* **1976**, *37*, C6--417.

114. Kushwaha, S.K.; Stolze, K.; Wang, Z.; Hirschberger, M.; Lin, J.; Bernevig, B.A.; Ong, N.P.; Cava, R.J. Crystal growth and stoichiometry-dependent properties of the ferromagnetic Weyl semimetal ZrCo2- xSn. *J. Phys. Condens. Matter* **2017**, *29*, 225702.

115. Yin, M.; Chen, S.; Nash, P. Enthalpies of formation of selected Co2YZ Heusler compounds. *J. Alloys Compd.* **2013**, *577*, 49–56.

116. Difalco, A.; Aversano, F.; Boldrini, S.; Ferrario, A.; Baricco, M.; Castellero, A. Synthesis and Characterization of Thermoelectric Co2XSn (X = Zr, Hf) Heusler Alloys. *Metals (Basel).* **2020**, *10*, 624.

117. Lutterotti, L.; Matthies, S.; Wenk, H.-R. MAUD (material analysis using diffraction): a user friendly Java program for Rietveld texture analysis and more. In Proceedings of the Proceeding of the twelfth international conference on textures of materials (ICOTOM-12); 1999; Vol. 1, p. 1599.

118. Kainuma, Y. The theory of Kikuchi patterns. *Acta Crystallogr.* **1955**, *8*, 247–257.

119. Boldrini, S.; Famengo, A.; Montagner, F.; Battiston, S.; Fiameni, S.; Fabrizio, M.; Barison, S. Test rig for high-temperature thermopower and electrical conductivity measurements. *J. Electron. Mater.* **2013**, *42*, 1319–1323.

120. Rouleau, O.; Alleno, E. Measurement system of the Seebeck coefficient or of the electrical resistivity at high temperature. *Rev. Sci. Instrum.* **2013**, *84*.

121. Hohenberg, P.; Kohn, W. Inhomogeneous electron gas. *Phys. Rev.* **1964**, *136*, B864.

122. Kohn, W.; Sham, L.J. Self-consistent equations including exchange and correlation effects. *Phys. Rev.* **1965**, *140*, A1133.

123. Dirac, P.A.M. On the theory of quantum mechanics. *Proc. R. Soc. London. Ser. A, Contain. Pap. a Math. Phys. Character* **1926**, *112*, 661–677.

124. Löwdin, P.-O. Quantum theory of many-particle systems. III. Extension of the Hartree-Fock scheme to include degenerate systems and correlation effects. *Phys. Rev.* **1955**, *97*, 1509.

125. Jones, R.O.; Gunnarsson, O. The density functional formalism, its applications and prospects. *Rev. Mod. Phys.* **1989**, *61*, 689.

126. Dreizler, R.M.; Gross, E.K.U. *Density functional theory: an approach to the quantum many-body problem*; Springer Science \& Business Media, 2012;

127. Perdew, J.P.; Burke, K.; Ernzerhof, M. Generalized gradient approximation made simple. *Phys. Rev. Lett.* **1996**, *77*, 3865.

128. Woods, N. On the nature of self-consistency in density functional theory. *arXiv Prepr. arXiv1803.01763* **2018**.

129. Blöchl, P.E. Projector augmented-wave method. *Phys. Rev. B* **1994**, *50*, 17953.

130. Togo, A. First-principles phonon calculations with phonopy and phono3py. *J. Phys. Soc. Japan* **2023**, *92*, 12001.

131. Madsen, G.K.H.; Carrete, J.; Verstraete, M.J. BoltzTraP2, a program for interpolating band structures and calculating semi-classical transport coefficients. *Comput. Phys. Commun.* **2018**, *231*, 140–145.

132. Edwards, D.M.; Wohlfarth, E.P. Magnetic isotherms in the band model of ferromagnetism. *Proc. R. Soc. London. Ser. A. Math. Phys. Sci.* **1968**, *303*, 127–137.

133. Wohlfarth, E.P. Very weak itinerant ferromagnets; Application to ZrZn2. *J. Appl. Phys.* **1968**, *39*, 1061–1066.

134. Yeung, I.; Roshko, R.M.; Williams, G. Arrott-plot criterion for ferromagnetism in disordered systems. *Phys. Rev. B* **1986**, *34*, 3456.

135. Barry, A.; Coey, J.M.D.; Ranno, L.; Ounadjela, K. Evidence for a gap in the excitation spectrum of CrO2. *J. Appl. Phys.* **1998**, *83*, 7166–7168.

136. Villars, P.; Prince, A.; Okamoto, H.; others *Handbook of ternary alloy phase diagrams*; ASM international Materials Park, OH, 1995; Vol. 5;.

137. Ponton, C.B.; Rawlings, R.D. Vickers indentation fracture toughness test Part 1 Review of literature and formulation of standardised indentation toughness equations. *Mater. Sci. Technol.* **1989**, *5*, 865–872.

138. Roebuck, B.; Bennett, E.G.; Lay, L.A.; Morrell, R. *The measurement of palmqvist toughness for hard and brittle materials.*; Queen's Printer for Scotland, 2008;

139. Madeiros, E.E.; Dias, A.M.S. Experimental and numerical analysis of Vickers hardness testing. *Int. J. Res. Rev. Appl. Sci* **2013**, *17*, 9–18.

140. Faisal, N.H.; Ahmed, R.; Prathuru, A.K.; Spence, S.; Hossain, M.; Steel, J.A. An improved Vickers indentation fracture toughness model to assess the quality of thermally sprayed coatings. *Eng. Fract. Mech.* **2014**, *128*, 189–204, doi:10.1016/j.engfracmech.2014.07.015.

141. Sktani, Z.D.I.; Rejab, N.A.; Ratnam, M.M.; Ahmad, Z.A. Fabrication of tougher ZTA ceramics with sustainable high hardness through (RSM) optimisation. *Int. J. Refract. Met. Hard Mater.* **2018**, *74*, 78–86, doi:10.1016/j.ijrmhm.2018.03.006.

142. Liang, K.M.; Orange, G.; Fantozzi, G. Evaluation by indentation of fracture toughness of ceramic materials. *J. Mater. Sci.* **1990**, *25*, 207–214, doi:10.1007/BF00544209.

143. Bradt, R.C. *Fracture Mechanics on Ceramics: 3rd International Symposium Held July 15-17, 1983, at the Pennsylvania State University in University Park, Pennsylvania*; Plenum Press, 1983;

144. Shetty, D.K.; Wright, I.G.; Mincer, P.N.; Clauer, A.H. Indentation fracture of WC-Co cermets. *J. Mater. Sci.* **1985**, *20*, 1873–1882.

145. Ashby, M.F. Materials selection in mechanical design.: Kidlington 2011.

146. Rogl, G.; Grytsiv, A.; Gürth, M.; Tavassoli, A.; Ebner, C.; Wünschek, A.; Puchegger, S.; Soprunyuk, V.; Schranz, W.; Bauer, E.; et al. Mechanical properties of half-Heusler alloys. *Acta Mater.* **2016**, *107*, 178–195.

147. Shimizu, M. Itinerant electron magnetism. *Reports Prog. Phys.* **1981**, *44*, 329.

148. Yamasaki, A.; Imada, S.; Arai, R.; Utsunomiya, H.; Suga, S.; Muro, T.; Saitoh, Y.; Kanomata, T.; Ishida, S. Orbital angular momentum and interpretation of core-absorption magnetic circular dichroism on the band picture in Co-based Heusler alloys Co2YSn (Y= Ti, Zr, and Nb). *Phys. Rev. B* **2002**, *65*, 104410.

149. Buschow, K.H.J. Differences in magnetic properties between amorphous and crystalline alloys. *J. Appl. Phys.* **1982**, *53*, 7713–7716.

150. Fujii, H.; Pourarian, F.; Wallace, W.E. Appearance of spontaneous ferromagnetism in non-stoichiometric ZrCo2. *J. Magn. Magn. Mater.* **1981**, *24*, 93–96.

151. Ikeda, K. Electrical Resistivity of Laves Phase Compounds Containing Transition Elements. II. Co2A (A= Ti, Y, Zr, and Nb). *J. Phys. Soc. Japan* **1977**, *42*, 1541–1546.

152. Li, S.X.; Yu, K.M.; Wu, J.; Jones, R.E.; Walukiewicz, W.; Ager III, J.W.; Shan, W.; Haller, E.E.; Lu, H.; Schaff, W.J. Fermi-level stabilization energy in group III nitrides. *Phys. Rev. B* **2005**, *71*, 161201.

153. Dashevsky, Z.; Shusterman, S.; Dariel, M.P.; Drabkin, I. Thermoelectric efficiency in graded indium-doped PbTe crystals. *J. Appl. Phys.* **2002**, *92*, 1425–1430.

154. De Souza, S.D.; Saxena, R.N.; Shreiner, W.; Zawislak, F.C. Magnetic hyperfine fields in Heusler alloys Co YZ (Y= Ti, Zr; Z= Al, Ga, Sn). *Hyperfine Interact.* **1987**, *34*, 431–434.

155. Mehdizadeh Dehkordi, A.; Zebarjadi, M.; He, J.; Tritt, T.M. Thermoelectric power factor: Enhancement mechanisms and strategies for higher performance thermoelectric materials. *Mater. Sci. Eng. R Reports* **2015**, *97*, 1–22, doi:10.1016/j.mser.2015.08.001.

156. Alleno, E. Review of the thermoelectric properties in nanostructured Fe2VAl. *Metals (Basel).* **2018**, *8*, 864.

157. Kurosaki, K.; Muta, H.; Endo, Y.; Charoenphakdee, A.; Uno, M.; Yamanaka, S. Effect of Nb substitution for V on the thermoelectric properties of Fe2VAl. *J. Alloys Compd.* **2009**, *486*, 507–510, doi:10.1016/j.jallcom.2009.06.202.

158. Al-Yamani, H.; Hamad, B. Thermoelectric Properties of Fe2VAl and Fe2V0.75M0.25Al (M = Mo, Nb, Ta) Alloys: First-Principles Calculations. *J. Electron. Mater.* **2016**, *45*, 1101–1114, doi:10.1007/s11664-015-4265-8.

159. Hinterleitner, B.; Knapp, I.; Poneder, M.; Shi, Y.; Müller, H.; Eguchi, G.; Eisenmenger-Sittner, C.; Stöger-Pollach, M.; Kakefuda, Y.; Kawamoto, N.; et al. Thermoelectric performance of a metastable thin-film Heusler alloy. *Nature* **2019**, *576*, 85–90.

160. Kimura, Y.; Chai, Y.W. Ordered Structures and Thermoelectric Properties of MNiSn (M = Ti, Zr, Hf)-Based Half-Heusler Compounds Affected by Close Relationship with Heusler Compounds. *Jom* **2015**, *67*, 233–245, doi:10.1007/s11837-014-1233-3.

161. Pierre, J.; Skolozdra, R. V; Tobola, J.; Kaprzyk, S.; Hordequin, C.; Kouacou, M.A.; Karla, I.; Currat, R.; Lelievre-Berna, E. Properties on request in semi-Heusler phases. *J. Alloys Compd.* **1997**, *262*, 101–107.

162. Otto, M.J.; Feil, H.; Van Woerden, R.A.M.; Wijngaard, J.; Van Der Valk, P.J.; Van Bruggen, C.F.; Haas, C. Electronic structure and magnetic, electrical and optical properties of ferromagnetic Heusler alloys. *J. Magn. Magn. Mater.* **1987**, *70*, 33–38.

163. Kresse, G.; Furthmüller, J. Efficient iterative schemes for ab initio total-energy calculations using a plane-wave basis set. *Phys. Rev. B* **1996**, *54*, 11169.

164. Kim, H.-S.; Gibbs, Z.M.; Tang, Y.; Wang, H.; Snyder, G.J. Characterization of Lorenz number with Seebeck coefficient measurement. *APL Mater.* **2015**, *3*.

165. Xu, X.; Nagasako, M.; Kataoka, M.; Umetsu, R.Y.; Omori, T.; Kanomata, T.; Kainuma, R. Anomalous physical properties of Heusler-type Co 2 Cr (Ga, Si) alloys and thermodynamic study on reentrant martensitic transformation. *Phys. Rev. B* **2015**, *91*, 104434.

166. Roth, N.; Zhu, T.; Iversen, B.B. A simple model for vacancy order and disorder in defective half-Heusler systems. *IUCrJ* **2020**, *7*, 673–680.

167. Maier, S.; Denis, S.; Adam, S.; Crivello, J.-C.; Joubert, J.-M.; Alleno, E. Order-disorder transitions in the Fe2VAl Heusler alloy. *Acta Mater.* **2016**, *121*, 126–136.

168. Nolze, G.; Kraus, W. PowderCell 2.0 for windows. *Powder Diffr.* **1998**, *13*, 256–259.

169. Diack-Rasselio, A.; Rouleau, O.; Coulomb, L.; Georgeton, L.; Beaudhuin, M.; Crivello, J.-C.; Alleno, E. Influence of self-substitution on the thermoelectric Fe2VAl Heusler alloy. *J. Alloys Compd.* **2022**, *920*, 166037.

170. Mahat, R.; Kc, S.; Karki, U.; Law, J.Y.; Franco, V.; Galanakis, I.; Gupta, A.; LeClair, P. Possible half-metallic behavior of Co 2- x Cr x FeGe Heusler alloys: Theory and experiment. *Phys. Rev. B* **2021**, *104*, 14430.

171. Webster, P.J. Magnetic and chemical order in Heusler alloys containing cobalt and manganese. *J. Phys. Chem. Solids* **1971**, *32*, 1221–1231.

172. Toby, B.H. R factors in Rietveld analysis: How good is good enough? *Powder Diffr.* **2006**, *21*, 67–70.

173. Cui, S.; Ouyang, G.; Ma, T.; Macziewski, C.R.; Levitas, V.I.; Zhou, L.; Kramer, M.J.; Cui, J. Thermodynamic and kinetic analysis of the melt spinning process of Fe-6.5 wt.\% Si alloy. *J. Alloys Compd.* **2019**, *771*, 643–648.

174. Hordequin, C.; Pierre, J.; Currat, R. Magnetic excitations in the half-metallic NiMnSb ferromagnet: From Heisenberg-type to itinerant behaviour. *J. Magn. Magn. Mater.* **1996**, *162*, 75–84.

175. Ristoiu, D.; Nozieres, J.P.; Ranno, L. Epitaxial NiMnSb thin films prepared by facing targets sputtering. *J. Magn. Magn. Mater.* **2000**, *219*, 97–103.

176. Hu, C.; Xia, K.; Fu, C.; Zhao, X.; Zhu, T. Carrier grain boundary scattering in thermoelectric materials. *Energy \& Environ. Sci.* **2022**, *15*, 1406–1422.

177. Slack, G.A. The thermal conductivity of nonmetallic crystals. *Solid state Phys.* **1979**, *34*, 1–71.

178. Csonka, G.I.; Perdew, J.P.; Ruzsinszky, A.; Philipsen, P.H.T.; Lebègue, S.; Paier, J.; Vydrov, O.A.; Ángyán, J.G. Assessing the performance of recent density functionals for bulk solids. *Phys. Rev. B* **2009**, *79*, 155107.

179. Kresse, G.; Joubert, D. From ultrasoft pseudopotentials to the projector augmented-wave method. *Phys. Rev. b* **1999**, *59*, 1758.

180. Monkhorst, H.J.; Pack, J.D. Special points for Brillouin-zone integrations. *Phys. Rev. B* **1976**, *13*, 5188.

181. Blanco, J.A.; Pisonero, J. Itinerant band weak ferromagnetism from the Stoner equations. *Eur. J. Phys.* **1999**, *20*, 289.

182. Palumbo, M.; Burton, B.; e Silva, A.; Fultz, B.; Grabowski, B.; Grimvall, G.; Hallstedt, B.; Hellman, O.; Lindahl, B.; Schneider, A.; et al. Thermodynamic modelling of crystalline unary phases. *Phys. status solidi* **2014**, *251*, 14–32.

183. Körmann, F.; Breidi, A.A.H.; Dudarev, S.L.; Dupin, N.; Ghosh, G.; Hickel, T.; Korzhavyi, P.; Munoz, J.A.; Ohnuma, I. Lambda transitions in materials science: Recent advances in CALPHAD and first-principles modelling. *Phys. status solidi* **2014**, *251*, 53–80.

184. Barreteau, C.; Crivello, J.-C.; Joubert, J.-M.; Alleno, E. Optimization of criteria for an efficient screening of new thermoelectric compounds: The tinisi structure-type as a case-study. *ACS Comb. Sci.* **2020**, *22*, 813–820.

185. Belomestnykh, V.N. The acoustical Grüneisen constants of solids. *Tech. Phys. Lett.* **2004**, *30*, 91–93.

186. Breidi, A.; Fries, S.G.; Palumbo, M.; Ruban, A. V First-principles modeling of energetic and mechanical properties of Ni--Cr, Ni--Re and Cr--Re random alloys. *Comput. Mater. Sci.* **2016**, *117*, 45–53.

187. Hill, R. The elastic behaviour of a crystalline aggregate. *Proc. Phys. Soc. Sect. A* **1952**, *65*, 349.

188. Voigt, W.; others On the relation between the elasticity constants of isotropic bodies. *Ann. Phys. Chem* **1889**, *274*, 573–587.

189. Reuss, A. Berechnungderfliegrenzevonmischkristallenaufgrund der plastizittsbedingung fr einkristalle. *ZAMM J. Appl. Math. Mech* **1929**, *9*, 49–58.

190. Mehl, M.J. Pressure dependence of the elastic moduli in aluminum-rich Al-Li compounds. *Phys. Rev. B* **1993**, *47*, 2493.

191. Domb, C.; Salter, L. CIX. The zero point energy and Θ crystals. *London, Edinburgh, Dublin Philos. Mag. J. Sci.* **1952**, *43*, 1083–1089.

Appendix A

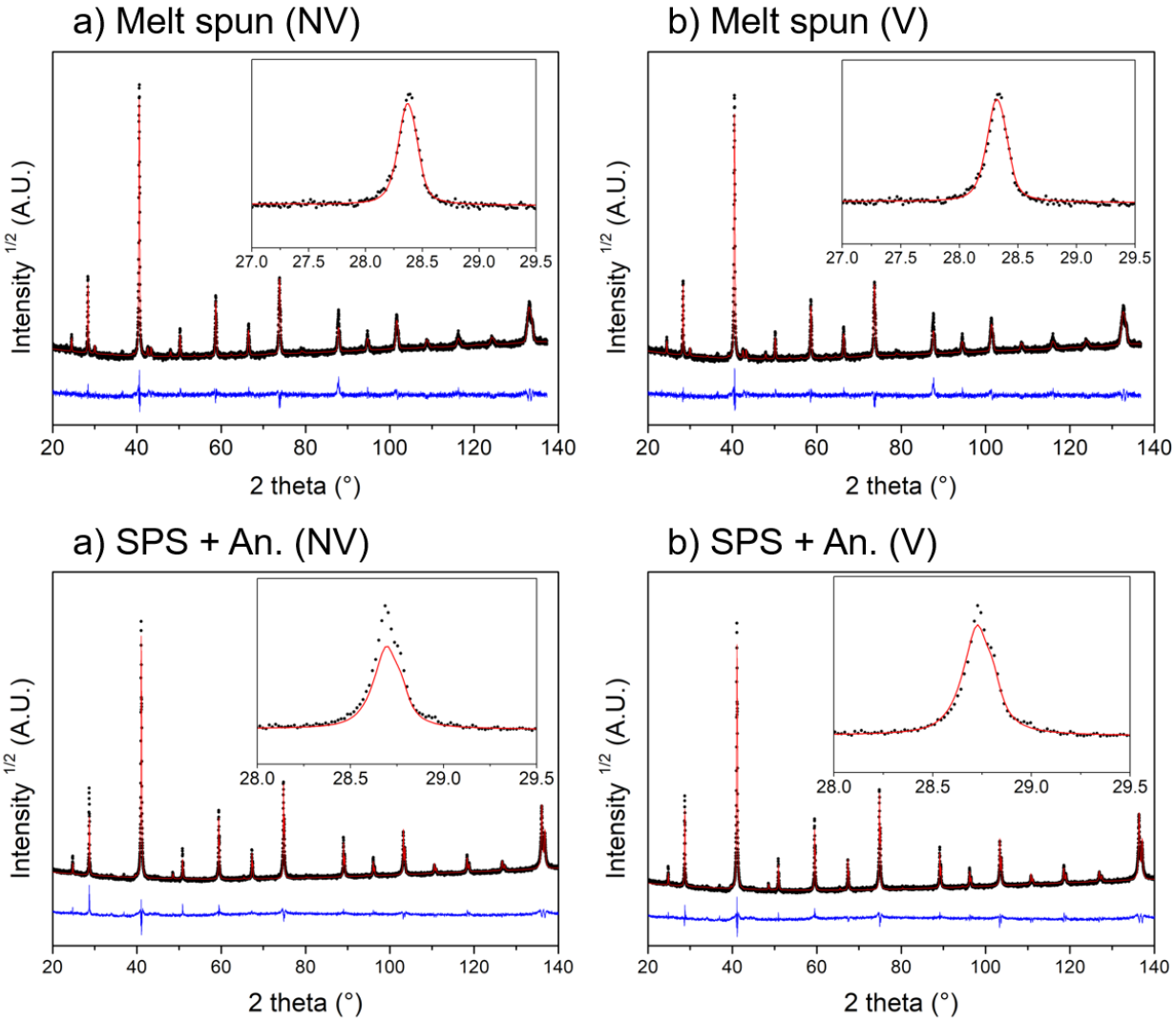

Figure A1: Rietveld refinements of a) non-defective (NV) melt-spun; b) defective (V) melt-spun; c) non-defective SPS+annealed; d) defective SPS+annealed Co_2ZrSn samples.

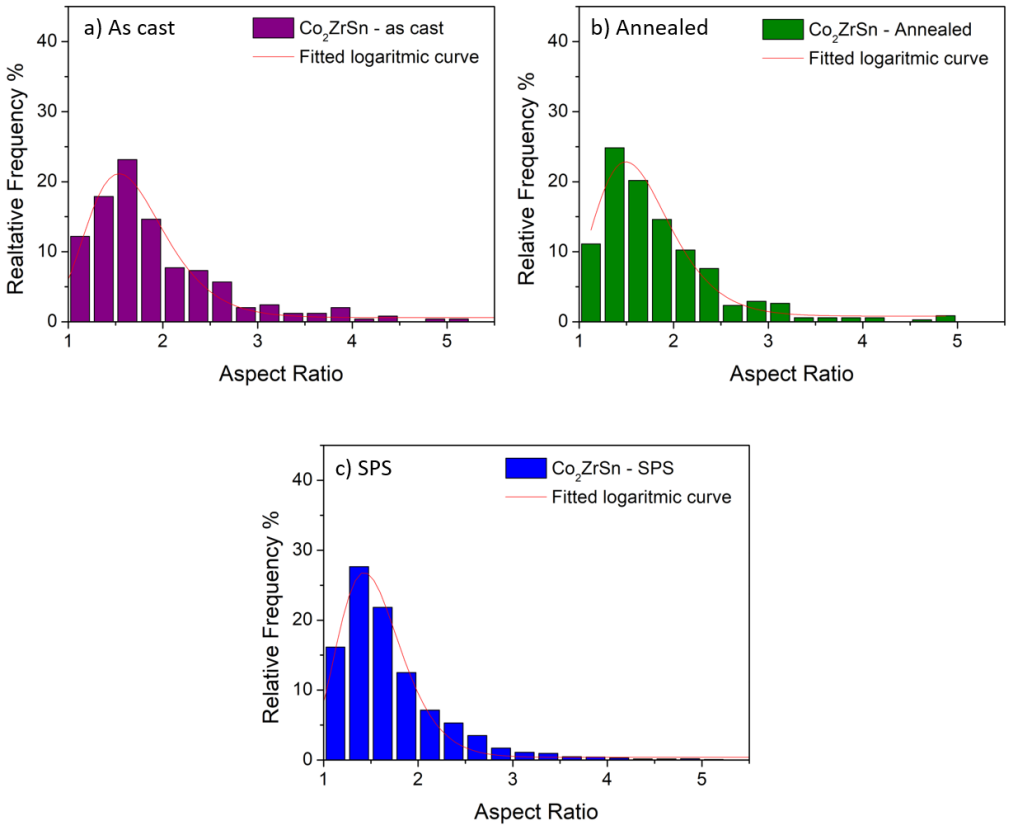

Figure A2: Ellipsoid aspect ratio distribution of (a) as cast, (b) annealed, (c) SPS Co_2ZrSn samples.

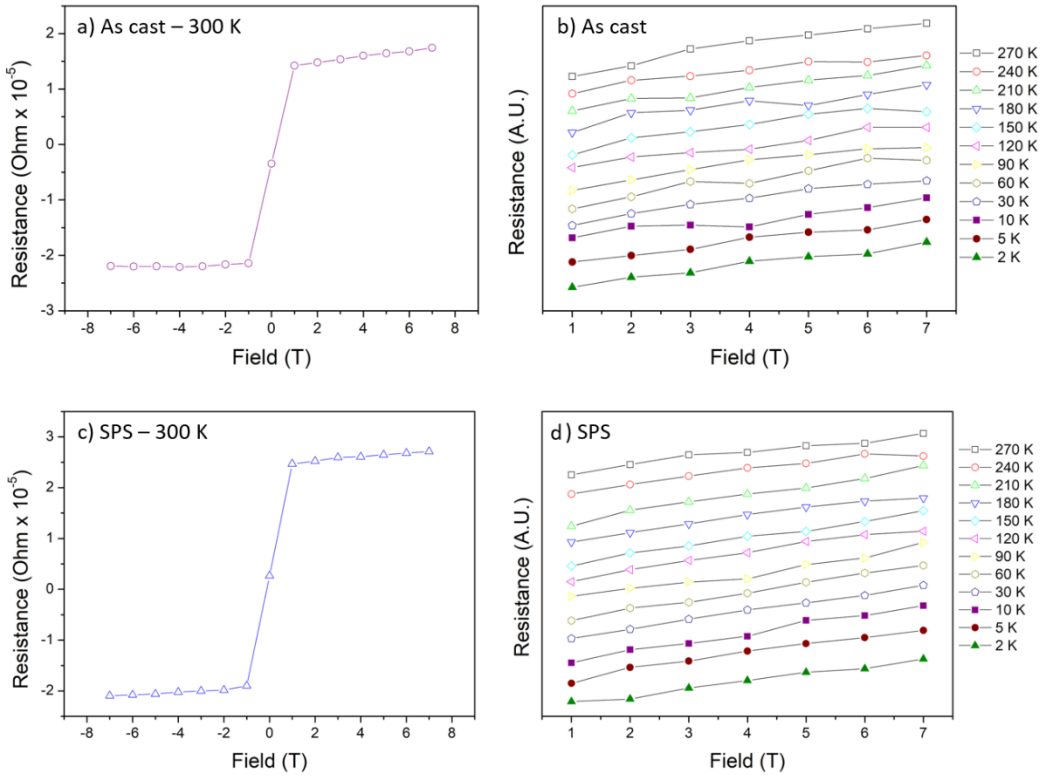

Figure A3: Hall resistivity at 300 K (a), (c) and from 2 to 270 K (b), (d) for the as cast and SPS samples, respectively.

Appendix B

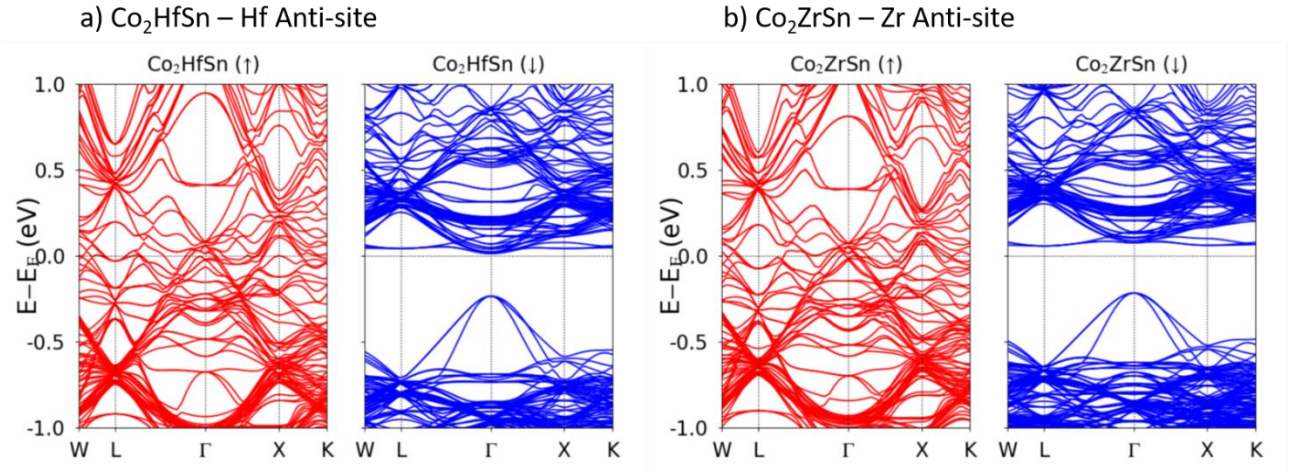

Figure B1: Electronic band structures of a) Hf anti-site defective Co_2HfSn and b) Zr anti-site defective Co_2ZrSn.

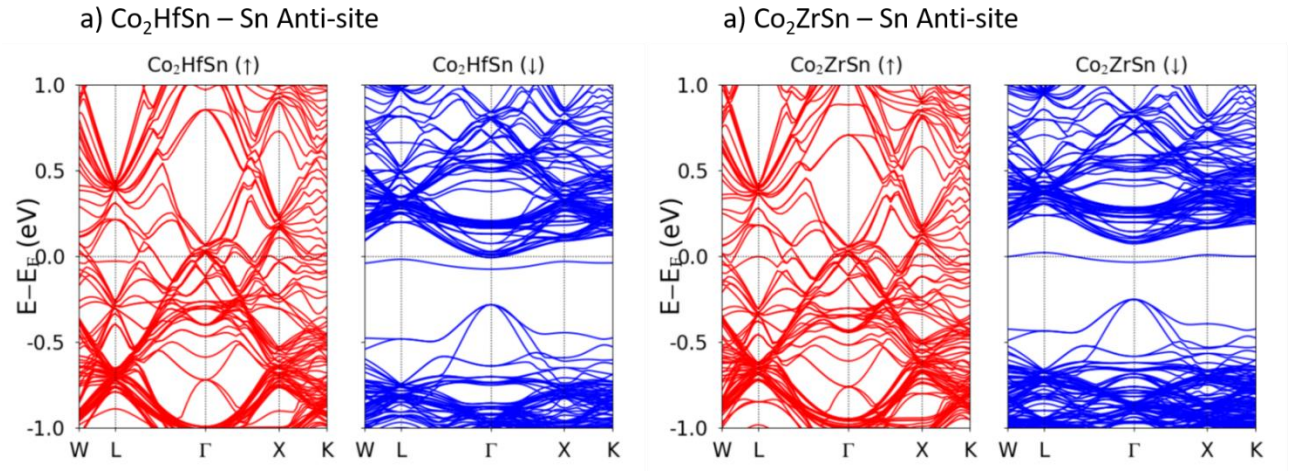

Figure B2: Electronic band structures of a) Sn anti-site defective Co_2HfSn and b) Sn anti-site defective Co_2ZrSn.

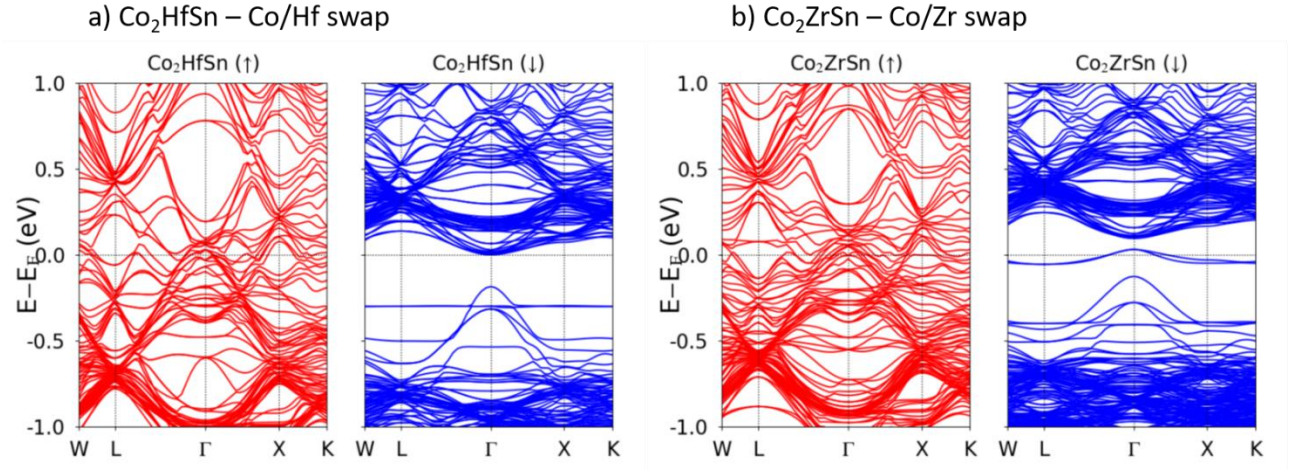

Figure B3: Electronic band structures of a) Co/Hf swap defective Co_2HfSn and b) Co/Zr swap defective Co_2ZrSn.

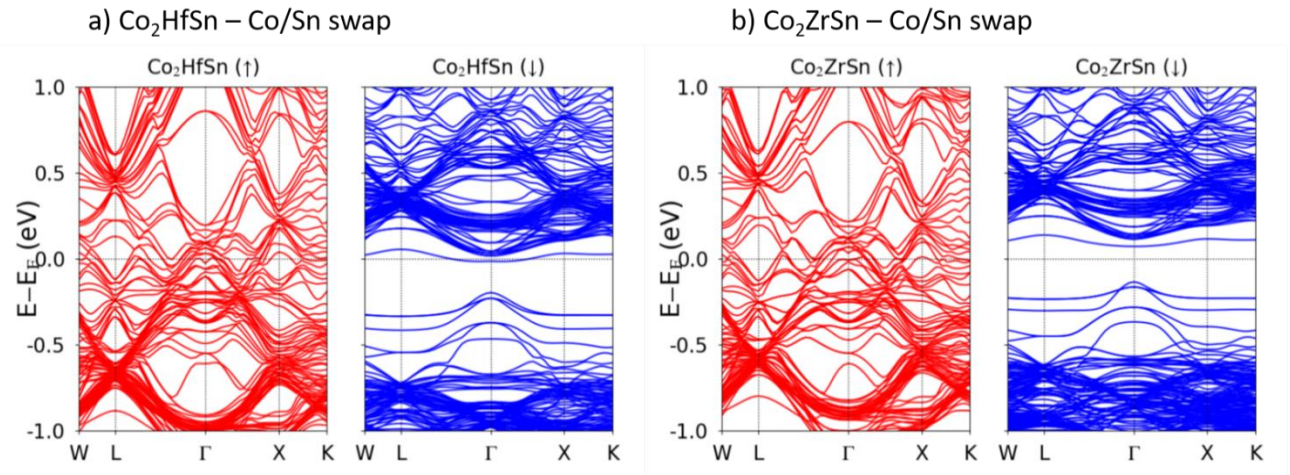

Figure B4: Electronic band structures of a) Co/Sn swap defective Co_2HfSn and b) Co/Sn swap defective Co_2ZrSn.

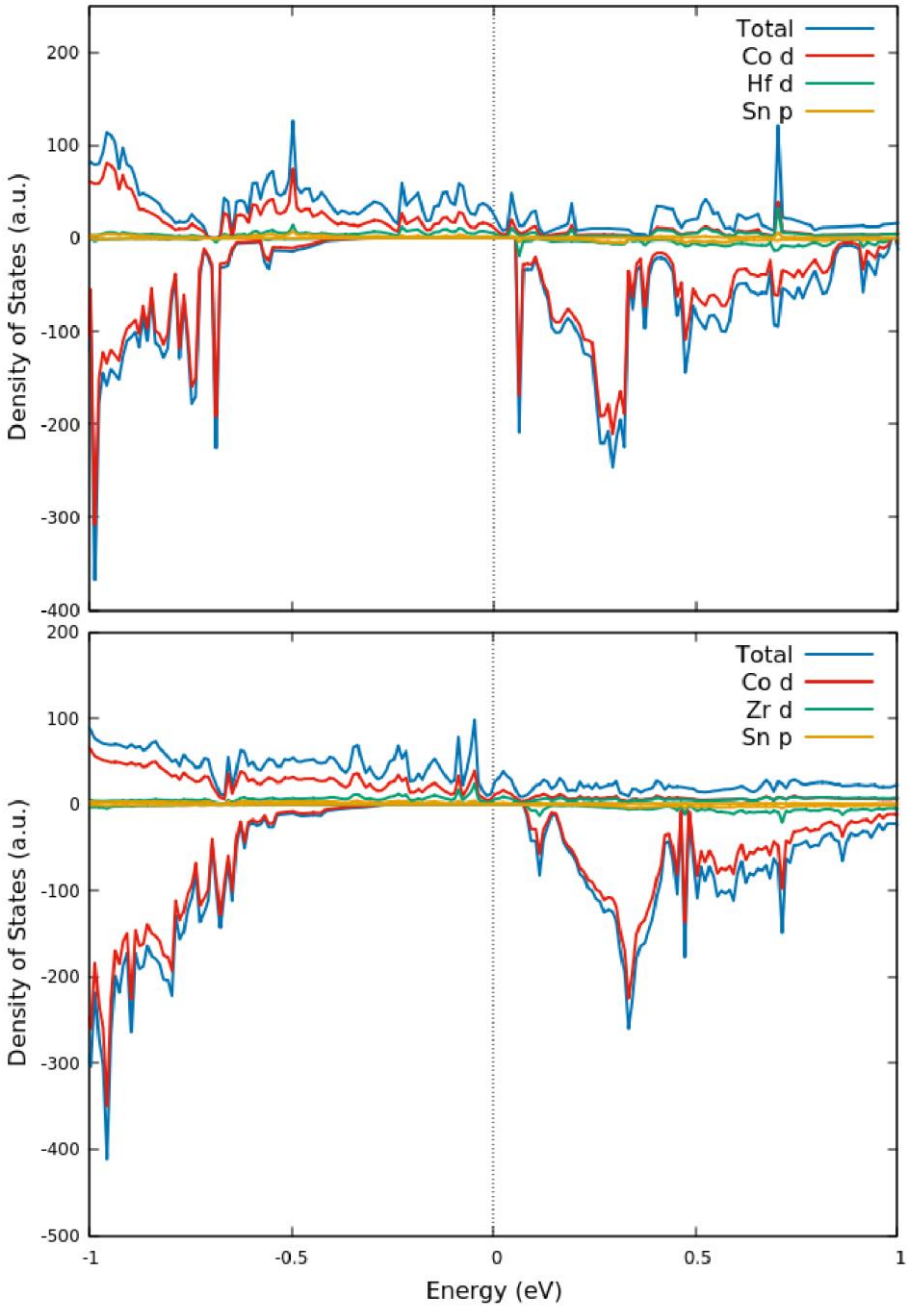

Figure B5: Electronic density of states of (top) Hf anti-site defective Co_2HfSn and (bottom) Zr anti-site defective Co_2ZrSn.

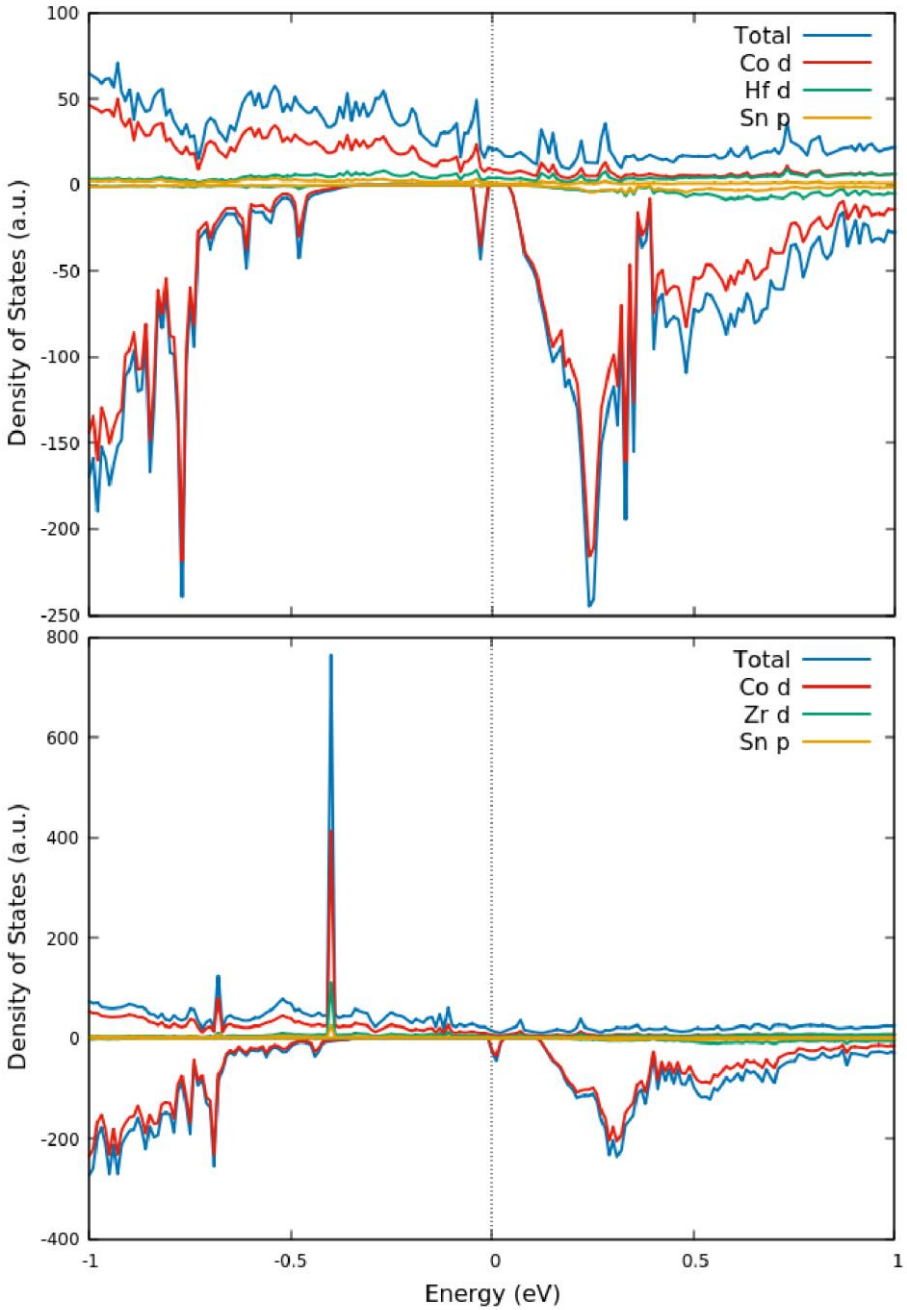

Figure B6: Electronic density of states of (top) Sn anti-site defective Co_2HfSn and (bottom) Sn anti-site defective Co_2ZrSn.

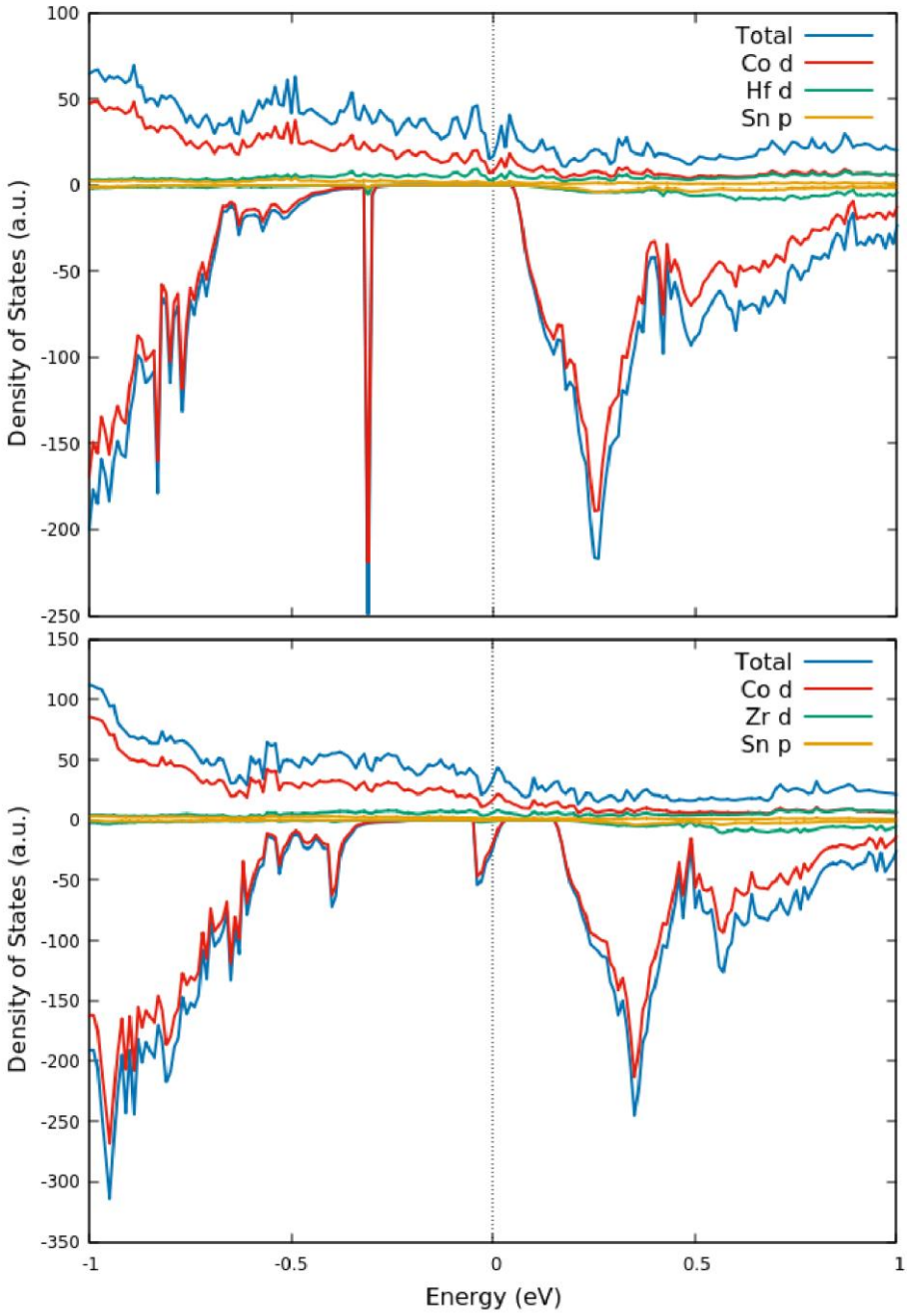

Figure B7: Electronic density of states of (top) Co/Hf swap defective Co_2HfSn and (bottom) Co/Zr swap defective Co_2ZrSn.

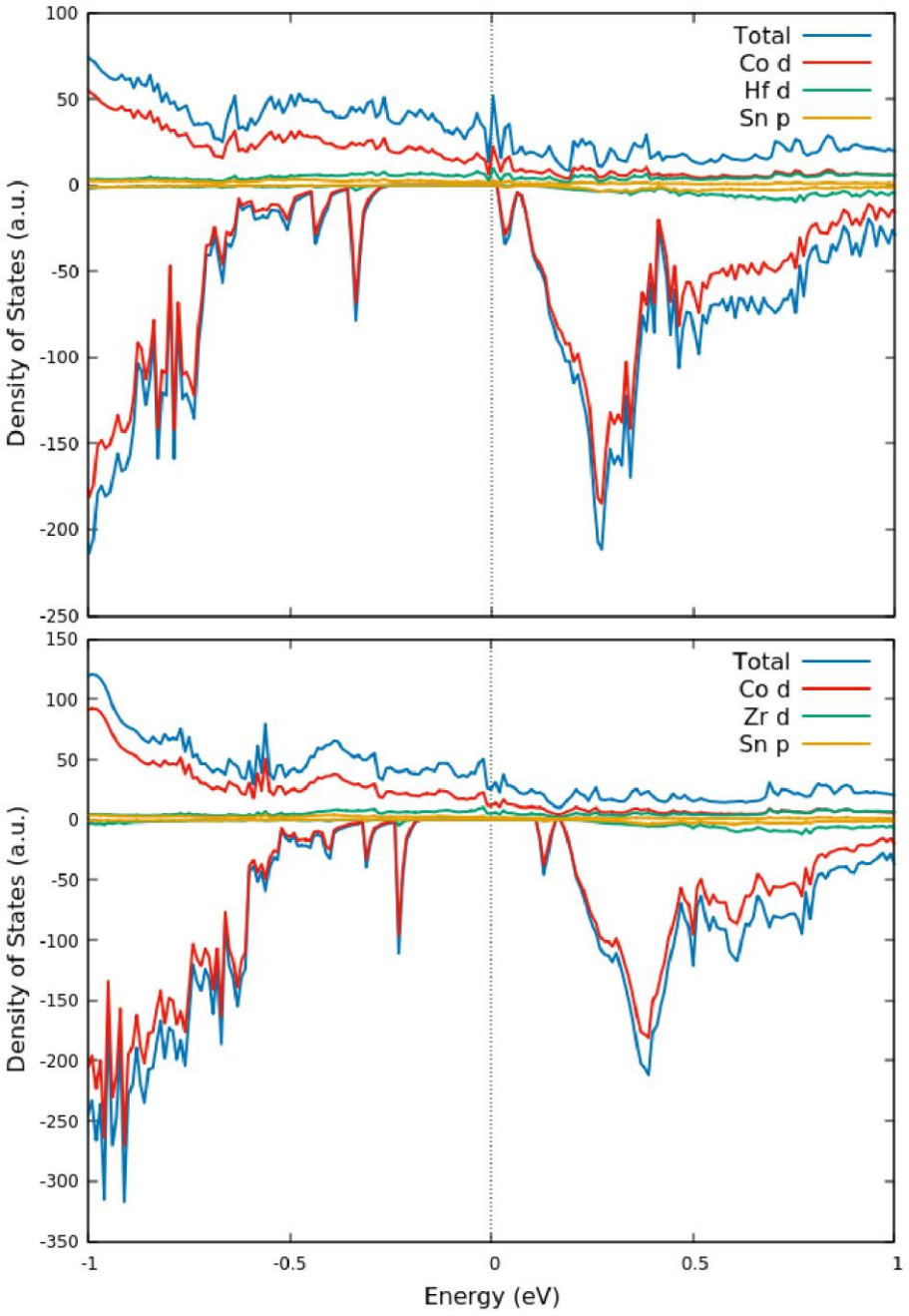

Figure B8: Electronic density of states of (top) Co/Sn swap defective Co_2HfSn and (bottom) Co/Sn swap defective Co_2ZrSn.

Final report of PhD activities

Courses and schools:

- Lyondell-Basell: From the first Ziegler-Natta catalyst to polymer circularity, virtual school, 22-26/2/2021.
- CrisDi 2021, virtual school, 21/6/2021 – 22/7/2021:
    - BC1: Introduction to crystallography
    - BC2: X-ray diffraction
    - BC3: Electron diffraction
    - BC4: Instrumentation for X-ray diffraction
    - BC5: X-ray diffraction methods: polycrystalline
    - BC6: X-ray diffraction methods: single crystal
    - SC1: The Rietveld method
    - SC2: High pressure in-situ experiments: diamond and anvil cell
    - SC3: Use of TEM-EDS for the characterization of natural and synthetic sub-micrometric inorganic phases
    - SC4: In-situ/operando X-ray powder diffraction
    - SC5: Pair distribution function analysis of complex, disorder, and amorphous materials from total scattering data
    - SC6: The Debye scattering equation: a total scattering approach for characterizing nanomaterials
- Raman Day, Prof. Ferrando-Turci, Unito – Dep. Of Earth Sciences.
- An insight into epistemological and didactic issues related with science teaching, Prof. Ghibaudi-Cerrato, Unito – Dep. Of Chemistry.
- From biomass to chemicals and biopolymers towards a sustainable future, Prof. Tabasso, Unito – Dep. of Chemistry.
- Engine exhaust after-treatment systems, Prof. Sgroi, Unito – Dep. of Chemistry.
- Lean thinking for innovation and innovation, Prof. Bianco Prevot-Prenesti, Unito – Dep. of Chemistry.
- Corso di corrosione per non corrosionisti, virtual school, AIM, 24-25/11/2021.
- Microscopia elettronica in scansione per metallurgist, Milano-Lecco, CNR, 21-22/6/2022.
- EBSD: come e perché, Aosta, Cogne Acciai Speciali, 14/11/2023.

Participation to conferences and seminars:

- $LiBH_4$ as solid state electrolyte for Li-ion batteries: modelling, synthesis, characterization and application, Doc. Gulino, Torino, 2/11/2020.
- Venerdì della SCI, Prof. Bordiga-Farinola-Cozzi, virtual seminar, 13-20-27/11/2020.
- ECOscienza Europea, virtual congress, 26-27/11/2020.
- sTE^2C Virtual Colloquium, virtual conference, 19/11/2020.
- Eureka! Venture incontra i ricercatori dell'Università di Torino, virtual conference, 14/12/2020.
- Aluminum alloys in additive manufacturing: from powder production to post-processing thermal treatments; Doc. Gianoglio, virtual seminar, 22/1/2021.
- 38° Convegno AIM, virtual conference, 25-26/1/2021.
- GiTe 2021, virtual conference, 17-18/2/2021.
- WOCTS – World Online Conference on Sustainable Technologies 2021, virtual conference, 17-18/3/2021.
- The life cycle assessment methodology to support the study of materials, M. Costamagna, virtual seminar, 24/4/2021.
- New-Times in material and science engineering 2021, virtual conference, 17-19/3/2021.
- Aging phenomena in Li-ion batteries: an automotive perspective, Doc. Dotoli, Torino, 7/7/2021.

- EUROMAT 2021, virtual conference, 13-17/9/2021.
- Innovative secondary aluminum alloys for HPDC structural components, E. Bongiovanni, Torino, 17/12/2021.
- GiTe 2022, Pisa, 16-17/2/2022.
- Hydrides for solid state magnesium batteries; looking to the state of art to design the future, A. Mazzucco, Torino, 8/3/2022.
- Hydrogen storage and compression based on metal hydrides, Doc. Barale, 1/6/2022.
- Metallurgy laboratory meeting 2022, Vaie, 6/7/2022.
- Physical chemistry and the challenges of ecological transition, 4-5-7/7/2022.
- ECT – European Conference on Thermoelectrics 2022, Barcelona, 14-16/9/2022.
- Science of Dirty Alloys (SoDA) and semi-solid casting processes: the future of foundry for the automotive sector? S. Ferraro, Torino, 10-2-2023.
- GiTe 2023, Trento, 13-14/2/2023.
- PhD days, Torino, 23/2/2023.
- Circular economy of AHSS: life cycle thinking and mechanical properties, F. Bruno, Torino, 3/4/2023.
- Metallurgy laboratory meeting 2023, Vaie, 17/7/2023.
- EUROMAT 2023, Frankfurt, 3-7/9/2023.
- ECT – European Conference on Thermoelectrics 2023, Prague, 17-21/9/2023.

Conference and seminar contributions (S: speaker, P: posters):

- Heusler alloys in thermoelectrics and spintronics (S), Metallurgy seminars, Torino, 20/10/2020.
- Synthesis and characterization of Co-based Heusler alloys (S), GiTe 2021, virtual conference, 18/2/2021.
- Synthesis and characterization of Co-based Heusler alloys for waste heat recovery (S), WOCST 2021, virtual conference, 19/3/2021.
- Co-based thermoelectric Heusler alloys: synthesis, transport and magnetic properties (S), New-Times in material and science engineering conference, virtual conference 16/6/2021.
- Co_2HfSn and Co_2ZrSn: synthesis, thermoelectric and magnetic properties (P), VCT 2021, virtual conference, 27/7/2021.
- Synthesis and characterization of Co-based Heusler alloys (P), EUROMAT 2021, virtual conference, 17/9/2021.
- Half-metallicity, itinerant magnetism and electronic properties of Co_2ZrSn and Co_2HfSn Heusler alloys (S), GiTe 2022, Pisa, 16/2/2022.
- Thermoelectric and magnetic properties of Co_2ZrSn and Co_2HfSn Heusler alloys, Physical chemistry and the challenges of the ecological transition (S), Genova, 5/7/2022.
- The effect of secondary phases and magnetic disorder in spintronic Co_2ZrSn and Co_2HfSn Heusler alloys (S), Metallurgy laboratory meeting 2022, Vaie, 6/7/2022.
- Thermoelectric and magnetic properties of Co_2ZrSn and Co_2HfSn Heusler alloys (P), ECT 2022, Barcelona, 15/9/2022.
- Magnetic and transport properties of Co2ZrSn and Co2HfSn obtained by rapid solidification and sintering (S), GiTe 2023, Trento, 13/9/2023.
- The role of processing on the transport properties of Co2ZrSn Heusler alloy for thermoelectric applications (P), EUROMAT 2023, Frankfurt, 7/9/2023.
- Transport properties of Co2HfSn Heusler alloy obtained by rapid solidification and sintering (S), ECT 2023, Prague, 18/9/2023.

Assistance for teaching:

- 25/11/2020 – 11/12/2020, Impianti chimici con laboratorio, Prof. Castellero.
- 11/12/2020 – 19/1/2021, Metallurgia, Doc. Scaglione.

- December 2021, Impianti chimici con laboratorio, Prof. Castellero.
- January 2022, Metallurgia, Doc. Scaglione.
- January 2023, Metallurgia; Doc. Scaglione.

Periods abroad:

- 5/9/2022 – 5/12/2022, CNRS-ICMPE (Thiais, France), Prof. Alleno.

Papers:

- On the PhD project:
  - A. Difalco, F. Aversano, S. Boldrini, A. Ferrario, M. Baricco and A. Castellero, Synthesis and Characterization of Thermoelectric Co_2XSn (X=Zr,Hf) Heusler alloys, Metals, 10(5), 624, https://doi.org/10.3390/met10050624.
  - A. Difalco, G. Barrera, M. Palumbo, A. Castellero, M. Baricco, P.M. Tiberto and P. Allia, "Itinerant magnetism, electronic properties and half-metallicity of Co_2ZrSn and Co_2HfSn Heusler alloys", Journal of Alloys and Compounds, 2022, 165464, https://doi.org/10.1016/j.jallcom.2022.165464.
  - A. Difalco, et al. "Transport properties of Co_2HfSn Heusler alloy obtained by rapid solidification and sintering.", Solid State Sciences 149 (2024): 107455, https://doi.org/10.1016/j.solidstatesciences.2024.107455.
  - A. Difalco, et al. "The role of vacancies on structural, transport, magnetic and half-metallic properties of Co2ZrSn Heusler alloy for spintronics.", Submitted.
- Outside the PhD project:
  - Gentile, F. S., Difalco, A., Pascale, F., Salustro, S., Mackrodt, W., and Dovesi, R. (2020). The spectroscopic characterization of interstitial oxygen in bulk silicon: A quantum mechanical simulation. The Journal of Chemical Physics, 152(5), https://doi.org/10.1063/1.5139564.
  - Matencio, A., Rubin Pedrazzo, A., Difalco, A., Navarro-Orcajada, S., Khazeai Monfared, Y., Conesa, I., ... and Trotta, F. (2021). Advances and classification of cyclodextrin-based polymers for food-related issues. Polymers, 13(23), 4226, https://doi.org/10.3390/polym13234226.

Acknowledgements

I would like to thank Prof. Castellero and all the people who collaborated and helped in the achievement of all these results, as Prof. Baricco, Prof. Palumbo, Prof. Allia, Prof. Tiberto, Prof. Alleno, Doc. Boldrini, Doc. Ferrario, Doc. Fanciulli, Doc. Barrera, Doc. Fiore, Doc. Rouleau, Doc. Villeroy, Doc. Aversano, and the others too.

Special thanks to my students, colleagues and friends S. Zappia, A. Righelli, and I. Winning, who also contributed with their scientific and moral support.

I am thankful to my parents and brother, who gave me the opportunity to study and achieve the highest possible degree of education. To my old ones, nonno Vittorio and Giovanni, and nonna Rosanna and Leonarda, who sixty years ago came in Turin with suitcases full only of clothes and hopes, and started all of this.

To my mentors during my University years and before, Prof. Dovesi, Prof. Urigu, Prof. Bertelli, Doc. Salustro, Doc. Gentile. To the people who bet the farm since the beginning, Gerardo, Daniela, and Ivano.

Thanks to the members of my "orchestra", Federico, Pietro, Stefano, Alberto, and Leonardo.

A warm regard goes also to Giancarla, Rinaldo, Davide, Kirti, Luca, Sara, Giulio, Marzia, Fabio, Federica, Stefano, Anna Maria, and Mr. "Getz" Cesare, and Mr. "Reno" Roger too.

The most important thought goes to the most cherished person in my life during the last three years, Annalisa. We achieved both marvelous greatness and abysmal wretchedness, we have been both lively and weary, we lived both as singlet and triplet electrons, and, most importantly, we did all this together.

+++

But they that wait upon the Lord shall renew their strength;

they shall mount up with wings as eagles;

they shall run, and not be weary;

and they shall walk, and not faint.

+ Isaiah 40:31 +